Hitching a ride:
Are vault RNAs selectively loaded into head and neck cancer derived extracellular vesicles?

Xinming Liu

A thesis submitted in partial fulfilment of the requirements for the degree of

Doctor of Philosophy

The University of Sheffield

Faculty of Medicine, Dentistry and Health

School of Clinical Dentistry

September 2021

Acknowledgements

First and foremost, I would like to express my deepest appreciation to Stuart. Thanks for your constant support and guidance throughout the past four years, and for always being there for me. I could not ask for a better supervisor, it was your endless patience, trust, and the willingness to always go extra miles that made me believe in myself and have come this far. I feel extremely lucky to be your student.

I would also like to say thank you to Prof Dan Lambert, the rest of the Hunt Lab, technical stuff and other colleagues in the Dental School for their knowledge and support. You have made the Dental School a fantastic place to work, and I knew I could always turn to you all for help whenever I need it.

Thanks to Liz Martin and Phil Mitchell from MBB, Chris Hill from EM facility, Sarah Elliott from Medical School, Zubair Nizamudeen and Kenton Arkill from University of Nottingham, Ben Peacock from NanoFCM, for your help and collaboration in this project, it would not be the same without you.

Thanks to all my friends in and outside Dental School, in particular Ash Gains, Kittie Ansbro, Beth Ollington, Cher Farrugia, Wenyi Jiang, Irene Zhang. Thanks for always being sympathetic and willing to listen, your company has made my PhD journey an enjoyable one. Thanks to my "friends in the time of corona", Gus, Louisa, Imo, Miryam, Emilio, the pandemic sucks, but I'm glad I had you all.

Special thanks to Tom for keeping me sane during writing up with your positivity and love, along with endless beautiful walks and tasty meals, I could not imagine doing it without you.

Thanks to Micky for being you and always being there for company.

Last but not least, thanks to my parents back in China, for always having confidence in me, supporting my decisions and taking part through numerous video calls along the way.

Abstract

Head and neck cancer (HNC) is the seventh most common cancer worldwide, of which oral squamous cell carcinoma (OSCC) accounts for 90% of all cases. Extracellular vesicles (EVs) have been shown to deliver functional RNA to recipient cells including vault RNA (vtRNA), which has been linked to many cancer-related cellular activities including multidrug resistance. VtRNA and major vault protein (MVP) have been repeatedly reported as EV cargo, and were also detected in OSCC-derived EVs in unpublished data from the Hunt Lab. In this study, the presence of vault particle components in EV preparations were determined and interrogated, followed by attempts to investigate their potential export mechanisms.

A cell panel including normal and immortalised oral cells, and three OSCC cell lines was used in this study. Cellular abundance of vault components was determined by western blotting and quantitative real-time polymerase chain reaction (qPCR). VtRNA abundance in EV preparations was determined by RNA-sequencing. The presence of vault components in EV preparations was interrogated by biochemical assays. Finally, siRNA transfection and CRISPR-Cas9 genome editing was performed to determine the effect of MVP/vault particle on the extracellular transport of vtRNA.

Vault components were abundant in OSCC cells and EV preparations, especially in small EV pellets. However, this was mainly due to co-isolated vault particles through commonly used EV isolation techniques. A vault-free EV isolation strategy was established by immunocapture of marker-positive EVs. MVP-knockdown reduced the extracellular abundance of full length vtRNA. MVP-knockout cell lines were successfully created to investigate vault-independent export of vtRNA.

Vault particles can contaminate EV preparations, confounding the determination of EV cargo. Vault-free isolation of EVs can be achieved by an immunoaffinity-based isolation. We demonstrated that the majority of extracellular full length vtRNA was vault-associated, highlighting a possible mechanism of vault particle export. Small RNA sequencing also suggested the presence of vtRNA fragments in small EVs, which could be advantageous to a developing tumour and its interaction with the tumour microenvironment.

Publication and presentations

Publication:

Liu X, Nizamudeen Z, Arkill K, Lambert DW, and Hunt S. Presence of vault RNA and proteins indicates contamination of extracellular vesicle preparations with vault particles. *In preparation*.

Oral presentations:

Liu X, Nizamudeen Z, Arkill K, Lambert DW, and Hunt S (2020). Presence of vault RNA and proteins indicates contamination of extracellular vesicle preparations with vault particles. *ISEV2020 Virtual Annual Meeting*.

Liu X, Lambert DW, and Hunt S (2019). Seeing is believing? Presence of vault RNA and major vault protein indicates vault particle contamination in extracellular vesicle preparations. *UKEV Forum 2019, the Francis Crick Institute, London.*

Liu X, Lambert DW, and Hunt S (2019). Transcriptomic analysis of oral cancer derived extracellular vesicles. *White Rose RNA Salon, University of Sheffield, Sheffield*.

Poster presentation:

Liu X, Lambert DW, and Hunt S (2019). Vault RNAs are overexpressed in oral cancer and enriched in small cancer-derived extracellular vesicles. *White Rose RNA Salon, University of Leeds, Leeds*.

Liu X, Lambert DW, and Hunt S (2018). Transcriptomic analysis of oral cancer derived extracellular vesicles. *UKEV Forum 2018, University of Sheffield, Sheffield*.

Liu X, Lambert DW, and Hunt S (2018). Transcriptomic analysis of oral cancer derived extracellular vesicles. *BACR Student Conference, The Francis Crick Institute, London*.

Abbreviations

Ψ	Pseudouridylation
A	Adenine
A_{280}	Absorbance at 280 nm
A_{488}	Absorbance at 488 nm
ADP	Adenosine diphosphate
AF4	Asymmetric flow field-flow fractionation
Ago2	Argonaute 2
Akt	Protein kinase B
ALIX	Programmed cell death 6-interacting protein
APS	Ammonium persulfate
ARF6	Adenosine diphosphate ribosylation factor 6
ARRDC1	Arrestin domain-containing protein 1
ATP	Adenosine triphosphate
B2M	Beta-2-microglobulin
Bag3	BAG family molecular chaperone regulator 3
BAX	Bcl-2-associated X
BCA	Bicinchoninic acid
Bcl-2	B-cell lymphoma 2
Bcl-xL	B-cell lymphoma-extra large
bp	Base pair
BSA	Bovine serum albumin
C	Cytosine
CAF	Cancer-associated fibroblast
CCL	C-C motif chemokine ligand
CCL2	Chemokine (C-C motif) ligand 2
CCR6	C-C chemokine receptor type 6
CD106	Cluster of differentiation 106
CD49d	α4 subunit of the integrin heterodimer α4β1
cDNA	Complementary DNA
circRNA	Circular RNA
CL	Cell lysate
CLL	Chronic lymphocytic leukaemia
CM	Conditioned medium
cryo-EM	Cryogenic electron microscopy
CXCL14	Chemokine (C-X-C motif) ligand 14
CXCL5	C-X-C motif chemokine 5
CX3CR1	C-X3-C motif chemokine receptor 1
CYP3A4	Cytochrome P450 3A4
DAPI	4′, 6-diamidino-2-phenylindole
dBroccoli	Dimeric Broccoli
DC	Differential centrifugation
DE	Differentiated expression
DEPC	Diethyl pyrocarbonate
DFHBI-1T	(5Z)-5-[(3,5-Difluoro-4-hydroxyphenyl)methylene]-3,5-dihydro-2-methyl-3-(2,2,2-trifluoroethyl) -4H-imidazol-4-one
DG	Density gradient

dH2O	Distilled H_2O
DMEM	Dulbecco's Modified Eagle's Medium
DMEM: F12	Dulbecco's Modified Eagle's Medium: Nutrient Mixture F-12 Ham
DMSO	Dimethyl sulfoxide
DNA	Deoxyribonucleic acid
dNTP	Deoxynucleoside triphosphate
DoL	Degree of labelling
DRF3	Diaphanous related formin 3
dsDNA	Double-stranded DNA
E	Elution
E. coli	*Escherichia coli*
ECACC	European Collection of Authenticated Cell Cultures
ECL	Enhanced chemiluminescence
ECM	Extracellular matrix
EDTA	Ethylenediaminetetraacetic acid
EEA1	Early Endosome Antigen 1
EGF	Epithelial growth factor
EGFR	Epithelial growth factor receptor
EM	Electron microscopy
EMT	Epithelial to mesenchymal transition
EP	Extracellular particle
ERK	Extracellular signal-regulated kinase
ESCRT	Endosomal sorting complex required for transport
EV	Extracellular vesicle
FAK	Focal adhesion kinase
FBS	Fetal bovine serum
FU	Fluorescence unit
G	Guanine
GAGE6	G antigen 6
GFP	Green fluorescent protein
GM130/GOLGA2	Golgin subfamily A member 2
GST	Glutathione S-transferases
GTPase	Nucleotide guanosine triphosphate binding protein
HCC	Hepatocellular carcinoma
HDF	Human diploid fibroblast
HIF	Hypoxia-inducible factor
HIF-1α	Hypoxia-inducible factor 1-alpha
HLA	Human leukocyte antigen
HNC	Head and neck cancer
hnRNP	Heterogeneous nuclear ribonucleoprotein
hnRNPA2B1	Heterogeneous nuclear ribonucleoprotein A2/B1
hnRNPH1	Heterogeneous nuclear ribonucleoprotein H1
hnRNPM	Heterogeneous nuclear ribonucleoprotein M
HNSCC	Head and neck squamous cell carcinoma
HPRT	Hypoxanthine-guanine phosphoribosyltransferase
HPRT+	Hypoxanthine-guanine phosphoribosyltransferase positive
HPRT-	Hypoxanthine-guanine phosphoribosyltransferase negative
HPV	Human papillomavirus
HRP	Horseradish peroxidase
Hsp	Heat shock protein

Hsp72	Heat shock 70 kDa protein 1
HSP90AB1	Heat shock protein 90 alpha family class B member 1
HSPG	Heparan sulfate proteoglycan
hTERT	Human telomerase reverse transcriptase
hU6	Human U6
IgG	Immunoglobulin G
IGV	Integrative Genomics Viewer
IL-6	Interleukin 6
ILV	Intraluminal vesicle
IMS	Industrial methylated spirit
IP	Immunoprecipitation
IPA	Ingenuity pathway analysis
ISEV	International Society of Extracellular Vesicles
kb	Kilo base pair
kDa	Kilodalton
KGM	Keratinocyte growth medium
LB	Luria-Bertani
LC3	Microtubule-associated protein 1A/1B-light chain 3
lncRNA	Long non-coding RNA
LPA	Lipopolysaccharide
LPS	Lipopolysaccharide
LRP	Lung resistance-related protein
m^5C	5-methylcytosine
m^6A	N^6-methyladenosine
MAPK	Mitogen-activated protein kinase
MEG3	Maternally expressed 3
MHC II	Major histocompatibility complex class II
mIgG	Mouse immunoglobulin G
miRNA	Micro ribonucleic acids
MISEV2018	Mininal information for studies of extracellular vesicles 2018
MLCK	Myosin light-chain kinase
MMP-1	Matrix metalloproteinase-1
mRNA	Messenger ribonucleic acids
mTOR	Mechanistic target of rapamycin
MTT	3-[4,5-dimethylthiazol-2-yl]-2,5-diphenyltetrazolium bromide
MVE	Multivesicular endosome
MVP	Major vault protein
MVP-KO	Major vault protein knockout
n	Number
NaB	Sodium butyrate
NaCl	Sodium chloride
ncRNA	Non-coding RNA
NF-κB	Nuclear factor kappa-light-chain-enhancer of activated B cells
$NF-H_2O$	Nuclease-free water
NGS	Next Generation Sequencing
NK	Natural killer
NKG2D	Natural killer group 2D
NOK	Normal oral keratinocyte
NOTCH1	Notch homolog 1
NSCLC	Non-small cell lung carcinoma

nt	Nucleotide
NTA	Nanoparticle tracking analysis
OME	Oral mucosa equivalent
OSCC	Oral squamous cell carcinoma
p53	Tumour protein p53
p62/SQSTM1	Sequestosome 1
PAM	Protospacer adjacent motif
PARP4/vPARP	Poly (adenosine diphosphate-ribose) polymerase 4
PBS	Phosphate buffered saline
PBST	PBS + Tween-20
PCR	Polymerase chain reaction
PDB	Protein data bank
PDCD4	Programmed cell death protein 4
PD-L1	Programmed death-ligand 1
PFA	Paraformaldehyde
pH	Power of hydrogen
PIK3CA	Phosphatidylinositol-4,5-bisphosphate 3-kinase catalytic subunit alpha
piRNA	Piwi-interacting RNA
PK	Proteinase K
PLD2	Phospholipase D2
PMSF	phenylmethanesulfonyl fluoride
PSF	Polypyrimidine tract binding protein associated splicing factor
PTEN	Phosphatase and tensin homolog
qPCR	Quantitative polymerase chain reaction
Rab	Ras-associated binding protein
Rab7	Ras-related protein Rab-7a
Ras	Rat sarcoma virus
RBP	RNA-binding protein
RNA	Ribonucleic acid
RNP	Ribonucleoprotein
RPM	Reads per million
rRNA	Ribosomal RNA
SD	Standard deviation
SDS	Sodium dodecyl sulfate
SDS-PAGE	Sodium dodecyl sulfate-polyacrylamide gel electrophoresis
sdRNA	SnoRNA derived RNA
SEC	Size exclusion chromatograpy
siRNA	Small interfering RNA
SMase	Ceramide-based sphingomyelinase
SNARE	Soluble N-ethylmaleimide-sensitive fusion attachment protein receptor
snRNA	Small nuclear RNA
snoRNA	Small nucleolar RNA
SSPE	Sodium chloride-sodium phosphate-EDTA
svRNA	Small vault RNA
T	Thymine
T7EI	T7 endonuclease
TAE	Tris-acetate-EDTA
TALEN	Transcription activator like effector nuclease
TBE	Tris-borate-EDTA
TBST	Tris-buffered saline supplemented with 0.1% (v/v) Tween-20
TEM	Transmission electron microscopy

TEMED	Tetramethylethylenediamine
TEP1	Telomerase protein component 1
TERT	Telomerase reverse transcriptase
TERT2	Telomerase reverse transcriptase 2
TGF-β	Transforming growth factor beta
TLR	Toll-like receptor
T_m	Melting teperature
TME	Tumour microenvironment
TNBC	Triple-negative breast cancer
tRNA	Transfer RNA
TSG101	Tumor susceptibility gene 101
Tspan8	Tetraspanin 8
tsRNA	Transfer RNA-derived small RNA
TX	Triton X-100
UB	Unbound
UC-FBS	Ultracentrifugation EV-depleted FBS
UF	Ultrafiltration
UF-FBS	Ultrafiltration EV-depleted FBS
UV	Ultraviolet
v/v	Volume by volume
VEGF	Vascular endothelial growth factor
VEGFR	Vascular endothelial growth factor receptor
VPS4	Vacuolar protein sorting-associated protein 4
vtRNA	Vault RNA
w/v	weight by volume
WT	Wildtype
Xist	X-inactive specific transcript
XPO5	Exportin-5
YBX1	Y-box binding protein 1
ZFN	Zinc finger nuclease

Contents

List of Tables

List of Figures

Chapter 1 Introduction

1.1 Introduction to head and neck cancer

Head and neck cancer (HNC) is a group of heterogeneous neoplasms that usually originates in the squamous cells that line the mucosal surfaces of the head and neck region (Chow, 2020). Common sites for HNC include the lip, oral cavity, nasal cavity, nasopharynx, paranasal sinuses, oropharynx, hypopharynx, larynx, and salivary glands (Rezende, Freire and Franco, 2010; Chow, 2020). It was the seventh most common cancer worldwide in 2018 and accounts for 3% of all cancer cases (Siegel, Miller and Jemal, 2016; Bray *et al.*, 2018). In the UK, the incidence of HNC has increased by 33% since the early 1990s (Cancer Research UK, 2020), which is reflected in 12,238 newly diagnosed cases in 2017 and 4,077 deaths in 2018 (Cancer Research UK, 2018). Globally, HNC causes approximately 2% of cancer-related deaths every year (Economopoulou and Psyrri, 2017; Cancer Research UK, 2018). Symptoms include a non-healing wound or sore, a lump in the neck, trouble swallowing and unusual bleeding or pain. It has been well established that consumption of tobacco increases the risk of developing cancers in the oral cavity and pharynx 4 to 5-fold compared to non-smokers whereas a 10-fold increase of risk was observed in laryngeal cancers (Economopoulou and Psyrri, 2017). With high incidence being found mainly in male and elderly population, increased risk of developing head and neck cancer is also associated with family history, alcohol consumption, poor diet, and pathogen infection (Blot *et al.*, 1988; Goldenberg *et al.*, 2004; Gillison *et al.*, 2008). In addition, human papillomavirus (HPV) type 16 is recognised as a causal factor for HNCs (zur Hausen and de Villiers, 1994). In Europe, 73% of the oropharyngeal cases are HPV-positive and 12% of oral cavity, hypopharynx and larynx cancers are HPV-positive (Mehanna *et al.*, 2013).

1.1.1 Oral squamous cell carcinoma

Among all the subtypes of HNC, oral squamous cell carcinoma (OSCC) is the most common malignancy that affects the oral cavity and accounts for more than 90% of all HNC cases (Perdomo *et al.*, 2016). OSCC can originate in any location of the mucosa, though the tongue and the floor of the

mouth are the most frequently affected sites (Duray *et al.*, 2012; Kouketsu *et al.*, 2016). OSCC is often seen in males in their fifties and sixties with a significantly increased risk linked with tobacco usage, alcohol consumption and betel quid usage (Petti, 2009). Additionally, the incidence of OSCC in younger patients has increased in recent decades, however the role of the risk factors in this population has not been fully understood due to shorter exposure time (Kaminagakura *et al.*, 2012). Despite the strong link between HPV infection and oropharyngeal cancer, the role of HPV in OSCC pathogenesis remains controversial. High-risk HPV types (HPV-16/18) showed a more significant association with OSCC compared to low-risk types, whilst the incidence of HPV-positive OSCC has increased significantly in recent decades (Jiang and Dong, 2017). Despite a variety of well-developed clinical treatments including surgery, radiotherapy and chemotherapy, the overall survival of OSCC remains poor (around 50-60%) due to the late diagnosis in most patients (Blatt *et al.*, 2017).

Like other cancers, OSCCs are derived from genetically mutated keratinocytes at the primary site, which form pre-malignant/dysplastic lesions that form spontaneously but also can be promoted by frequent exposure to various risk factors. Genetic alterations have been found to be associated with the development of OSCC. In particular, deletions on 3p chromosome in 3p25.3-p26.1, 3p25.1-p25.3, 3p24.1, 3p21.31-p22.3, 3p14.2 and 3p14.1 regions and gains in 3q26, 8q22.3, 8q11-q21, 8q24, 11q13, 11q13.2-q13.4 regions have shown strong link to oral epithelial dysplasia, which often leads to precancerous leisions, a precursor of OSCC (Salahshourifar *et al.*, 2014). More than 90% of the chromosomal deletions has been found in OSCC. In addition, chromosomal alterations at 2q21-24, 2q33-35 and 2q37 also affect tumour suppressor genes, including LDL receptor related protein 1B and caspase 8 (Cengiz *et al.*, 2007).

Common gene mutations such as tumour protein p53 (p53), phosphatidylinositol-4,5-bisphosphate 3-kinase catalytic subunit alpha (PIK3CA) and notch homolog 1 (NOTCH1) are found in various frenquencies in OSCC (Sharma *et al.*, 2017; Cai *et al.*, 2020). The disruptive mutation of p53 is highly prevalent (ranges from 35.9% to 81%) in HPV-negative OSCC, which has been associated with poor prognosis and therapeutic resistance (Poeta *et al.*, 2007; Olivier, Hollstein and Hainaut,

2010; Kim, Lee and Park, 2020). It is rare in HPV-positive tumours due to the ubiquitinylation and proteasomal degradation facilitated by the E6 viral oncoprotein.

Around 2-8% of OSCC is associated with HPV infection (Hübbers and Akgül, 2015). The oncogenic potential of high-rish HPV subtypes is due to the insertion of the E6 and E7 genes into the host cell genome. This leads to the disruption of the normal expression of some major tumour suppressor gene including p53, resulting in altered cell phenotypes such as proliferation, apoptosis and genome stability (Hübbers and Akgül, 2015).

1.1.2 Tumour microenvironment in OSCC

The progression of OSCC largely depends on the interactions between cancer cells and the tumour microenvironment (TME). The TME is a complex environment that consists of many cell types, including cancer cells, fibroblasts, macrophages, T cells, adipocytes, pericytes and endothelial cells (Figure 1.1) (Pink *et al.*, 2018). As the tumour grows it induces phenotypic changes in surrounding stromal cells that favour further proliferation and progression of the tumour. Fibroblasts and macrophages are "corrupted" by cancer cells and promote tumour progression by multiple molecular interactions (Prajapati and Lambert, 2016). For instance, cancer-associated fibroblasts (CAFs) release inflammatory molecules such as chemokine (C-C motif) ligand 2 (CCL2) and chemokine (C-X-C motif) ligand 14 (CXCL14) that attract macrophages and other immune cells (Augsten *et al.*, 2009; Hembruff *et al.*, 2010). CAFs also support tumour growth by retaining a major role in extracellular matrix (ECM) remodelling. Tumour desmoplasia, characterised by increased deposition of type I and III collagens and degradation of type IV collagen, have been linked with poor prognosis (Cirri and Chiarugi, 2012). CAFs secrete factors that can promote tumour progression and metastasis (Ishii, Ochiai and Neri, 2016). Macrophage-derived epithelial growth factor (EGF) also directly interacts with its receptors expressed on the surface of tumour cells which assists with tumour invasion and metastasis (Wyckoff *et al.*, 2004).

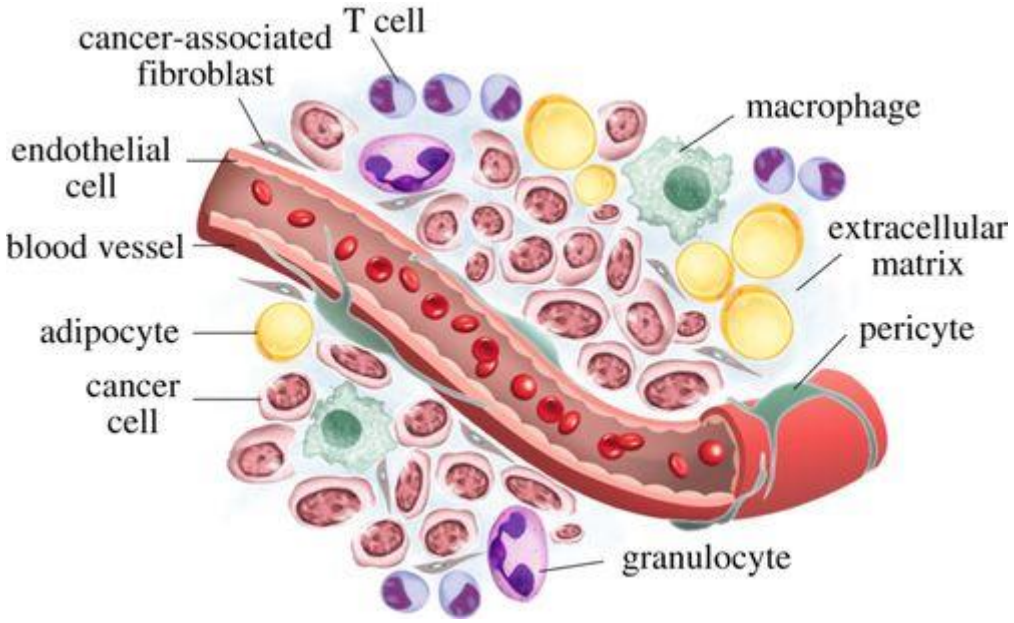

Figure 1.1 Exosome-delivered microRNAs modulate the inflammatory response to endotoxin
Cancer cells (brown) and other main cell types, including T cells (purple), macrophages (green with nuclei), pericytes (green), granulocytes (purple with multiple nuclei), adipocytes (yellow), endothelial cells (light orange), and cancer-associated fibroblasts (grey), together with blood vessels (red), lymphatic vessels (not shown) and surrounding extracellular matrix, compose of a heterogeneous neighbourhood of tumour. Figure was adapted from Pink *et al*., 2018 with permission (licence number 1146877-1) to reuse the figure (Pink *et al.*, 2018).

1.1.3 Extracellular vesicles in the tumour microenvironment

In addition to intercellular signalling by soluble molecules, one of the major signalling pathways within the TME is through the transmission of extracellular vesicles (EVs) (Sansone *et al.*, 2017; Zhou *et al.*, 2018), which has been described as an efficient process of both matter and message exchange between donor and recipient cells by generating and uptake of lipid-bound vesicles carrying complex cargos. EVs are lipid bilayer-enclosed vesicles that can be generated either intracellularly or by directly budding from the plasma membrane, traditionally named exosomes and microvesicles, respectively (Desrochers, Antonyak and Cerione, 2016). Moreover, they could also derive from the disassembly of cells undergoing apoptosis into small apoptotic bodies (Atkin-Smith *et al.*, 2015). The production of EVs also results in the encapsulation/incorporation of various molecular cargo originated from the donor cells. Recipient cells uptake EVs and their enclosed information by directly merging with the plasma membrane or via a variety of endocytic pathways, including both clathrin-

dependent and independent endocytosis (Mulcahy, Pink and Carter, 2014). The biogenesis of EVs and their molecular cargo will be described in detail in Section 1.2.

Tumour-derived EVs have been shown to mediate intercellular communication contributing to tumorigenesis and metastasis in both regional and distant microenvironment (Becker *et al.*, 2016). They sustain tumour development by regulating multiple major biological functions including proliferation, immunity, angiogenesis, and reprogramming stromal cells to promote a pre-metastatic niche (Ratajczak *et al.*, 2006; Peinado, Lavotshkin and Lyden, 2011; Becker *et al.*, 2016; Kalluri and LeBleu, 2020). For example, breast cancer-derived small EVs were able to reprogram the transcriptome of normal epithelial cells into a neoplastic profile through delivery of micro ribonucleic acids (miRNAs) (Melo *et al.*, 2014). EVs generated from glioblastoma cancer cells also stimulate cell growth and survival (Skog *et al.*, 2008). EVs are known to alter the immune response and angiogenesis in cancer. Tumour-derived small EVs were shown to activate the expression of immunity-associated genes in human T cell subsets (Mrizak *et al.*, 2015; Muller *et al.*, 2016). EVs are able to transform the TME into an immunosuppressive environment favouring tumour growth through extracellular vesicle cargos including programmed death-ligand 1 (PD-L1) and heat shock 70 kDa protein 1 (Hsp72) (Chalmin *et al.*, 2010; Chen *et al.*, 2018).

As one of the most characteristic markers of EVs, the tetraspanin protein family have the function of mediating cell adhesion and motility, which also play a role in angiogenesis (Hemler, 2005). Tumour-derived small EVs carrying tetraspanin 8 (Tspan8) significantly induced angiogenesis in tumour and normal tissues, mainly by recruiting certain proteins, including CD106 and CD49d, which were implicated in exosome-mediated endothelial cell binding and internalisation, and messenger ribonucleic acids (mRNAs) that are involved in the activation and maturation of endothelial cells. Uptake of these EVs resulted in stimulated proliferation, sprouting and migration in endothelial cells, together with elevated expression of angiogenic-associated genes including vascular endothelial growth factor (VEGF), VEGF receptor (VEGFR), C-X-C motif chemokine 5 (CXCL5), Tspan8 etc. (Nazarenko *et al.*, 2010). Another essential molecule, a certain mutated form of epidermal growth factor receptor (EGFR) named EGFRvIII, was observed in glioma-derived EVs, which was then

transferred to other cancer cells and caused activation of mitogen-activated protein kinase (MAPK) and protein kinase B (Akt) pathways. This led to increased expressions of a variety of genes (VEGF, B-cell lymphoma-extra large, cyclin-dependent kinase inhibitor 1B) that are involved in angiogenesis and cell morphological changes (Al-Nedawi *et al.*, 2008). The core of large tumours often lack oxygen. There is increasing evidence that hypoxia causes an increase in production of cancer cell-derived EVs and their altered molecular cargos facilitate tumour growth and angiogenesis (Park *et al.*, 2010; Wang *et al.*, 2014; Nakurte *et al.*, 2018). Hypoxic breast cancer cell-derived EVs stimulate invasion and metastatic abilities of recipient cancer cells in a hypoxia-inducible factor (HIF)-dependent manner, where knockdown of hypoxia-inducible factor 1-alpha (HIF-1α) prevented the increase of EV release in response to hypoxia (King, Michael and Gleadle, 2012; Wang *et al.*, 2014).

1.1.4 Extracellular vesicles in oral squamous cell carcinoma

There is increasing evidence that EVs play a unique role in OSCC, mainly through the regulatory effects of their complex molecular cargos. Higher concentrations of EVs have been found in saliva and plasma from OSCC patients compared to healthy controls (Zlotogorski-Hurvitz *et al.*, 2016; Momen-Heravi and Bala, 2018b), whilst increased vesicle size and irregular morphology were also reported from OSCC-patient derived EV samples (Sharma *et al.*, 2011). In addition, increased EV release from OSCC cell lines can be induced by exposure of cells to lipopolysaccharide (LPS), ethanol, and radiation (Mutschelknaus *et al.*, 2016; Momen-Heravi and Bala, 2018b). A study using irradiated and untreated OSCC cells revealed more small EVs were released from and taken up by irradiated cells compared to their untreated counterparts. Thus, suggesting a role for OSCC-derived EVs in modulating radioresistance-related cell survival (Mutschelknaus *et al.*, 2016).

Experimental evidence suggested that the nucleic acid cargo of OSCC-derived EVs differs to that of control EVs (Gai *et al.*, 2018; He *et al.*, 2020). A study comparing exosomal miRNA profiles from 4 HNSCC cell lines (including two OSCC lines) to non-neoplastic control cells identified a list of 32 differentially expressed miRNAs, of which 19 were upregulated in HNSCC-derived EVs (Langevin *et al.*, 2017). Another study focusing on EVs isolated from the plasma of OSCC patients identified 4 miRNAs (miR-21, miR-155, miR-27a, and miR-27b) that were upregulated compared to control

individuals (Momen-Heravi and Bala, 2018b). The same study also identified the enrichment of 29 miRNAs in OSCC-EVs compared to the parental cell lines (Momen-Heravi and Bala, 2018b), indicating selective packaging of oncogenic miRNA into EVs involved in OSCC tumorigenesis. Additionally, the involvement of EV-miRNA in tumour metastasis was confirmed by Sakha *et al*. comparing exosomal miRNA expression of a highly metastatic HOC313 OSCC cell line to the parental cells (Sakha *et al.*, 2016). 18 miRNA were upregulated in highly metastatic cells, whereas 60 miRNAs were increased in metastatic cell-derived EVs, of which 7 were identified as oncogenic miRNAs in previous studies (Cittelly *et al.*, 2010; Li *et al.*, 2011; Sun *et al.*, 2015; Wang *et al.*, 2015, 2016; Yuan *et al.*, 2016; Zhou *et al.*, 2016). Transfer of miR-200c-3p in EVs derived from highly invasive OSCC has been shown to pass the trait to non-invasive cells (Kawakubo-Yasukochi *et al.*, 2018). However, there is a lack of concordance when comparing the miRNA cargo of OSCC-derived EVs reported by several studies (Sakha *et al.*, 2016; Langevin *et al.*, 2017; Kawakubo-Yasukochi *et al.*, 2018; Momen-Heravi and Bala, 2018b). This could be partially due to the materials used and because EV isolation methods varied among these studies.

Tumour drug resistance is still a persistent problem in OSCC, in which EVs have been identified as a key mediator (Law *et al.*, 2021). EVs can transmit cargos that contribute to a drug resistant phenotype in recipient cells, such as EV-mediated transfer of miR-21 in OSCC which targeted phosphatase and tensin homolog (PTEN) and programmed cell death protein 4 (PDCD4) pathways (Valadi *et al.*, 2007). Apart from shuttling molecules between cells, EVs are also involved in several drug-resistant mechanisms such as drug efflux and conveying anti-apoptotic signalling (Law *et al.*, 2021). For instance, treatment with chemotherapeutic drug in resistant OSCC cells resulted in more drug found in EVs with downregulated expression of ATP1B3, a key metal ion transporter, whilst less drug compound was found accumulated in cells, compared to sensitive OSCC cell lines (Khoo *et al.*, 2019). Furthermore, EVs from CAFs were found to confer cisplatin resistance and promoted cell survival to OSCC cell lines via transmission of exosomal miR-196a (Qin *et al.*, 2019). The collection of evidence suggests a crucial role of EVs in mediating chemoresistance in OSCC by multiple mechanisms.

EVs are associated with the immunological regulation of the TME by delivering regulatory messages to a variety of immune cells. OSCC-derived EVs have been documented to activate the nuclear factor kappa-light-chain-enhancer of activated B cells (NF-κB) pathway in monocytes, resulting in a cytokine-enriched microenvironment favouring tumour growth (Momen-Heravi and Bala, 2018b). Plasma-derived small EVs from head and neck cancer patients (in which 50-61% patients had primary tumours in the oral cavity) with active diseases featuring a high exosomal PD-L1 expression phenotype showed significant effects in suppressing T cell functions while they also suppressed natural killer group 2D (NKG2D) expression in natural killer (NK) cells (Ludwig *et al.*, 2017; Theodoraki *et al.*, 2018). On the other hand, anti-cancer EVs also exist and have active interactions with the components of the TME. EVs produced by immune cells help with fighting against tumour growth by a dual effect upon tumour cells and other immune cells. Gamma delta T cell-derived EVs inhibit tumorigenesis by impairing tumour cell growth and boosting the effectiveness of cytotoxic T cells in an miRNA dependant manner (Li *et al.*, 2019).

Since the oral cavity is bathed in saliva, identification of salivary biomarkers for OSCC has been a major research objective for non-invasive cancer screening and diagnosis (Gai *et al.*, 2018; Cristaldi *et al.*, 2019), and salivary EVs are naturally a suitable source for such a purpose. The concentration and size of salivary EVs in OSCC patients have been shown to increase (Sharma, Boyd M. Gillespie, *et al.*, 2011; Zlotogorski-Hurvitz *et al.*, 2016), whilst the most identified markers in salivary EVs are miRNAs, including miR-512-3p, miR-412-3p, miR-302b-3p, and miR-517b-3p (Gai *et al.*, 2018). These miRNA have been found to be differentially expressed in cancer patient EVs compared to normal controls, making them potential marker candidates for OSCC diagnosis, prognosis, and follow-up (Winck *et al.*, 2015; Zlotogorski-Hurvitz *et al.*, 2016; Greither *et al.*, 2017). In addition, OSCC patient derived salivary EVs also contained more protein marker CD63, but less CD9 and CD81, which could potentially be used as for oral cancer diagnosis (Zlotogorski-Hurvitz *et al.*, 2016).

1.2 Extracellular vesicles

It has been known for a long time that cells undergoing apoptosis release lipid bilayer-enclosed vesicles to the extracellular space, which contain a variety of molecules and organelles from the parent cell. In recent years, EVs have attracted more attention due to the knowledge that all healthy cells in the human body produce EVs. The name "extracellular vesicles" describes a heterogeneous collection of particles with sizes range from 50 nm to 5 μm, enclosed by cell-derived lipid bilayer membrane (Théry *et al.*, 2018). Their origins can be either from the intracellular endosomal system or directly shedding from the plasma membrane.

EVs are considered an essential vehicle for intercellular communication. Once released their fate remains to be fully elucidated, nevertheless, they are present in a large range of body fluids including blood (serum), saliva, urine, and breast milk (Melo *et al.*, 2015; de la Torre Gomez *et al.*, 2018; Gai *et al.*, 2018; Channavajjhala *et al.*, 2019; Khayrullin *et al.*, 2019). Traditionally EVs are categorised into three subtypes based on their biogenesis: exosomes, microvesicles and apoptotic bodies (Figure 1.2). The EV nomenclature has evolved in recent years due to EV heterogeneity and complexity being better characterised. As specific markers for different EV subtypes are yet to be discovered, non-conclusive terms describing the physical characteristics of EVs were recommended by the minimal information of studies of extracellular vesicles 2018 (MISEV2018) guidelines, such as small/large EVs, or low/high density EVs (Théry *et al.*, 2018). Where the biochemical composition or biological origins of EVs were characterised, the corresponding descriptions can be used to define such EV populations, such as CD63+ EVs, apoptotic bodies. When the EV identity cannot be confirmed, inconclusive terms like extracellular particles (EPs) can be used instead (Théry *et al.*, 2018). Here, we discuss the three broadly accepted EV subpopulations separately based on their biogenesis.

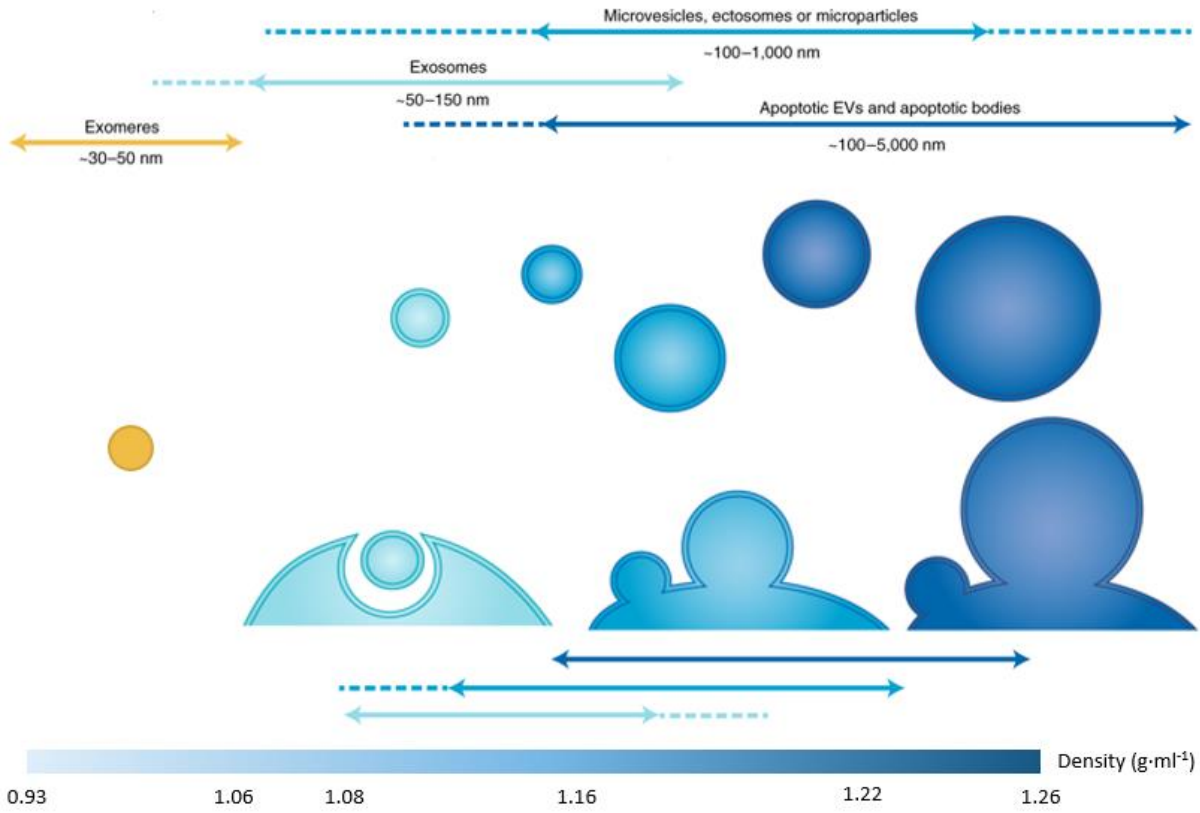

Figure 1.2 Extracellular vesicle subtypes: exosomes, microvesicles and apoptotic bodies.
The schematic shows the subtypes of EVs with subcellular origins and respective size ranges and densities. Exosomes generated from intracellular endosomal system range from 50 to 150 nm. Microvesicles are around 100 to 1,000 nm and directly bud from the plasma membrane. Another budding EV subtype is apoptotic bodies, which range from 100 to 5,000 nm. Due to the heterogeneity and overlapping size ranges of the EVs, different subtypes of EVs could co-exist in the purified EV pellets. Image was adapted from Mathieu *et al.*, 2019 (Mathieu *et al.*, 2019), permission (licence number 5145420742708) has been obtained to reuse this figure.

1.2.1 Exosomes

Exosomes were first described in 1987 as vesicles that can be pelleted by ultracentrifugation at 100,000 × *g* for 90 minutes (Johnstone *et al.*, 1987). They are uniquely distinguished from other EVs by their smaller size and endosomal biogenesis.

Exosomes are the smallest EVs among all three subtypes with diameters range from 50 to 150 nm, with potential overlaps in size range with other EV subtypes. However, recently a new class of small (typically ~30-50 nm) non-membranous nanoparticles was identified called exomeres (Zhang *et al.*, 2018), which are reported to contaminate exosome preparations (Mathieu *et al.*, 2019) (Figure 1.2).

The biogenesis of exosomes is summarised in Figure 1.3. They are firstly generated as intraluminal vesicles (ILVs) in multivesicular endosomes (MVEs). This process initially involves the enrichment of the cargos at the generation sites of the vesicles, which are normally cell type-specific and cell status-specific. One of the most dominant surface cargos promoting MVE formation and the generation of ILVs is the major histocompatibility complex class II (MHC II) (Ostrowski *et al.*, 2010). Other generally present surface cargos include lipids, tetraspanin proteins and other intracellular trafficking proteins (van Niel, D'Angelo and Raposo, 2018).

The endosomal sorting complex required for transport (ESCRT) family plays an important role in coordinating formation of ILVs (Figure 1.3). This protein family is composed of more than 30 proteins that form into four cytosolic protein complexes: ESCRT-0, ESCRT-I, ESCRT-II, and ESCRT-III, which enables membrane remodelling and budding of vesicles (Schmidt and Teis, 2012). Another functional complex, vacuolar protein sorting-associated protein 4 (VPS4) allows the final membrane scission and recycling of ESCRT proteins (Henne, Stenmark and Emr, 2013). Baietti *et al*., 2012 evidenced the key role of ESCRT subcomponants in exosomal biogenesis (Baietti *et al.*, 2012). Like ESCRT-dependent viral budding, the binding of an ESCRT-associated protein programmed cell death 6-interacting protein (ALIX) with the cytoplasmic adapter protein Syntenin allows the interaction between the PDZ domain of Syntenin and the cytoplasmic tail of Syndecan – a transmembrane (type I) heparan sulfate proteoglycan (HSPG) that mediates cell binding and cytoskeletal organization (Mali *et al.*, 1990; Baietti *et al.*, 2012). The assembled syndecan-syntenin-ALIX complex then enables ILV formation with the presence of the adenosine diphosphate ribosylation factor 6 (ARF6) and the phospholipase D2 (PLD2) (Ghossoub *et al.*, 2014). The regulatory function of this small nucleotide guanosine triphosphate binding protein (GTPase) and its effector on syntenin exosomes could be due to their lipid-metabolizing ability, resulting in formation of the lipid acid products promoting the bending of MVE membrane (Ghossoub *et al.*, 2014). In addition, ESCRT componants also play a role in cell-specific exosomal cargo selection, highlighted by disruption of tumour susceptibility gene 101 (TSG101) that resulted in altered cargos in retinal pigmented epithelial cell-derived exosomes (Abrami *et al.*, 2013). Although the involvement of

ESCRT in exosome biogenesis has been largely addressed, ESCRT-independent formation may be involved in some way as mammalian cells were still able to generate exosomes in the absence of key ESCRT factors (Stuffers *et al.*, 2009). Mechanisms including the ceramide-based sphingomyelinase (SMase) pathway and tetraspanin-dependent pathway provide further evidence for the heterogeniety of the exosome population and their biogenesis (Figure 1.3) (Trajkovic *et al.*, 2008). Prior to release, the exosome trafficking is largely regulated by a group of small GTPase which belong to the Ras-associated binding (Rab) protein families (Mathieu *et al.*, 2019). Finally, the docking of exosomes and fusing with plasma membrane is facilitated by the soluble N-ethylmaleimide-sensitive fusion attachment protein receptor (SNARE) complexes and syntaxin 5 proteins, resulting in the extracellular release of exosomes (Figure 1.3).

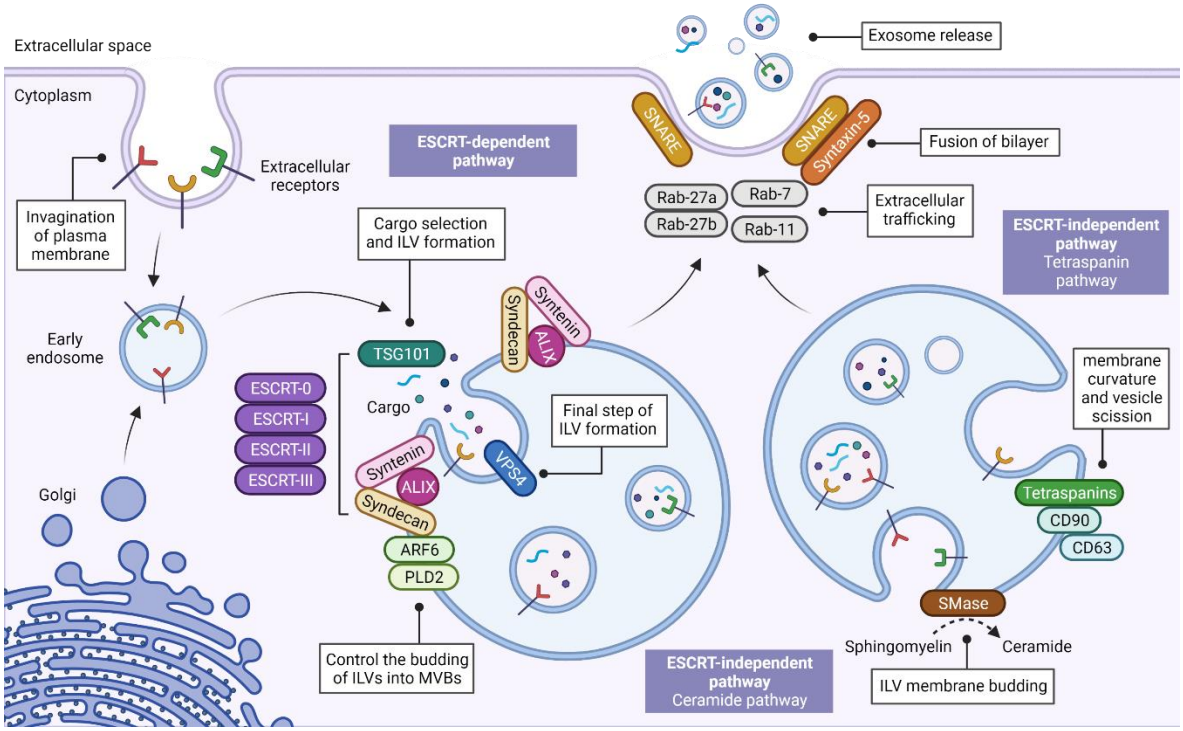

Figure 1.3 Pathways involved in exosome biogenesis.
The ESCRT-dependent endosomal pathway initiates from the formation of early endosome, which can be a result of plasma membrane recycling or Golgi body-originated. The ILV formation is largely regulated by the ESCRT pathway, in which ESCRT-I member TSG101 is playing a role in cargo selection. The inward budding and membrane curvature are regulated by the Syntenin-Syndecan-ALIX complex, followed by the final membrane scission mediated by VPS4. The ESCRT-independent pathways include the ceramide pathway and tetraspanin pathway. They describe the exosome production caused by the hydrolysation of sphingomyelin into phosphorylcoline and ceramide, and by the formation of tetraspanin-enriched microdomains, respectively. Finally, exosomes were trafficked towards the plasma membrane through the regulation of small GTPases, and the SNARE complexes and syntaxin 5 enable the final secretion into the extracellular space. Figure was adapted from Aheget *et al.* (Aheget *et al.*, 2020).

1.2.2 Microvesicles

Distinct to exosomes, the second subtype of EVs, microvesicles, have a size range from 100 to 1,000 nm and are produced by membrane budding. The release of surface vesicles was firstly discovered when cells were undergoing apoptosis, thus they have been understood as a way that cells release unwanted 'junk' until similar activity was also observed in healthy cells (Holme *et al.*, 1994). It is now well understood that a single cell can release both exosomes and microvesicles through different pathways as observed in platelets, endothelial cells and cancer cells (Heijnen *et al.*, 1999; Deregibus *et al.*, 2007; Muralidharan-Chari *et al.*, 2009). In prostate cancer cells, the activation of oncogenes such as diaphanous related formin 3 (DRF3), Akt, and EGFR led to the increased release of microvesicles (Di Vizio *et al.*, 2009). Noticeably, a certain amount of literature confuses microvesicles with other types of EVs (especially exosomes) of the same size range without defining their origins. As none of the existing technologies can distinguish one from another, unless a combination of methods are applied, the development of a clear characterisation method is still one of the major technical problems hindering EV research.

The biogenesis of microvesicles is distinct from exosomes. Due to the outward budding of the plasma membrane, local lipids and proteins are largely redistributed, coupled with a vertical redistribution and enrichment of protein and nucleic acid cargos in the newly-formed microvesicle area, of which the molecular mechanisms are not yet fully understood (D'Souza-Schorey and Clancy, 2012). Like other forms of membrane deformation, genesis of microvesicles initiates from the membrane curvature that is potentially induced by a protein-driven pushing force at the location where the future microvesicle forms (Boulbitch, 1998). Membrane curvature has been proposed to be a result of protein-protein crowding, in which the interactions between proteins generate pressure leading to the membrane bending (Stachowiak *et al.*, 2012). Interestingly, proteins involved in endosomal machinery and the ESCRT pathway have also been reported to play a role in microvesicle genesis. The small guanosine triphosphate-binding protein ARF6 regulates microvesicle formation by enabling myosin light-chain kinase (MLCK)-mediated MLC phosphorylation via the recruitment of the extracellular signal-regulated kinase (ERK) to the plasma membrane to activate MLCK

(Muralidharan-Chari *et al.*, 2009). The interaction between TSG101 and arrestin domain-containing protein 1 (ARRDC1) has also drawn attention as it induced the relocation of TSG101 to the plasma membrane and therefore mediated the blebbing of microvesicles that are positive for both TSG101 and ARRDC1 (Nabhan *et al.*, 2012). Apart from proteins, lipids also dynamically regulate the membrane curvature process as phosphatidic acids can be locally recruited to assist with membrane curvature and vesicle formation (Yang *et al.*, 2008). The pinching of the plasma membrane is a result of the local enrichment of assorted lipids and proteins, which can be cell type-specific, and some are therefore loaded into the microvesicles as cargos.

1.2.3 Apoptotic bodies

Apoptotic bodies have been recognised as EVs that are only released by cells undergoing apoptosis. They are generally larger and heterogeneous in size (100-5,000 nm), containing genomic deoxyribonucleic acid (DNA) fragments, cytoplasm and organelles. They have also been hypothesised as vehicles carrying "find-me" and "eat-me" signals that are sent by apoptotic cells to recruit macrophages and immature phagocytes to promote cell clearance (Depraetere, 2000; Ravichandran, 2010). Meanwhile, apoptotic bodies themselves are also cleared locally by phagocytosis mediated by the receptors on macrophages (Savill, 1997). These signals have been reported to be a variety of chemokines (i.e. C-X3-C motif chemokine ligand 1) and nucleotides (i.e. nucleotides ATP and uridine 5' triphosphate) (Truman *et al.*, 2008; Elliott *et al.*, 2009).

One of the major events happening on the apoptotic cell membrane is the transverse redistribution of the phosphatidylserine to the outer leaflet of the lipid layer. This then allows the binding of Annexin V to facilitate the recognition by phagocytes (Martínez and Freyssinet, 2001). Other membrane surface changes include the exposure of binding sites for thrombospondin and C3b (Takizawa, Tsuji and Nagasawa, 1996; Friedl, Vischer and Freyberg, 2002). These two, together with Annexin V, have now been used as generally accepted markers in apoptotic body characterisation.

Apoptotic bodies themselves are a heterogeneous group that have been suggested to consist of at least two main subpopulations (Hauser, Wang and Didenko, 2017). Due to their less organised cargo

selection, researchers should bear in mind that apoptotic bodies could be dense (those packed with nucleotide cargos) or light (those with enclosed cytoplasm), resulting in EVs with distinct physical properties and even unique detectable markers, which would inform the isolation and characterisation techniques applied. Due to the large variation in size range, it is likely that they will be co-purified with other EV types.

1.2.4 RNA cargo

As stated above, EV populations are highly diverse and heterogeneous due to their different biogenesis and physical characteristics. EVs contains a variety of molecular cargos that they export from the parental cells, including DNA, RNA, proteins, and lipids (Balaj *et al.*, 2011). The most intensely researched cargo in recent years has been RNA, with new RNA species being gradually discovered. Deep sequencing of RNA cargos derived from EVs released by immune cells revealed a rich selection of both protein-coding and non-coding RNAs. EV RNA cargo is reported to differ from the total cellular RNA, suggesting selective packaging mechanisms (Nolte'T Hoen *et al.*, 2012).

mRNAs packaged into EVs can be transported to the recipient cells and translated to functional proteins (Montecalvo *et al.*, 2012). Transcriptomic analysis of immune cell-derived EVs revealed 26.1% of the extracellular RNA reads were mapped to introns and exons (Nolte'T Hoen *et al.*, 2012). In glioblastoma, some 4,700 mRNAs were only detectable in EVs but not in parental cells. Furthermore, they also confirmed the translation of these mRNAs by the recipient cells, as previously demonstrated by Valadi *et al*. (2007) (Skog *et al.*, 2008). Highly metastatic ovarian cancer cell-derived EVs promote cell apoptosis and degrade peritoneal mesothelium by carrying matrix metalloproteinase-1 (MMP1) mRNA, resulting in a more metastatic phenotype in human mesothelial cells (Yokoi *et al.*, 2017). Therefore, the enrichment and selection of mRNAs in EVs appears to be a possible mechanism allowing cancer cells to transmit favourable behaviours and phenotypes within their microenvironment.

In addition to protein coding RNAs, EVs carry non-coding RNAs that have received much interest due to their gene regulatory functions. This RNA population consists of several types, including

miRNAs, long non-coding RNAs (lncRNAs), circular RNAs (circRNAs), small nucleolar RNAs (snoRNAs), small nuclear RNAs (snRNAs), transfer RNAs (tRNAs), ribosomal RNAs (rRNAs), piwi-interacting RNAs (piRNAs), and vault RNAs (vtRNAs) (Nolte'T Hoen *et al.*, 2012). miRNAs have been shown to play significant roles in cell-to-cell communication and post-transcriptional regulation, especially in inflammatory responses, disease progression, and tumorigenesis (Alexander *et al.*, 2015; Tominaga *et al.*, 2015). For example, exosome-shuttled miR-494 has been associated with tumour growth and a more metastatic phenotype in melanoma, whilst the same molecule in salivary EVs has been suggested as one of the biomarkers for OSCC (Gai *et al.*, 2018; J. Li *et al.*, 2019). Drug resistance can be induced by elevated miR-21-5p and miR-486-3p levels in lung adenocarcinoma cell line-derived EVs, together with the differential expression of lncRNA maternally expressed 3 (MEG3) and X-inactive specific transcript (Xist) compared to the sensitive subline (Kwok *et al.*, 2019). Due to the easy access and large variety of EV-miRNAs in body fluids, they are widely accepted as the newest source of biomarkers and potential therapeutic target candidates for many diseases (Takahashi *et al.*, 2017).

EV RNA cargo is abundant in RNA species of 20-200 nt in length (Tosar *et al.*, 2015), suggesting the presence of numerous RNAs other than miRNA. For instance, enrichment of Y RNA has been identified from EV total RNA derived from dendritic cells/T cells, which accounted for ~5% of total EV-RNA reads, whereas it accounted for less than 1% of cellular RNA (Nolte'T Hoen *et al.*, 2012). Y RNAs are highly-conserved small non-coding RNAs that serve as an initiation factor for DNA replication in mammalian cells while they have also been linked with intracellular transport of proteins and nucleic acids (Christov *et al.*, 2006; Dieci *et al.*, 2007). The level of EV-transmitted Y-RNAs are regulated by Toll-like receptor (TLR) signalling (Driedonks and Nolte-'t Hoen, 2019). In chronic lymphocytic leukaemia (CLL)-derived EVs, Y4-RNA was highly abundant and induced the release of cytokines including chemokine (C-C motif) ligand 2, chemokine (C-C motif) ligands 4, interleukin 6 (IL-6), and PD-L1 in monocytes by activating TLR7 signalling (Haderk *et al.*, 2017).

Deep sequencing of dendritic cell/T cell-derived EVs have also revealed an enriched small non-coding RNA species named vault RNAs and also their fragments (Nolte'T Hoen *et al.*, 2012). In this

study, vtRNAs were identified to be the most abundant RNA population (accounting for ~27% of total reads of EV-shuttled RNA and ~1% of total cellular RNA). Due to their RNA selection restriction of <70 nt, a large amount of vtRNA fragments were also identified, which predominantly consist of the internal stem loop structures of the full-length vtRNAs (Nolte'T Hoen *et al.*, 2012). Interestingly, another study focusing on vtRNA fragments identified in breast cancer cells cultured *in vitro* suggested cellular vtRNA fragments were derived mainly from the 3' and 5' ends of vtRNAs, while similar results were confirmed by the comparison of EV-vtRNA fragment and cellular-vtRNA fragment sequences published by Nolte-'T Hoen *et al.* (2012) (Persson *et al.*, 2009).

1.2.5 Protein cargo

Comprehensive proteomic studies describing the rich protein content of EVs from different cell types have been generated (Théry *et al.*, 2001; Conde-Vancells *et al.*, 2008; Graner *et al.*, 2009; Demory Beckler *et al.*, 2013). Due to the diversity of the isolation and characterisation techniques applied and also the heterogeneous nature of the EVs, protein cargos with enrichments in EVs varied among individual studies. However, proteins involved in intracellular transportation and endosomal systems tend to be mentioned repeatedly during the review of the literature, such as proteins of the ESCRT machinery (i.e. TSG101, ALIX) and tetraspanin family (i.e. CD9, CD63, CD81). Thus, these proteins were generally accepted as characteristic markers of EVs by many sources.

Théry *et al*. have reported 21 exosomal proteins identified in dendritic cell-derived exosomes with most of the proteins associated with endocytic compartments, exosome biogenesis, cytoskeleton, and intracellular membrane transport, together with a novel category related to cell apoptosis (Théry *et al.*, 2001). This finding contributed to the further identification and characterisation of EVs released by apoptotic cells and apoptotic bodies as each of them distinguish themselves both biochemically and morphologically. A study investigating the proteome of non-cancerous hepatocyte-derived EVs identified regular exosomal EV-protein profiles as well as proteins associated with metabolising lipoproteins, endogenous compounds and xenobiotics, which provided an insight into the use of EV-protein as potential therapeutic tools (Conde-Vancells *et al.*, 2008). Proteomic studies profiling cancer cell-derived EVs have illustrated the presence of oncogenic proteins in tumour-derived EVs, for

example, EGFR, EGFRvIII, and transforming growth factor beta (TGF-β) were detected in the sera from brain tumour patients (Graner *et al.*, 2009). Oncogenic EVs, also known as "oncosomes" contain several oncoproteins and sometimes their transcripts, such as EGFRvIII, rat sarcoma virus (Ras) GTPase, and BCR-ABL (Choi, Spinelli, *et al.*, 2019). Similar to miRNA cargos, protein cargos transmitted by EVs serve as regulators in the recipient cells, leading to the changes in cell morphology, downstream signalling pathways, and other tumorigenic properties (Maas, Breakefield and Weaver, 2017).

A recent study revealed the presence and potential functions of RNA-binding proteins (RBPs) in exosomes derived from an *in vitro* human epithelial cell line (HTB-177) model (Statello *et al.*, 2018). The authors demonstrated the detection of 30 RBPs in exosomes by an RNA-RBP complex biotinylated pull-down assay, including heat shock protein 90 alpha family class B member 1 (HSP90AB1), exportin-5 (XPO5), heterogeneous nuclear ribonucleoprotein H1 (hnRNPH1), heterogeneous nuclear ribonucleoprotein M (hnRNPM), heterogeneous nuclear ribonucleoprotein A2/B1 (hnRNPA2B1), and major vault protein (MVP). Of those, the knockdown of MVP was found to have significant effect on the amount of total exosomal RNAs. Furthermore, higher amount of total exosomal RNA was recovered from a MVP-transfected HEK293F cell line, compared to the non-transfected controls, suggesting a possible role for MVP serving as an RBP in exosomal RNA transport and extracellular stabilisation (Statello *et al.*, 2018).

1.2.6 Cellular uptake of EVs

The cellular uptake of EVs can be achieved by either endocytosis or via direct fusion with plasma membrane. Depending on the type of recipient cells, several types of endocytosis-mediated uptake process have been reported. For example, clathrin-mediated endocytosis has been reported in neurons, phagocytosis happens in neurons and dendritic cells, and cancer cells have cholesterol and lipid raft-mediated endocytosis of EVs (Morelli *et al.*, 2004; Feng *et al.*, 2010; Montecalvo *et al.*, 2012; Frühbeis *et al.*, 2013; Svensson *et al.*, 2013). Noticeably, even the same cell can also have multiple types of endocytosis depending on the expression of different EV surface marker and EV subtype.

Heparin sulfate proteoglycans within the plasma membrane have been shown to play an impartant role in EV internalisation, as its inhibition has reduced EV uptake *in vitro* (Christianson *et al.*, 2013). As for membrane fusion-induced EV uptake, low pH condition was required which can be found in tumours (Parolini *et al.*, 2009).

Due to the extremely high heterogeneity of EV populations, the understanding of different fates of EVs upon cellular internalisation remains limited. However, although EVs have been reported to be able to trigger phenotypic changes through surface marker recognition (Tkach *et al.*, 2017), the main characterisation of intercellular EV transmission remains the exchange and delivery of molecule cargo.

1.2.7 EV isolation and characterisation

EVs can be isolated from conditioned medium from *in vitro* cultured cells, or from a variety of biological fluids. Current EV isolation methods can be categorised into global concentration methods, size and/or weight-based techniques, and immunoaffinity-based seperation (Konoshenko *et al.*, 2018). Techniques performing a global concentration of extracellular particles with or without a size cut-off provide high yield of particles with high heterogeneity, such as filtration/ultrafiltration (UF) and polymer-based precipitation (Cocozza *et al.*, 2020). Specifically, UF isolates particles by allowing particles that are smaller than the selected pore size through the semi-pemealised membrane during high-speed centrifugation, which was firstly described as a time-saving version of traditional ultracentrifugation in 2007 (Cheruvanky et al., 2007). However the size range of particles purified are largely limited by the selected size of pores on the filtration membrane.

Size-based isolation includes size-exclusion chromatography (SEC), differential centrifugation (DC), and asymmetric flow field-flow fractionation (AF4). Among all techniques, DC is the most commonly used and accounts for 56% of all EV isolation techniques reported (Zarovni *et al.*, 2015). Traditionally, large/medium EVs (e.g. apoptotic bodies and microvesicles) can be pelleted at lower centrifugal speed for less time whilst small EVs such as exosomes can be enriched by ultracentrifugation at 100,000 × *g* for more than 60 minutes from a heterogeneous EV suspension

(Momen-Heravi, 2017). However, due to the high heterogeneity of EVs in conditioned medium and biological fluids, DC enriches (but does not purify) EV subtypes with other similar-sized non-vesicular nanoparticles (e.g. exomeres and lipoproteins). Noticably, improvement of DC has been made by coupling with isopycnic or moving-zone density gradient (DG) techniques to achieve optimal enrichment of exosomes by their unique biophysical properties (Booth *et al.*, 2006; Grapp *et al.*, 2013). Similar to DC, SEC is also widely applied in EV research which separates large particles from small ones by a micron-scale polymer bead-loaded SEC column. When samples are loaded onto the column, larger particles pass through the column more quickly as they can not enter into the pores present in the filtration medium. Compared to DC, SEC-isolated EVs are more intact structually when analysed by transmission electron microscopy as they were not damaged by high centrifugal forces (Böing *et al.*, 2014; Sidhom, Obi and Saleem, 2020). Some studies also suggested DC coupled with a subsequent enrichment by SEC gave an optimal exosome yield compared to any of the separate techniques when using urine and plasma samples (Rood *et al.*, 2010; Koh *et al.*, 2018). This combination allows the the effective removal of dead cells and other larger molecules followed by a high-efficiency seperation from soluble proteins and out-of-range sized particles and therefore was promoted in more recent studies (Koh *et al.*, 2018).

For more specific seperation, immunoprecipitation (IP) or immunocapture can be performed using antibodies specific to certain surface antigens. EVs derived from these techniques are proven to be of higher purity (Chen *et al.*, 2020). However, such techniques are relatively less popular due to high cost, low yield and a lack of specific EV subtype markers (Li *et al.*, 2017). Neverthless, a large amount of cell-specific surface antigens have been applied to EV characterisation in the literature. For instance, in tumour cell-derived microvesicles, surface antigens specific for tumour cells including human leukocyte antigen (HLA) class I, CD29, CD44, CD51, C-C chemokine receptor type 6 (CCR6) and CX3C chemokine receptor 1 (CX3CR1) were detected with altered expression levels compared to the parental cells (Baj-Krzyworzeka *et al.*, 2006).

Most isolation methods co-isolate different EV subtypes or other extracellular particles. A schematic comparison of all commonly used EV isolation techniques is shown in Figure 1.4, based on the yield

and specificity of the EVs recovered, together with the advantages and disadvantages of each method summarised based on the literature (Cocozza *et al.*, 2020). Therefore, a combination of methods are often necessary to first separate general extracellular particles with follow-up purification steps to achieve optimal EV enrichment. Researchers should be aware of the drawbacks of different methods so that an informed choice of EV isolation strategy can be made to better serve the specific purposes of the study.

After isolation of EVs by the above techniques it is necessary to characterise them by multiple complementary techniques. According to the MISEV2018 guidelines, both the source of EVs and EV isolates need to be described quantititively, in which the EV preparation quantification could be reported as total particle count, total protein and/or lipid amount (Théry *et al.*, 2018). In addition, western blotting is widely used to confirm the presence of vesicle markers, in which at least three distinct marker proteins should be interogated. Due to the fact that none of the common markers are specific for only one EV subtype, it is encouraged that researchers exclude other EV types by selecting appropriate isolation methods instead of depending on characterising markers (Théry *et al.*, 2018). Common markers used for EV protein characterisation include tetraspanins (CD63, CD81, CD82), ESCRT-associated proteins (TSG101, ALIX, VPS4A/B), heat shock proteins (HSC70 and HSP84), and also enzymes (glyceraldehyde 3-phosphate dehydrogenase). When confirming the isolation of small EVs, the absence of markers present in large EVs/particles are suggested such as nuclear proteins, histones, mitochondria, and secretory pathway counterparts (Théry *et al.*, 2018). Furthermore, single vesicle characterisation is required from two or more different but complementary techniques, including imaging of single EVs at high resolution and nanoparticle tracking analysis (NTA).

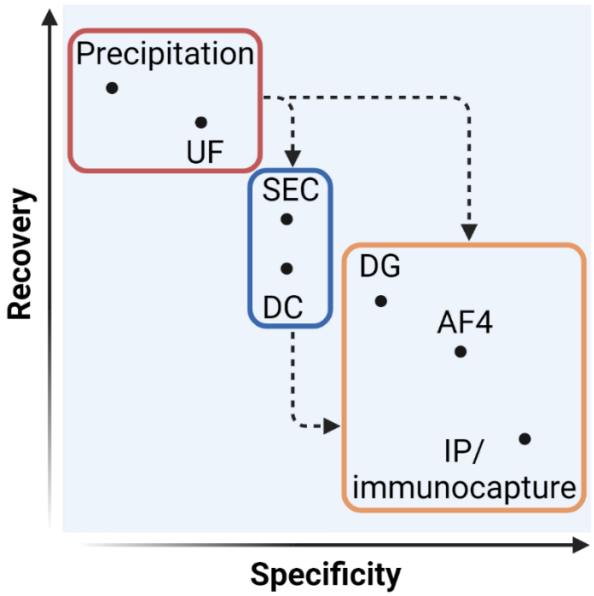

Technique	Pros	Cons
Precipitation	• High yield • Time-saving	• Additional reagents added • Low specificity • High heterogeneity • Potential particle aggregation
Ultra filtration (UF)	• Particle size cut-off • Suitable for large sample volume	• Exclusion of subpopulation of larger size particles • High heterogeneity
Size exclusion chromatography (SEC)	• High reproducibility • Low particle aggregation • Intact particle morphology and structure • Separation by size	• Low specificity • Co-isolation of all particles of similar size
Differential centrifugation (DC)	• Cheap and accessible • Suitable for large sample volume • Size-based separation	• Time-consuming • Low specificity • Co-isolation of aggregated and similar sized particles
Density gradient (DG)	• Density-based separation • High purity	• Complex procedure • Potential cross contamination between fractions
Asymmetric flow field-flow fractionation (AF4)	• High purity • Separation of both soluble and colloidal components over a wide size range • no column material is used	• Special equipment needed • Technically demanding
Immunoprecipitation (IP) /immunocapture	• High purity • Highly specific to selected markers/antibodies • No particle aggregation	• Higher cost • Biased isolation of marker-positive vesicles • Low yield

Figure 1.4 Comparison of different EV isolation methods.
Diagram and table comparing the recovery and specificity of the most common EV isolation techniques. Red, blue, and yellow boxes indicate global concentration techniques, size-based isolation techniques, and high specificity EV isolation techniques, respectively. Dotted arrows indicate follow-up purification steps. UF: ultrafiltration, SEC: size-exclusion chromatography, DC: differential centrifugation, DG: density gradient, AF4: asymmetric flow field-flow fractionation, IP: immunoprecipitation. Figure adapted from Cocozza, *et al*. with permission (licence number 5145430423004) (Cocozza *et al.*, 2020).

1.3 The vault particle

The vault particle is the largest known ribonucleoprotein complex in eukaryotic cells and is highly conserved among eukaryotes both structurally and compositionally (Kedersha and Rome, 1986; Kedersha *et al.*, 1990). They measure almost three times the size of ribosomes with a morphology similar to the vaulted ceiling of Gothic cathedrals, displaying 39-fold symmetry as imaged by electron microscopy (Figure 1.4A) (Kedersha and Rome, 1986). Vaults have a hollow barrel-like shape composed of two identical halves, which are able to open up into an eight-petal structure like a flower surrounding a ring in the centre. These 13 MDa subcellular organelles primarily consist of three vault proteins: MVP, telomerase protein component 1 (TEP1), poly (adenosine diphosphate-ribose) polymerase 4 (PARP4/vPARP), and vtRNAs (Figure 1.4B). The 99 kDa MVP accounts for over 70% of the particle mass, with the outer shell of the vault containing 78 MVP copies. TEP1 (290 kDa) and PARP4 (193 kDa) localise inside the particle, with vtRNAs (80-150 nucleotides) localising at the end of the caps.

Despite the molecular features of the vaults being illustrated since its first discovery, their function remains elusive (Slesina *et al.*, 2006; Galbiati *et al.*, 2018). *In vivo* disruption of MVP and TEP1 in mouse models revealed no obvious phenotype, despite the presence of MVP being essential for vault particle assembly (Kickhoefer *et al.*, 2001; Mossink *et al.*, 2002). Inspired by their subcellular localisation near the cytoskeleton, a role in modulating nuclear-cytoplasmic transport has been suggested by several studies (Kedersha and Rome, 1990; Hamill and Suprenant, 1997; Herrmann *et al.*, 1999). For example, Li *et al*. (1999) reported the axonal transport of vaults between the soma and the nerve terminal, suggesting the potential involvement of vaults in cytoskeletal transport (Li *et al.*, 1999). As already agreed by several reviews, vaults may be involved in multiple processes of several cellular activities, including multidrug resistance, signalling pathway regulation, and immunity (Mossink *et al.*, 2003; Berger *et al.*, 2009). Here, we discuss the function of the vault particles by each of the components.

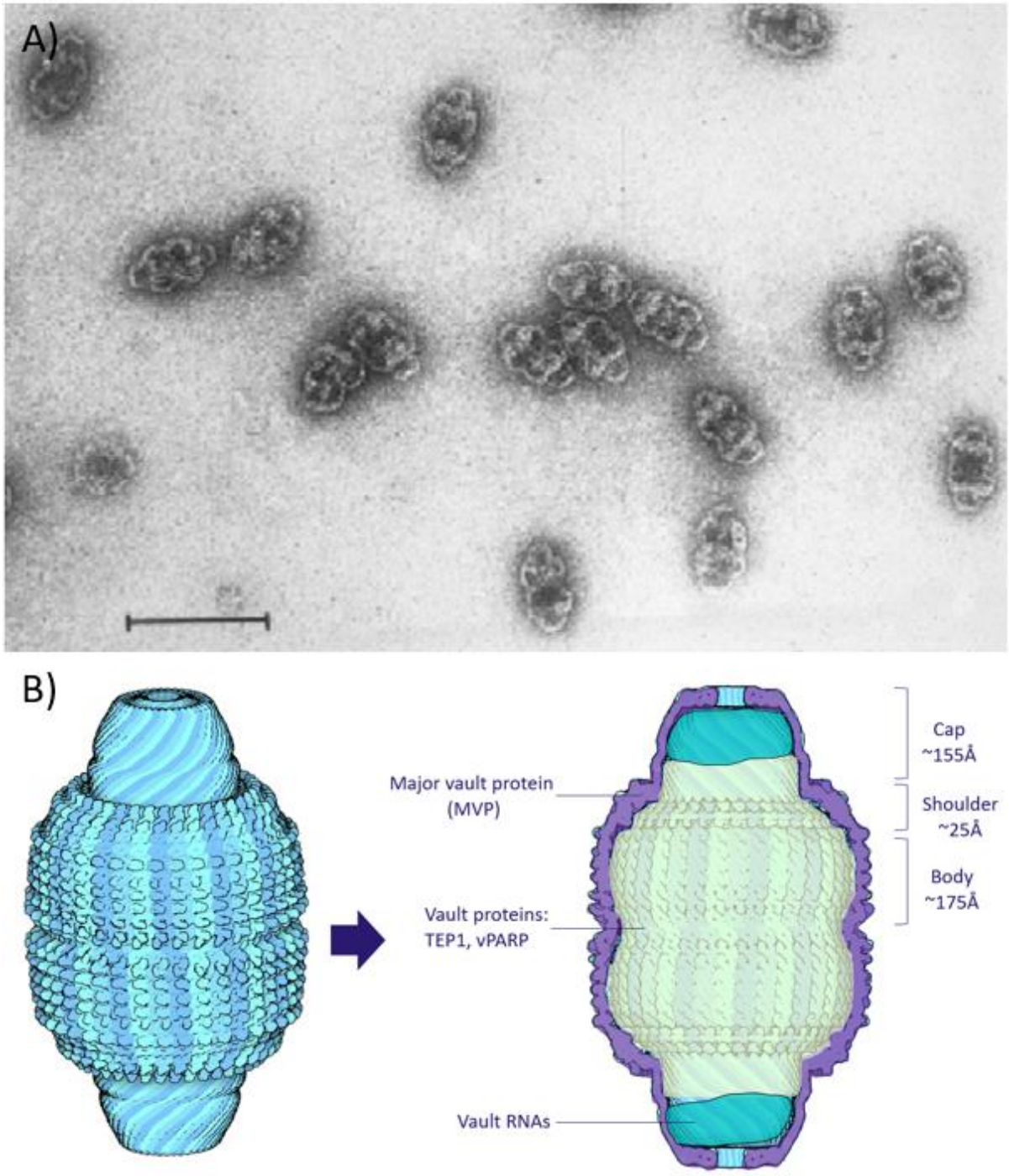

Figure 1.5 Electron microscopy image and structure of vault particles.
A) Electron microscopy illustrates the morphology of vault particles with calibration bar (lower left) showing 100 nm. Image taken from Kedersha and Rome, 1986 with permission (licence number 1146890-1) (Kedersha and Rome, 1986). **B)** Diagram shows the molecular composition of the vault particle: MVP, TEP1, PARP4/vPARP, and vtRNAs.

1.3.1 MVP

As the main structural component of vaults, the disruption of MVP has been used to prevent the assembly of the vault particle (Berger *et al.*, 2009). Vault formation is largely dependent on the expression of MVP rather than the minor vault proteins (TEP1, PARP4), suggesting that a normal level of MVP is the prior condition for vault particle being assembled (Kickhoefer *et al.*, 1998). However, MVP (-/-) mice showed no observable abnormalities (Mossink *et al.*, 2002).

There is evidence that MVP serves a diverse range of functions. It has been linked with resistance to apoptosis in senescent human diploid fibroblasts (HDFs), as knockdown of MVP significantly reduced the expressions of anti-apoptotic proteins B-cell lymphoma 2 (Bcl-2) and increased c-Jun expression in senescent HDFs (Ryu *et al.*, 2008). A strong link between MVP and cell death was evidenced by MVP knockdown inducing apoptosis in macrophages, human airway smooth muscle cells, hepatocellular carcinoma (HCC), and breast cancer cell lines (Ben *et al.*, 2013; Pasillas *et al.*, 2015; Das *et al.*, 2016; Lee *et al.*, 2017). Cell-surface MVP also contributes to promoting tumour cell proliferation, migration and invasion in HCC cells, potentially by activating the mechanistic target of rapamycin (mTOR), focal adhesion kinase (FAK), ERK and Akt pathways (Lee *et al.*, 2017). Overexpression of MVP has been linked with significantly lower expression of Ku70/80 and Bcl-2-associated X protein (BAX), indicating a role for vaults involved in non-homologous end-joining repair mechanisms (Lloret *et al.*, 2009). Furthermore, MVP has been shown to suppress obesity and atherosclerosis, negatively regulate osteoclastogenesis, and is closely associated with viral infection and pathogenesis (Ben *et al.*, 2019; Wang *et al.*, 2020; Yuan *et al.*, 2021).

The vault particle was implicated in doxorubicin resistant lung cancer, where MVP was found to be overexpressed (Scheper *et al.*, 1993). Overexpression of MVP has been found in various multidrug-resistant cancer cell lines (Schroeijers *et al.*, 2000). A recent study has linked MVP to the poor recurrence-free survival of patients with triple-negative breast cancer (TNBC). They also evidenced the contribution of MVP to chemo-resistance in a TNBC cell line by activating Akt pathway and promoting epithelial to mesenchymal transition (EMT), driven by the binding of Notch1 to the promoter sequences of MVP (Xiao *et al.*, 2019). MVP is also known as lung resistance-related protein

(LRP) due to its essential role identified in human non-small cell lung carcinoma (NSCLC) cell line SW-1573 in the 1990s (Scheper *et al.*, 1993). Initially, the resistance to a series of chemotherapeutic drugs including doxorubicin was induced by elevated MVP expression upon sodium butyrate (NaB) treatment of SW-620 cells, which can be abolished by insertion of either of two ribozymes specific to MVP. NaB-induced MVP overexpression also resulted in the re-localisation of doxorubicin, adriamycin, and VP-16 from nucleus to the cytoplasm (Kitazono *et al.*, 1999, 2001). Similar results derived from pharyngeal carcinoma cells further demonstrated that MVP can mediate multidrug resistance by transporting agents away from the nuclear targets (Cheng *et al.*, 2000). A later update from the same group further confirmed the MVP upregulation in SW-620 cell line can be generally induced by hyperosmotic stress (including NaB, sucrose, or sodium chloride) through the p38 MAPK pathway (Ikeda *et al.*, 2008). Moreover, results from a study knocking down three individual vault proteins supported the vital role of MVP (and potentially PARP4) in maintaining cell viability in drug-resistant cell lines (Wojtowicz *et al.*, 2017).

Noticeably, MVP has been shown to mediate nucleus-cytoplasm translocation of chemotherapeutic drugs by facilitating the formation of cytoplasmic vesicles. Less-sensitive cancer cells tend to display subcellular relocation of chemotherapeutic drugs into well-defined intracytoplasmic vesicles, which were co-localised with MVP (Meschini *et al.*, 2002). MVP overexpressed by tumour-surrounding adipocytes also mediated the intracellular and extracellular transport of doxorubicin-containing EVs in breast cancer cells (Lehuédé *et al.*, 2019). As the cytosolic sequestration of doxorubicin in lysosomes was abolished upon MVP knockdown, a fundamental role for MVP in mediating a multidrug resistant phenotype of tumour cells was suggested (Herlevsen *et al.*, 2007). Despite the evidence that MVP is involved in drug resistance there are contradictory studies. In MVP-deficient mice no hypersensitivities to multiple drugs was found in neither embryonic stem cells nor the bone marrow cells derived from the knockout animal model (Mossink *et al.*, 2002). A correlation between the expression of MVP and the resistance to cisplatin was observed in NSCLC cells but not to five other chemotherapeutic drugs including doxorubicin (Berger, Elbling and Micksche, 2000). Another

study in an ovarian carcinoma cell line, A2780, also failed to observe any resistance to doxorubicin, vincristine and VP16 despite the overexpression of MVP (Scheffer *et al.*, 1995).

More interestingly, in dendritic cells MVP was found to be co-localised with the lysosomal marker CD63, which is also generally expressed by late endosomes (also known as multivesicular bodies) and widely accepted as one of the common EV markers (Schroeijers *et al.*, 2002; Pols and Klumperman, 2009). Further evidence of MVP mediated exosomal cargo sorting has been reported in colon cancer cells, where selectively loaded miRNA cargo in EVs promoted tumour progression (Teng *et al.*, 2017). These studies have suggested a potential role of MVP in intracellular and extracellular vesicular trafficking and selective cargo sorting.

1.3.2 TEP1

TEP1 is a telomerase-associated protein component, encoded by the *TEP1* gene. Apart from functioning as a minor vault protein, this 290 kDa protein also serves as a major component of another ribonucleoprotein complex responsible for catalysing the newly-formed telomerases on the chromosome ends (Saito *et al.*, 1997; Kickhoefer, Stephen, *et al.*, 1999). The interacting counterparts of TEP1 include telomerase RNA and the catalytic protein telomerase reverse transcriptase (TERT) in mammalian cells, which enables the biochemical function of the complex. However, the levels of telomerase RNA and the telomerase activity were not affected in the *mTEP1*-/- mouse models (Liu *et al.*, 2000; Kickhoefer *et al.*, 2001). Although TEP1 is shared by two ribonucleoprotein complexes, researchers have failed to detect any telomerase activity related to vault particles, indicating a potential role for TEP1 in facilitating ribonucleoprotein structure or assembly in vaults (Kickhoefer, Stephen, *et al.*, 1999).

Kickhoefer *et al*. (2001) have stressed the importance of TEP1 in stabilising vtRNAs in vault particles (Kickhoefer *et al.*, 2001). Three-dimensional reconstruction of vaults revealed that deficiency of mTEP1 in mice resulted in structurally intact vaults with less dense caps. Furthermore, a complete absence of vtRNA was observed in *mTEP1*-/- mouse-derived vaults compared to the wild type, which was complementary to the presence of vtRNA detected in the supernatant fractions derived from vault

purifications (Kickhoefer *et al.*, 2001). The biochemical interactions of TEP1 with vtRNAs or telomerase are dependent on its Tetrahymena p80 homology region, which is also responsible for targeting TEP1 to the vaults during the particle assembly (Poderycki *et al.*, 2005).

More recently, in a study assessing ovarian cancer samples from patients free of chemotherapy treatment, the expression of TEP1, together with MVP and PARP4, has been found to be significantly downregulated at the mRNA level in tumour samples compared to the healthy group, but upregulated at the protein level (Szaflarski *et al.*, 2013). The altered expressional levels of vault proteins were related to the deregulation of other multidrug resistance-associated proteins in high-grade tumours. Thus, the post-transcriptional regulation of the vault proteins was illustrated to be important in cancer-related drug resistance (Szaflarski *et al.*, 2013).

1.3.3 PARP4

PARP4 is a 193 kDa enzyme encoded by human *PARP4* gene, which is also known as vPARP. With a homologous domain to the poly (adenosine diphosphate-ribosyl) transferase, it cannot bind to DNA directly due to the lack of the N-terminal DNA binding domain, which indicates its transferase activity may be subject to the interactions with other protein counterparts (Kickhoefer, Siva, *et al.*, 1999). The polymerase activity of PARP4 was found to be unnecessary for incorporating glutathione S-transferases (GST)-tagged-C-terminal region of PARP4 into *E. coli*-synthesised vault-like structures assembled by protein C-tagged human MVP (Zheng *et al.*, 2004). Although the activity of PARP4 seemed to be irrelevant to the self-assembly of vault-like particles by MVP, an activating role of PARP4 for MVP-induced drug resistance was highlighted in multidrug-resistant cell lines (Wojtowicz *et al.*, 2017). Furthermore, a study imaging green fluorescent protein (GFP)-tagged MVP in a NSCLC cell line reported the nearly complete co-localisation of tube-like vault structures in the cytoplasm with PARP4 proteins (van Zon *et al.*, 2003). Taking together, these results suggest a structural role for minor vault proteins in the assembly and stabilisation of the vault complex.

1.3.4 Vault RNA

Approximately 5% of the mass of the vault particle comes from short polymerase III transcripts named vtRNAs (Kedersha and Rome, 1986). While the polymerase III promoter elements are highly conserved, vtRNAs have shown species-specific differences in their lengths ranging from 86 to 141 nucleotides (nt). However, all vtRNAs have a similar stem-loop secondary structure (van Zon *et al.*, 2003). The number of vtRNA paralogues also differ among species: mice and rats have only one 141 nt long vtRNA, bullfrogs have two vtRNAs with lengths of 89 and 94 nt. In human cells, four vault RNA paralogs are encoded by the *VTRNA1-1*, *VTRNA1-2*, *VTRNA1-3*, and *VTRNA2-1* genes (Figure 1.5A), with vtRNA 3-1P encoded by the *VTRNA3-1P* gene on the X chromosome which is now generally accepted as a pseudogene (van Zon *et al.*, 2001; Stadler *et al.*, 2009).

Disruption of vtRNA by nuclease treatment had no effect on the assembly of the vault complex, indicating a functional but not structural role of vtRNA in vaults (Kedersha *et al.*, 1991). Similar to MVP, vtRNAs have also been linked with drug resistance in human malignancies. High levels of vtRNA expressions have been found in human glioblastoma, leukaemia, and osteocarcinoma cell lines, together with higher resistance to chemotherapeutic agents (Gopinath, Wadhwa and Kumar, 2010). A study using *in vitro* MCF7 breast cancer line suggested the close interaction between vtRNA 1-1 and the polypyrimidine tract binding protein associated splicing factor (PSF), which has been previously linked with the regulation of cell sensitivity to chemotherapy (Chen *et al.*, 2018). vtRNA 1-1-regulated PSF level intermediates with the transcriptional expression of an oncogene G antigen 6 (GAGE6), which then induced drug resistance by enhancing cell proliferation and colony formation *in vitro*. vtRNA 1-1 induced PSF transcriptional activity and MCF7 chemoresistance were independent of the expression of MVP (Chen *et al.*, 2018). In agreement with these findings, vtRNA1-1 induced resistance to mitoxantrone can be abolished by RNA interference in multi-cancer cell line models (Gopinath, Wadhwa and Kumar, 2010). vtRNA 1-1 and 1-2 have been shown to bind to the chemotherapeutic compound mitoxantrone, which may facilitate the extracellular export of the compounds (Gopinath *et al.*, 2005). In addition to drug resistance, vtRNAs have also been linked with protecting cells from undergoing apoptosis and supressing anti-viral immunity, with vtRNA 2-1 (also

known as nc886) being largely associated with multiple processes involved in tumourigenesis (Amort *et al.*, 2015; Li *et al.*, 2015; Ahn *et al.*, 2018; Golec *et al.*, 2019). Importantly, most of the vtRNA is not associated with the vault particle (Kickhoefer *et al.*, 2002), implying it could be involved in other cellular activities independent of vaults. Some vault-free vtRNA were found to be complexed with the Lupus La autoantigen in a separate smaller ribonucleoprotein particle (Kickhoefer *et al.*, 2002; Rome and Kickhoefer, 2012). Recently, a novel role of vtRNA 1-1 in autophagy has begun to be elucidated. It has been shown to directly bind to sequestosome 1 (p62/SQSTM1), a selective autophagic receptor that ushers cargo into phagophores, and mediate the normal autophagic function by interfering with its oligomerisation, revealing a novel mode of direct regulation of protein's activity by RNA molecules (Horos *et al.*, 2019a; Horos *et al.*, 2019b).

Although multiple proteins have been identified to bind to vtRNAs, their affinity to certain proteins (e.g. serine/arginine rich splicing factor 2, SRSF2) is largely influenced by post-transcriptional modifications (Sajini *et al.*, 2019). The regulatory functions of vtRNA 1-1 can be derived from an NSUN2-mediated deposition of 5-methylcytosine (m^5C), which also resulted in the formation of small vtRNA fragments (svRNAs) with regulatory activity (Figure 1.5B) (Hussain *et al.*, 2013; Sajini *et al.*, 2019). These svRNAs were produced by a Dicer-dependent but Drosha-independent manner from the stem region of full-length vtRNA and their miRNA-like regulatory functions were detected in their target genes (e.g. CYP3A4 and CACNG7/8) (Persson *et al.*, 2009). Deep sequencing of small RNA from MCF7 cells showed at least six svRNA clusters (mostly fragments of vtRNA 1-1) matched to 180 sequences out of 5 million total RNA reads (Figure 1.5C) (Persson *et al.*, 2009). Four mature forms of svRNA (svRNA2/svRNAa, svRNA3/svRNAb, svRNA1/svRNAb*, svRNA4/svRNA*) have been suggested (Persson *et al.*, 2009; Hussain *et al.*, 2013). An increase of svRNA1, svRNA2, and svRNA3 abundance was observed in multidrug resistance models (Persson *et al.*, 2009), and svRNA4 was linked to a functional role in regulating the epidermal differentiation programme, whose processing was dependent on the methylation activity of NSUN2 (Sajini *et al.*, 2019). Other vtRNA modifications also include N^6-methyladenosine (m^6A) and pseudouridylation (Ψ) (Warda *et al.*, 2017; Guzzi *et al.*, 2018).

Lässer *et al*. have reported distinct vtRNA profiles in two different EV subpopulations distinguished by their densities, where enrichment of vtRNAs was found in high-density, small EVs (30 to 100 nm) most likely to be exosomes (Lässer *et al.*, 2017). In accordance with these results, vtRNA paralogues have also been found to be enriched in small EVs compared to other EV subsets derived from melanoma cells, DC cells and prion-infected neuronal cells (Bellingham, Coleman and Hill, 2012; Nolte'T Hoen *et al.*, 2012; Lunavat *et al.*, 2015). The presence of svRNA fragments from all vtRNA paralogues was observed in human endothelial cells and EVs, where higher abundance of 5' fragments of vtRNA 1-3 and vtRNA 2-1 was observed in cells compared to that in EVs (van Balkom *et al.*, 2015). Whereas in colon cancer cells, small vtRNA detected by short RNA sequencing was found dominantly in the EV preparations and non-vesicular fractions, whilst full-length vtRNA detected by long RNA sequencing was more abundant in parental cells. This led the authors to postulate that the majority of extracellular vtRNA is either processed svRNA or fragments of vtRNA (Jeppesen *et al.*, 2019). However, this remains to be elucidated.

Few studies have focused on the sorting and packaging of vtRNA and vtRNA fragments into EVs. An RNA-binding protein, Y-box binding protein 1 (YBX1), has been identified as a major player in transporting small non-coding RNA molecules including vtRNAs into EVs derived from HEK293T cells (Shurtleff *et al.*, 2017). This study also reported the resistance of vtRNA 1-1 (but not vtRNA1-2 and vtRNA1-3) to RNase + detergent treatment of EVs, indicating the possibility that vtRNAs could be stabilised in EV preparations by existing as RNP or RBPs.

To date there have been no published studies investigating the packaging of vtRNAs into EVs derived from OSCC cells.

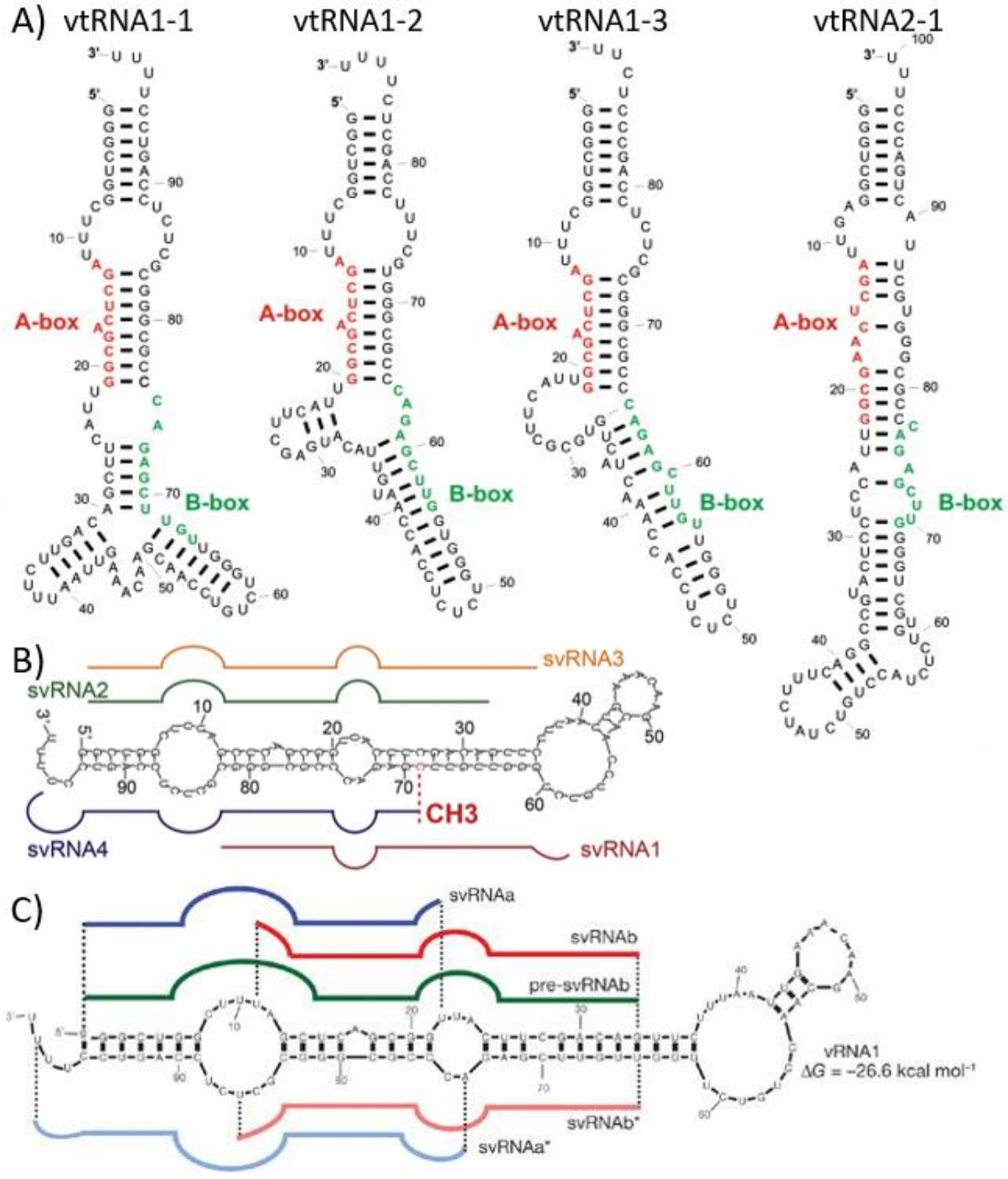

Figure 1.6 Secondary structure of vtRNA 1-1, 1-2, 1-3, and 2-1.
A) Schematic shows the secondary-structure of four vtRNA paralogs, in which the conservative polymerase III promoter elements A-box and B-box are indicated in red and green, respectively. Image was taken from Nandy *et al*., 2009 with permission (licence number: 5145440549619) (Nandy *et al.*, 2009). **B,C)** vtRNA 1-1-derived svRNA sequences (shown in colour) suggested by Hussain *et al*. (2013) (licence to reuse figure: 5145440717799) and Persson *et al*. (2009) (licence to reuse figure: 5145440902301), respectively.

1.4 Hypothesis

Previous work from the Hunt lab has found high-levels of vtRNAs in OSCC-derived EV preparations, together with the presence of MVP. The hypothesis is that vtRNAs are selectively packaged into oral cancer-derived extracellular vesicles, which is a process assisted by MVP or the vault particle.

1.5 Aims and objectives

The aims and objectives of this study were to:

- Characterise the relative abundance of vault components in cells and EV preparations among a panel of normal cells, immortal cells, and OSCC cell lines. Transcript abundance will be assessed by quantitative real-time polymerase chain reaction (qPCR) and vault protein abundance will be determined by western blotting. The abundance of vtRNAs in EV pellets derived from a panel of OSCC cell lines will be assessed by small RNA sequencing and validated by qPCR.
- Investigate the involvement of MVP in the sorting and trafficking of vtRNA into EVs. siRNA knockdown of MVP coupled with qPCR will be used to determine if packaging of vtRNAs into EVs is dependent on MVP/vault particles. Immunofluorescence microscopy of whole cells will then be used to determine if MVP/vault particles associate with the endosomal compartment to shuttle vtRNAs to be packaged into EVs (exosomes).
- Examine whether extracellular vault proteins and vtRNAs are *bona fide* EV cargo. The presence of vault components in different EV pellets will be interrogated by biochemical assays, to determine the topological association of vault components and EVs.
- Reassess the EV isolates derived from several commonly used EV separation techniques, including differential centrifugation, size-exclusion chromatography, and immunoaffinity-based EV capture. Generate an EV isolation workflow that allows successful separation of EVs from similar-sized contaminating particles.
- Establish a methodology that allows detection of small vtRNA fragments in EVs and further investigate the cargo sorting mechanisms of such molecules in OSCC.

Chapter 2 Materials and methods

2.1 Materials, media, and chemical supplies

All laboratory chemicals and reagents were ordered from Merck (previously known as Sigma-Aldrich) and molecular biology reagents were ordered from Thermo Fisher Scientific unless otherwise stated.

2.2 Mammalian cell culture

2.2.1 Primary cells

Primary normal oral keratinocytes (NOKs), a gift from Dr Sven Niklander and Dr Helen Colley, were derived from oral mucosal biopsies from 3 healthy volunteers with ethical approval (09/H1308/66) as previously described (Colley *et al.*, 2011). NOK805 was derived from a 28-year-old female smoker; NOK829 was from a 22-year-old female smoker; NOK830 was from a 28-year-old non-smoker male donor. All NOKs were originally isolated from the buccal area and were used within passage 1-5 in this study.

2.2.2 Cell lines

Three OSCC cell lines were used in this study. H357 (ESACC Catalogue No.: 06092004, RRID: CVCL_2462) was originally isolated from a 74-year-old male patient with a squamous cell carcinoma of the tongue, which displays a relatively small and polygonal morphology (Prime *et al.*, 1990). SCC9 (ESACC Catalogue No.: 89062003, RRID: CVCL_1685) was derived from a tongue squamous cell carcinoma from a 25-year-old male patient that has an spindle-shapled epithelial morphology (Rheinwald and Beckett, 1981). SCC4 (ESACC Catalogue No.: 89062002, RRID: 1684) was established from a human tongue squamous cell carcinoma of a 55-year-old male and has a large cobblestone-shaped epithelial-like morphology (Rheinwald and Beckett, 1981) (Figure 2.1).

FNB6 (a gift from Prof Keith Hunter, RRID: CVCL_F734) is an immortalised human buccal keratinocyte cell line that resembles normal oral keratinocytes in 2D *in vitro* culture (Figure 2.1), created by transfection of human telomerase reverse transcriptase (hTERT) (Mcgregor *et al.*, 2002).

A human lung carcinoma cell line that displays the morphology of type II alveolar epithelial cells, A549 (ECACC Catalogue No.: 86012804, RRID: CVCL_0023), derived from a 58-year-old Caucasian male was used as a positive control for cellular expression of MVP (Giard *et al.*, 1973).

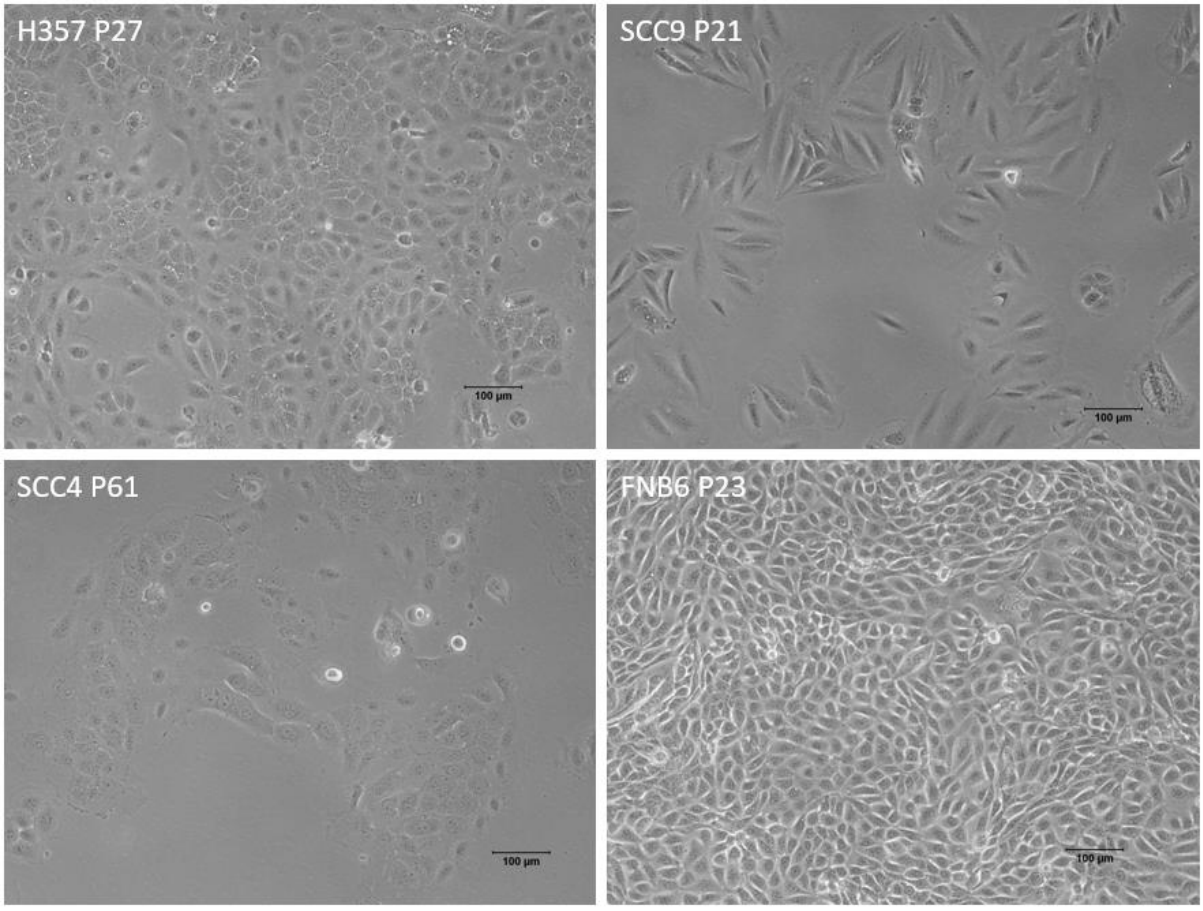

Figure 2.1 Images of OSCC and FNB6 cell lines.
Images of H357, SCC9, SCC4, and FNB6 cells cultured in vivo. Scale bars indicate 100 µm.

2.2.3 Cell culture medium

NOKs were cultured on flasks coated with recombinant human type-I collagen (supplied as part of a Coating Matrix Kit, Gibco) in keratinocyte growth medium (KGM). Medium composition is described in Table 2.1.

For direct comparison purposes, OSCC cell lines and FNB6 were routinely cultured in KGM supplemented with 10% (v/v) FBS. A549 cells were maintained in 1:1 ratio of Dulbecco's Modified Eagle's Medium: Nutrient Mixture F-12 Ham (DMEM: F12) with 10% (v/v) FBS. In addition, the transfection experiments and after-transfection maintenance of H357 and SCC4 cells were also performed in this medium as recommended in the original cell line information upon purchase (Rheinwald and Beckett, 1981; Fahey *et al.*, 1996). Compositions of both media are listed in Table 2.1.

Table 2.1 Composition of cell culture growth media.

Composition	Stock concentration	Final concentration in 500 ml medium	
		KGM	DMEM:F12
Dulbecco's Modified Eagle's Medium (DMEM) – low glucose	- (With 1000 mg/l glucose, and sodium bicarbonate, without L-glutamine)	67% (v/v)	45% (v/v)
Nutrient Mixture F-12 Ham	- (With sodium bicarbonate, without L-glutamine)	23% (v/v)	45% (v/v)
Fetal Bovine Serum (FBS)	-	10% (v/v)	10% (v/v)
Penicillin-Streptomycin	Solution stabilised, with 10,000 units penicillin and 10 mg streptomycin/ml	100 IU/ml penicillin and 100 µg/ml streptomycin	100 IU/ml penicillin and 100 µg/ml streptomycin
Amphotericin B	250 µg/ml	2.5 µg/ml	-
L-Glutamine	200 mM	2 mM	2 mM
Adenine	1.8×10^{-2} M	1.8×10^{-4} M	-
Hydrocortisone	295 µg/ml	0.5 µg/ml	0.5 µg/ml
Insulin	9.5-11.5 mg/ml	5 µg/ml	-
Epidermal Growth Factor human (hEGF)	-	10 ng/ml	-

2.2.4 Cell culture and maintenance

Cell culture was conducted in Class II Biosafety Cabinets. Cells were cultured in incubators at 37˚C with 5% CO_2 supply. After reaching 80-90% confluency in the tissue culture flasks, cells were washed with phosphate buffered saline (PBS) twice followed by trypsinisation with 0.25% trypsin-ethylenediaminetetraacetic acid (EDTA) at 37°C. During trypsinisation, monolayers were checked every 5 min under an inverted light microscope until fully detached. Normal growth medium containing 10% (v/v) FBS was added to the flask when cells were detached to neutralise the trypsin. The cell suspension was then split at a 1:5 ratio to fresh flasks containing normal growth medium and further cultured.

2.2.5 Cell counting and seeding

Cells were counted using a haemocytometer. Briefly, confluent cells were trypsinised as above and resuspended in fresh growth medium containing FBS, taking care to achieve a single-cell suspension. 10 µl of cell suspension was mixed with 10 ul 0.4% Trypan Blue solution and incubated for 1-2 minutes at room temperature. The mixture was then loaded into one of the chambers on a haemocytometer, and viable cell number was counted in each quadrant to calculate the number of cells in the suspension.

The cells were then pelleted by centrifuging at 300 × *g* for 5 min at room temperature. Following centrifugation, the supernatant was discarded and cells were resuspended in fresh medium to achieve the desired concentration for cell seeding. Typically, 200,000 cells were seeded per well in 6-well plates and 10,000 cells were seeded per well in 96-well plates. Monolayers were washed twice with PBS before solubilisation of cells for downstream analysis.

2.2.6 Storage of mammalian cells

Cells were trypsinised from flasks and counted as above. Cells were then pelleted by centrifugation and resuspended in 90% (v/v) FBS with 10% (v/v) dimethyl sulfoxide (DMSO) to reach the concentration of 1×10^6 cells/ml. 1 ml of cell suspension was added to each cryogenic storage vial and incubated overnight at -80°C in a Mr. Frosty™ freezing container before being transferred and stored in liquid nitrogen.

2.3 Bacteria and growth media

2.3.1 Growth media and antibiotic

Luria-Bertani (LB) agar and LB broth media were used to routinely grow *Escherichia coli* (*E. coli*) on plates and in liquid culture, respectively (Table 2.2). Medium was made with distilled H_2O (dH_2O) and sterilised by autoclaving. Where appropriate, ampicillin stock (50 mg/ml) was added to the medium after cooling down to 50°C to reach a final concentration of 50 µg/ml. The molten LB agar

was poured into Petri dishes (20 ml/dish) and allowed to set. Plates were stored at 4°C and used within 4 weeks.

Table 2.2 Composition of *E. coli* growth media.

Composition	LB broth	LB agar
Tryptone	10 g/l	10 g/l
Yeast extract	5 g/l	5 g/l
NaCl	10 g/l	10 g/l
Bacteriological agar	-	15 g/l

2.3.2 Growth and storage of *E. coli*

E. coli was cultured aerobically at 37°C. Overnight liquid cultures were set up for 16-24 h with shaking (250 rpm) in a volume of 50 ml medium in sterile flasks.

E. coli strains were stored at -80°C in LB broth with 50 µg/ml ampicillin with 25% (v/v) glycerol.

2.3.3 Transformation of competent cells

NEB® 5-alpha Competent *E. coli* (Genotype: *fhu*A2 Δ(*arg*F-*lac*Z)U169 *pho*A *gln*V44 Φ80 Δ(*lac*Z)M15 *gyr*A96 *rec*A1 *rel*A1 *end*A1 *thi*-1 *hsd*R17) was purchased from New England Biolabs and transformed with plasmid DNA (see details of plasmids in Section 2.5.1) following the manufacturer's protocol. Briefly, a 50 µl vial of competent cells was thawed on ice for 10 min, mixed with ~10 ng plasmid DNA and incubated for a further 30 min on ice. The mixture was then incubated at 42°C for 30 s and placed back on ice for 5 min. Following incubation, 950 µl of room temperature LB broth medium was added to the vial and the cells were incubated at 37°C for 1 h with shaking (250 rpm). To select transformed cells, 20-100 µl of cell suspension was spread onto LB agar plates with selective antibiotic and incubated overnight at 37°C.

2.4 Extracellular vesicle methods

2.4.1 Preparation of EV-depleted FBS

Bovine EVs present in commercial FBS were removed prior to addition to the growth medium. Conventionally, FBS is ultracentrifuged at 100,000 × *g* overnight at 4°C to pellet most of the bovine EVs and the supernatant used as ultracentrifugation EV-depleted FBS (UC-FBS). Kornilov *et al.* (2018) suggested a novel method of achieving a more efficient elimination of bovine EVs through ultrafiltration, to obtain UF-FBS, which was adopted in the current study. According to the original study, UF-FBS contained comparably low level of bovine EVs as commercially available EV-depleted FBS. In addition, it was able to maintain normal cell growth, metabolism and EV production for up to 96 h (Kornilov *et al.*, 2018).

FBS was filtered through 0.2 µm filters and loaded into the upper chamber of the Amicon Ultra-15 centrifugal filter units (100 kDa molecular weight cut-off). After centrifugation at 2,500 × *g* for 2 h at 4°C, flow-through was recovered in the lower chamber as ultrafiltered EV-depleted FBS (UF-FBS). UF-FBS aliquots were sterilised by being filtered again through 0.2 µm filters and stored at -20°C.

2.4.2 Cell culture conditioned medium

For 72 h conditioned medium, 2×10^6 cells were seeded per T175 cm^2 tissue culture flasks in a total volume of 20 ml normal growth medium on day 1. Cells were incubated for 24 h to allow attachment. On day 2, the medium was discarded, monolayers were washed twice with PBS, and the medium was replaced with 15 ml fresh growth medium supplemented with 10% (v/v) UF-FBS. After incubation for further 72 h, conditioned medium was collected from the flasks on day 5 and centrifuged at 300 × *g* for 10 min to pellet unattached cells and debris. The supernatant was then used for downstream EV isolation methods (Section 2.4.3).

Where a smaller volume, but more concentrated conditioned medium was required, a 24 h medium conditioning protocol was used. In which case, 2×10^6 cells were seeded in T75 flasks in a total volume of 10 ml growth medium on day 1. Cells were washed and the medium was replaced with 10

ml growth medium supplemented with 10% (v/v) UF-FBS on day 2. Cells were then incubated for 24 h before conditioned medium was collected and pre-cleared at 300 × *g* for 10 min ready for EV isolation.

2.4.3 EV isolation methods

2.4.3.1 Differential centrifugation

Differential centrifugation methodology was adapted from the protocol previously described by Théry *et al*. and is illustrated in Figure 2.2 (Théry *et al.*, 2006).

Pre-cleared conditioned medium from Section 2.4.2 was firstly centrifuged at 2,000 × *g* for 10 min. The supernatant was transferred to a fresh tube and the pellet was washed with PBS and re-centrifugation at the same speed for another 10 min. Large vesicles (e.g. apoptotic bodies) were enriched at this step. Next, the supernatant collected from the previous step was centrifuged at 10,000 × *g* for 30 min, in a Beckman Coulter Avanti J26 centrifuge with a JA 12 conical rotor, to enrich medium sized EVs (e.g. microvesicles), followed by washing the pellet with PBS and re-centrifugation for 30 min at the same speed. Similarly, 100,000 × *g* pellets were obtained after centrifuging the supernatant from last step at 100,000 × *g* for 1 h followed by a wash step and re-centrifugation, in a Beckman Coulter Optima L-90K ultracentrifuge with a Ti45 fixed-angle rotor, to enrich the smallest EVs which include exosomes. Alternatively, this step `was performed in a Beckman Coulter TL-100 benchtop ultracentrifuge with a TLA-100.4 fixed-angle rotor for centrifuging smaller volumes of conditioned medium.

All centrifugation steps were performed at 4°C to minimise degradation of samples. Pellets obtained from differential centrifugation were resuspended in PBS for most downstream applications and were stored at -20°C. Where EV-protein or RNA was desired, pellets were lysed with protein or RNA lysis buffer and the lysates were stored at -20°C and -80°C, respectively, until purification.

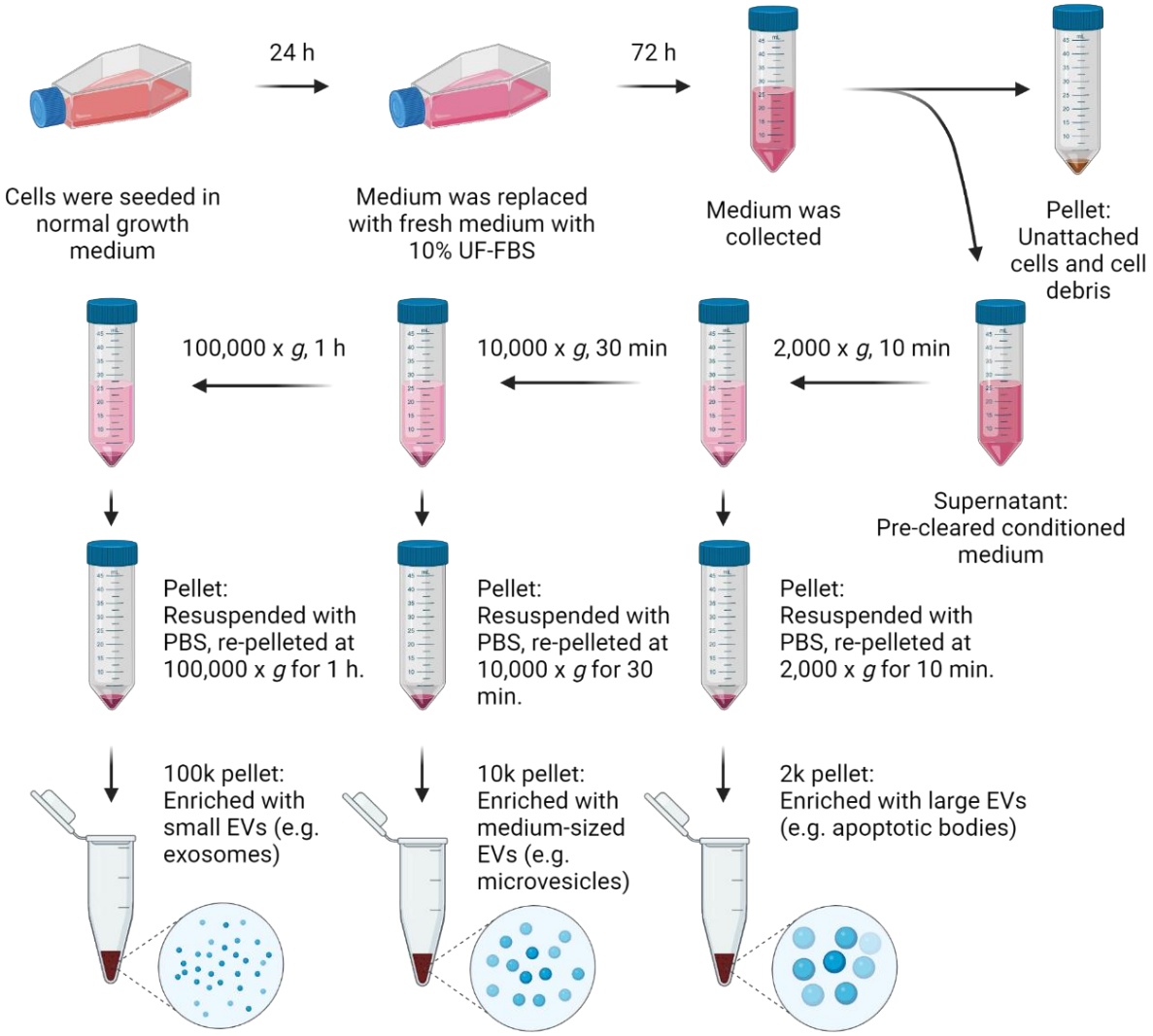

Figure 2.2 Diagram illustrating differential centrifugation.
Cells were seeded at 2 million cells per flask on Day 1 and cultured at 37 °C with 5% CO_2 supply for 24 hours. On Day 2, the medium was discarded. After washing cells with PBS twice, fresh medium containing 10% UF-FBS was added to the flasks and incubated for 72 hours. On Day 5, the medium was collected and serial centrifugation performed at 300 × *g* for 10 min, 2,000 × *g* for 10 min, 10,000 × *g* for 30 min, and 100,000 × *g* for 1 h. After each centrifugation, pellets were resuspended in PBS and re-centrifuged at the same speed for the same amount of time as the last centrifugation (except for the 300 × *g* centrifugation), whereas the supernatant was taken to the next centrifugation. In the end, 2k, 10k, and 100k pellets were collected and resuspended in appropriate buffer for further analysis.

2.4.3.2 Size exclusion chromatography

2.4.3.2.1 Column preparation

A disposable 20 ml Econo-Pac® chromatography column (Bio-Rad) with a porous 30 µm polyethylene bottom bed support was loaded with 14 ml Sepharose CL-2B resin/ethanol slurry (GE Healthcare) and topped up with 6 ml PBS + 0.03% (v/v) Tween-20 (PBST) at least 2 h prior to use to

allow the resin to settle by gravity. An upper bed support was carefully placed on top of the resin without disturbing the stacked Sepharose. The bottom cap was removed to drain away the ethanol and PBS and the column was washed with 30 ml PBST.

2.4.3.2.2 Vesicle purification

Pre-cleared conditioned medium from Section 2.4.2 was loaded into the upper chamber of a Vivaspin-20 spin column (100 kDa molecular weight cut-off) (GE Healthcare) and centrifuged at 6,000 × *g* for ~45 min until a total volume of 30 ml had been concentrated down to 0.5 ml. Concentrated conditioned medium was then loaded to a prepared SEC column and allowed to fully enter the resin. The column was then topped up with 10 ml PBST and 0.5 ml fractions were collected immediately from the bottom of the column. The first 12 fractions collected were stored at -20°C. SEC fractions were analysed for particle counts and soluble protein concentration by ZetaView analysis (Section 2.4.4.1) and BCA assay (Section 2.7.2), respectively.

2.4.3.3 Dynabead immunocapture

2.4.3.3.1 Antibody coupling to Dynabeads

Buffers used in antibody coupling and EV isolation are listed and described in Table 2.3.

For negative control beads that were included in the immunocapture experiments, Dynabeads™ M-450 Epoxy (Invitrogen) were coupled with mouse IgG (mIgG) antibody (sc-2025, Santa Cruz Biotechnology) following the manufacturer's protocol. 300 µl M-450 Dynabeads (4×10^8 beads/ml) was taken from the vial after resuspending by vortexing for more than 30 s and added to a 2 ml U-bottom microfuge tube. To wash the beads, 1 ml Buffer 1 was added to the tube and mixed with the beads. The tube was then placed on a DynaMag™-2 magnet (Invitrogen) for 1 min and the supernatant was discarded. The beads were washed one more time and resuspended in 850 µl Buffer 1 and 150 µl mIgG antibody (400 µg/ml) and incubated for 15 min at room temperature. Following incubation, 200 µl bovine serum albumin (BSA) solution (2 mg/ml) was added to the tube to reach ~0.03% (w/v) and the bead-antibody mix was further incubated overnight at room temperature with gentle tilting and constant rotation. The tube was placed on the magnet for 1 min and the supernatant

was discarded. The beads were washed with 1ml Buffer 2 by mixing and incubating for 5 min with gentle tilting and rotation. After being washed twice more with Buffer 2, the beads were eventually resuspended in 1 ml Buffer 2 (final concentration 1.2×10^8 beads/ml) and stored at 4°C.

Table 2.3 Description of buffers used in EV isolation by Dynabeads.

Buffer	Description	Storage
Isolation Buffer	PBS with 0.1% (w/v) bovine serum albumin (BSA), filtered through a 0.2 μm filter	Store at 4°C, use within a week
Buffer 1	0.1 M sodium phosphate (pH 7.4) was made by adding 0.31 g of $NaH_2PO_4 \cdot H_2O$ and 1.09 g of Na_2HPO_4 (anhydrous) to 100 ml distilled H_2O, filtered through a 0.2 μm filter	Store at 4°C, use within a month
Buffer 2	Ca^{2+} and Mg^{2+} free PBS supplemented with 0.1% (w/v) BSA and 2 mM ethylenediaminetetraacetic acid (EDTA), pH 7.4, filtered through a 0.2 μm filter	Store at 4°C, use within a month

2.4.3.3.2 Dynabeads preparation

Commercially available Dynabeads™ pre-conjugated with human CD63, CD9, and CD81 antibodies were purchased from Invitrogen (Catalogue numbers: 10606D, 10614D, and 10616D). The beads were vortexed for more than 30 s before every use to ensure even suspension. 100 μl CD63 Dynabeads (1×10^7 beads/ml), 40 μl CD9 (1.3×10^8 beads/ml) and 40 μl CD81 Dynabeads (1.3×10^8 beads/ml) were mixed in a 2 ml U-bottom microfuge tube. The tetraspanin bead mix was then washed with 500 μl Isolation Buffer and placed on a DynaMag™-2 magnet for 1 min. The supernatant was discarded and the beads were ready for sample loading.

As a negative control, Dynabeads coupled with mIgG antibody (from Section 2.4.3.3.1) were used to measure the baseline affinity between bead-non-targeting antibody complexes and EVs. An equivalent number of mIgG Dynabeads was used to the total number of tetraspanin antibody-coated beads. In which case, 95 μl mIgG Dynabeads was added to a 2 ml U-bottom microfuge tube and washed the same way as the tetraspanin Dynabeads stated above.

2.4.3.3.3 Immunocapture following differential centrifugation

100k EV pellets as described in Section 2.4.3.1 were resuspended in 2 ml PBS and divided into two equal volumes: One was added to the tube containing washed tetraspanin bead mix, whilst the other half was mixed with mIgG beads (final concentration 1.14×10^7 beads/ml). The tubes were placed on a shaker and incubated with gentle tilting and rotation at 4°C overnight.

After incubation, the tubes were pulsed in a centrifuge for a few seconds to collect the samples at the bottom of the tube. If the supernatant containing unbound fraction was desired, the tubes were firstly placed on the magnet and the supernatant was collected. The unbound EVs and other particles remaining in the supernatant were sedimented by centrifugation at 100,000 × *g*, 4°C for 1 h, followed by a wash with PBS and re-centrifugation. The resulting pellets were lysed with protein lysis buffer (see Section 2.7.1) ready for analysis by western blot.

To elute the EVs, the remaining bead-EV complexes in the tubes were washed with 500 µl Isolation Buffer, followed by 2 more washes with 500 µl PBS. The washed Dynabead-bound EVs were then lysed with protein lysis buffer following the protein lysis protocol (described in Section 2.7.1). Dynabeads were removed by placing the tubes on the magnet after boiling the samples mixed with 5× Loading Buffer at 95°C for 5 min.

2.4.3.3.4 Immunocapture from conditioned medium

10 ml of pre-cleared conditioned medium (from Section 2.4.2) was loaded in a Vivaspin-20 spin column (100 kDa molecular weight cut off) and centrifuged at 6,000 × *g* for ~15 min or until 2 ml liquid remained in the upper chamber. The concentrated conditioned medium was separated into two equal volumes and each was mixed with tetraspanin bead mix or mIgG beads. The samples were then incubated and washed as above. Following incubation, the unbound fraction and captured EVs were retained and lysed as stated above.

2.4.4 EV characterisation methods

2.4.4.1 Nanoparticle tracking analysis by ZetaView

NTA was carried using a ZetaView nanoparticle tracking video microscope PMX-120 (Particle Metrix GmbH). The instrument detects particles of the selected size ranges throughout 11 positions in the sample cell, with settings suggested by the manufacturer (Table 2.4), and tracks their Brownian motion, which allows the measurement of size and concentrations of particles in solution. According to the company's instruction, the ZetaView instrument was calibrated with polystyrene particles with a known average size of 100 nm diluted in 1/500,000 in Milli-Q water, following by washing thoroughly with 5 ml Milli-Q water for 3 times prior to the sample loading.

Cell culture conditioned medium (from Section 2.4.2), differential centrifugation derived EV pellets (from Section 2.4.3.1) and SEC fractions enriched with EVs (from Section 2.4.3.2.2) were analysed on the ZetaView instrument. Samples were firstly diluted with PBS to reach a concentration that was between 10^6 to 10^7 particles/ml, the dilution factors were noted for calculating the original concentrations. 3 ml diluted sample was then injected into the sample cell with a syringe, followed by image acquisition by the instrument and automatic analysis to remove any outliers. The cell was washed thoroughly by injecting 5 ml Milli-Q water for 3 times or until no particles were detected in the cell before the next sample was loaded. Measurements for both small (~100 nm) and large (>200 nm) particles in the samples were performed using different settings stated in Table 2.4. Acquisitions for small particles were completed with three technical repeats whereas for large particles only one was recorded due to prolonged imaging time.

The concentration and the size distribution of the particles were taken from the generated report and used for further analysis. When particles in conditioned medium from different cell lines were measured, the volumes of the media recovered and the cell numbers counted were also recorded to assist with normalising particle number.

Table 2.4 ZetaView settings used for measuring small and large particles.

Parameters	Settings for small particles (~100 nm)	Settings for large particles (~200 nm)
Sensitivity	85	65
Shutter	70	90
MinBright	25 pixels	15 pixels
MaxArea (size)	500 pixels	3000 pixels
MinArea (size)	20 pixels	25 pixels
Framerate	30 frames per second (fps)	3.75 frames per second (fps)
Tracelength	15	15
Video quality	Medium	Highest
Positions	11 positions	11 positions
#Cycles	3	1-2

2.4.4.2 ExoView microchip assay

EVs in conditioned medium from H357 and SCC4 cells were characterised using the ExoView™ R100 imaging platform (NanoView Biosciences) coupled with ExoView tetraspanin microarray chips (NanoView Biosciences). Each chip was pre-coated with three tetraspanin capture antibodies (anti-CD9, anti-CD63 and anti-CD81) and a mIgG negative control, arranged in an array of spots.

Following the manufacturer's protocol, pre-cleared conditioned medium (from Section 2.4.2) was diluted 1/2 - 1/5 in proprietary incubation solution and loaded onto the chip coated with capture antibodies. The chip was then incubated at room temperature overnight, followed by several wash steps and the incubation with fluorescent secondary antibodies (detection antibodies). Finally, the chip was analysed by the ExoView™ R100 reader and images were captured and analysed by the corresponding acquisition software ExoScan v0.998 (NanoView Biosciences). Numbers of EVs captured by each antibody-coated spot were recorded for further analysis. ExoView analysis was performed by Dr Alexandra Shephard (NanoView Biosciences) as part of an instrument demonstration by the manufacturer.

2.4.4.3 EV flow cytometry

2.4.4.3.1 Antibody labelling

Anti-MVP antibody (ab175239, abcam) and recombinant rabbit IgG antibody (ab172730, abcam) were labelled and purified with the Alexa Fluor™ 488 antibody labelling kit following the manufacturer's protocol. Briefly, 100 µl antibody with 0.1 M sodium bicarbonate was added to the reactive Alexa488 dye and incubated for 1 h with occasional mixing. During the incubation, the purification spin columns were assembled and 1.5 ml purification resin was loaded and allowed to settle by gravity. The antibody-dye mix was then added dropwise to the spin column and centrifuged at 1,100 × *g* for 5 min. The labelled antibody was recovered in the collection tube.

NanoDrop™ 1000 spectrophotometer (Thermo Fisher Scientific) was used to measure the absorbance with a 1 mm pathlength at 280 nm (A_{280}) and the absorbance maximum (λ_{max}) for the dye (A_{488}). The degree of labelling (DoL), represented by moles dye per mole protein, was calculated as following:

$$\textbf{Protein concentration (M)} = \frac{\mathbf{A_{280} - (A_{488} \times CF_{280})}}{\boldsymbol{\varepsilon_{280} \times 10}}$$

$$\textbf{Moles dye per mole protein} = \frac{\mathbf{A_{488}}}{\boldsymbol{\varepsilon_{488} \times 10 \times \text{protein concentration (M)}}}$$

CF_{280}: A correction factor for the fluorophore's contribution to the absorbance at 280 nm. CF_{280} for Alexa488 is 0.11.

ε_{280}: The molar extinction coefficient in cm^{-1} M^{-1} of a typical IgG at 280 nm. ε_{280} = 203,000.

ε_{488}: The approximate molar extinction coefficient of the dye. ε_{488} = 71,000.

Fluorophore-labelled antibodies were covered in foil and stored at -20°C.

2.4.4.3.2 Sample preparation

2k, 10k and 100k pellets (derived from 10 ml conditioned medium) were resuspended in 50 µl PBS after differential centrifugation (see Section 2.4.3.1). A volume of 20 µl of PE-conjugated mouse anti-human CD63 antibody (557305, BD Biosciences) and 2 µl Alexa488-labelled anti-MVP antibody (or

2 µl Alexa488-labelled rabbit IgG antibody for negative control samples) from Section 2.4.4.3.1 were added to each sample and incubated at 37°C for 30 min. The labelled particles were washed with PBS by ultracentrifuging at 100,000 × *g* for 1 h at 4°C to remove excess antibodies. The pellets were resuspended in 100 µl PBS and kept at 4°C overnight for analysis the next day.

2.4.4.3.3 EV flow cytometry by Flow NanoAnalyzer

Fluorescently labelled samples from Section 2.4.4.3.2 were analysed on a Flow NanoAnalyzer (NanoFCM). The instrument was firstly calibrated with S16M-Exo size standards (NanoFCM), which created a calibration curve of the particle size and side scatter intensity.

Where necessary, the samples were diluted 1 in 10 – 1 in 30 with PBS to reach a particle concentration that fell into the optimal detection range of the instrument. The size distribution profiles of the detected particles were obtained by converting the side scatter intensity to size according to the standard curve. MVP/IgG-positive and CD63-positive particles were detected by the FITC channel (BP525/40 nm) and PE channel (BP580/40 nm), respectively. The instrument was washed between each sample to minimise contamination. To analyse the results, a manually set threshold was introduced to the auto-generated event plots to reduce background noise.

NanoFCM data capture and analysis was performed by Dr Ben Peacock at the NanoFCM UK laboratory.

2.4.5 Electron microscopy

2.4.5.1 Transmission electron microscopy (TEM)

2.4.5.1.1 TEM of differential centrifugation derived EVs

2k, 10k, 100k EV pellets derived from 60 ml conditioned medium from SCC4 cells following differential centrifugation (from Section 2.4.3.1) were resuspended in 50 ul PBS and prepared for TEM imaging following a protocol described by Galbiati *et al.* with minor adaption (Galbiati *et al.*, 2018). Briefly, formvar-coated copper grids (Agar Scientific) were firstly processed on a Glow Discharge unit to ensure optimal sample adhesion. The discharged grids were gently placed onto a 10

µl sample drop on a parafilm with a pair of forceps and left for 5 min, taking care that the membrane side was facing downwards. Afterwards, the excess liquid was absorbed carefully with a filter paper, and the grids were floated on a drop of 1% (w/v) phosphotungstic acid (pH 7.2) for 1 min. After being briefly dried with filter paper, stained grids were then washed twice by floating on drops of distilled water for 1 min each. Finally, the grids were air-dried and analysed by a Tecnai T12 Spirit TEM (FEI) at an accelerating voltage of 80 kV. The sample processing and imaging was carried out with training provided by Chris Hill at the Electron Microscopy Service, The University of Sheffield.

2.4.5.1.2 Resin-embedded TEM

Washed Dynabead-EV complexes that had not yet been subject to EV elution and/or lysis (from Section 2.4.3.3.3 and Section 2.4.3.3.4) were resuspended in 20 µl PBS and processed according to a protocol previously described by Yamada *et al.* (Yamada *et al.*, 2013). Samples collected at the end of the microfuge tube were pre-fixed with 2% (w/v) glutaraldehyde in 100 mM phosphate buffer (pH 7.4) at room temperature for at least 2 h, followed by the post-fixation with 2% (w/v) osmium tetroxide in 100 mM phosphate buffer (pH 7.4). Fixed samples were washed several times in distilled water to remove excess phosphate ions prior to dehydration through a series of ethanol (30%, 50%, 70%, 90%, v/v) for 15 min each followed with 100% (v/v) ethanol for 30 min with 3 changes of solution, and finally in propylene oxide for 15 min with 2 changes of solution. Taking care not to let samples be exposed to the air, the Quetol 812 epoxy resin (Nissin EM) was infiltrated by mixing propylene oxide and the resin as 2:1, 1:1, 1:2 ratios and samples were left for 1 h in each solution and finally in 100% resin overnight. The sample embedding was completed the following day by changing into fresh resin for 1 h with polymerisation.

The embedded samples were trimmed to have a block face of 1-2 mm in diameter and were sectioned into 100 nm ultra-thin slices with the Leica EM UC6 ultramicrotome (Leica). Each section was carefully collected onto a grid and left to dry before being stained with 2% (w/v) uranyl acetate in distilled water for 15 min and washed twice with distilled water. The stained grids were imaged on the Tecnai T12 Spirit TEM at 80 kV.

Resin-embedded samples were processed by Chris Hill at the Electron Microscopy Service, The University of Sheffield.

2.4.5.2 Cryogenic electron microscopy (cryo-EM)

100k EV pellets following differential centrifugation resuspended in 50 µl PBS (Section 2.4.3.1) were imaged by Cryo-EM with the help of Dr Zubair Nizamudeen and Dr Kenton Arkill (The University of Nottingham).

2.5 DNA methods

2.5.1 Plasmids used in this study

Plasmids used in this study are listed in Table 2.5.

Table 2.5 List of plasmids used in this study.

Plasmid	Description	Antibiotic resistance	Source
pAV U6+27	Cloning vector with human U6 promotor for nuclear expression of small RNAs in mammalian cells	Ampicillin	Addgene #25709
pAVU6+27-F30-2xdBroccoli	pAVU6+27 vector with two dimeric Broccoli aptamers in the F30 scaffold	Ampicillin	Addgene #66842
pMA-vtRNA1-1-Broccoli	pMA holding vector with vtRNA1-1 and two dimeric Broccoli aptamer insert	Ampicillin	Thermo Fisher Scientific
pAVU6+27-vtRNA1-1	pAVU6+27 vector with vtRNA1-1 sequence insert cloned in between *Sal*I and *Xba*I sites	Ampicillin	This study
pAVU6+27-vtRNA1-1-Broccoli	pAVU6+27 vector with the vtRNA1-1-NheI-F30-2xBroccoli insert cloned in between *Sal*I and *Xba*I sites	Ampicillin	This study
pcDNA3.1(+)IRES GFP-FLAG-Tag CRTC1-MAML2	pcDNA3.1(+)IRES GFP vector with a 3,105 bp insert between *Nhe*I and *Not*I sites	Ampicillin	Dr Esra B Amoura

2.5.2 DNA isolation and quantification

2.5.2.1 Isolation of genomic DNA

The QIAamp DNA mini kit (QIAGEN) was used for isolating genomic DNA from mammalian cells in culture. Cells were seeded (Section 2.2.5) and incubated for 24 h prior to cell lysis to allow attachment and reach a confluency of 80%. Cells were harvested by trypsinisation and centrifugation at 300 × *g* for 5 min. The genomic DNA was isolated following the kit's protocol and finally eluted in 100 µl nuclease-free water (NF-H_2O).

For quick extraction of genomic DNA from small number of cells growing in 96-well plates, the QuickExtract™ DNA extraction solution (Lucigen) was used following the manufacturer's instructions. 50 µl of the extraction solution was added to the wells and the cell monolayer was lysed and scraped with the end of a 200 µl pipette tip. The lysate was transferred to a fresh tube, vortexed and heated at 65°C for 10 min followed by 98°C for 5 min. The DNA was then diluted with 100 µl NF-H_2O.

The concentration of isolated DNA was determined by a NanoDrop 1000 spectrophotometer. DNA was stored at -20°C.

2.5.2.2 Isolation of plasmid DNA

Plasmid DNA was isolated using the QIAprep spin miniprep kit (QIAGEN) and ZymoPURE II plasmid midiprep kit (Zymo Research) following the manufacturer's instructions. 5 ml and 50 ml overnight liquid culture of bacteria (from Section 2.3.2) was used as starting material for miniprep and midiprep, respectively.

The concentration of plasmid DNA was measured with a NanoDrop 1000 spectrophotometer prior to storage at -20°C.

2.5.3 Polymerase chain reaction (PCR)

Standard PCR amplification was carried out in a reaction volume of 25 µl, using DreamTaq Green PCR 2× Master Mix (Thermo Fisher Scientific) or PCRBIO VeriFi™ Mix Red (PCR Biosystems). Primers were purchased from Sigma-Aldrich as detailed in Table 2.6. Reactions were set up by mixing 12.5 µl 2× master mix, 1 µl forward primer stock (10 µM), 1 µl reverse primer stock (10 µM), ~100 ng of genomic DNA or plasmid DNA, and NF-H_2O to a final volume of 25 µl. The PCR cycles were set up as described in Table 2.7 in an Applied Biosystems 2720 Thermal Cycler (Thermo Fisher Scientific), with the annealing temperature being 3-5°C below the T_m (melting temperature) of the primers.

Table 2.6 List of primers for PCR.

Primer	Sequence (5' – 3')
vtRNA1-1-F	CGGCAGCACATATACTAGTCG
vtRNA1-1-R	CAAAAGGACTGGAGAGCGC
vtRNA1-1Broc-F	TATACTAGTCGACGGCTGGC
vtRNA1-1Broc-R	TGAATGATCCAGCCCACACT
MVP-F	AGGACAATGAGAGGTGGGTG
MVP-R	GGAGGTGAGTGGAGGTACAG
YB1-F	TTCTGGCTGCAGTTAGAGGG
YB1-R	AATGAGTCTGCAGGAGAGGC

Table 2.7 Settings for PCR cycles.

Step	DreamTaq 2× Master Mix			2× VeriFi Mix Red		
	Temperature °C	Time	Cycle	Temperature °C	Time	Cycle
Initial denaturation	95	1-3 min	1	95	1	1
Denaturation	95	30 s	30	95	15 s	30
Annealing	T_m-5	30 s		60	15 s	
Extension	72	1 min		72	30 s	
Final extension	72	5-15 min	1	-	-	-
Hold	4	∞	1	4	∞	1

2.5.4 Agarose gel electrophoresis

DNA and PCR products were analysed by agarose gel electrophoresis. 1-2% (w/v) agarose was added to 1× Tris-acetate-EDTA (TAE) buffer (40 mM Tris, 40 mM acetate and 1 mM EDTA, pH 8.3) and heated in a microwave until fully dissolved. The gel was then cooled down to ~55°C before ethidium bromide (final concentration 200 ng/µl) was added and mixed thoroughly. The gel was poured into a gel cast fitted with a sample well comb and allowed to set. DNA was mixed with 6× gel loading dye (New England Biolabs). Samples were then loaded into the wells (10 µl/well) alongside 5 µl GeneRuler 1 kb DNA ladder (Thermo Fisher Scientific) and 5 µl GeneRuler 100 bp DNA ladder

(Thermo Fisher Scientific). Separation of DNA was achieved by electrophoresis in 1× TAE buffer at a constant voltage of 100 V for 30-60 min. The gel was then imaged under an ultraviolet (UV) light on a transilluminator (Syngene) using the GeneSys image acquisition software (Syngene).

2.5.5 DNA purification from agarose gel

Where isolation and purification of DNA from an agarose gel was required, ethidium bromide-stained DNA separated by electrophoresis on an agarose gel was imaged on an UV transilluminator (Vilber Lourmat), and small blocks of gel containing the desired DNA fragments were sliced with a scalpel blade. DNA fragments were then purified using the QIAquick gel extraction kit (QIAGEN) following the manufacturer's instructions.

2.5.6 Restriction digestion of DNA

Restriction endonucleases XbaI, NheI, and SalI (New England Biolabs) were used for digesting 1 µg plasmid DNA in a final reaction volume of 50 µl. Alongside double digestion of vector and the inserts, single enzyme digestion of vector was also set up as control. The digestion was carried out following the manufacturer's guidelines in the provided 10× CutSmart buffer at 37°C for 1.5 h. Following incubation, digested vectors were dephosphorylated to prevent the circulation and self-ligation of the DNA, by adding the rSAP Shrimp Alkaline Phosphatase (New England Biolabs) and supplied 10× rSAP reaction buffer to the reaction and incubated at 37°C for further 30 min. The reactions were heat inactivated at 65°C for 5 min.

2.5.7 Ligation of DNA fragments

DNA concentration was measured by the NanoDrop 1000 spectrophotometer. 18 ng (~1 µl) of vector plasmid was used per ligation reaction, the amount of insert added to achieve the insert to vector molar ratios of 3:1 and 5:1 was determined using the following equation:

$$\text{Mass insert (ng)} = \text{Ratio of insert: vector} \times \frac{\text{Mass of vector (ng)} \times \text{Size of insert (kb)}}{\text{Size of vector (kb)}}$$

Each individual reaction was set up in a final volume of 20 µl, containing 1 µl T4 DNA ligase (New England Biolabs), 2 µl 10× T4 DNA ligase buffer (New England Biolabs), 1 µl vector DNA and calculated volume of insert DNA. Vector only controls (following single and double digestion from Section 2.5.6) were also set up without addition of insert DNA. The ligation was performed at room temperature for 10 min, followed by heat inactivation of the ligase at 65°C for 10 min. The ligation products were used to transform competent cells as detailed in Section 2.3.3.

2.5.8 DNA sequencing

DNA was sequenced using the external Sanger sequencing services provided by GATC Biotech. 5 µl of plasmid DNA (80-100 ng/µl) was mixed with 5 µl hU6-F primer (5 µM, 5'-3' sequence: GAGGGCCTATTTCCCATGATT) and sent to the sequencing service.

2.6 RNA methods

All RNA experiments were carried out using NF-H_2O, RNase-free microfuge tubes and filtered pipette tips where possible. Extra care was paid not to introduce RNase and other contaminants during sample handling.

2.6.1 RNA extraction

Total cellular and EV RNA used for RNA expression assays was isolated by Monarch® total RNA miniprep kit (New England Biolabs). For total cellular RNA extraction, cells were seeded (Section 2.2.5) and incubated for 24 hours. Monolayers were washed twice with PBS before harvesting using a cell scraper with addition of 300 µl lysis buffer provided in the kit. For EV RNA extraction, EV pellets derived from differential centrifugation (Section 2.4.3.1) were resuspended in 300 µl lysis buffer. The RNA lysates were transferred into RNase-free tubes and stored at -80°C until ready for RNA extraction. RNA was then extracted following the manufacturer's protocol including the recommended DNase I treatment step.

EV RNA used for sequencing experiments were isolated with miRCURY™ RNA isolation kit (Exiqon). EV pellets from Section 2.4.3.1 or Dynabeads-EV complexes from Section 2.4.3.3.4 were

lysed with 300 µl lysis buffer included in the kit, Dynabeads were then removed from RNA lysates using a magnet prior to RNA extraction. EV-RNA was isolated following the manufacturer's protocol.

Isolated RNA was stored at -80°C and used for further analysis within 6 months.

2.6.2 RNA quantification

Concentration of cellular RNA was measured on a NanoDrop™ 1000 spectrophotometer, whereas EV-RNA was quantified by Agilent 2100 Bioanalyzer (Agilent Technologies) with an RNA 6000 Pico kit (Agilent Technologies) by Dr Paul Heath (SiTraN, The University of Sheffield) following the manufacturer's instructions. Briefly, 9 µl gel-dye mix composed of filtered gel and dye (65:1) was loaded into the gel wells on a Picochip and the plunger was depressed for 60 s. After 9 µl conditioning solution, 5 µl marker, and 1µl ladder were loaded, 1 µl of extracted EV total RNA was loaded in sample wells on the RNA chip. RNA concentrations were then calculated according to the electropherogram profiles.

2.6.3 qPCR

2.6.3.1 Complementary DNA (cDNA) synthesis

Typically, cDNA was reverse transcripted from extracted RNA (from Section 2.6.1) using a High Capacity cDNA reverse transcription kit (Thermo Fisher Scientific), whereas miRNA reverse transcription was performed using the TaqMan™ MicroRNA reverse transcription kit (Thermo Fisher Scientific) coupled with 5× TaqMan MicroRNA RT primers (Thermo Fisher Scientific). The reactions were set up on ice following the manufacturer's protocol as detailed in Table 2.7, in which 100 ng of cellular total RNA or 10 ng of EV total RNA was used as template per reaction. The reverse transcription was then performed in an Applied Biosystems 2720 Thermal Cycler using the cycles described in Table 2.8. cDNA was stored at -20°C and used within 4 weeks.

Table 2.8 Composition of per cDNA reverse transcription reaction.

Component	High Capacity cDNA reverse transcription	TaqMan™ MicroRNA reverse transcription
25× dNTP Mix (100 nM)	0.8 µl	0.15 µl
MultiScribe™ reverse transcriptase (50 U/µl)	1 µl	1 µl
10× reverse transcription buffer	2 µl	1.5 µl
RNase inhibitor (20 U/µl)	-	0.19 µl
NF-H_2O	4.2 µl	4.16 µl
10× RT random primers	2 µl	-
5× TaqMan™ MicroRNA RT primer	-	3 µl
Template RNA	10 µl (contains 100 ng RNA)	5 µl (contains10 ng RNA)
Total RT reaction mix volume	**20 µl**	**15 µl**

Table 2.9 Conditions used for reverse transcription reaction.

Step	High Capacity cDNA reverse transcription		TaqMan™ MicroRNA reverse transcription	
	Temperature	Time	Temperature	Time
Reverse transcription	25°C	10 min	16°C	30 min
	37°C	120 min	42°C	30 min
Stop reaction	85°C	5 min	85°C	5 min
Hold	4°C	Hold	4°C	Hold

2.6.3.2 TaqMan qPCR reaction

qPCR reactions were carried out to quantify RNA expressions in cells and EVs using TaqMan and SYBR Green primers, in which beta-2-microglobulin (B2M) and beta-actin were used as endogenous controls, respectively. All reactions were assembled on ice and handled with RNase-free equipment.

For reactions using TaqMan primers to detect cellular RNA expression, 5 µl of 2× qPCRBIO Probe Blue Mix Lo-ROX (PCR Biosystems) containing buffer, dNTP, dye, and DNA polymerase was combined with 0.5 µl B2M endogenous control VIC™/MGB probe (Thermo Fisher Scientific), 0.5 µl TaqMan probe (Thermo Fisher Scientific, see Table 2.10 for details), 3.5 µl NF-H_2O, and 0.5 µl cDNA for each sample. Samples were loaded in technical triplicate to minimize pipetting error. In a Rotor-Gene Q 2plex real-time PCR cycler (QIAGEN), a two-step run was conducted and

programmed as following: 10 min at 95 °C for initial denaturation, 15 s at 95 °C for denaturing and 60 s at 60 °C for annealing and extension for 40 cycles, in which green and yellow fluorescence channels were acquired for signals related to target probes and B2M during the second step.

For reactions detecting EV RNA abundance, no endogenous control probe was added to the mix. Instead, three miRNAs (miR-23a-3p, miR-30d-5p, and miR-31-5p) were chosen to be used as EV-RNA endogenous controls, based on their read counts from the small RNA sequencing data (Table 4.2). Therefore, the reaction mix for miRNA qPCR composed of 5 µl of 2× qPCRBIO Probe Blue Mix Lo-ROX, 0.5 µl TaqMan miRNA probes (Thermo Fisher Scientific, see Table 2.9 for details), 0.5 µl cDNA synthesised with the corresponding MicroRNA RT primer, and 4 µl NF-H_2O. The amplification was carried out using the same conditions stated above.

Table 2.10 List of TaqMan probes.

Probe	Gene name	Assay ID	Amplicon length (nt)
B2M	Beta-2-microglobulin	4326319E	75
MVP	Major vault protein	Hs00911188_m1	53
TEP1	Telomerase associated protein 1	Hs00200091_m1	66
PARP4	Poly(ADP-ribose) polymerase family member 4	Hs00173105_m1	118
vtRNA1-1	Vault RNA 1-1	Hs03676993_s1	64
vtRNA1-2	Vault RNA 1-2	Hs06632430_gH	67
vtRNA1-3	Vault RNA 1-3	Hs04330458_s1	63
vtRNA2-1	Vault RNA 2-1	Hs04273370_s1	62
hsa-miR-23a-3p	-	478532_mir	21
hsa-miR-30d-5p	-	478606_mir	22
hsa-miR-31-5p	-	478015_mir	21

2.6.3.3 SYBR Green qPCR reaction

SYBR Green primers were pre-designed by Dr Stuart Hunt and the custom oligos were synthesised and purchased from Merck (Table 2.11). The reactions were set up on ice by mixing 5 µl of 2×

qPCRBIO SyGreen Mix Lo-ROX (PCR Biosystems) with 0.5 µl forward primer (10 µM), 0.5 µl reverse primer (10 µM), 3.5 µl NF-H_2O and 0.5 µl cDNA. The mix was loaded in technical triplicates for each reaction while beta-actin was used as endogenous control and was probed for all samples in each run. A three-step program was performed as follows: 10 min at 95 °C for initial denaturation, 10 s at 95 °C for denaturation and 15 s at 60 °C for annealing followed by 20 s at 72 °C for extension for 40 cycles, then 5 min at 72°C for final extension. Only green channel was acquired in the second step.

Table 2.11 List of SYBR Green primers.

Target	5' primer sequences (F)	3' primer sequences (R)
Beta-actin	5' ATGTACCCTGGCATTGCCGAC 3'	5' GACTCGTCATACTCCTGCTTG 3'
vtRNA 1-1	5' AGCTCAGCGGTTACTTCGAC 3'	5' ACCCAGACAGGTTGCTTGTT 3'
vtRNA 1-2	5' CTGGCTTTAGCTCAGCGGT 3'	5' CCACCCAGAGAGGTGGTTAC 3'
vtRNA 1-3	5' CGGTTACTTCGCGTGTCATC 3'	5' CGGGTCTCGAACAACCCAG 3'

2.6.3.4 Data analysis

qPCR quantification was conducted using the $2^{-\Delta CT}$ method (Schmittgen and Livak, 2008). Data analysis was performed in Excel (Microsoft) and Prism 8 (GraphPad Software).

After the run was complete, a threshold of 0.04 was set to obtain Ct values across all experiments. For TaqMan experiments, ΔCt was calculated by subtracting Ct values of endogenous control from the Ct values of target gene, followed by the fold change calculation with the formula $2^{-\Delta Ct}$. Fold changes of technical repeats were averaged for each biological repeat and standard deviation were automatically calculated and shown as error bars. In the analysis for SYBR Green experiments, average Ct values from three technical repeats were firstly calculated before the subtraction to minimize pipetting errors. ΔCt values were obtained by subtracting Ct values of endogenous control from Ct values of target gene of the same sample, whose fold changes were then calculated using the same formula.

2.6.4 RNA sequencing

2.6.4.1 Small RNA sequencing by Ion Torrent Platform

Purified EV-RNA from 10k and 100k pellets (section 2.6.1) was sent to Edinburgh Clinical Research Facility (The University of Edinburgh) for small RNA sequencing using the Ion Proton Platform (Thermo Fisher Scientific). RNA sample quality control was performed on the Agilent 2100 Electrophoresis Bioanalyzer instrument with the Agilent RNA 6000 Pico kit, followed by the quantification using a Qubit 2.0 fluorometer and the Qubit RNA HS Assay kit (Thermo Fisher Scientific). Using the Ion Total RNA-Seq kit v2 (Thermo Fisher Scientific) with an optimised protocol for low amount of short RNA (<200 nt), the RNA was hybridised prior to cDNA reverse transcription and purification using magnetic beads. Next, the purified cDNA was amplified for 18 cycles of PCR with Ion Torrent adapters before the products were quantified with the Qubit 2.0 fluorometer and the dsDNA HS Assay kit while the library size distributions were obtained on an Agilent Bioanalyzer with the DNA HS kit. Equal molar quantities of libraries were combined for template preparation before sequencing on an Ion Proton instrument on a P1 v3 chip. In addition to the automatically produced BAM files by on-board software, microRNA reads were examined using a small RNA analysis plugin v5.0.3.0, by which the reads were aligned to mature miRNAs. Any unmapped RNA was then aligned to the whole genome and counted as other RNA molecules.

2.6.5 Northern blot

Northern blot was carried out with the help of Dr Philip Mitchell at the Department of Molecular Biology and Biotechnology, University of Sheffield. Radioactive materials were handled carefully only in specific radioactive work area by a trained individual. Workflow and probe designing is briefly summarised in Figure 2.3.

A polyacrylamide gel was made between two glass sheets (gel thickness: 1 mm) sealed by solidifying 1% (w/v) agarose at the bottom of the gel. 60 ml gel mix, containing 30g Urea, 15 ml acrylamide/bis 19:1 40% (w/v) solution, 3 ml 10× Tris-borate-EDTA (TBE) buffer, and 18 ml diethyl pyrocarbonate (DEPC) treated H_2O, was prepared and microwaved for a few seconds, followed by addition of 400 µl

10% (w/v) ammonium persulphate solution (APS) and 40 µl tetramethylethylenediamine (TEMED) to start polymerisation.

100 ng EV-RNA was diluted to equal volume and mixed with 2× RNA loading dye. The 20 µl mixture was denatured at 65°C for 5 min prior to loading to the gel. RNA samples, along with oligo markers of known size were separated on the polyacrylamide gel at constant 30 V for ~22 h. Following electrophoresis, the gel was carefully removed from the glass sheets and was stained in 1% (w/v) ethidium bromide for 20 min with gentle shaking. The gel was then imaged under an UV light on a transilluminator using GeneSnap software (SynGene) to ensure satisfactory RNA separation.

Semi-dry transfer of RNA onto a Hybond-N+ nylon membrane was conducted by sandwiching the following, from bottom to top: pre-wetted (in 0.5× TBE) thick filter paper, gel, pre-wetted nylon membrane, pre-wetted thick filter paper, in a transfer cassette, and electrophorised for 30 h at 700 mA (constant current).

The membrane was then incubated with 50 ml pre-hybridisation buffer, containing 29 ml NF-H_2O, 15 ml 20× sodium chloride-sodium phosphate-EDTA (SSPE) buffer, 1 ml 10% (w/v) sodium dodecyl sulfate (SDS), and 5 ml 50× Denhardt's solution. The pre-hybridisation was carried out at 37°C for 30 min with gentle shaking, during which the probe was radioactively labelled with α-^{32}P-dATP. The probe labelling was performed by combining 5 µl of 10× T4 polynucleotide kinase reaction buffer (New England Biolabs), 1 µg of DNA probe, 100 µM adenosine diphosphate (ADP), 1 µl of α-^{32}P dATP (3000 Ci/mmole, 10 mCi/ml), 2 µl T4 polynucleotide kinase (New England Biolabs), and up to 50 ml of NF-H_2O. The mixture was incubated at 37°C for 30 min followed by heat inactivation at 65°C for 20 min.

Hybridisation with labelled probe was performed using the same hybridising solution from pre-hybridization. The labelled probe mixture was added to the solution by passing through a 0.22 µm filter and mixed thoroughly. The membrane was left in the solution overnight at 37°C.

The membrane was briefly washed for three times with 6× SSPE buffer. Following the last wash, 50 ml 6× SSPE was added to the membrane and incubated at 37°C for 30 min. The damp membrane was

briefly dried and sealed in cling film, followed by exposure to a phosphor screen in a cassette for varied time (depending on the desired signal strength). The blots were then obtained by scanning the exposed screen on a Typhoon FLA 7000 Imager (GE Healthcare).

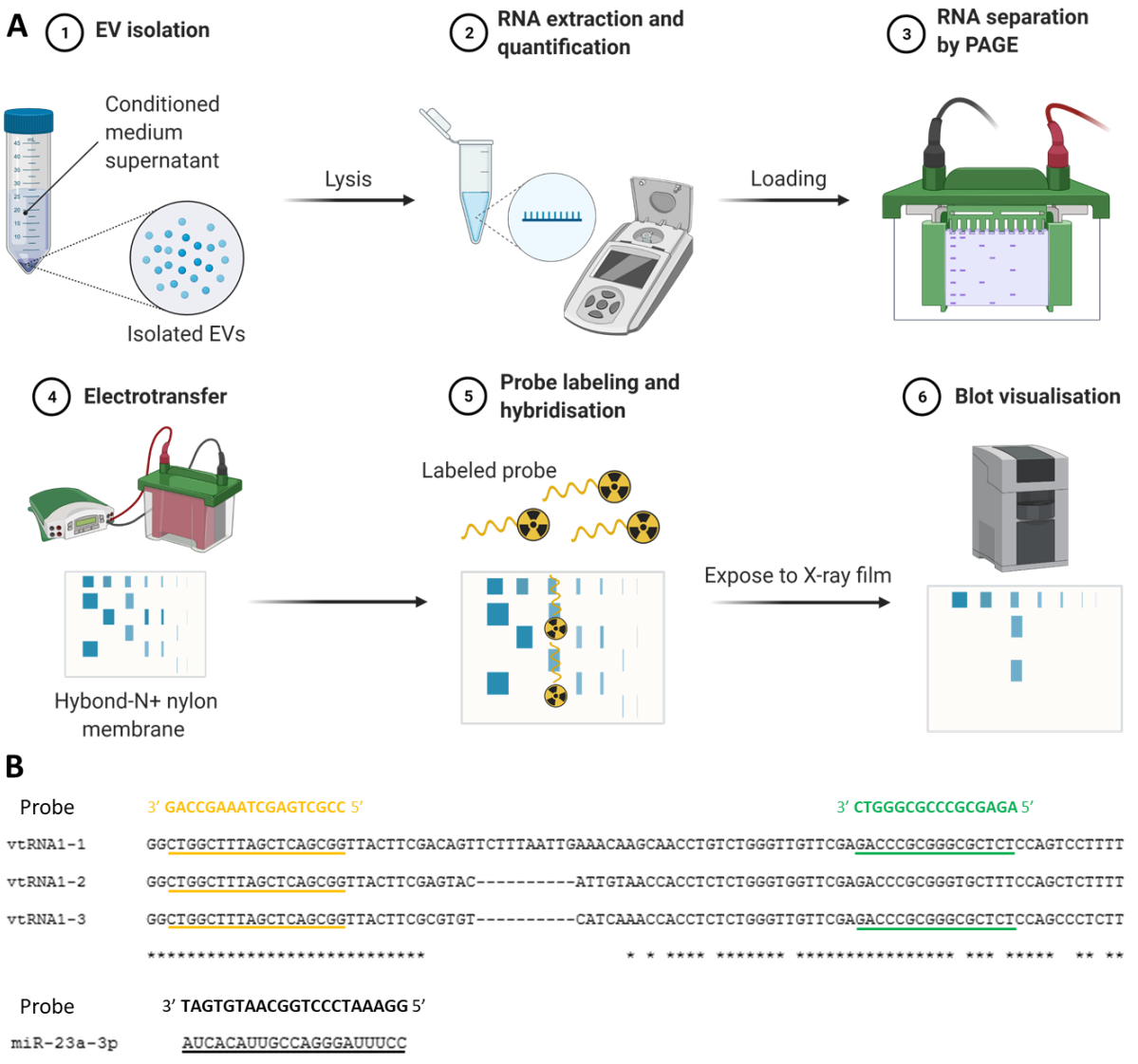

Figure 2.3 Illustration of northern blot and probe designing.
A) Diagram shows the process of northern blot. EVs were isolated from cell conditioned medium from FNB6, H357, SCC9, and SCC4 cells by ultracentrifugation, resulting in 2k, 10k, and 100k EV pellets. Total EV-RNA was then extracted and quantified on a Bioanalyzer. 100 ng total EV-RNA was loaded in each well and separated on a 10% (w/v) polyacrylamide gel together with DNA oligos with known size as markers. Following PAGE separation, the RNA was transferred onto a nylon membrane and hybridised with labelled probe targeting vtRNA 1-1 3' fragments as well as full-length vtRNAs. Finally, the blot was obtained after exposing the membrane to a phosphor screen for varied time (depending on the desired signal strength). **B)** Probes complimentary to 5' and 3' vtRNA fragments were designed and showed in yellow and green respectively. Probe targeting miR-23a-3p was also designed. Complimentary sequences in full-length vtRNAs and miRNA were underlined with corresponding colours.

2.7 Protein methods

2.7.1 Sample preparation

Cells were seeded as described (Section 2.2.5) and lysed in 50 µl protein lysis buffer (Table 2.12). Cell lysates were scraped, transferred to fresh microfuge tubes and incubated for 30 min on ice, followed by another incubation for 10 min at room temperature to allow efficient nucleic acid degradation. Following centrifugation at 13,000 × *g* for 5 min, to pellet cell debris, the supernatant containing soluble proteins was transferred to a fresh tube and kept on ice for immediate use or stored at -20°C.

EV-protein was extracted from EV pellets following differential centrifugation (Section 2.4.3.1) or Dynabead-EV complexes (Section 2.4.3.3.3 and 2.4.3.3.4) by resuspending the pellets with 20-50 µl of protein lysis buffer to lyse the EVs, depending on the desired protein concentration and incubated as stated above.

Table 2.12 Components of protein lysis buffer.

Component	Source	Description	Volume per 1 ml
10× RIPA lysis buffer	Merck	Contains 0.5M Tris-HCl, pH 7.4, 1.5M NaCl, 2.5% deoxycholic acid, 10% NP-40, 10mM EDTA	100 µl
cOmplete™ mini EDTA-free protease inhibitor	Merck	7× stock solution was made by dissolving one tablet in 1.5 ml dH_2O	143 µl
Pierce™ Universal Nuclease	Thermo Fisher Scientific	Stock concentration: 250 U/µl	0.1-0.2 µl
dH_2O	-	-	757 µl

2.7.2 Protein quantification

Protein concentration was determined by the bicinchoninic acid (BCA) assay, using the Pierce™ BCA protein assay kit following the manufacturer's instructions. Two series of diluted BSA standards (20-2,000 µg/ml and 5-250 µg/ml) were prepared by serial dilution with protein lysis buffer and used for establishing standard curves for quantifying cellular and EV protein, respectively. Samples exceeding the working ranges of the standards were diluted 1 in 10 with protein lysis buffer prior to BCA assay.

In a 96-well plate, 10 µl standards and sample protein were loaded into individual wells in technical duplicate. Solution A and solution B were mixed at a 50:1 ratio and 200 µl mixture was added to each well. The plate was then sealed and incubated at 37°C for 30 min before the absorbance at 562 nm was measured on an Infinite M200 microplate reader (TECAN).

To calculate the protein concentration, the average absorbance of the blank standard was firstly subtracted from the absorbance of all other standards and samples. The standard curve was created by plotting the average blank-corrected absorbance for each standard against its known concentration. A polynomial equation derived from the standard curve was used to determine the protein concentration of samples based on absorbance.

2.7.3 Sodium dodecyl sulfate-polyacrylamide gel electrophoresis (SDS-PAGE)

All the buffers used for polyacrylamide gel, SDS-PAGE, and western blotting were made in-house as described in Table 2.13.

7.5% and 12% polyacrylamide gels were prepared between two glass plates using the components described in Table 2.14 and the Mini-PROTEAN tetra handcast system (Bio-Rad), in which 7.5% gels were used to separate larger proteins (e.g. TEP1 and PARP4) whereas other proteins were separated by 12% SDS-PAGE in this study. Once the resolving gel was poured, a thin layer of isopropanol was applied on top of the resolving gel to ensure a flat surface upon setting. After the resolving gel was set, isopropanol was poured off and the gel was washed carefully with dH_2O. Following this, the stacking gel mixture was poured on top of the resolving gel and a sample comb inserted. The gel was left to polymerise for 10 min and sample wells were washed with copious amounts of dH_2O prior to sample loading.

Protein samples were diluted with protein lysis buffer to ensure 10 µg of total cellular protein or 2 µg of EV protein in a total volume of 20 µl, which was then mixed with 5 µl of 5× protein loading buffer (National Diagnostics). The mixture was boiled at 95°C on a heat block for 5 min to denature the protein and was briefly vortexed before loading onto the gel.

In a Mini-PROTEAN Tetra Vertical Electrophoresis Cell (Bio-Rad), two gels were assembled in the chamber filled with 1× SDS-PAGE running buffer. Samples were loaded alongside 5 µl Precision Plus protein dual colour standards (Bio-Rad) and were electrophoresed at 100 V until the tracking dye had migrated into the resolving gel. The electrophoresis was then continued for another 90 min at 120 V until all protein standards were well separated.

Table 2.13 Components for buffers used for SDS-PAGE and western blot.

Buffer	Reagent	Method
SDS-PAGE upper tris buffer	Tris base, sodium dodecyl sulfate (SDS)	18.17 g Tris base and 0.4 g SDS were weighed out and dissolved in 100 ml dH_2O, pH was adjusted to 8.8
SDS-PAGE lower tris buffer	Tris base, SDS	6.06 g Tris base and 0.4 g SDS were weighed out and dissolved in 100 ml dH_2O, pH was adjusted to 6.8
10× SDS-PAGE running buffer	Tris base, glycine, SDS	30 g Tris base, 144 g glycine, and 10 g SDS were weighed out and dissolved up to a total volume of 1000 ml with dH_2O
10× TBS buffer	Tris base, sodium chloride (NaCl)	24 g Tris base and 88 g NaCl were dissolved in dH_2O to a final volume of 1000 ml. pH was adjusted to 7.6
1× TBS-Tween 20 (TBST) buffer	10× TBS buffer, Tween 20	10× TBS buffer was diluted at 1:10 with dH_2O, in which 1 ml Tween 20 was added per 1000 ml buffer
5% skimmed-milk blocking buffer	1× TBST buffer, skimmed milk powder	2.5 g skimmed-milk power was weighed out and dissolved in 50 ml 1× TBST buffer

Table 2.14 Components for polyacrylamide gels.

Reagent	Source	Resolving (upper) gel		Stacking (lower) gel
		7.5%	12%	
40% (w/v) acrylamide	Thermo Fisher Scientific	1.875 ml	3 ml	0.975 ml
Upper tris buffer	Table 2.12	2.5 ml	2.5 ml	-
Lower tris buffer	Table 2.12	-	-	2.1 ml
dH_2O	-	5.425 ml	4.3 ml	4.725 ml
Tetramethylethylenediamine (TEMED)		5 µl	5 µl	17 µl
10% (w/v) ammonium persulfate solution (APS)	0.5 g APS powder dissolved in 5 ml dH_2O	350 µl	350 µl	100 µl

2.7.4 Western blot

2.7.4.1 Transfer, blocking, and antibody incubation

Protein separated by SDS-PAGE was then transferred using a Trans-Blot Turbo transfer system (Bio-Rad) and the Trans-Blot Turbo mini 0.2 µm nitrocellulose transfer packs (Bio-Rad). In a transfer chamber, the gel was placed on top of the nitrocellulose membrane and was sandwiched between two buffer-saturated ion reservoir stacks. The stack was gently flattened by a roller to remove air bubbles and fixed in the chamber by locking the lid. Protein was transferred to a nitrocellulose membrane at 25 V for 7 min (or 10 min for 1.5 mm gels).

Following transfer, the sandwich was disassembled and the membrane was incubated in 5% (w/v) skimmed-milk blocking buffer at room temperature for 1 h prior to primary antibody incubation.

All primary antibodies used in this study were purchased from Abcam unless stated otherwise (Table 2.15). Primary antibodies were diluted in blocking buffer and added to the blocked membrane followed by incubation on a shaker at 4°C overnight. Following three washes with 1× Tris-buffered saline supplemented with 0.1% (v/v) Tween-20 (TBST) for 10 min each, the membrane was incubated with secondary antibodies diluted in blocking buffer at 1:3000 at room temperature for 1 h, or at 4°C overnight for EV protein. Secondary antibodies were purchased from GeneTex. Rabbit polyclonal anti-mouse IgG horseradish peroxidase (HRP)-conjugated antibody and goat polyclonal anti-rabbit IgG HRP-conjugated antibody was used depending on the primary antibody species.

Table 2.15 List of primary antibodies used for western blot.

Primary Antibody	Catalogue No.	Host species	Antibody type	Dilution factor used for western blot	Predicted molecular weight
Anti-MVP antibody	ab175239	Rabbit	Monoclonal	1/2,000 of the stock	99 kDa
Anti-TEP1 antibody	ab64189	Rabbit	Polyclonal	1/4,000 of the stock	290 kDa
Anti-PARP4 antibody	ab133745	Rabbit	Monoclonal	1/1,000 of the stock	193 kDa
Anti-β-Actin antibody	A1978 (Merck)	Mouse	Monoclonal	1/10,000 of the stock	42 kDa
Anti-CD81 antibody	ab109201	Rabbit	Monoclonal	1/1,000 of the stock	26 kDa
Anti-CD63 antibody	ab134045	Rabbit	Monoclonal	1/1,000 of the stock	26 kDa
Anti-CD9 antibody	ab92726	Rabbit	Monoclonal	1/1,000 of the stock	25 kDa
Anti-TSG101 antibody	612697 (BD Biosciences)	Mouse	Monoclonal	1/500 of the stock	46 kDa
Anti-GM130 antibody	ab52649	Rabbit	Monoclonal	1/1,000 of the stock	140 kDa
Anti-YB1 antibody	ab76149	Rabbit	Monoclonal	1/1,000 of the stock	36 kDa

2.7.4.2 Detection and imaging

Next, the membrane was washed three times with 1× TBST for 10 min each. Antibody binding was visualised using chemiluminescent substrate, chosen from the Clarity Western enhanced chemiluminescence (ECL) substrate (Bio-Rad), the SuperSignal™ West Pico PLUS chemiluminescent substrate (Thermo Fisher Scientific), and the WESTAR SUPERNOVA (Cyanagen) depending on the target protein abundance. The substrate was applied according to the manufacturer's instructions, solution A and B was mixed at 1:1 ratio and added onto the membrane. After a 5 min incubation, the membrane was gently dried and scanned on a C-DiGit Blot Scanner (Li-Cor). Otherwise, the membrane was sealed in an X-ray cassette and covered by a CL-XPosure film (Thermo Fisher Scientific) for exposure. The exposed film was developed and fixed on a Compact X4 developer (Xograph).

Where needed, antibodies were stripped off the membrane using the Restore™ western blot stripping buffer (Thermo Fisher Scientific) by incubating the membrane in the buffer for 15 min at room temperature on a shaker, followed by three washes (10 min each) with 1× TBST. The stripped membrane was then ready for blocking and antibody incubation.

2.7.4.3 Densitometry

Densitometry for western blot was performed using an Image Studio Software (Li-Cor), in which blots were circled manually and signals from pixels were generated automatically by the software.

Post analysis was conducted in Microsoft Excel and GraphPad Prism. Where normalisation was required, the signal values of target bands were divided by the signal values of the corresponding beta-actin bands to minimize loading error.

2.7.5 Immunofluorescence

2.7.5.1 Immunostaining

Coverslips were sterilised in 24-well plates with 70% (v/v) industrial methylated spirit (IMS), followed by three washes with PBS to remove any IMS residue. Cells were seeded onto the coverslips at a density of 20,000 cells per well and incubated overnight to attach. On the next day, the medium from the wells were discarded and cells were washed three times with PBS, followed by incubation with 4% (w/v) paraformaldehyde (PFA) for 10 min at room temperature. Fixed cells were washed three times for 10 min each with ice-cold PBS on a shaker, followed by incubation with 1% (w/v) BSA/10% (v/v) normal goat serum/0.3 M glycine in PBS + 0.1% (v/v) Tween 20 (PBST) for 1 h at room temperature. Cells were then washed with PBS for three times (10 min each) on a shaker, before primary antibodies (Table 2.16) were added to the wells and incubated overnight at 4°C.

The following day, unbound antibodies were washed off with 500 µl PBS for three times (10 min each). Secondary antibodies (Anti-rabbit IgG Alexa Flour 488, A32731 and Anti-mouse IgG Alexa Flour 594, A32744 both purchased from Thermo Fisher Scientific) diluted 1 to 1,000 with 1% (w/v) BSA in 0.1% (v/v) PBST were added to the cells and incubated for 1 h at room temperature (the plates and slides were protected with foil from light from this step onwards). After three more washes with PBS, 4′, 6-diamidino-2-phenylindole (DAPI) solution (Thermo Fisher Scientific) diluted to 300 nM with PBS was added to the wells for <5 min to stain the cell nucleus. Following a wash with PBS, the coverslips were carefully removed from the wells with tweezers and briefly dried from the edge,

before being mounted on a slide with a drop of ProLong™ Gold antifade mountant (Thermo Fisher Scientific) and allowed to dry.

Table 2.16 Primary antibodies used for immunofluorescence.

Primary Antibody	Catalogue No.	Host species	Antibody type	Dilution factor used for incubation	Final concentration
Anti-MVP antibody	ab175239	Rabbit	Monoclonal	1/300 of the stock	3 µg/ml
Anti-TEP1 antibody	ab64189	Rabbit	Polyclonal	1/1,000 of the stock	1 µg/ml
Anti-EGFR antibody	ab52849	Rabbit	Monoclonal	1/200 of the stock	0.5 µg/ml
Anti-EEA1 antibody	ab70521	Mouse	Monoclonal	1/1,000 of the stock	1 µg/ml
Anti-RAB7 antibody	ab50533	Mouse	Monoclonal	1/2,000 of the stock	1 µg/ml
Rabbit IgG-UNLB	0111-01 (Southern Biotech)	Rabbit	Isotype control	1/5,000 of the stock	1 µg/ml
Mouse IgG1 kappa	14-4714-85 (Thermo Fisher Scientific)	Mouse	Isotype control	1/500 of the stock	1 µg/ml

2.7.5.2 Confocal fluorescent imaging with AiryScan

Slides were imaged on a Zeiss LSM880 AiryScan confocal microscope coupled with ZEN image acquisition and processing software (Carl Zeiss Microscopy GmbH). The images were obtained using a 63×/1.4 oil objective lens whilst 405 nm, 488 nm and 561 nm lasers were used to excite DAPI, Alexa488 and Alexa594 fluorophores, respectively.

2.8 Biochemical assays

2.8.1 Proteinase K protection assay

Isolated EV pellets resuspended in PBS (Section 2.4.3.1) were divided into four aliquots of equal volume and treated with: 1) PBS only, 2) Proteinase K (QIAGEN) diluted with PBS to 20 µg/ml final concentration, 3) Triton-X 100 (Merck) diluted with PBS to 0.1% (v/v) final concentration, 4) Proteinase K (20 µg/ml final concentration in PBS) and 0.1% (v/v) Triton X-100 (final concentration in PBS). All samples were then incubated at 37°C for 30 min before phenylmethanesulfonyl fluoride (PMSF) was added to 5 mM final concentration. Samples were incubated for further 10 min at room temperature to terminate proteinase digestion. Treated EV isolates were mixed with 5× loading buffer

and boiled at 95°C for 5 min prior to SDS-PAGE (Section 2.7.3) and western blot analysis (Section 2.7.4).

2.8.2 RNase A protection assay

EV isolates in PBS (from Section 2.4.3.1) were divided into five aliquots of equal volume and each was treated with: 1) PBS only, 2) RNase A (20 μg/ml final concentration), 3) RNase A (20 μg/ml final concentration) and Proteinase K (20 μg/ml final concentration), 4) RNase A (20 μg/ml final concentration) and 0.1% (v/v) Triton-X (final concentration), 5) RNase A (20 μg/ml final concentration), Proteinase K (20 μg/ml final concentration), and 0.1% (v/v) Triton-X (final concentration). Proteinase was firstly added to the relevant samples, followed by incubation at 37°C for 30 min. PMSF (5 mM final concentration) was added to all samples to stop proteinase activity by incubation at room temperature for 10 min. Then, Triton X-100 and RNase A were added to the appropriate samples and incubated at 37°C for 30 min, before RNaseOUT recombinant ribonuclease inhibitor (Thermo Fisher Scientific) was added to all samples at a final concentration of 8 U/μl with an incubation at room temperature for 5 min. Where reagents were added to some samples, an equal volume of PBS was added to the rest. All samples were then lysed in 300 μl RNA lysis buffer and RNA extracted ready for qPCR analysis described (Sections 2.6.1 - 2.6.3).

2.9 Cell transfection and genome editing

2.9.1 siRNA transfection

MVP and negative control siRNA transfection was conducted with SCC4 cells. 800,000 cells were seeded per petri dish and allowed to adhere overnight to achieve an even 30% - 50% confluency across the dish on the next day. After 24 h, transfection reagent was prepared in sterile microfuge tubes by combining 60 μl Oligofectamine (Thermo Fisher Scientific) transfection reagent in 240 μl Opti-MEM reduced serum medium (Thermo Fisher Scientific) with 6 μl MVP Silencer pre-designed siRNA (5 nmol) or Silencer negative control No. 1 siRNA (5 nmol) diluted in 294 μl Opti-MEM, the mixture was incubated at room temperature for 30 min. Next, cells were washed twice with 5 ml Opti-MEM before the addition of 1.8 ml of Opti-MEM to each per petri dish. At the end of the incubation,

600 µl Opti-MEM was added to each reaction tube and the transfection mixture was added to the petri dish dropwise. Cells were then incubated at 37°C for 3 h before 3 ml KGM containing 20% (v/v) FBS was added to the dishes and cultured overnight. The medium was discarded 24 h post transfection. Cells were washed with 5 ml PBS for three times before 6 ml fresh medium supplemented with 10% (v/v) UF-FBS was added to each dish. Finally, medium from all experimental groups was collected 48 h post transfection and used for differential centrifugation isolation of EVs (Section 2.4.3.1), while protein and RNA lysis buffer were added to individual dishes for downstream analysis by western blot (Section 2.7.4) and qPCR (Section 2.6.3), respectively.

2.9.2 Stable transfection of cell lines

No Penicillin-Streptomycin was added in the cell culture medium in this experiment to facilitate the transfection and post transfection selection process.

2.9.2.1 Establishment of G418 kill curve

To determine the optimal concentration of disulfate salt G-418 to use for selecting stable transfected cells, a G418 kill curve using H357 and SCC4 cells was established by MTT assay. Cells were seeded at 10,000 cells per well in 96-well plates (Figure 2.4) and allowed to attach overnight. On the next day and every three days afterwards, the old medium in the wells was discarded and replenished with fresh medium containing G418 of increasing final concentration (Figure 2.4). On the tenth day after initial cell seeding, following the removal of the medium, cells were washed twice with PBS and 100 µl sterile 3-[4,5-dimethylthiazol-2-yl]-2,5-diphenyltetrazolium bromide (MTT) solution (0.5 mg/ml made in PBS) was added per well incubated at 37°C for 1 h. MTT solution was removed from the wells followed by addition of 50 µl acidified isopropanol (200 µl of 10M HCl per 200 ml isopropanol). The absorbance of the formazan product was measured on an Infinite M200 microplate reader at 540 nm with a reference absorbance of 630 nm.

Using Microsoft Excel and GraphPad Prism software, the absorbance of blank wells was subtracted from the absorbance of wells with cells and a curve was established using the percentage of viable

cells following different concentration of G418 treatment for 10 days. The lowest concentrations that killed all the cells on day 10 in each cell line were chose to use for stable transfection selection.

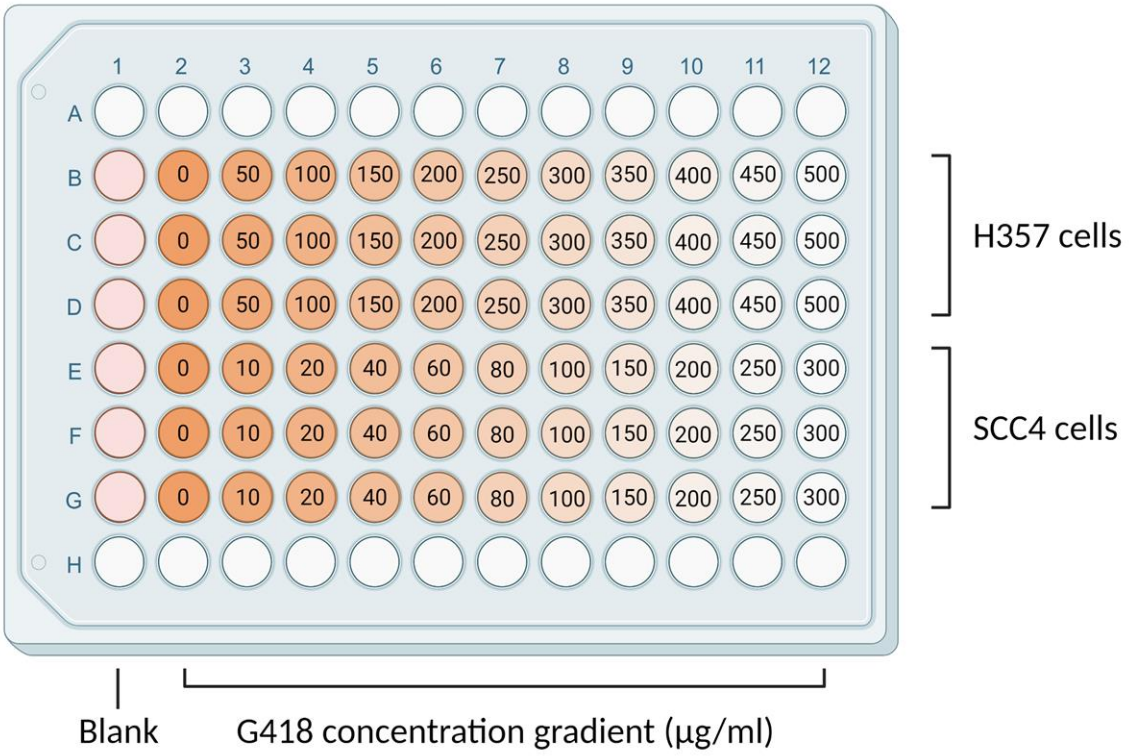

Figure 2.4 Illustration of G418 kill curve 96-well plate layout.
10,000 cells were seeded in each well (row B-G, column 2-12) in a 96-well plate as indicated. Medium containing indicated final concentration of G418 was added to the well the next day following cell seeding and changed every three days. Cell viability was measured at day 10 by MTT assay.

2.9.2.2 Mammalian cell transfection of vtRNA and Broccoli constructs

200,000 cells, in 3 ml growth medium, were seeded per well in 6-well plates and allowed to attach overnight. Following the manufacturer's recommended protocol for cell transfection, 9 µl FuGENE® HD transfection reagent (Promega) and 3 µg plasmid DNA (from Section 2.5.2.2) in a total volume of 150 µl Opti-MEM were combined in a sterile tube and incubated at room temperature for 15 min before being added dropwise to the wells. Each cell line was transfected with pAV U6+27, pAVU6+27-vtRNA1-1, pAVU6+27-vtRNA1-1-Broccoli, pAVU6+27-F30-2xdBroccoli, and pcDNA3.1(+)IRES GFP-FLAG-Tag CRTC1-MAML2 plasmids (included as a positive control for flow cytometry).

Construct expression was assayed by qPCR (Section 2.6.3) on pooled cells 48 h post transfection. For selection of stably transfected clones, transfected cells were trypsinised after 48 h. The cell suspension was then serial diluted and seeded at 1 cell per well in 96-well plates. Cells were maintained in medium containing G418 (concentration determined as above) and were regularly observed until colonies from single cells appeared. The colonies were then expanded, and cells were subject to further analysis to confirm genomic incorporation and stable expression of constructs.

2.9.2.3 Detection of Broccoli tag by flow cytometry

Successful genome incorporation and expression of Broccoli-tagged vtRNA was assessed by adding (5Z)-5-[(3,5-Difluoro-4-hydroxyphenyl)methylene]-3,5-dihydro-2-methyl-3-(2,2,2-trifluoroethyl) -4H-imidazol-4-one (DFHBI-1T) to live cells which produces green fluorescence that can be detected in standard FITC channel (488 nm excitation and 530/30 emission filter) by flow cytometry upon binding to the folded Broccoli aptamer (Figure 2.5), following Filonov and Jaffrey's protocol (Paige, Wu and Jaffrey, 2011; Filonov and Jaffrey, 2016).

48 h post transfection, cells in 6-well plates were trypsinised with 200 µl trypsin and carefully resuspended in 800 µl PBS containing 4% (v/v) FBS and 50 µM DFHBI-1T (final concentration 40 µM). Cells were then kept in dark until subject to analysis on a FACSMelody cell sorter (BD Biosciences) using standard FITC channel (488 nm excitation and 530±15 emission filter) at the Flow Cytometry Core Service with help from Ms Susan Clark and Miss Eva Wild.

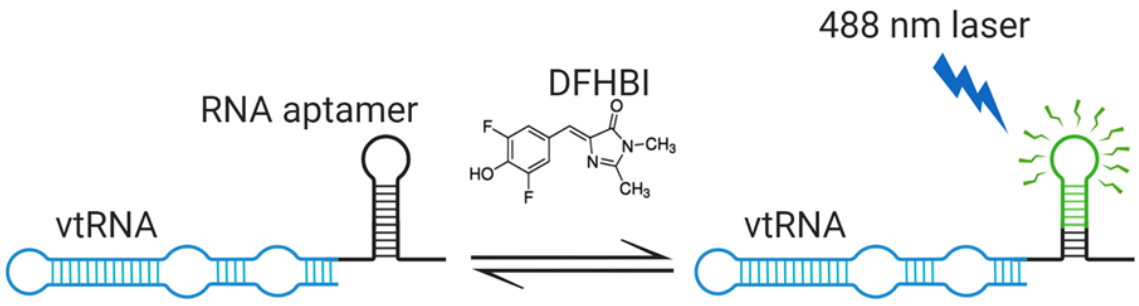

Figure 2.5 Illustration of detection of Broccoli RNA aptamer.
Broccoli RNA aptamer sequence was added to the 3' end of vtRNA1-1, which should bind to DFHBI or DFHBI-1T compound and emit green fluorescence when excited by a 488 nm laser.

2.9.3 CRISPR/Cas9 genome editing

Knockout of MVP and YBX1 genes were performed in H357 and SCC4 cells using the Alt-R CRISPR-Cas System products (Integrated DNA Technologies) following the manufacturer's instructions (summarised in Figure 2.6), which included MVP/YBX1 targeting Alt-R CRISPR-Cas9 crRNA (2 nmol), Alt-R CRISPR-Cas9 tracrRNA (5 nmol), Alt-R *S.p.* HiFi Cas9 nuclease V3 (100 µg), Alt-R CRISPR-Cas9 control kit (human, 2 nmol, contained tracrRNA, HPRT positive control crRNA, negative control crRNA#1, HPRT primer mix, and nuclease-free duplex buffer), and Alt-R genome editing detection kit (contained T7EI endonuclease, T7EI reaction buffer, and T7EI assay controls). 5'-3' crRNA sequences for MVP and YBX1 are GGGACGGTCACCATGCGCAT (PAM: GGG) and CGTGGAGGACCCCTACGACG (PAM: TGG), respectively.

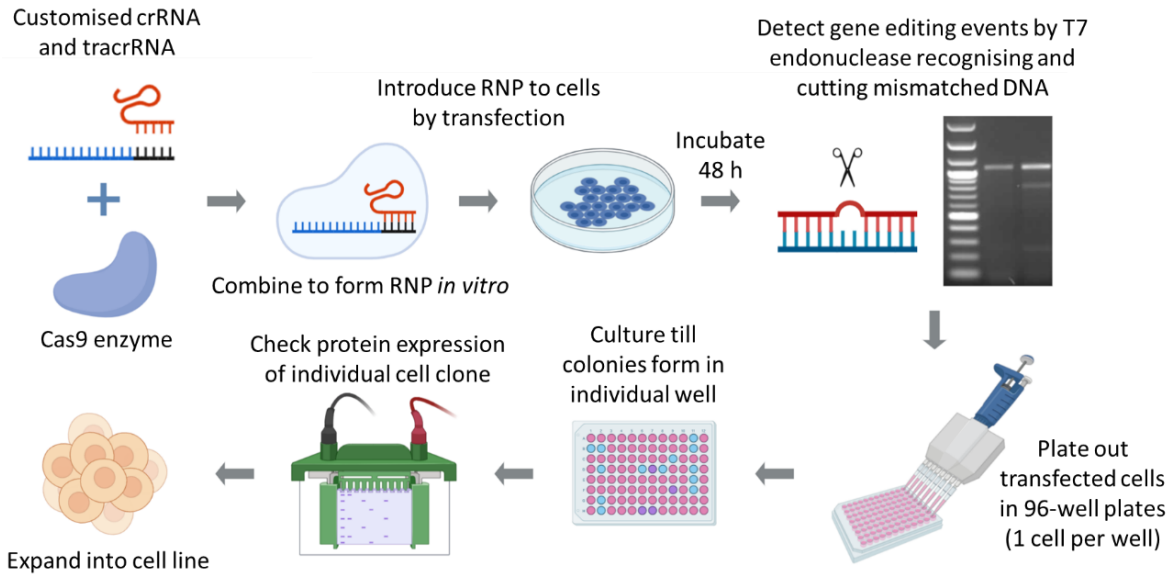

Figure 2.6 CRISPR/Cas9 genome editing workflow.
crRNA and tracrRNA were firstly combined to form ribonucleoprotein (RNP) complex, which was then combined with the Cas9 enzyme to form RNP. The RNP complex was transfected into mammalian cells using lipofectamine CRISPRMAX for 48 h. Genome editing events were detected by T7 endonuclease recognising DNA mismatch occurred when cells attempted to fix DNA double strand break caused by Cas9 enzyme. Upon confirmation of genome editing, transfected cells were plated and cultured in 96-well plates at 1 cell per well, until colony formation had occurred. The single clones were then subject to western blot analysis to confirm functional gene knock out at the protein level. Clones with gene knockout were expanded into cell lines.

2.9.3.1 Transfection of Cas9:gRNA RNP complex

Alt-R CRISPR-Cas9 crRNA and tracrRNA were resuspended in nuclease-free duplex buffer to reach 100 µM stock concentration. 1 µM crRNA:tracrRNA duplex was created by mixing 1 µl of each RNA

oligo stock and 98 µl nuclease-free duplex buffer prior to heating at 95°C for 5 min then cooling down to room temperature. Cas9 enzyme stock was diluted 1:61 with Opti-MEM to reach 1 µM working concentration. For cell transfection in 24-well plates, 6 µl RNA duplex (1 µM), 6 µl diluted Cas9 enzyme (1 µM), 2.4 µl Cas9 PLUS reagent (Thermo Fisher Scientific), and 85.6 µl Opti-MEM were combined per reaction and incubated at room temperature for 5 min to allow the assembly of the RNP complexes. The RNP complex was then combined with 4.8 µl Lipofectamine CRISPRMAX transfection reagent and 95.2 µl Opti-MEM and incubated at room temperature for 20 min before being added to the wells. Cells were reverse transfected where twice the volume of diluted cell suspension (400,000 cells/ml) was added to the wells containing the transfection complexes and incubated for 48 h.

2.9.3.2 Mutation detection with T7 endonuclease (T7EI)

48 h after transfection, cells were trypsinised and split into two halves: one was used for mutation detection whilst the other was plated into 96-well plate for single clone selection (as stated in Section 2.9.3.3).

For mutation detection, the genomic DNA was extracted from the cells using QIAamp DNA mini kit (Section 2.5.2.1). To amplify genomic DNA and detect mutations, PCR reactions were assembled (Table 2.17) and PCR was performed (Section 2.5.3) with an annealing temperature of 60°C for all reactions.

To form heteroduplexes for T7EI digestion, 10 µl PCR product from experimental group and HPRT controls were combined with 2 µl 10× T7EI reaction buffer and 6 µl NF-H_2O, which were then subject to a PCR cycle described in Table 2.18. As positive and negative control for T7EI digestion, respectively, 10 µl Control A and 5 µl Control A + 5 µl Control B were also combined with T7EI reaction buffer and included in the PCR. Next, 2 µl T7EI (1 U/µl) was added to the PCR heteroduplexes and incubated at 37°C for 1 h.

T7EI digested PCR heteroduplexes were separated by 2% (w/v) agarose gel electrophoresis (Section 2.5.4), to assess whether gene editing events had occurred.

Table 2.17 Composition of PCR reactions for CRISPR/Cas9 mutation detection.

Component	Reaction for samples	Reaction for HPRT control samples	Alt-R Control A reaction	Alt-R Control B reaction
Genomic DNA	~40 ng	~40 ng	-	-
10 µM forward primer (MVP/YBX1)	1 µl	-	-	-
10 µM reverse primer (MVP/YBX1)	1 µl	-	-	-
Alt-R HPRT PCR primer mix	-	1 µl of 10 µM stock	-	-
Alt-R Control A (template/primer mix)	-	-	1 µl	-
Alt-R Control B (template/primer mix)	-	-	-	1 µl
2× VeriFi Red PCR mix	12.5 µl	12.5 µl	12.5 µl	12.5 µl
Nuclease-free water	Up to 25 µl	Up to 25 µl	Up to 25 µl	Up to 25 µl
Total volume	25 µl	25 µl	25 µl	25 µl

Table 2.18 PCR cycle to form heteroduplexes for T7EI digestion.

Step	Temperature (°C)	Time
Denature	95	10 min
Ramp 1	95-85	Ramp rate -2°C/sec
Ramp 2	85-25	Ramp rate -0.3°C/sec

2.9.3.3 Single clone selection and cell line establishment

Cells generated from CRISPR transfection were serial diluted and seeded into 96-well plates (1 cell per well) to allow attachment and division. Cells were closely monitored until colony formation had occurred. The genomic DNA of the colonies were extracted using the QuickExtract DNA extraction solution (Section 2.5.2.1) and T7EI digestion was performed to confirm genome mutation. Colonies were gradually expanded into culture vessels with a larger surface area before protein was harvested and analysed by western blot to determine protein abundance (Section 2.7.1-2.7.4). Clones with no protein expression of the target gene were eventually expanded in flasks and stored as cell lines with knockout mutations.

Chapter 3 Characterisation of vault components in OSCC cells and EV preparations

3.1 Introduction

OSCC is the most common malignancy that affects the oral cavity (Choi and Myers, 2008). Like other cancers, OSCC often originates from genetically mutated keratinocytes at the primary site, which could then form pre-malignant/dysplastic lesions that lead to tumourigenesis upon exposure to risk factors (Johnson *et al.*, 2020). Cancer progression is thought to rely on the interactions between all cell types within the TME (Mughees *et al.*, 2021). In addition to intercellular signalling by soluble molecules, the transmission of EVs is a major signalling pathway facilitating the exchange of molecular messages between donor and recipient cells (Tao and Guo, 2020).

An increasing amount of evidence has suggested that EVs play a pivotal role in OSCC, mainly through the intercellular transfer of their molecular cargo with potential regulatory functions. A higher concentration of EVs have been observed in plasma and saliva samples from OSCC patients compared to healthy controls (Zlotogorski-Hurvitz *et al.*, 2016), whilst an increase in EV release can be induced by exposing OSCC cells to lipopolysaccharide, ethanol and radiation (Mutschelknaus *et al.*, 2016; Momen-Heravi and Bala, 2018b). In addition to increased EV release, OSCC-EVs have also been reported to contain altered cargo favouring the tumour growth. One of the most frequently enriched cargo is miRNA, which contributes to multiple pro-tumourgenic phenotypes in OSCC including macrophage polarisation, angiogenesis, and metastasis (Li *et al.*, 2016; de Andrade *et al.*, 2018; Cai *et al.*, 2019; Baig *et al.*, 2020). Moreover, evidence has suggested OSCC-EVs are able to regulate cisplatin resistance due to their altered protein contents, which represents one of the biggest challenges were currently faced in head and neck cancer treatment (Khoo *et al.*, 2019; Picon and Guddati, 2020).

Vault particles are the largest known ribonucleoprotein complex in eukaryotic cells, consisting of three vault proteins (MVP, TEP1 and PARP4) and vtRNAs (Kedersha and Rome, 1986; Kedersha *et al.*, 1991). Whilst their function remains to be fully understood, vaults and their molecular components have been closely linked with multidrug resistance in cancers (Mossink *et al.*, 2003). Until now, vault particles have not been investigated in OSCC, however, some studies have linked the overexpression of MVP in OSCC with reduced long-term survival of patients and potential resistance to cisplatin (Henríquez-Hernández *et al.*, 2012; Zhang *et al.*, 2012).

By searching the ExoCarta database (Keerthikumar *et al.*, 2016), we found that all vault components have been reported in EVs from various sources by independent researches. Specifically, MVP was identified as exosomal cargo in thirteen separate studies and vtRNAs have also been repeatedly reported in transcriptomic analysis of EV RNA (Herlevsen *et al.*, 2007; Nolte'T Hoen *et al.*, 2012; Lässer *et al.*, 2017). Unpublished data from the Hunt lab also suggested that high-levels of vtRNAs and MVP are present in OSCC-derived EVs. Therefore, it is essential to examine whether these components are part of the EV luminal cargo, are EV associated or exist as intact vault particles. In this chapter, the transcript abundance of vault proteins (MVP, TEP1 and PARP4) and vtRNAs was firstly confirmed by qPCR in three OSCC cell lines, an immortalised keratinocyte cell line, and primary NOKs. The abundance of vault proteins was assessed by western blotting. Next, immunofluorescence microscopy of whole cells was performed to visualise whether vault particles associate with the endosomal compartment, which might be a potential mechanism for the packaging of vtRNAs and MVP into EVs. Lastly, EVs present in OSCC cell line conditioned medium and those enriched by differential centrifugation were characterised by NTA, ExoView and western blotting, with MVP abundance also determined in EV preparations.

3.2 Results

3.2.1 Characterisation of vault component expression in normal cells and OSCC cell lines

Before focusing on EVs, the cellular expression of vault particle components in a panel of primary cells and cell lines were determined by qPCR and western blot.

NOKs, which were used to provide a reference for vault component expression in normal oral epithelial cells in comparison to cancer cells, were previously obtained with ethical approval from oral mucosal biopsies from 3 healthy volunteers. Due to the limited passage number of primary cells before their senescence, an immortalised oral keratinocyte cell line, FNB6, was used as a representative normal epithelial cell line. OSCC cell lines (H357, SCC9, and SCC4) were selected as they are all originated from the same anatomical site (tongue) from male patients, but have showed distinct morphologies in cell culture. H357 cells are most similar to NOKs and FNB6 cells in cell shape with a polygonal monolayer morphology. SCC9 cells have a spindle-like appearance, whereas SCC4 cells are flattened with a rounded appearance (Figure 2.1).

3.2.1.1 Cellular expression of vault particle components

The expression of three vault protein transcripts (MVP, TEP1, and PARP4) were quantified by qPCR using TaqMan probes and reported relative to B2M endogenous control. Pre-designed SYBR Green primers were used for quantifications of vault RNA 1-1, vault RNA 1-2, and vault RNA 1-3 with expression reported relative to β-actin.

NOKs and FNB6 cells expressed higher levels of MVP compared to all cancer cell lines (Figure 3.1A). Strong significance was observed when comparing NOKs to the OSCC cell lines, MVP expression in NOKs was 13.16-fold higher ($p < 0.0001$) than in H357, 3.91-fold higher ($p < 0.0001$) than in SCC9, and 2.34-fold higher ($p < 0.0001$) than in SCC4. FNB6 showed high expression of all vault proteins and displayed the highest levels of TEP1 and PARP4 transcripts among the cell panel (Figure 3.1B, C). Within the OSCC cells, H357 cells expressed least and SCC4 cells expressed most MVP relative to cellular B2M expression, with a 5.62-fold difference ($p < 0.01$) observed between the two. SCC4 was observed to express more TEP1 transcripts than SCC9 cells (Figure 3.1B).

Among OSCC cell lines, SCC4 cells expressed more vtRNA 1-1 than NOKs ($p < 0.01$) (Figure 3.1D). Moreover, NOKs and FNB6 cells were found to express very low levels of vtRNA 1-2 compared to other cells. Abundant vtRNA expression were observed in all OSCC cell lines, however the expression pattern of the vtRNA paralogs among the cell panel seemed to vary (Figure 3.1D, E, F).

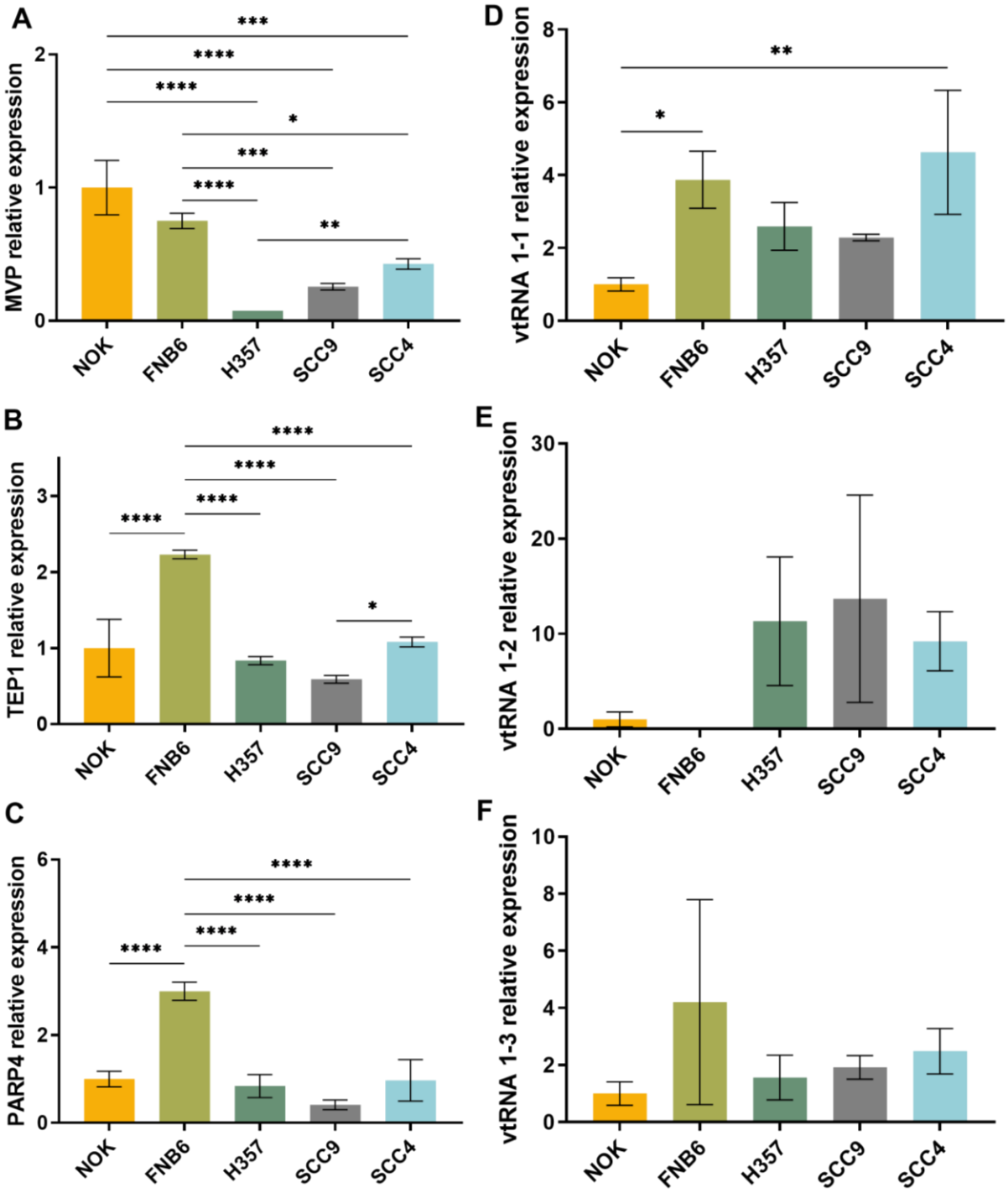

Figure 3.1 Cellular expression of vault components detected by qPCR.
Real-time qPCR detecting **A)** MVP, **B)** TEP1, and **C)** PARP4 was conducted with cDNA samples that were reverse transcripted from 100 ng total RNA extracted from 200,000 cells seeded in 6-well plates. Normalised fold changes of cellular expression of vault proteins were probed with TaqMan primers using a two-step programme with an endogenous control of B2M. For vtRNA expressions, SYBR Green primers targeting **D)** vtRNA 1-1, **E)** vtRNA 1-2, and **F)** vtRNA 1-3 were used to quantify cellular expression relative to beta-actin. Data are shown as mean ± SD, n=3 (*$p < 0.05$, **$p < 0.01$, ***$p < 0.001$, ****$p < 0.0001$ by Tukey's multiple comparisons test).

3.2.1.2 Cellular abundance of vault proteins

To validate the findings and patterns observed in gene expression, western blotting was performed to determine cellular vault protein abundance. An equal amount of total protein was loaded as confirmed by beta-actin blots (Figure 3.2). All primary cells and cell lines were positive for MVP, TEP1, and PARP4 proteins, albeit at different levels. H357 showed lower ($p < 0.01$) cellular abundance of MVP compared to NOKs. This result indicated that the components required to form vault particles were present in all the cells tested. Particularly, normal oral cells (keratinocytes and fibroblasts) were found to contain abundant MVP protein. The MVP protein expression reflected the pattern observed from the MVP transcript expression (Figure 3.2A). Protein abundance of TEP1 and PARP4 was similar to transcript expression data (Figure 3.2B, C). However, no statistical significance was observed possibly due to the limitation of densitometry for images with different exposure in post analysis.

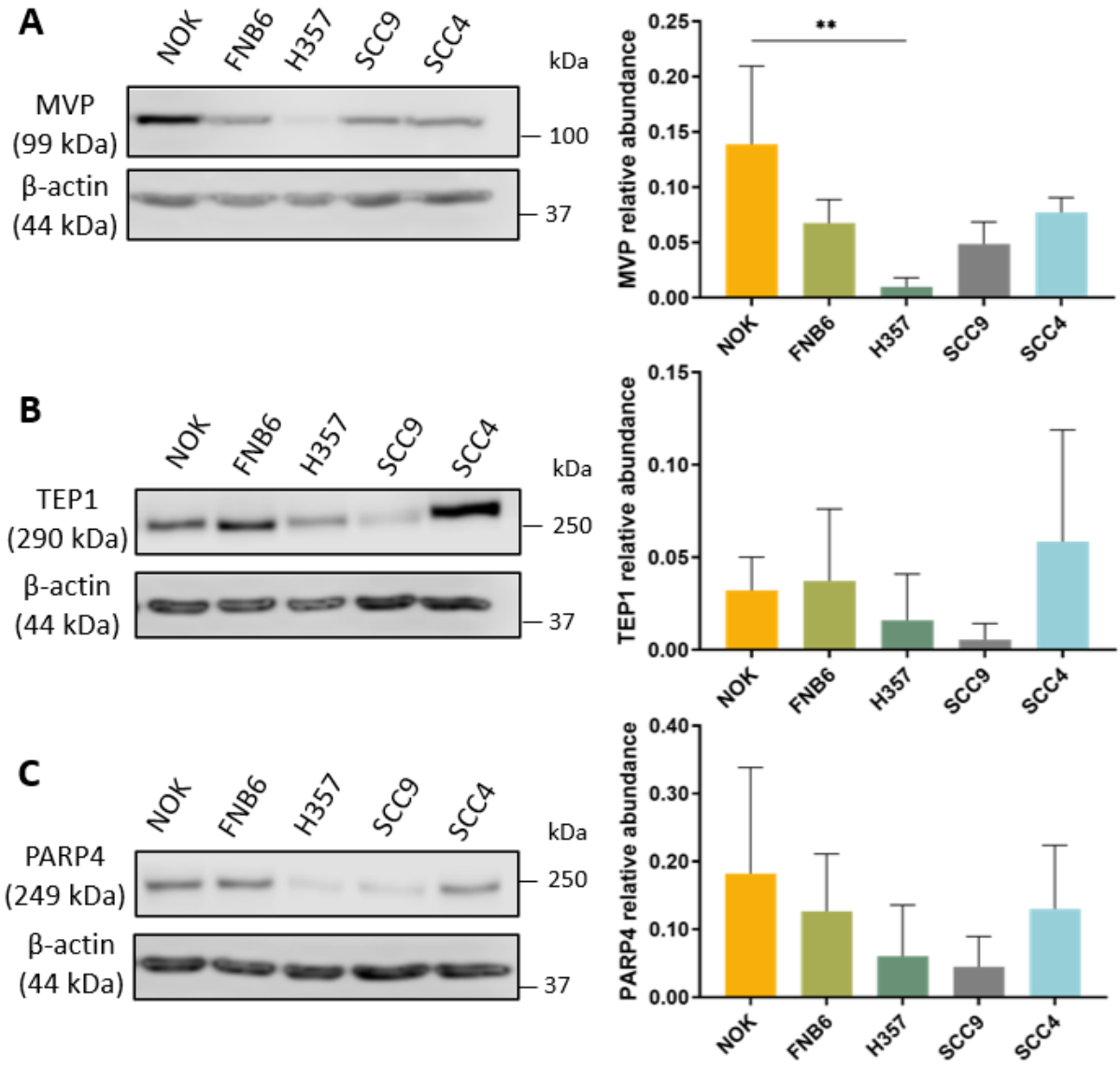

Figure 3.2 Western blot and densitometry of cellular abundance of vault proteins.
Cellular total protein was extracted from 400,000 cells seeded in 6-well plates by adding 50 µl protein lysis buffer and protein lysates were quantified by BCA assay. 10 µg total protein diluted into a total volume of 25 µl (containing 5× loading buffer) was loaded to each lane for SDS-PAGE. Protein was transferred onto a nitrocellulose membrane followed with 1 h blocking with 5% (w/v) milk in 1× TBS-T. The membrane was incubated with **A)** MVP, **B)** TEP1, **C)** PARP4 and β-actin primary antibodies overnight and with appropriate secondary antibodies for 1 h before the ECL substrate was applied. The Li-Cor scanner was used for blot scanning and the Image Studio software was used for densitometry analysis (n=3). Data are shown as mean ± SD (**$p < 0.01$ Tukey's multiple comparisons test).

3.2.2 Isolation and characterisation of OSCC-derived EVs

After gaining a basic understanding of the protein abundance of vault proteins and the cellular expression of vtRNAs, we next focused on EVs (and their molecular cargo) produced by FNB6 and OSCC cell lines.

3.2.2.1 NTA and EV-tetraspanin characterisation of cell conditioned medium

The size and concentration of nanoscale particles in the conditioned medium of FNB6 and OSCC cells was determined by NTA using a ZetaView instrument.

In all conditioned medium samples analysed, higher concentration ($p < 0.0001$) of small particles was detected than large particles, with large variation among three biological repeats (Figure 3.3A). The size distribution profiles of small and large particles were also obtained from the ZetaView analysis (Figure 3.3B, C). Using the settings focusing on the small particles, all conditioned medium samples had a peak particle size of ~100 nm (Figure 3.3B), with a similar particle distribution seen for particles larger than 200 nm diameter. However, among the conditioned medium from three OSCC cell lines, the size distribution profiles of small particles were very similar. In large particles, large variations in particle counts among the biological replicates were observed with multiple particle peak sizes in all samples (Figure 3.3C), whilst the majority of the particles detected were from 100 to 300 nm in diameter.

NTA is unable to discriminate between EVs and other nanoscale sized particles present in conditioned medium. Therefore, we performed ExoView microarray analysis to determine the abundance of tetraspanin positive particles in the conditioned medium derived from H357 and SCC4 cells. Tetraspanins are widely accepted as EV markers and have been reported to be enriched in EV membranes (Hemler, 2005; Pols and Klumperman, 2009). Not all cell lines were included in this analysis due to a limited number of microarrays provided by the company. However, H357 and SCC4 cells were chosen as representative of OSCC cell lines. Conditioned medium from growing cells was added to microarrays coated with tetraspanin capture antibodies (CD9, CD63 and CD81) and mouse IgG negative control. Representative images of fluorescent signals detected on antibody capture spots are shown in Figure 3.4A, B for H357 and SCC4 conditioned medium samples, respectively.

Conditioned medium from H357 and SCC4 had abundant particle counts detected by all three tetraspanin antibodies, indicating the presence of abundant tetraspanin positive EVs (Figure 3.4C, D). Overall, more marker positive EVs were detected from SCC4 conditioned medium than from H357,

which agreed with the results obtained from NTA particle counts. By plotting the captured marker-positive particles against particle diameter (ranging from 0-200 nm), we found that all particles captured by the tetraspanin antibodies showed a peak size at ~60 nm, rather than ~100 nm determined by ZetaView (Figure 3.4E, F). CD9 antibody captured the most EVs in conditioned medium samples from both cell lines. CD81 antibody detected the least EVs from the CD63 capture spots whilst among all CD81 captured EVs, those positive for CD63 were also less than those positive for CD9 and CD81 (Figure 3.4C, D). In conditioned medium from H357 cells, CD63 and CD81 antibodies captured low levels of particles, where as in SCC4 conditioned medium, the level of CD63-positive particles was found to be similar levels to CD9-positive ones. In addition, CD81 antibody captured similar number of particles and only very low levels of particles were captured by mIgG antibody (Figure 3.4E, F).

These data suggest that OSCC conditioned medium contains abundant EVs that are positive for at least three tetraspanin markers, which provided confidence going forward with EV isolation from conditioned medium and further characterisation of common EV markers by western blot.

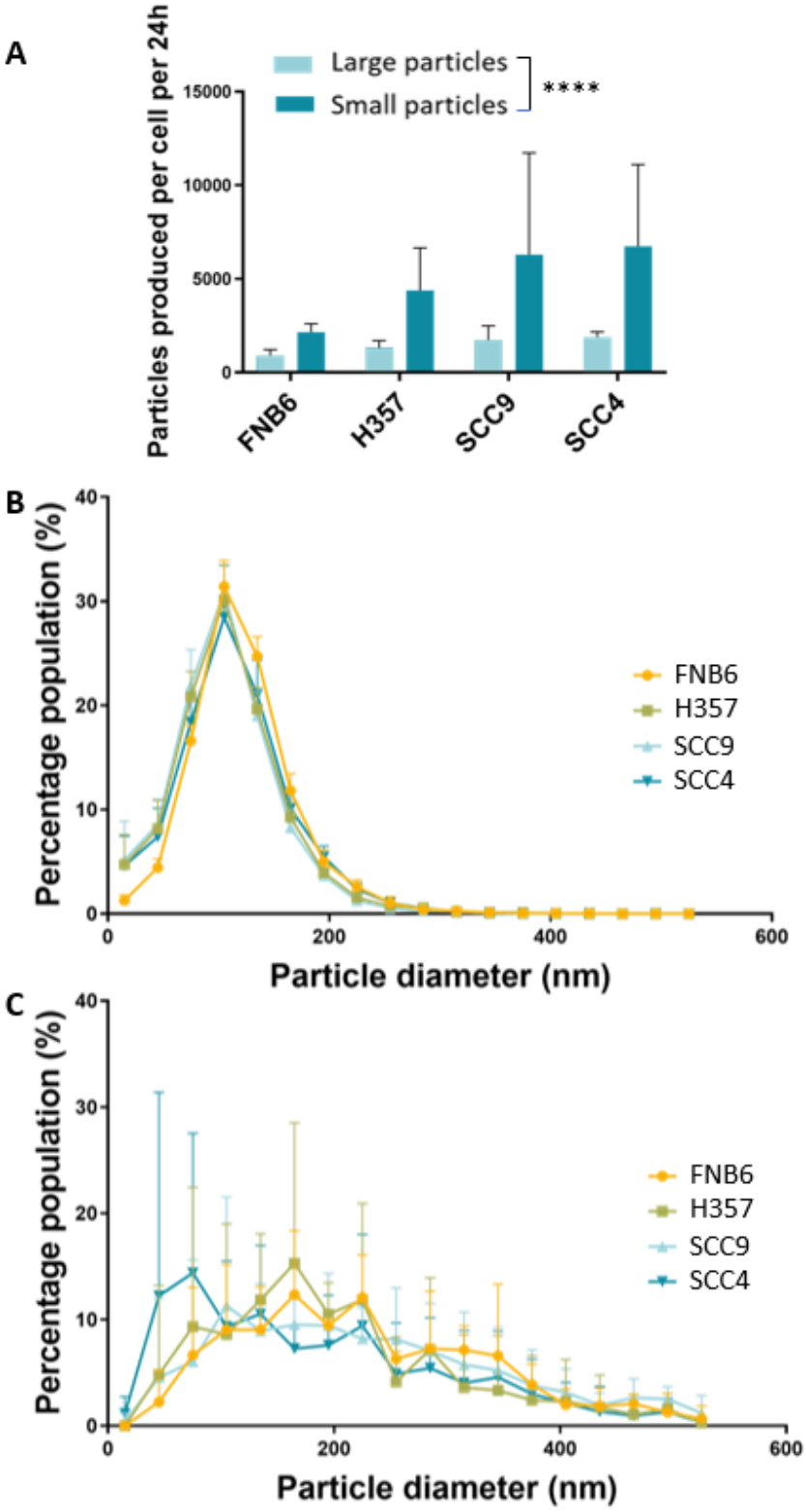

Figure 3.3 ZetaView NTA for cell conditioned medium from OSCC.
A) ZetaView NTA showing concentration of the particles in the conditioned medium from FNB6 and OSCC cell lines, normalized by the volume of the medium recovered and the cell number counted. Small particles (~100 nm) and large particles (~200 nm) were measured using the corresponding settings on the instrument according to the manufacturer's instructions. Data shown are mean ± SD, n=3. ****$p < 0.0001$ by two-way ANOVA. ZetaView NTA showing the size distribution profiles of **B)** small and **C)** large EVs from FNB6 and OSCC cell conditioned medium using the corresponding settings. Data are mean of three independent experiments.

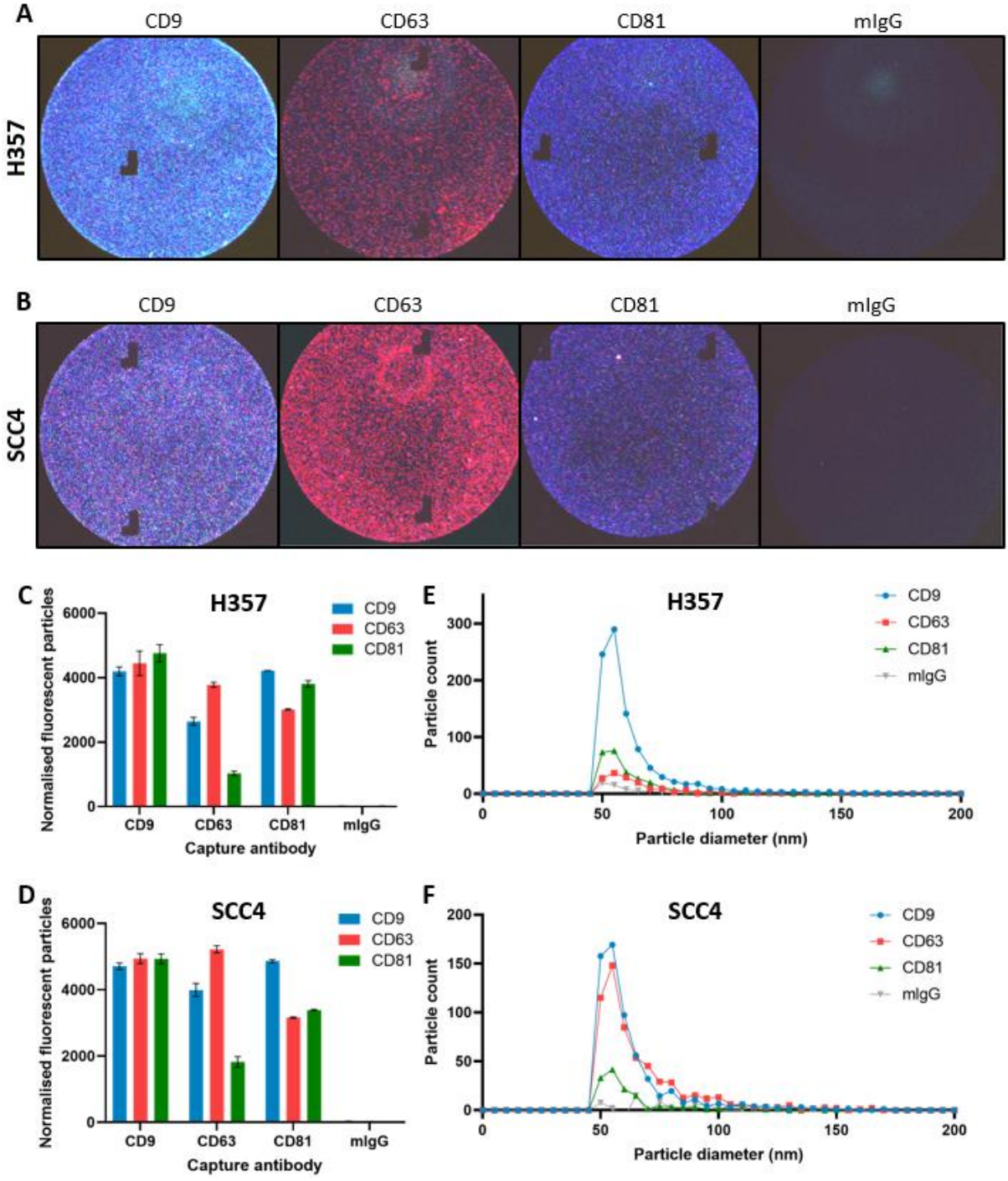

Figure 3.4 ExoView analysis for cell conditioned medium from H357 and SCC4.
ExoView microchips coated with CD9, CD63, CD81 and mIgG antibodies were incubated with conditioned medium samples from H357 and SCC4 cells, particles captured were detected with fluorescently labelled CD9, CD63, and CD81 detection antibodies. Representative fluorescence images of antibody capture spots after incubation were shown with **A)** H357 and **B)** SCC4 conditioned medium.The automatic ExoView analysis software then provided the fluorescent particle counts on each capture spot from **C)** H357 and **D)** SCC4 samples (data shown are means ± SD, n=3), the size distribution of all captured particles on each spot from **E)** H357 and **E)** SCC4 samples, data shown are means, n=3.

3.2.2.2 Characterisation of EVs isolated from OSCC conditioned medium

After identifying the presence of small and large particles in the conditioned medium, we next sought to fractionate these particles by differential centrifugation and to further characterise isolated pellets to determine if they were enriched with different EV subpopulations.

NTA was performed on pellets resuspended in PBS to determine the particle concentration (Figure 3.5A, B) and size distribution profile (Figure 3.5C-F) of small and large particles. The number of particles was too low and outside the limit of detection of the Zetaview instrument for some samples (FNB6 2k, 10k for small EV measurement and FNB6 10k for large EV measurement). In general, more particles were detected in pellets isolated from OSCC cells than FNB6 ($p < 0.05$, $p < 0.05$, $p < 0.001$ for H357, SCC9, and SCC4, respectively), agreeing with the results observed from NTA of conditioned medium. Small particles were predominantly enriched in 100k pellets, which were approximately 20-fold higher than that in 2k and 10k pellets detected by ZetaView when using the setting focusing on particles around 100 nm in diameter (Figure 3.5A). SCC4 cells produced the most small and large EVs among the OSCC lines, followed by H357 and SCC9. SCC4 ($p < 0.01$) and SCC9 ($p < 0.01$) also produced more large EVs than H357 (Figure 3.5B). By visualising the particle size distribution, the majority of the small particles in 100k pellets fell into a size range of about 100 nm (a slight shift to larger peak size was seen in FNB6 small particles), accounting for 30-40% of all particles detected. Meanwhile, particles in 2k and 10k pellets showed flatter curves with a peak size shift towards larger diameters. Although particles from the OSCC cell lines showed diverse concentrations, no major difference in size distribution profile was observed. The same samples were analysed using an NTA setting that focused on larger particles (those around 200-500 nm in diameter), which revealed enrichments of distinct particle populations in the pellets with more widely spread size profiles, ranging from 50 to 1000 nm. Lower concentrations were revealed for the large particles in general, especially some in 10k pellets were close to the detection limit of the instrument. Although more large particles were detected in 100k pellets than that in 2k and 10k pellets from H357 and SCC4 cells, these particles were mostly smaller than 500 nm. Whereas 2k and 10k pellets were enriched with particles larger than 300 nm. However large particles in all pellets displayed multiple

size peaks, in contrast to the single peaks showed in small particle analysis (Figure 3.5C-F). By comparing data from two NTA settings side by side, we weren't blinded by the "preference" of a single set of NTA parameters, and were able to gain information on a wider particle size range.

In addition, pellet lysates were characterised by western blotting for the presence of EV markers - TSG101, CD63, and CD9 and the negative control Golgi marker golgin subfamily A member 2 (GM130/GOLGA2). Lysates were firstly quantified by BCA assay, which revealed the concentration of the EV protein samples range from 25 µg/ml to 320 µg/ml (data not shown). Due to low protein concentrations in SCC9 derived lysates, these samples were unable to be analysed by western blotting and therefore excluded from the dataset. Lysates from the other cell lines were equally loaded as 2 µg per lane and separated by 12% (w/v) SDS-PAGE. An equal quantity of whole cell lysate (CL) was also loaded alongside pellet lysates for comparison (Figure 3.6A).

All three cell lines were positive for TSG101 in cell lysate and 100k pellet lanes and negative in 2k and 10k EV pellets (except a very faint band was detected in 10k pellet from H357). CD9 was consistently detected in 2k pellets, with a very low abundance in the FNB6 2k pellet. The commonly used EV marker CD63 was enriched in all EV pellets derived from H357 and SCC4 cells, compared to the cell lysate. CD63 was detected in 2k pellets from FNB6 as well as the higher molecular weight form being detected at low abundance in 10k and 100k pellets. Finally, as suggested by the International Society of Extracellular Vesicles (ISEV), the intracellular marker GM130 was examined as a negative control (Lötvall *et al.*, 2014), which was only detected in the cell lysates from H357 and SCC4 cells but none of the pellet samples, suggesting that these samples were not contaminated with intracellular components.

Lastly, 2k, 10k and 100k pellets derived from SCC4 (chosen as a representative OSCC cell line) were negatively stained and imaged by TEM. TEM confirmed the presence of lipid bilayer-enclosed vesicles of a variety of sizes showed in the pellets. 2k pellets contained highly electron-dense structures which appeared to have small spherical structures within. 10k pellets contained small EVs (~50 nm) as well as large vesicle structures with membrane. Higher number of artefactual cup shaped small EVs were observed in 100k pellets than others (Figure 3.6B).

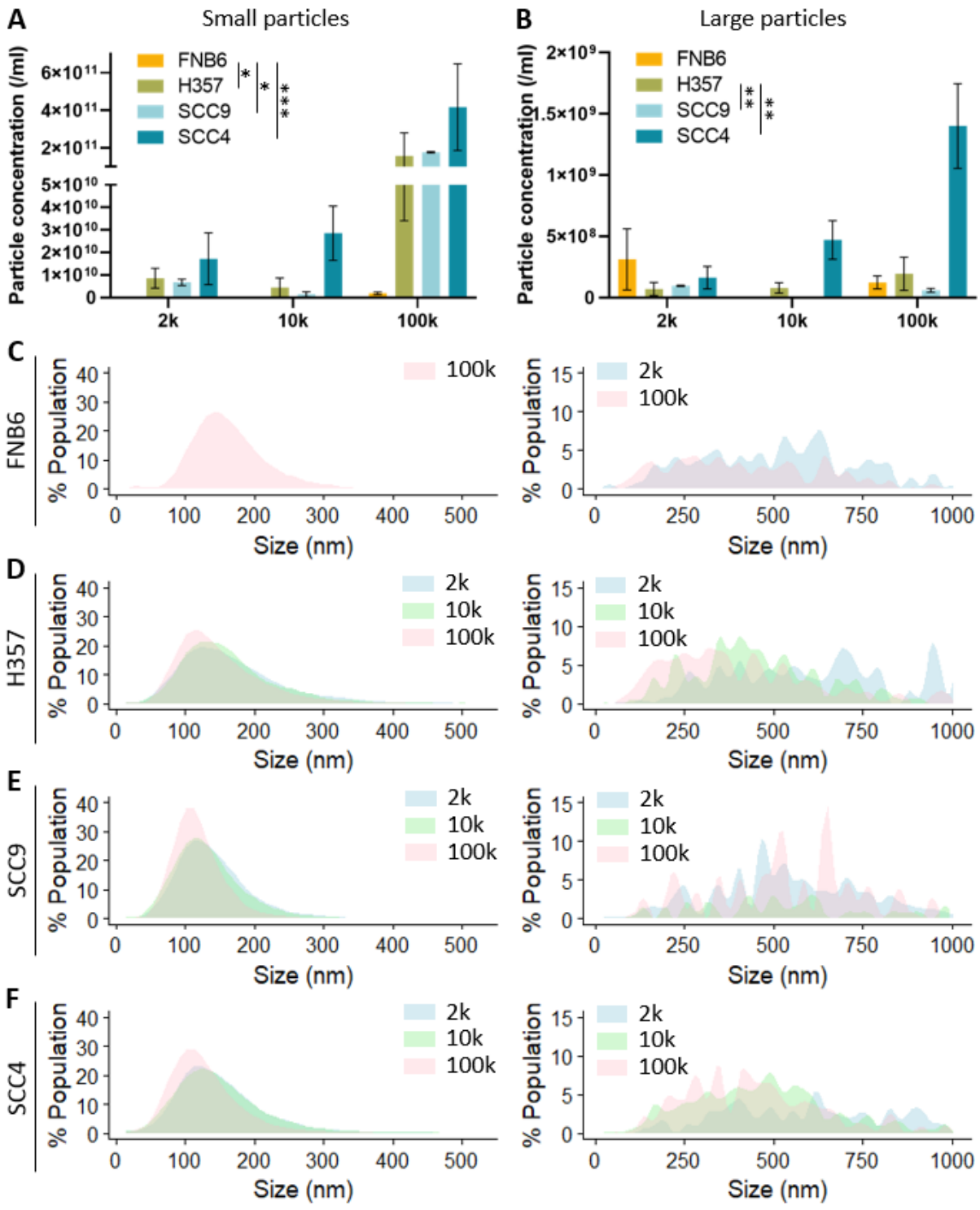

Figure 3.5 Characterisation of FNB6 and OSCC-derived pellets by NTA.
ZetaView NTA showing particle numbers per ml of 2k, 10k, and 100k pellets from FNB6 and OSCC cell lines. **A)** Small particles (~100 nm) and **B)** large particles (~200 nm) were measured using the corresponding settings on the instrument according to the manufacturer's instructions. Data shown are mean ± SD, n=3 (*$p < 0.05$, **$p < 0.01$, ***$p < 0.001$ by Tukey's multiple comparisons test). Datasets not shown were none detected. ZetaView NTA showing the size distribution profiles of 2k, 10k, and 100k pellets from **C)** FNB6, **D)** H357, **E)** SCC9, and **F)** SCC4 cell lines using settings focusing on small and large particles on the instrument. Data are mean of three independent experiments. Datasets not shown were below the limit of detection.

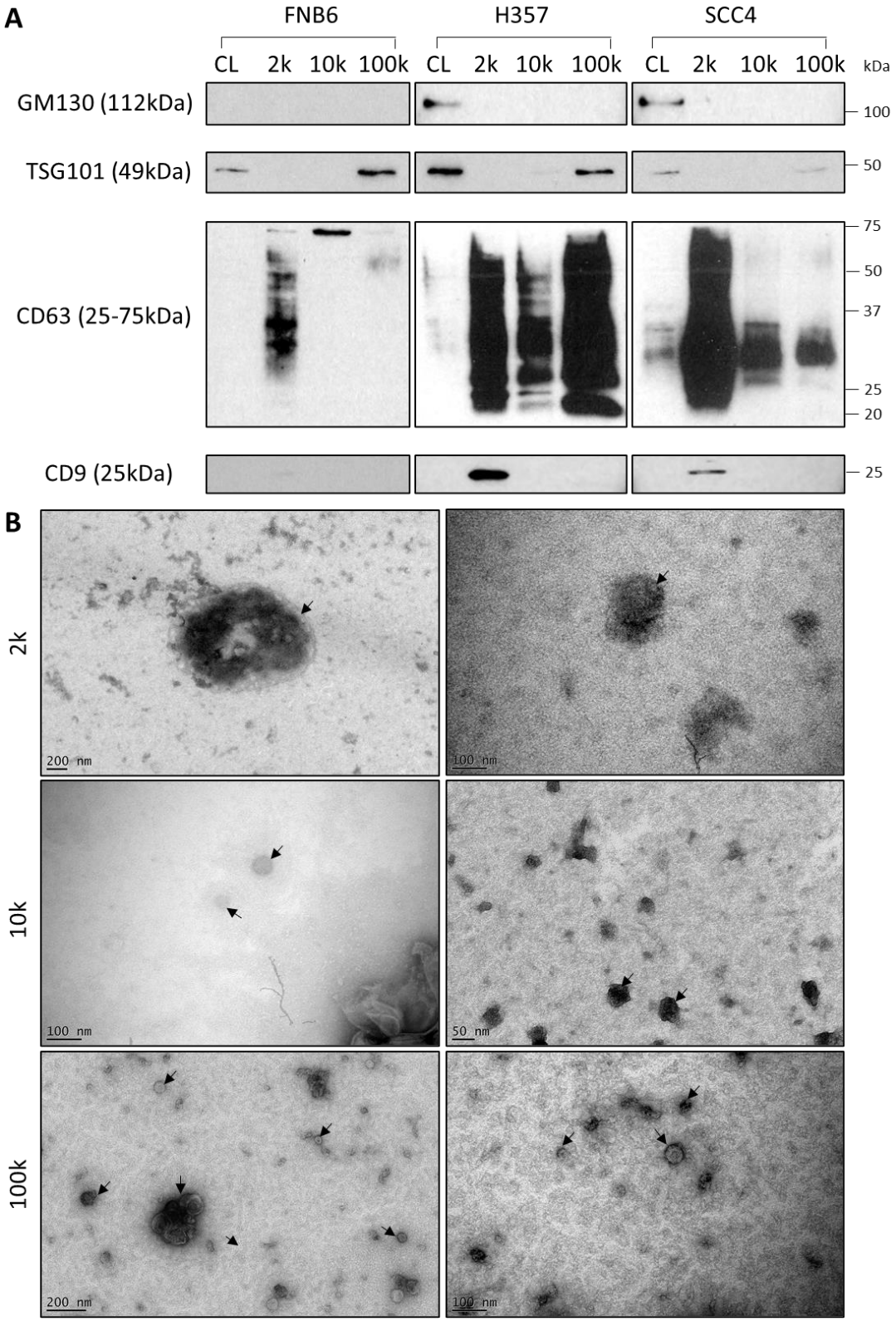

Figure 3.6 EV marker and TEM characterisation of EV pellets isolated by differential centrifugation. **A)** Western blots of H357 and SCC4 CL, 2,000 × *g* (2k), 10,000 × *g* (10k), and 100,000 × *g* (100k) pellets derived from differential centrifugation. Equal quantities (2 µg) of total protein was loaded and separated on SDS-PAGE gels. Common EV markers (CD9, CD63, TSG101) and EV-negative marker GM130 were blotted using the corresponding antibodies. Blots are representative of three independent repeats. **B)** Representative images of negatively stained transmission electron microscopy analysis of 2k, 10k and 100k EV pellets from SCC4 cell line. Arrows indicate the EVs. Scale bars represent 50-200 nm.

3.2.3 Characterisation of MVP in OSCC-EV preparations

The above data confirmed the presence of EVs in pellets produced by differential centrifugation. We next moved onto investigating the presence of vault components in EV preparations. MVP is the main protein component of the vault particle (Kedersha *et al.*, 1990). Our data confirmed that MVP transcript and protein were both present in OSCC cells (Section 3.2.1). Unpublished mass spectrometry data from the Hunt Lab detected MVP in OSCC-EV preparations (enriched by size-exclusion chromatography). In this study, the protein abundance of MVP in EVs enriched by 2,000 × *g*, 10,000 × *g*, and 100,000 × *g* centrifugation was determined by western blot. Equal amounts (2 µg) of pellet lysates and cell lysates from each cell line were analysed to determine the relative abundance of MVP.

FNB6 was included as an alternative to NOKs for comparing with OSCC cells. However due to the low concentration of EVs recovered from this cell line, only data from one biological replicate was obtained. Most of the EV pellets (except for 10k pellets from FNB6) showed abundant MVP protein, especially in 100k pellets enriching small EVs (exosomes). 2k pellet from H357 cells showed significant enrichment of MVP ($p < 0.05$), whilst no significance was observed in other pellets due to large variations in densitometry data (Figure 3.7).

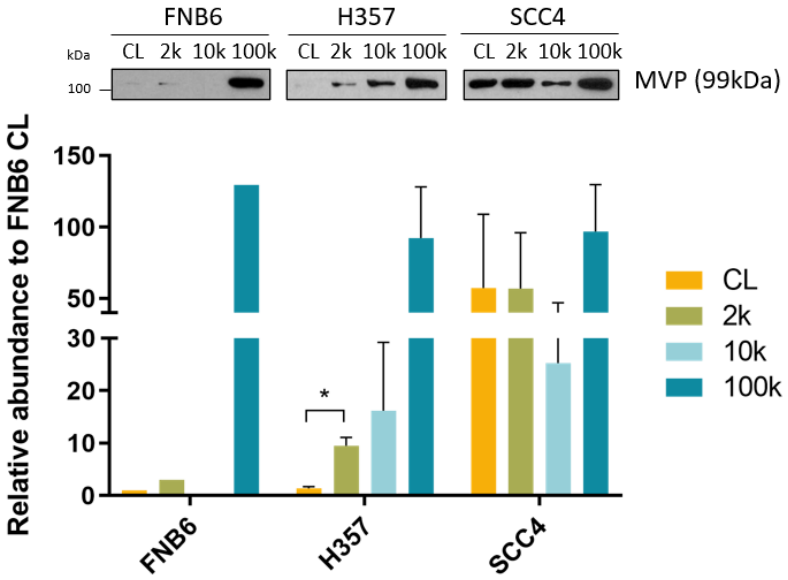

Figure 3.7 Western blot and densitometry of MVP in cellular and EV pellet lysates.
2 µg of total EV protein or cellular protein from FNB6, H357, and SCC4 cells was separated by 12% SDS-PAGE. Densitometry was performed based on the brightness of the specific band at 99 kDa using a Li-Cor Image Studio software and the data shown was normalized by cellular abundance of FNB6 cell line (n=1 for FNB6, n=3 for H357 and SCC4, *$p < 0.05$ by Dunnett's multiple comparisons test).

3.2.4 Investigating the involvement of MVP in endosomal pathways in OSCC

MVP/the vault particle has been suggested to serve a diverse range of functions in cancer, however no study has focused on the link between MVP and cancer-derived EVs. Previous studies have indicated MVP may play a role in the nucleus-cytoplasm transport of chemotherapeutic drugs in cancer cells, potentially by facilitating the formation of cytoplasmic vesicles (Kitazono *et al.*, 1999, 2001; Cheng *et al.*, 2000; Meschini *et al.*, 2002). In dendritic cells MVP was found to be colocalised with lysosomal marker CD63, which is also generally expressed by late endosomes (multivesicular bodies) and widely accepted as one of the common EV markers (Berger, Elbling and Micksche, 2000; Schroeijers *et al.*, 2002). In addition to intracellular trafficking, MVP has also been suggested to be an RNA binding protein which facilitated the exosomal sorting of miRNA in colon cancer (Teng *et al.*, 2017). Taken together, these studies hint at a role for MVP/the vault particle in intracellular trafficking and EV biogenesis, but did not explore the possibility that MVP/the vault particle might be associated with EVs and/or present in the extracellular space.

By assessing the cellular and EV MVP levels in an OSCC and normal oral cell panel, we have observed decreased MVP abundance in OSCC cells compared to the normal cells as well as enrichment of MVP protein in the OSCC-EV preparations. To further investigate whether MVP is involved in the endosomal sorting and trafficking in OSCC, immunofluorescent staining of MVP and endosome markers (early endosome antigen 1 and Ras-related protein Rab-7a for early and late endosomes, respectively) followed by super-resolution confocal microscopy was performed to detect any colocalisation of the two. From the OSCC cell panel, H357 and SCC4 were selected to represent cells displaying distinct morphological characteristics, in order to minimise the confounding effect during imaging caused by certain cell shape.

MVP was located largely in cytoplasm and was evenly distributed across the single cells (Figure 3.8). Whereas early endosome antigen 1 (EEA1) and Ras-related protein Rab-7a (Rab7) displayed more focal staining in certain areas of the cytoplasm, indicating the successful staining of intracellular endosomal structures. MVP showed colocalisation with EEA1 and Rab7 in both cell lines, although more colocalisation was seen in H357 cells (shown as yellow spots in merged images). However, this

was only observed in a subpopulation of all cells stained. The colocalisation provides preliminary evidence for a possible involvement of MVP in the endosomal pathways and cargo sorting in OSCC.

Noticeably, enrichment of MVP close to the cell membrane was detected in a proportion of SCC4 cells, overlaid with the area where Rab7 was located (Figure 3.8D). Previous studies have closely linked vault particles with multidrug resistance in many cancers and the possible involvement of MVP in lysosome-mediated drug export (Kickhoefer *et al.*, 1998; Scheffer *et al.*, 2000; Herlevsen *et al.*, 2007). This evidence has raised the question whether MVP/vault particles can be specifically enriched at the cell surface to facilitate extracellular cargo transport.

To address the question, we further examined the sublocation of another vault protein, TEP1, in SCC4 cells, and its relation to endosome markers EEA1 and Rab7. To assess whether vault proteins are enriched at the cell surface the transmembrane protein EGFR was included as a positive control surface protein, and isotope IgG as negative control for non-specific binding.

Staining of EEA1 and Rab7 showed a similar pattern as observed previously, reflecting the perinuclear localisation of early endosomes and more dispersed distribution of late endosomes (Figure 3.9). EGFR was detected dominantly at the cell surface, although some staining was observed in the cytoplasm (Figure 3.9C, D). TEP1 did not appear to colocalise with the endosome markers as observed for MVP and it was mainly found near the cell surface (Figure 3.9A, B). Staining with isotype IgG confirmed very low level of non-specific binding for both fluorescence (Figure 3.9E). In summary, these experiments have provided evidence supporting the hypothesis that MVP and perhaps vaults are associated with endosomal trafficking and vesicular release at the cell surface in OSCC. However, data from functional studies and investigations of molecular mechanisms are required before a certain conclusion could be drawn.

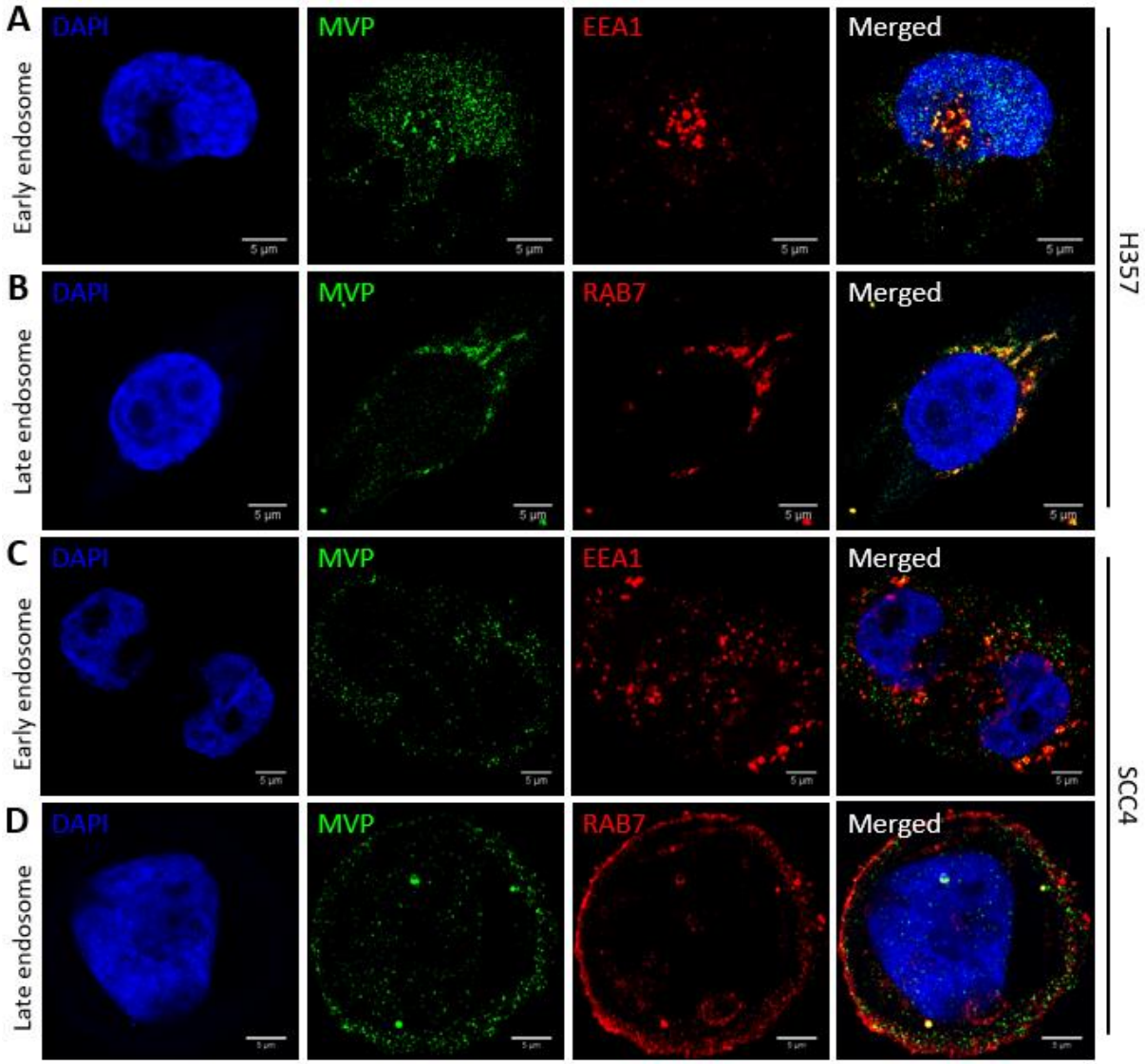

Figure 3.8 MVP partially co-localised with early and late endosome markers in OSCC cells.
Cells were seeded and fixed before being blocked for 1 h. Fixed cells were incubated with anti-MVP and anti-EEA1 or anti-RAB7 primary antibodies before being incubated with Alexa488 and Alexa568-conjugated secondary antibodies and DAPI staining. Fixed cells were imaged by Zeiss LSM 880 AiryScan confocal microscope. Representative images showing co-localisation of MVP in **A, B)** H357 and **C, D)** SCC4 and the early and late endosome markers (shown in yellow in merged images). Scale bars indicate 5 µm.

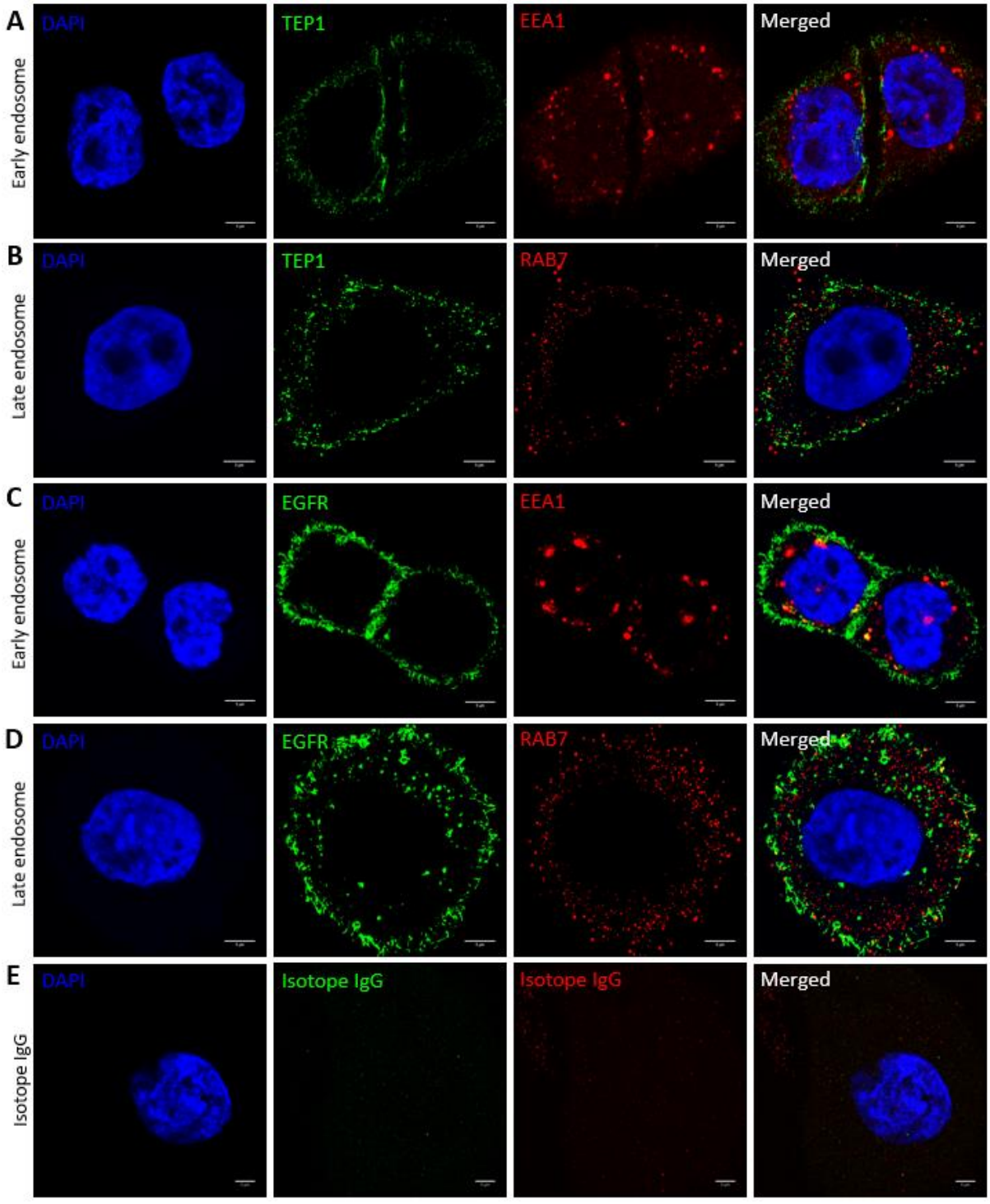

Figure 3.9 Immunofluorescence imaging of the sublocation of TEP1, EGFR and the endosome markers. SCC4 cells were seeded and fixed before being blocked for 1 h, prior to incubation with **A, B)** anti-TEP1/ **C, D)** anti-EGFR/ **E)** isotope IgG and anti-EEA1/anti-RAB7/isotope IgG primary antibodies before being incubated with Alexa488 and Alexa568-conjugated secondary antibodies and DAPI staining. Fixed cells were imaged by Zeiss LSM 880 AiryScan confocal microscope. Representative images showing the sublocations of TEP1 or EGFR and the endosome markers. Scale bars indicate 5 μm.

3.3 Discussion

3.3.1 Vault particle components are expressed in primary oral cells and OSCC cells

Several studies have revealed the ubiquitous presence of the vault particle in a variety of cell types, among many species (Kedersha and Rome, 1986; Kedersha *et al.*, 1990; Margiotta, Bain and Rice, 2017). By examining the expression of vault components at both the mRNA and protein level in a panel of normal oral cells and OSCC cell lines, our study showed the universal expression of vault components across the cell panel, except for vtRNA 1-2 which was not expressed in FNB6 cells. In particular, we observed higher levels of MVP transcript and protein in normal primary cells (NOKs) compared to FNB6 and OSCC cell lines.

In OSCC, the exact function of MVP and the vault particle remains unclear. MVP has been found to be diversely expressed in head and neck cancers. For example, it was found highly expressed in poor-prognosis-related OSCC tissue and tongue carcinoma tissue relative to adjacent non-malignant tissue, whilst no significant increase in MVP expression levels was found by another study focusing on head and neck squamous cell carcinoma (Hirata *et al.*, 2000; Henríquez-Hernández *et al.*, 2012; Zhang *et al.*, 2012). Among the OSCC cell panel selected in this study, we found MVP showed significantly decreased expression in all OSCC cells compared to NOKs, which is consistent with reports of varied MVP expression seen in head and neck cancer. However, the NOKs cultured *in vitro* are highly proliferative cells that are more representative of those in the basal layer of the epithelium. Hence, the high expression of MVP in proliferating NOKs *in vitro* may not represent the actual MVP expression in full thickness normal oral mucosa.

MVP has been largely linked to cellular resistance to apoptosis and inducing multidrug resistance in cancers (Persson *et al.*, 2009; Ryu and Park, 2009). Meanwhile, other studies have focused on the MVP-associated apoptosis resistance in senescent cells and aged organs (Ryu *et al.*, 2008; An *et al.*, 2009; Pasillas *et al.*, 2015). Pasillas *et al.* observed accumulation of MVP in nuclei and BAG family molecular chaperone regulator 3 (Bag3)-dependent subcellular re-localisation of MVP in therapy-induced senescent cells, therefore a model of Bag3 binding to MVP which induces MVP nuclear

accumulation and further activates the ERK1/2 pathway to resist apoptosis in senescent cells was proposed (Pasillas *et al.*, 2015). Furthermore, MVP was included in a paracrine circuit between senescent cells and their surrounding microenvironment hypothesised by an ingenuity pathway analysis (IPA) due to their common presence among different senescent phenotypes (Özcan *et al.*, 2016). According to the literature, MVP appeared to play a role in the common circuit involved in general cell response to senescence or apoptosis. In our study, primary cells were isolated from tissue biopsies then maintained by *in vitro* cell culture before cellular total RNA was extracted from cells with passage number of 1 to 5. Human cells undergo replicative senescence after reaching the proliferation limit, where human NOKs became senescent after five passages and showed increased doubling time with increased passage number *in vitro* (Min *et al.*, 1999; Jang *et al.*, 2015). Apart from donor-to-donor variability, our observation of higher expression of MVP in NOKs could be linked to a function in assisting cells with entering senescence where MVP level could be elevated to enable senescent programming and escape from cell apoptosis, whereas cancer cells do not senesce. This hypothesis could be further evidenced by assessing β-galactosidase activity and p16 expression (markers of senescence) in future experiments.

The FNB6 cell line was previously immortalised by telomerase reverse transcriptase 2 (TERT2) transfection and acquired immortality without presenting any other cancerous or dysplastic phenotypes (Mcgregor *et al.*, 2002). Although they were originally included in the cell panel as a normal keratinocyte control, FNB6 cells did not exhibit similar expression pattern as NOKs regarding cellular abundance of vault components. It had lower level of MVP transcripts and higher levels of TEP1, PARP4 and vtRNA1-1 transcripts compared to NOKs. FNB6 was used as a NOK alternative in oral mucosa equivalent (OME) generation, in which it formed a keratinocyte layer similar to NOK and distinct to H357 and was functionally responsive to pro-inflammatory cytokine stimulation (Jennings *et al.*, 2016). However, additional changes in molecular expression were also seen in FNB6 other than TERT2, which was also reflected by higher fold increase of cytokine levels in response to the pro-inflammatory stimulation of the OME model compared to that in NOK OME and H357 OME (Mcgregor *et al.*, 2002; Jennings *et al.*, 2016). Therefore, the potential molecular changes in FNB6

may have made them less suitable for representing NOK in our study, however it was still included in the follow-up EV experiments as a non-cancerous cell line in comparison to OSCC lines due to the passage limit of primary cells.

The OSCC cell lines used in this study vary in their cell morphology and differentiation status. Apart from SCC4 harbouring a large, flattened cell shape, SCC9 has a spindle-like cell shape whilst H357 cells show similar morphology to well-differentiated cells. In the literature, SCC9 has been described as a poorly invasive cell line (Prgomet *et al.*, 2015). Another study using both SCC4 and SCC9 cell lines hinted at a less invasive and migratory phenotype of SCC4 compared to SCC9 through crystal violet staining of migrated cells (Kashyap *et al.*, 2018). Chiu *et al*. also used SCC4 in their study as a representative low-invading cell (Chiu *et al.*, 2016). The well differentiated H357 has been shown to be more invasive than poorly differentiated SCC4 (Sapkota *et al.*, 2011). According to the literature, the moderate and poor differentiation status of SCC9 and SCC4, respectively, is not related to an aggressive phenotype. However, SCC4 was originally isolated from a patient who received radiotherapy and chemotherapy treatment for 16 months before the biopsy was taken, which could be linked to the highest MVP expression observed in SCC4 cells (Rheinwald and Beckett, 1981). Additionally, considering the important role of MVP played in mediating drug resistance in cancer cells, the higher abundance of vault proteins in SCC4 cells might associate with other aspects involved in the tumorigenesis.

Our study revealed, for the first time the intracellular abundance of vtRNAs in OSCC cell lines. vtRNAs expressed by the OSCC cell panel were found to be higher ($p < 0.01$ for vtRNA1-1 abundance in SCC4 compared to NOKs) than that in NOKs, agreeing with results from a study using human glioblastoma, leukaemia, and osteocarcinoma cell lines (Gopinath, Wadhwa and Kumar, 2010). The high expression of vtRNAs in cancer cells has been closely linked to a multidrug resistant phenotype (Gopinath *et al.*, 2005; Gopinath, Wadhwa and Kumar, 2010; J. Chen *et al.*, 2018). However, so far no research has been published focusing on vtRNAs and their roles in OSCC. One hypothesis that could explain the high expression of vtRNA displayed in cancer cells is the commonly elevated activities of RNA polymerase III during tumorigenesis, by which vtRNAs are transcribed

(Canella *et al.*, 2010). Noticeably, FNB6 and NOKs expressed very low or no cellular transcripts of vtRNA1-2. Although vtRNA paralogs are very similar, Amort *et al.* (2015) have indicated an NF-κB-driven promoter and apoptosis-resistant function of vtRNA1-1 but not vtRNA1-2, while Lee *et al.* (2011) revealed the distinct subcellular locations of vtRNA 2-1 and vtRNA1-1 (Lee *et al.*, 2011; Amort *et al.*, 2015). Our data show that vtRNA1-1 can be overexpressed in immortalised cells (but not all those tested) compared to normal cells, which could make them responsible for some malignant behaviours of the cancer cell, such as mediating drug resistance and protection from apoptosis.

3.3.2 Characterisation of OSCC derived EV pellets isolated by differential centrifugation

After obtaining a basic understanding of the cellular expressions of vault components in our cell panel, we moved on to characterise pellets containing EVs released by the parental cells. By looking at particle concentrations obtained from cell culture conditioned medium (CM) and isolated pellet samples, we observed more particles were produced by OSCC cells compared to non-cancerous cells (FNB6), with small particles enriched in 100k pellets being the most abundant. It has been well established that OSCC produces more EVs with altered molecular cargos compared to normal controls in both cell lines and patient-derived plasma samples (Momen-Heravi and Bala, 2018b). Principe *et al.* also showed 2 to 4-fold more salivary EVs were detected from OSCC patients than in healthy volunteers (Principe *et al.*, 2013). While drawing consistent conclusion with previous research, our study also characterised both small and large particle subpopulations in our samples via two sets of settings on the NTA instrument. Compared to large particles, NTA of CM and EV pellets revealed that small particles (diameter ranging from 30 to 160 nm) were the most abundant population derived from both cancer and normal cell lines. Analysis of large particles by NTA showed that this population were extremely heterogeneous in size. This could be partially due to the size range of large particles (including EVs like microvesicles and apoptotic bodies) was beyond the optimal detection range of the NTA instrument, as reported by another study focusing on isolating and characterising microvesicles that multiple peak sizes detected from the microvesicle samples (size range: 100-600 nm) as observed in our large particle pellets (Menck *et al.*, 2017). It is also possible that aggregates of

small particles can be recognised as large particles by the ZetaView instrument. Filipe *et al*. showed that protein aggregates can be identified as particles with a size range of 100-1000 nm by a similar NTA instrument (NanoSight LM20), which was reported to provide less accurate measurement of EV concentration but higher resolution than ZetaView (Filipe, Hawe and Jiskoot, 2010; Bachurski *et al.*, 2019). Upon confirming the presence of tetraspanin marker-positive particles in CM from two OSCC cell lines by ExoView analysis, the presence of other protein makers in EV preparations was assessed by western blotting for three commonly used EV markers (CD9, CD63, TSG101) and one intracellular control (GM130). Due to the heterogeneous nature of EVs and different isolation methods applied across the literature, there are currently no specific and universal markers for characterising EVs of specific subtypes. However, suggested by MISEV2014, at least two proteins present in EVs (one of membrane bound and one of cytosolic protein) should be used to characterise the protein contents of EVs. Meanwhile, one protein that is not expected in EVs and another protein representative for non-EV co-isolated structures should be also included to demonstrate the presence of EVs and to confirm that no cellular contamination has been carried over (Lötvall *et al.*, 2014). The requirement of a negative control for intracellular proteins has been deleted in MISEV2018, due to the variation in EV biogenesis and cargo loading making identification of such a control very difficult (Théry *et al.*, 2018). This study included three of the commonly accepted EV markers, of which CD9 and CD63 fell into the category of EV-membrane associated proteins and TSG101 represents a cytosolic EV protein. CD63 was commonly associated with all EVs while CD9 was only detected in large EVs (2k pellets). This is however in conflict with the number of CD9-positive particles being the highest observed by ExoView, as well as the general understanding that CD9 is an EV marker that is usually found in small EVs (enriched at a >100,000 × *g* speed) (Yoshioka *et al.*, 2013). This could be explained by different detection sensitivity of the two techniques, in which the exposure time for developing western blot could also dramatically affect the intensity of the blots. Additionally, as one of the first experiments conducted in this study, the technical skills and exposure time for immunoblotting individual EV marker were perhaps not optimal, which have since then been improved and evidenced in blots shown in figures included in the later chapters. As a protein involved

with ESCRT machinery, TSG101 was only seen in small EVs. We also included the Golgi marker GM130 as negative control which was only detected in cell lysates as expected.

3.3.3 MVP was enriched in OSCC-EV pellets

MVP has been detected in cancer-derived EVs by several individual studies, in most cases it was found enriched in exosome/small EVs in comparison to parental cells (Welton *et al.*, 2010; Peinado *et al.*, 2012; He *et al.*, 2015; Xu *et al.*, 2015). However little was known about their relative abundance in other EV subpopulations. Unpublished mass spectrometry data from the Hunt Lab also showed enrichment of MVP in OSCC-EVs. In this study, we first validated these data by determining the abundance of MVP in EV pellets enriching different EV subpopulations from OSCC and normal cell lines.

Assessment of MVP protein abundance in isolated EV pellets suggested an enrichment of MVP in EV pellets compared to that in total cell lysates in all three cell lines. In FNB6, a 120-fold increase in MVP abundance in 100k pellets was observed compared to cell lysate, although the data was collected from only one biological repeat due to overall low protein concentration of FNB6-derived EV lysates. In OSCC-EVs, MVP showed increased abundance from 10 to 100-fold compared to the cellular protein abundance, this was significant in 2k pellet vs CL in H357 cells however not significant in other pellets due to big variation in densitometry analysis. Overall, EV isolates derived from SCC4 cells contained the most abundant MVP protein. The cell line also had the highest cellular abundance of MVP compared to other two cell lines whilst it also showed the largest variation between the biological repeats. Noticeably the variation also included the errors from technical operation that were unable to be minimised during data analysis due to the lack of a constitutively expressed internal control for EV protein normalisation. Therefore, we have applied the alternative approach to present the data by utilising the cellular abundance of MVP in FNB6 cells to normalise protein abundance. The data shows abundant MVP present in CM of the cell lines tested, which can be pelleted at the different *g* forces used. The reason for this is unclear, but is tempting to speculate that MVP is associated with larger particles/complexes (e.g. EVs) that can be pelleted at the centrifugal forces used.

3.3.4 Involvement of MVP in endosomal pathways in OSCC cells

Studies have demonstrated a role of vault particles in mediating drug resistance in cancer by shuttling chemotherapeutic substance from nuclei to the cytoplasm (Kitazono *et al.*, 1999, 2001; Cheng *et al.*, 2000; Meschini *et al.*, 2002). Our observations from immunofluorescence imaging suggested MVP could be associated with early and late endosomes in OSCC. The colocalisation of MVP and endosome markers was only observed in a proportion of cells, which could be due to different cell cycle stages upon fixation. The exact percentage of cells showed colocalisation could be further quantified in follow up experiments and validated by synchronising cell cycle by a period of serum starvation prior to experiments.

Interestingly, by imaging MVP and TEP1 separately with endosome markers, we noticed different cellular localisation patterns of the two vault proteins. As reported by another study, MVP is a cytoplasmic protein and was mostly distributed evenly across the cytoplasm (Liu *et al.*, 2015). MVP was observed colocalising with the endosome markers, whilst in certain SCC4 cells it also localised near the cell membrane. Similar cell surface localisation of MVP was also observed in a proportion of hepatocellular carcinoma cells, which was linked to promoted cancer progression and a more metastatic phenotype (Lee *et al.*, 2017). The translocation dynamic of MVP was also seen in the literature upon EGF stimulation, which resulted in a promoted perinuclear and cytoskeletal MVP localisation (Kim *et al.*, 2006). We then further investigated the cell membrane localisation of vault proteins. As a transmembrane protein, EGFR was mainly detected at the cell surface, whilst the minor EGFR cytoplasmic staining could be the result of receptor endocytosis and its involvement in activating multiple downstream signalling pathways (Caldieri *et al.*, 2018). TEP1 predominantly was located near the cell surface and the late endosomes. This difference in vault protein subcellular localisation could suggest that vault proteins may be involved individually in multiple cellular activities and partially function in a vault-independent manner.

One of the main research questions this project aims to answer is whether MVP or the vault particle is involved in vtRNA sorting and trafficking into the EVs in OSCC cells. In this chapter, the colocalisation of MVP and endosomes observed through immunostaining provided preliminary

evidence of a link between MVP or the vault particle and endosomal pathways/cargo sorting. However, the proportion of cells displaying this relationship and the underlying mechanisms still need to be elucidated by further quantification and experiments.

Chapter 4 Transcriptomic analysis of OSCC-derived EVs

4.1 Introduction

It has been well-established that EVs contain a large variety of molecular cargo, including protein, lipid, DNA and RNA (Abels and Breakefield, 2016). In recent years, the most intensively researched EV cargo has been RNA, resulting in growing number of new RNA species being discovered. Deep sequencing of RNA cargo derived from EVs released by immune cells revealed a rich selection of both protein-coding and non-coding RNA (ncRNA). Furthermore, EV RNA cargo seemed to differ from the total cellular RNA, suggesting underlying mechanisms facilitating selective cargo sorting and packaging (Nolte'T Hoen *et al.*, 2012). Altered EV RNA cargo enrichment was also repeatedly seen in disease settings especially in cancers (W. Hu *et al.*, 2020). Research into disease-specific EV RNA cargo are significant as they can be easily accessed in body fluids for early-stage screening or potential therapeutic targets (Takahashi *et al.*, 2017).

Among all EV-RNA, ncRNA has attracted great interest due to their gene regulatory functions. For example, in oral cancer, EV-miRNAs have been shown to play essential roles in cell-to-cell communication and post-transcriptional regulation (Li *et al.*, 2018; Momen-Heravi and Bala, 2018a). EV RNA cargo is abundant in RNA species of 20-200 nt in length, suggesting the presence of numerous RNAs other than miRNA (Tosar *et al.*, 2015). With the help of Next Generation Sequencing (NGS), studies have revealed the enrichment of Y RNA, certain tRNA, snoRNA, lncRNA, rRNA, piRNA and vtRNA (Huang *et al.*, 2013; Chakrabortty *et al.*, 2015; van Balkom *et al.*, 2015).

VtRNA has been repeatedly reported as abundant EV cargo (van Balkom *et al.*, 2015; Capomaccio *et al.*, 2019). A study focusing on EVs derived from dendritic cell-T cell co-cultures revealed that vtRNA accounted for ~27% of total reads of EV-shuttled RNA and only ~1% of total cellular RNA

(Nolte'T Hoen *et al.*, 2012). As well as full-length vtRNA, a large amount of vtRNA fragments were also identified (due to their size selection restriction of <70 nt), which predominantly consisted of the internal stem loop structures of the full-length vtRNA. In addition, another study focusing on vtRNA fragments identified in breast cancer cells cultured *in vitro* suggested cellular vtRNA fragments were derived mainly from the 3' and 5' ends of vtRNAs, while similar results were confirmed by the comparison of EV-vtRNA fragment and cellular-vtRNA fragment sequences by Nolte-'t Hoen *et al*. (Persson *et al.*, 2009; Nolte'T Hoen *et al.*, 2012). These small fragments of cellular vtRNAs (named svRNAs by the authors), which were generated through a Dicer-dependent and Drosha-independent manner, have been demonstrated to downregulate a key enzyme CYP3A4 in drug metabolism (Persson *et al.*, 2009).

The oral cavity is bathed in saliva, a readily accessible biofluid that can be enriched with products released by oral cancer cells. Certain salivary miRNAs have been suggested to be used as disease-specific biomarker for oral cancer screening (Liu *et al.*, 2012; Duz *et al.*, 2016). However, most of the studies are currently focusing on profiling RNA contents from small EVs/exosomes. As EVs are a highly heterogenous population, RNA cargo was shown to be sorted differently into different types of EVs (O'Brien *et al.*, 2020). In this chapter, we performed NGS on small and large EV pellets derived from FNB6 and OSCC cell lines, aiming to establish the small RNA EV profile in OSCC as well as determining any differentially enriched RNA species in OSCC-EVs in comparison to FNB6-EVs as a normal control. In particular, we also aimed to characterise the abundance and variety of vtRNAs and vtRNA fragments in OSCC-EVs, and whether they are selectively loaded into the EVs and can be potentially considered as OSCC biomarkers. Following the fundamental characterisation, we also aimed to establish a fluorescently labelled vtRNA overexpressing cell line, which could be a useful tool for the visualisation of vtRNA cargo sorting into EVs and functional intercellular transfer.

4.2 Results

4.2.1 Transcriptomic analysis of FNB6 and OSCC-derived EVs

4.2.1.1 EV-RNA isolation and Bioanalyzer analysis

To determine differences in small RNA cargo in EVs produced by normal and cancerous oral keratinocyte cell lines, EVs were firstly isolated by differential centrifugation from 60 ml cell conditioned medium from FNB6, H357, SCC9, and SCC4 cells. Total RNA was extracted from 10k and 100k EV pellets using an Exiqon miRCURY RNA isolation kit with an on-column DNase treatment. The integrity of isolated RNA was firstly characterised using an Agilent 2100 Bioanalyzer coupled with an RNA 6000 Pico LabChip.

The Bioanalyzer traces showed skewed normal distributions. EV-RNA contained abundant small RNA species 25-200 nucleotides in length with peak size at ~50-100 nt across all samples (Figure 4.1). Both sample sets (10k and 100k) showed an enrichment of larger RNA species (~1,000 nt), but only the 10k pellets contained prominent 18S (~1,800 nt) and 28S (~3,600 nt) ribosomal RNA peaks. In comparison to 10k, 100k EV pellets also had a second peak that had wider areas at ~1,000-1,500 nt (Figure 4.1).

EV-RNA concentrations were automatically calculated based on the area under the curve and ranged from 2,644 pg/µl (from SCC9 100k samples) to 16,618 pg/µl (from SCC4 100k samples). Apart from SCC4 cells, 100k pellets in general had lower RNA concentration than 10k pellets.

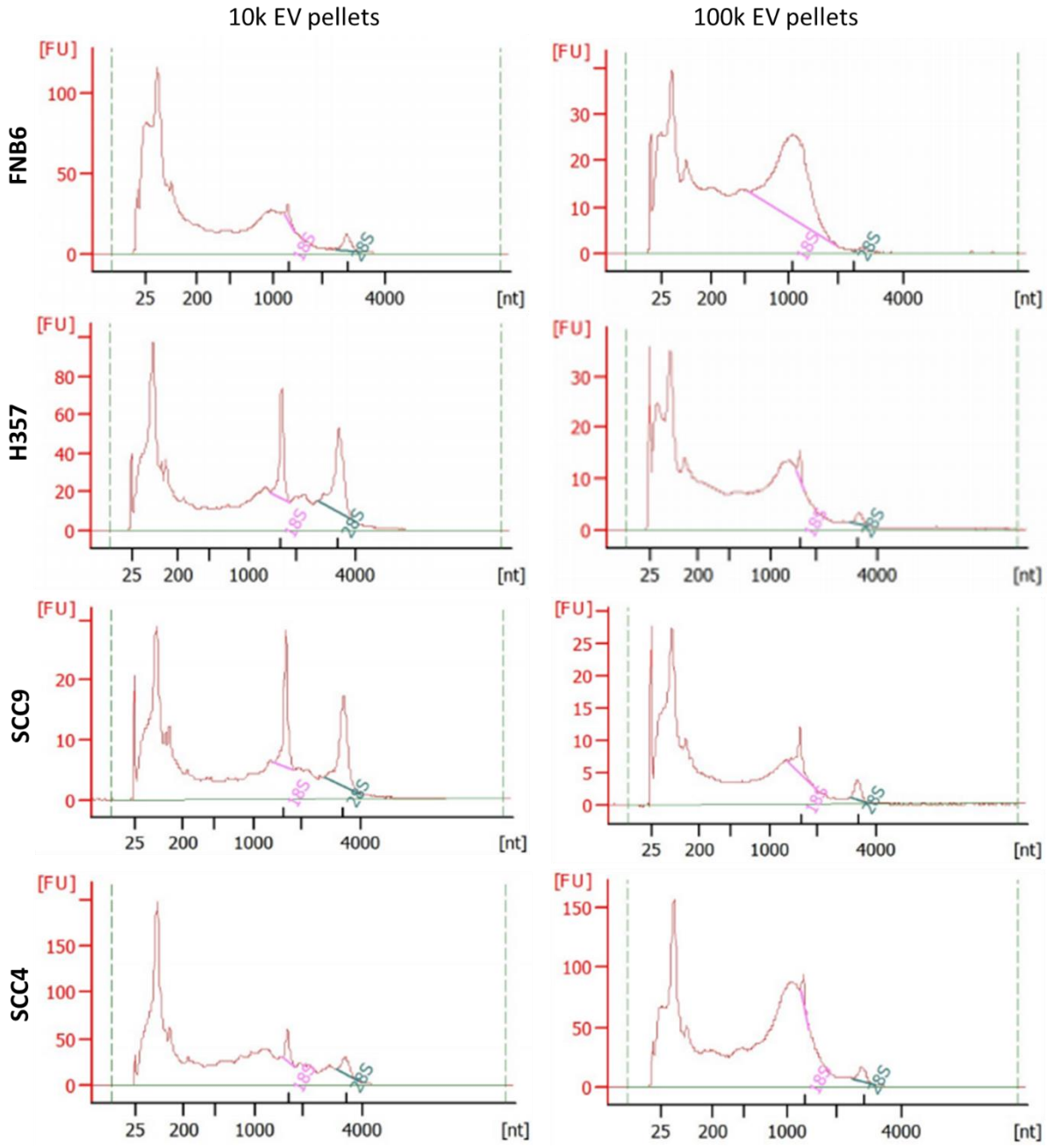

Figure 4.1 Analysis of EV-RNA distribution by Bioanalyzer trace.
The EV pellets isolated from conditioned medium from FNB6, H357, SCC9, and SCC4 cells by serial centrifugation at the 10,000 × *g* (10k pellets) and 100,000 × *g* (100k pellets) speed were resuspended in 350 µl RNA lysis buffer followed by RNA extraction using the Exiqon miRCURY RNA isolation kit. 3 µl of each purified RNA sample was used for RNA quantification on an RNA 6000 Pico LabChip on an Agilent 2100 Bioanalyzer together with an RNA standard (1000 pg/µl) provided in the kit. The histograms showing the RNA distributions range from 25 to 4000 nucleotides with peaks indicating the abundance of RNA of this length on an electrophoresis gel. The X axis shows number of nucleotides (nt). The Y axis shows fluorescence units (FU). 28S and 18S ribosomal RNA were marked as green and magenta, respectively.

4.2.1.2 Small RNA sequencing revealing the RNA profiles in FNB6 and OSCC-EVs

RNA quantification by Bioanalyzer confirmed all EV RNA samples contained more than the minimum concentration needed for small RNA sequencing on an Ion Torrent Platform, carried out at the Clinical Research Facility, University of Edinburgh.

Total reads per sample from small RNA sequencing ranged from 1,185,001 (H357 100k) to 4,874,903 (FNB6 10k), with 100% alignment in all samples except for FNB6 10k (90.36%). The mean read lengths for EV-RNA samples varied from 24.2 to 33.9 nucleotides, suggesting the presence of small RNA in the EV samples (Table 4.1).

Across all EV samples, FNB6 10k pellet had the most RNA species detected and almost half (47.3%) were only identified in this sample (Figure 4.2A). Each OSCC cell line had ~2% uniquely present RNA found in their 10k EV pellets whilst only 124 (0.4%) RNAs were found in common in all three. 2889 (9.8%) small RNAs were found commonly present from all four cell lines (Figure 4.2A). Amongst all 100k samples, SCC4 100k EVs had most uniquely detected RNA species (17.9%). FNB6-100k EVs also had 14.5% of RNA that were not found in any other samples. 2.4% of RNA was found in common between OSCC-100k EVs. A similar amount and percentage (9.9%, 2192 RNAs) of small RNA was detected in 100k EV pellets from all four cell lines compared to those in 10k EVs (Figure 4.2B).

We then focused on the most abundant small RNAs detected from the EV samples and identifying potential enrichment of certain RNA species in OSCC-EVs when compared to FNB6-EVs. By listing the top 20 most enriched small RNAs in both groups, we found most of them (30-40%) were miRNAs (Figure 4.3). Other enriched RNA categories included lncRNA, YRNA and tRNA. Being consistent with the Venn diagrams (Figure 4.2), enrichment of RNA species in 10k and 100k pellets seemed to differ. For example, MIR205HG was the most abundant RNA identified in FNB6 100k pellet however it ranked the fourth in the top 20 RNAs in 10k EVs (Figure 4.3A). Another example was MT-RNR2, the mitochondrially encoded 16S RNA, ranked the third in OSCC-10k RNAs but was only the fourteenth among those in 100k EVs (Figure 4.3B). Six out of the top 20 most enriched small

RNA detected in OSCC-EVs were not present in the list from FNB6-EVs, including MIR30A, RNA5-8SP2, RNY4, MIR106B, VTRNA1-2, and MIR93 (Figure 4.3).

Table 4.1 RNA-seq summary for 10k and 100k EV pellets from FNB6, H357, SCC9, and SCC4 cells.

Sample	Total reads	Aligned reads	Percent aligned	Mean read length	Genes detected	Isoforms detected
FNB6 10k	4,874,903	4,404,946	90.36%	24.2	1,545	23,233
FNB6 100k	2,182,816	2,182,816	100.00%	24.7	416	19,485
H357 10k	1,464,308	1,464,308	100.00%	33.9	628	18.665
H357 100k	1,185,001	1,185,001	100.00%	25.3	340	19,305
SCC9 10k	1,762,647	1,762,647	100.00%	28	492	15,578
SCC9 100k	1,296,619	1,296,619	100.00%	24.4	299	15,578
SCC4 10k	2,333,905	2,333,905	100.00%	31.4	584	13,982
SCC4 100k	2,370,267	2,370,267	100.00%	27.6	701	22,013

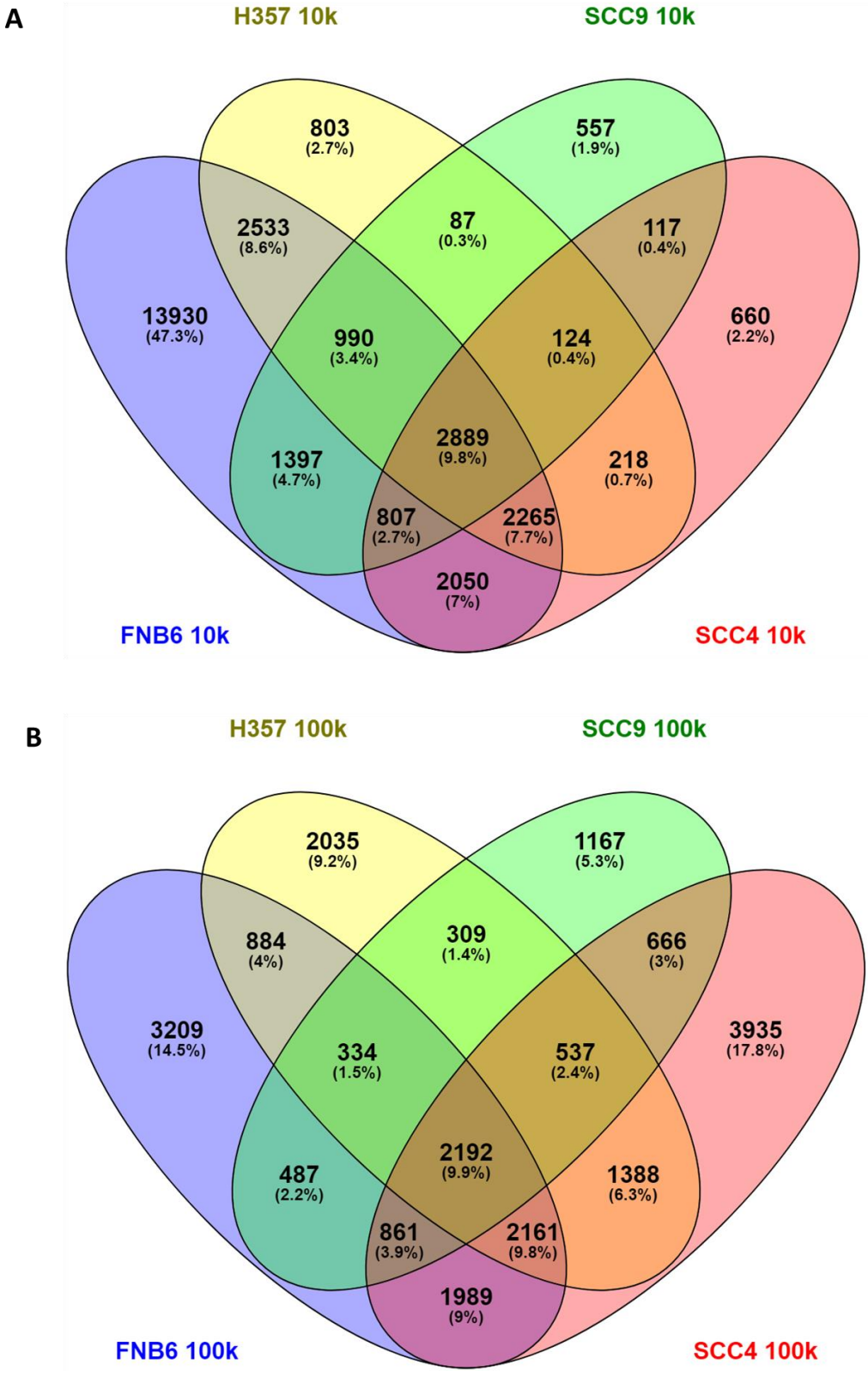

Figure 4.2 Venn diagrams of RNA species detected in FNB and OSCC-EVs.
A) Numbers of RNA species identified by small RNA sequencing from 10k EV pellets. **B)** Numbers of RNA species identified by small RNA sequencing from 100k EV pellets. Diagrams made with online program Venny 2.1 (*Oliveros, J.C. (2007-2015) Venny. An Interactive Tool for Comparing Lists with Venn's Diagrams. - References - Scientific Research Publishing*).

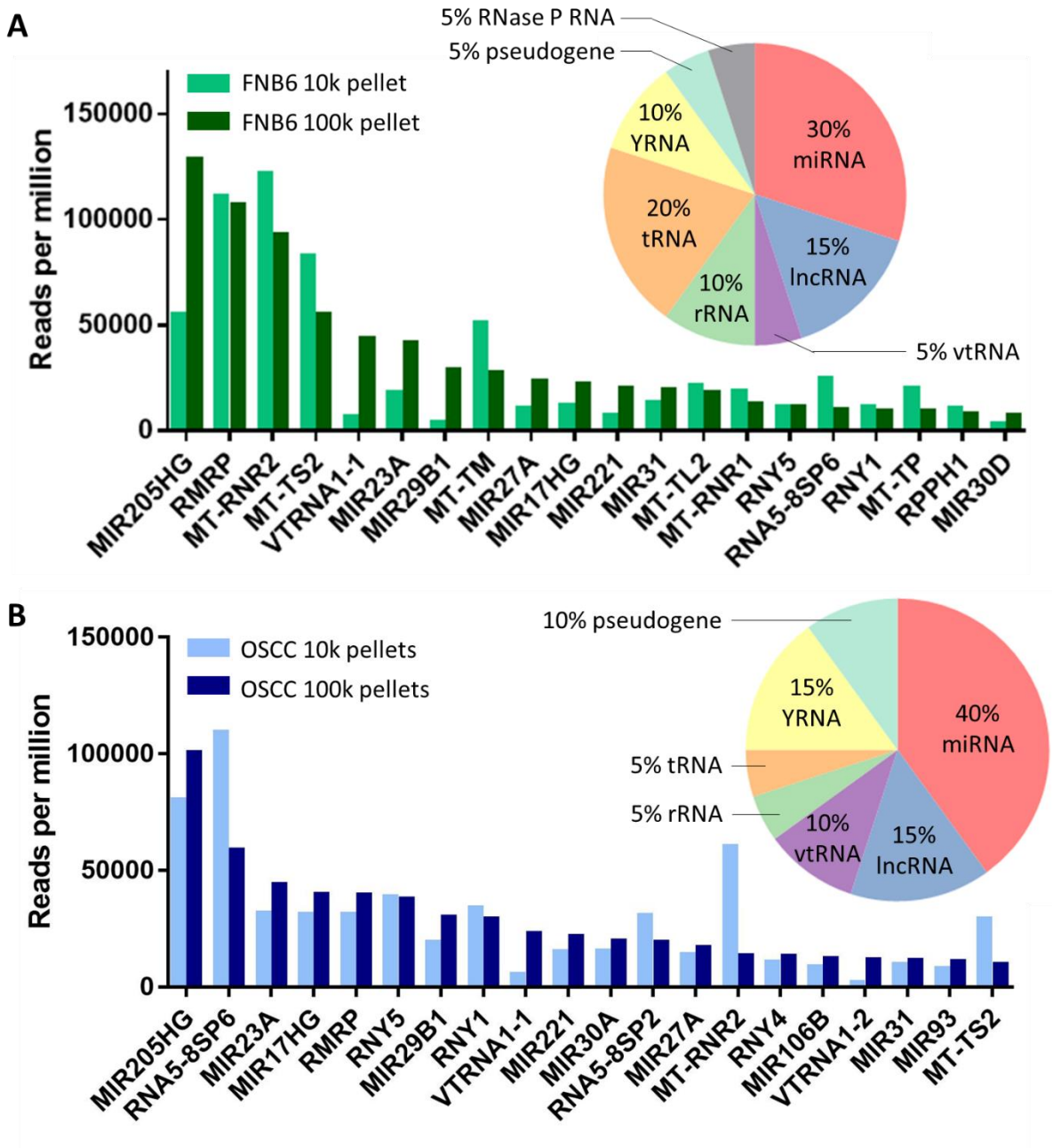

Figure 4.3 Top 20 most enriched small RNAs present in FNB6 and OSCC-EVs.
A) The top 20 small RNA species showed the most reads in FNB6-EV pellets detected by small RNA sequencing, sorted by abundance detected in FNB6 100k pellet. **B)** The top 20 small RNA species showed the most reads in OSCC-EV pellets in average detected by small RNA sequencing, sorted by abundance detected in 100k pellets. Pie charts indicate the percentage out of the top 20 in each RNA category.

4.2.1.3 Characterisation of vtRNA paralogs in FNB6 and OSCC-EVs

Noticeably, two vtRNA paralogs were identified in the top 20 most enriched small RNA from OSCC-EV pellets. As vault components are the primary focus of this study, the sequencing data related to all vtRNAs was taken forward for further analysis.

vtRNAs accounted for 2.2% of all RNA reads on average across the 8 samples tested, with 0.8% and 5.1% for 10k and 100k pellets, respectively, indicating a universal presence of vtRNA in EV pellets derived from the oral keratinocytes and OSCC cells tested in this study. Moreover, vtRNA 1-1 accounted for most of the vtRNA reads ranging from 1,000 to 40,000 reads per million (RPM), followed by vtRNA 1-2 and vtRNA 1-3. vtRNA 1-2 was mainly found in H357 and SCC4-derived EV pellets. On the contrary, vtRNA 2-1 and vtRNA 3-1P were only detected at very low levels (<200 RPM) in some samples (Figure 4.4A). Next, we looked at the cumulative abundance of vtRNAs in FNB6 and OSCC EV samples: All 100k pellets showed higher abundance of vtRNAs than 10k pellets from the same cell line; 100k EV pellet from SCC4 has the highest vtRNA reads, which mainly composed of vtRNA 1-1, vtRNA1-2 and a small amount of vtRNA 1-3; and SCC9 cells contained the least amount of vtRNAs in 10k and 100k EVs (Figure 4.4B).

Furthermore, all individual vtRNAs were enriched in 100k EV pellets. Small EVs derived from FNB6 cells contained the highest level of vtRNA 1-1, followed by SCC4, H357, and SCC9 (Figure 4.4C). This data showed a similar pattern that was observed in cellular expression of vtRNA 1-1 (Figure 3.1D). No vtRNA 1-2 was found in 10k pellets from FNB6 with only a very low amount found in 100k pellet, which also mirrors the cellular expression of vtRNA 1-2 in FNB6 cells where no expression was detected (Figure 3.1E). Moreover, the 100k EV pellet from SCC4 was found to be the most abundant for vtRNA 1-2 and 1-3. In comparison, SCC9 samples contained the least vtRNA among OSCC cell lines (Figure 4.4C, D, E). No vtRNA 2-1 was found in OSCC-EV pellets with only low amount detected in FNB6 samples (Figure 4.4F). Overall, vtRNA 3-1P showed very low reads across all EV samples (Figure 4.4G).

Next, the abundance of vtRNAs detected by small RNA sequencing was validated by qPCR using commercially available TaqMan primers targeting vtRNA 1-1, vtRNA 1-2, vtRNA 1-3 and vtRNA 2-1. Due to the lack of widely accepted internal controls for EV-RNA quantification, the small RNA sequencing data was firstly analysed to select potential reference RNA candidates. After excluding the low-abundance (<1,000 RPM) RNA species, three miRNAs (miR-23a-3p, miR-30d-5p, miR-31-5p) were selected due to their high abundance and relatively stable levels across all EV samples (Table 4.2).

Total RNA was extracted from the 2k, 10k and 100k EV pellets and CL from all four cell lines. RNA was reverse transcribed using random primers (for vtRNA quantification) and specific miRNA primers (for miRNA quantification) ready for qPCR analysis. The abundance of selected miRNAs in CL and EV pellets was determined by qPCR using TaqMan primers specific to the miRNA. Ct values of three miRNAs detected from individual biological repeats were plotted and most of them fell into the range between 20-30, indicating adequate expression across the samples to attempt normalisation (Figure 4.5A-D). Apart from SCC4, miRNA-30d-5p had the lowest expression (highest Ct values) in CL and EV samples from all other cell lines, mirroring the read counts from RNA sequencing (Figure 4.5A-D, Table 4.2). The Ct values for each miRNA detected CL samples were consistent amongst biological repeats. However, there was variation between the repeats where RNA was extracted from EV pellets, which may be due to the inaccuracy of RNA quantification for these samples. An average Ct value of the three reference miRNA was used for vtRNA normalisation.

As a result, the relative vtRNA abundance in 10k and 100k EV pellets were very similar to the pattern observed in small RNA sequencing, showing dominant enrichment of vtRNA 1-1 in all samples followed by vtRNA 1-3 (Figure 4.5E). Similar to the pattern in Figure 4.4A, vtRNA 1-2 was only detected in H357 and SCC4 EV pellets, whilst vtRNA 2-1 was only seen in FNB6 samples (Figure 4.5E). The accumulative plot of vtRNA abundance detected by qPCR against cell line origin also resembled the pattern shown in Figure 4.4B, in which 100k EVs had higher abundance of vtRNA overall and in particular the highest abundance was seen in FNB6 100k and SCC4 100k pellets (Figure 4.5F).

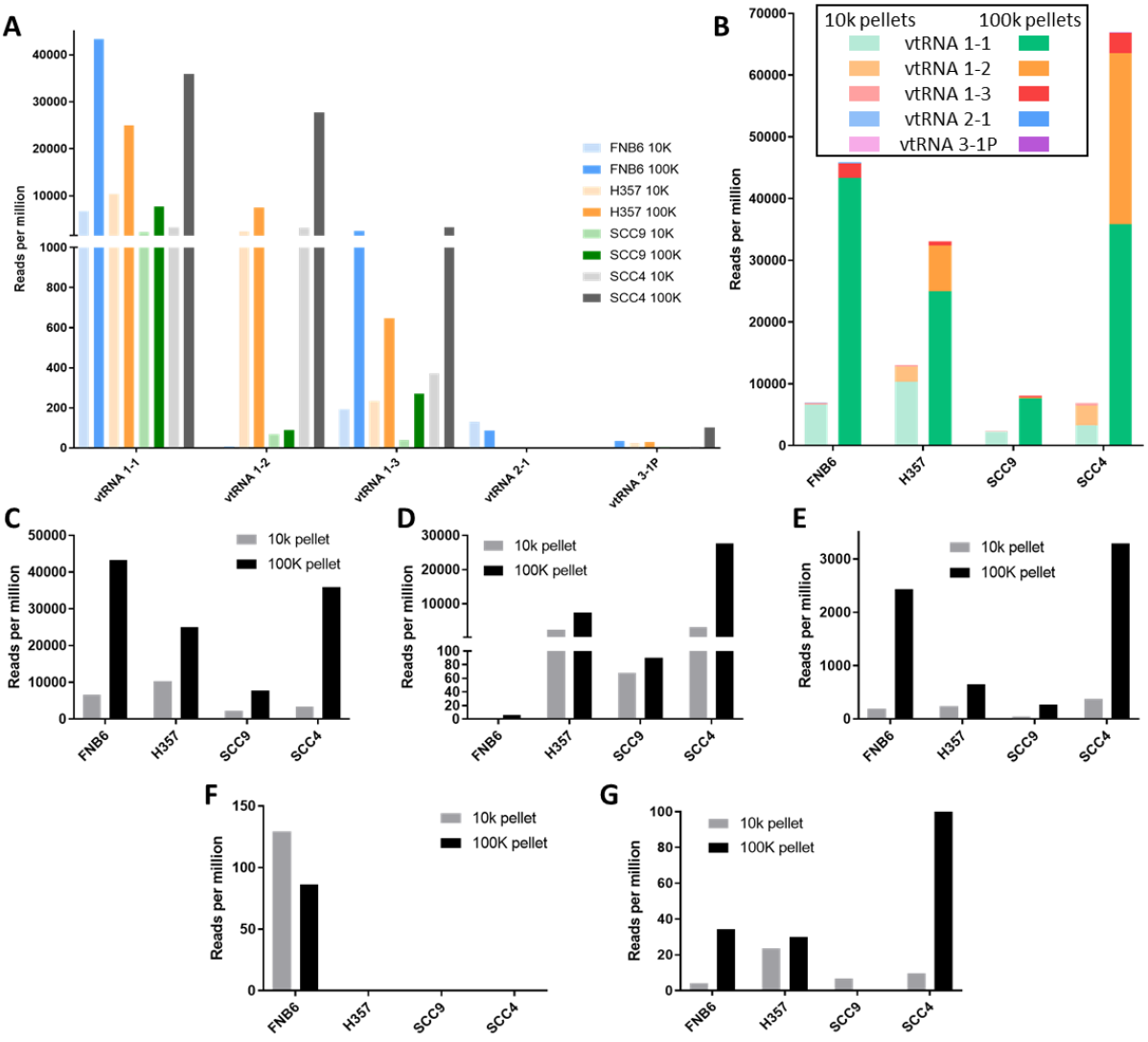

Figure 4.4 Analysis of small RNA sequencing for vault RNAs in 10k and 100k EV pellets from FNB6 and OSCC cells.
The RNA-seq data for vault RNAs was normalized by the total reads for each sample and plotted as reads per million against **A)** vault RNA subtypes and **B)** cell line origin. The reads for **C)** vtRNA 1-1, **D)** vtRNA 1-2, **E)** vtRNA 1-3, **F)** vtRNA 2-1, and **G)** vtRNA 3-1P in 10k (shown in grey) and 100k (shown in black) pellets from these 4 cell lines were also normalized by total RNA reads and shown as reads per million.

Table 4.2 Abundance (RPM) of selected miRNAs in all EV-pellets.

Gene	FNB6 10k	FNB6 100k	H357 10k	H357 100k	SCC9 10k	SCC9 100k	SCC4 10k	SCC4 100k
MIR23A	17698.69	41330.054	26493.943	32771.381	40410.48	70311.56	27787.256	28779.757
MIR30D	3376.847	7475.379	5885.797	6094.906	6124.65	11232.407	6378.303	9109.665
MIR31	13572.128	19461.267	11186.157	10523.471	14345.11	18961.265	3712.921	4732.252

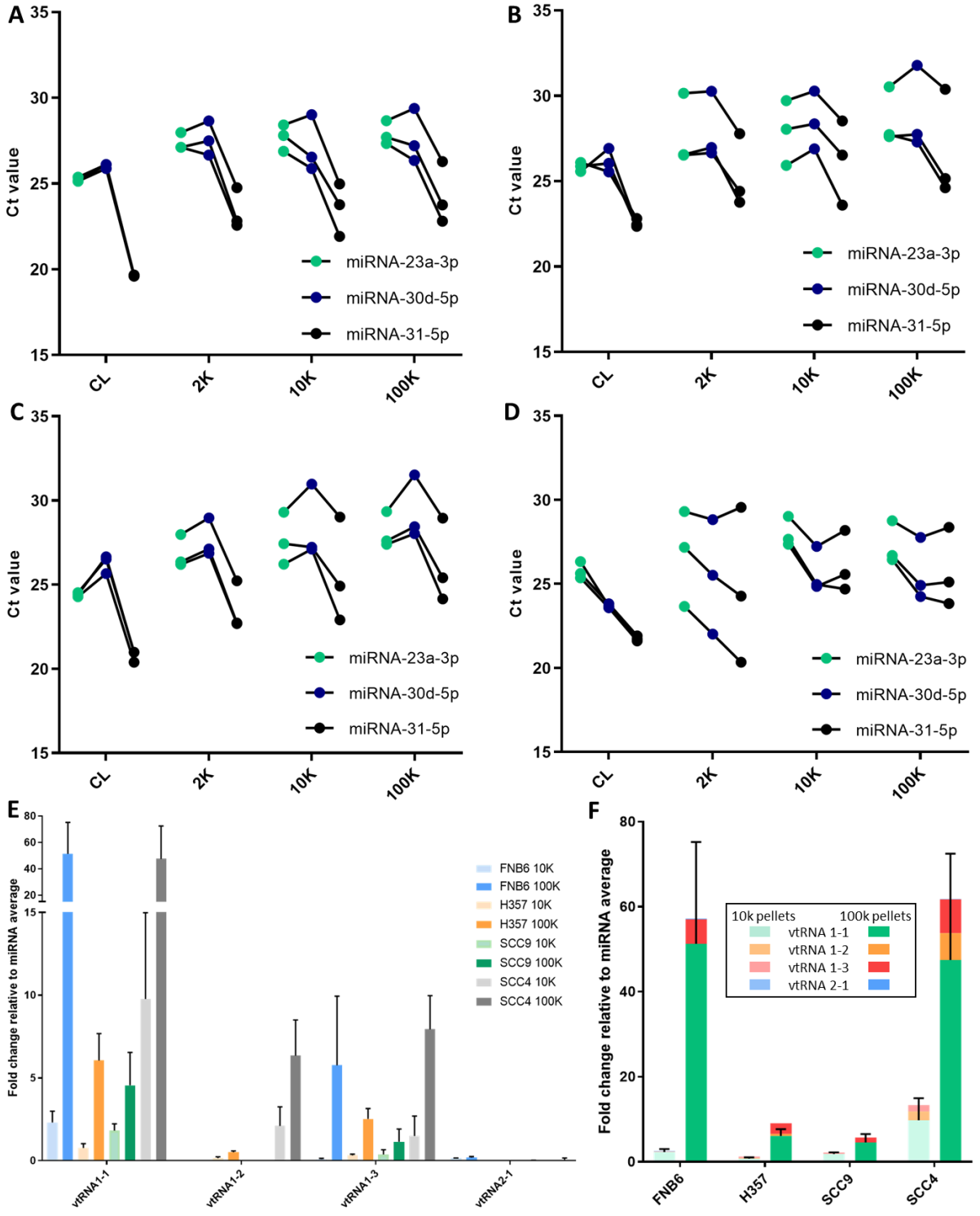

Figure 4.5 qPCR validation of vtRNA and miRNA abundance in EVs.
Ct value of miRNA from **A)** FNB6, **B)** H357, **C)** SCC9, and **D)** SCC4 were plotted. Individual dot indicates one sample, dots connected by lines were from the same biological repeats. CL: Cell lysate. Data are means ± SD, n=3. **E)** qPCR validation of normalised vtRNA abundance in 10k and 100k EV pellets. Average expression of three miRNA (miR-23a-3p, miR-30d-5p, and miR-31-5p) were used as internal control for EV-RNAs. Data are means ± SD, n=3. **F)** Accumulative vtRNA abundance determined by qPCR plotted cell line origin. Data shown are means ± SD, n=3, error bars indicate SD for vtRNA 1-1.

4.2.2 Investigating vtRNA fragments in OSCC-EVs

4.2.2.1 Enrichment of vtRNA fragments detected by small RNA sequencing

In addition to the full-length vtRNAs, small RNA sequencing detected 5' and 3' vtRNA end fragments in OSCC-EV pellets. Read coverage of full-length vtRNA and fragments from SCC4 10k and 100k pellets are presented here as representative samples due to highest levels of vtRNAs were detected from this cell line (Figure 4.6). Overall, 5' fragments (32 nt) were longer than 3' fragments (25-26 nt) and 3' fragments of vtRNA 1-1 and vtRNA 1-2 were more enriched than 5' fragments in SCC4-EV pellets (Figure 4.6A, B). Whilst the read coverage and sequence of fragments of vtRNA 1-1 and 1-2 were almost identical, fragments from vtRNA 1-3 showed a different pattern to the other paralogs: More 5' fragments (34 nt) of vtRNA 1-3 were observed than 3' end ones (19 nt), with 3' end fragments being shorter than those seen in vtRNA 1-1 and 1-2 (Figure 4.6C).

Looking across the reads mapped to vtRNA 1-1 from all EV pellets derived from four cell lines, the 3' end fragments appeared to be more abundant, especially those from H357 and SCC9 cell lines, despite SCC9-EVs had the least vtRNA 1-1 reads (Figure 4.7). The identified vtRNA 1-1 fragment reads were of very similar lengths and locations when mapped to the full-length vtRNA from different cell lines, suggesting the presence of vtRNA fragments of specific sequences is common in EV samples from OSCC cells and normal oral keratinocytes included in this study (Figure 4.7).

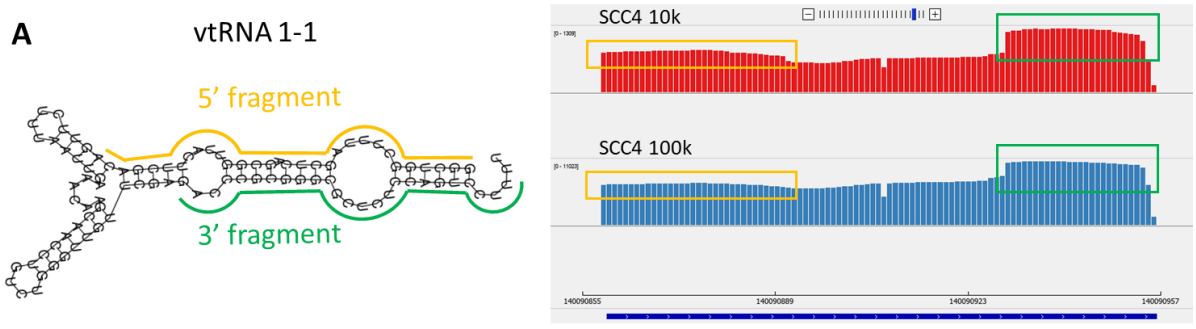

5' fragment sequence: GGGCTGGCTTTAGCTCAGCGGTTACTTCGACA
3' fragment sequence: GACCCGCGGGCGCTCTCCAGTCCTT

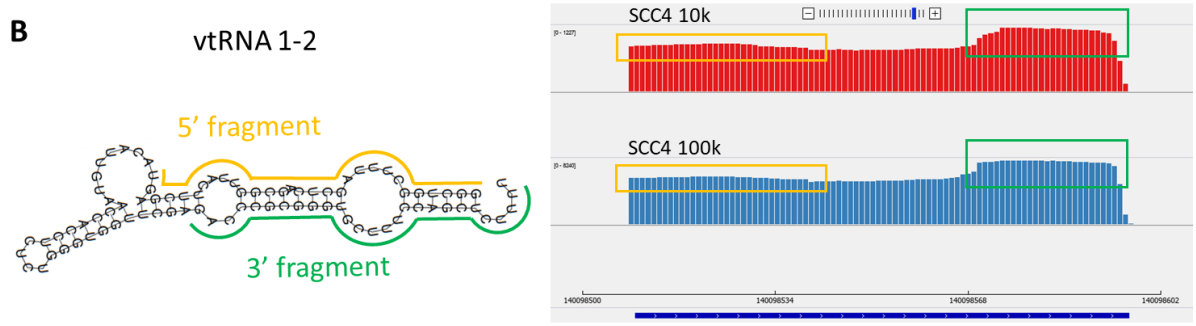

5' fragment sequence: GGGCTGGCTTTAGCTCAGCGGTTACTTCGAGT
3' fragment sequence: GACCCGCGGGTGCTTTCCAGCTCTTT

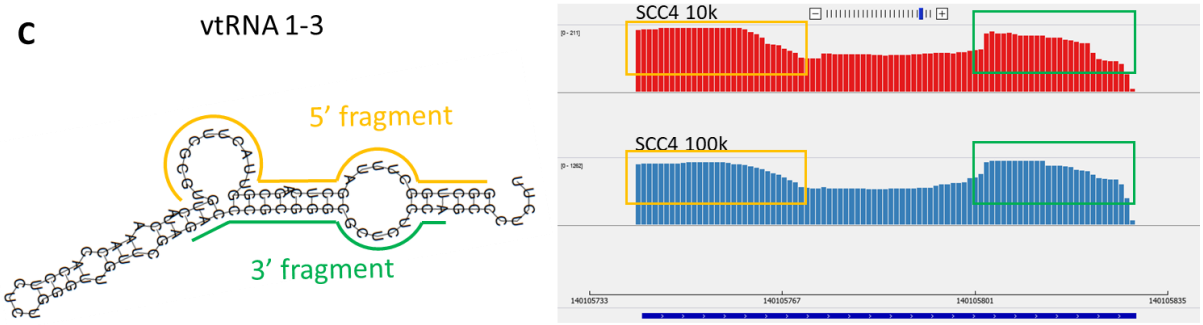

5' fragment sequence: GGGCTGGCTTTAGCTCAGCGGTTACTTCGCGTGT
3' fragment sequence: GACCCGCGGGCGCTCTCCA

Figure 4.6 Enrichment of vault RNA fragments in OSCC-EV pellets.
Presence of small vault RNA fragments generated from 3' and 5' ends as well as full-length **A)** vtRNA 1-1, **B)** vtRNA 1-2, and **C)** vtRNA 1-3 from SCC4 10k and 100k EV samples. Read coverage graphs were generated using raw reads in Integrative Genomics Viewer (IGV) software (Thorvaldsdóttir, Robinson and Mesirov, 2013). Secondary structure and sequence illustration were generated by online RNAfold server (Gruber *et al.*, 2008). Yellow and green boxes indicate 5' and 3' fragments, respectively.

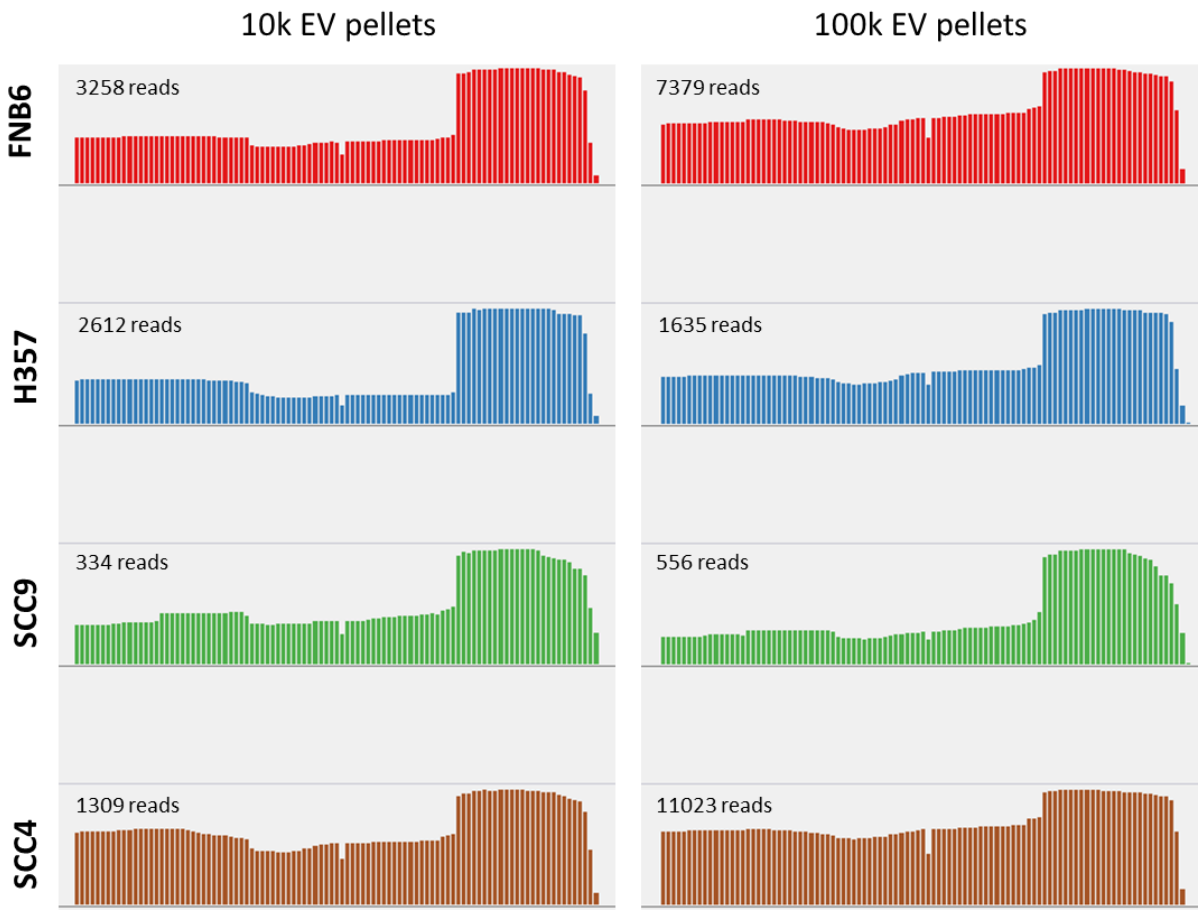

Figure 4.7 vtRNA 1-1 read mapping from 10k and 100k EV pellets across the cell panel.
Reads from small RNA sequencing from all EV pellets from four cell lines were mapped to the vtRNA 1-1 sequence. Sashimi plots were obtained from the IGV 2.8.6 software (Thorvaldsdóttir, Robinson and Mesirov, 2013).

4.2.2.2 Attempt to validate vtRNA fragment abundance by northern blot

Next, we aimed to validate the enrichment of vtRNA fragments observed from small RNA sequencing by another technique. Standard qPCR validation cannot be applied because TaqMan primer/probes and SYBR primers are unsuitable to detect vtRNA fragments (due to their small size). Stem-loop RT primers (traditionally used for miRNA qPCR) would also be unsuitable because they would not be specific for the fragments only (leading to detection of full length vtRNA). Therefore, we designed probes targeting the 3' and 5' end of the vtRNA paralogs. Binding of the probes to full length vtRNA and fragments could then be resolved by northern blot.

A probe complimentary to the 5' fragments (a common sequence found in vtRNA 1-1, 1-2, and 1-3) was designed to detect all the 5' fragments and full-length vtRNAs. Similarly, a 3' fragment probe

was designed to also target a shared sequence between vtRNA 1-1 and 1-3. A probe complimentary to miR-23a-3p (a miRNA found to be abundant in EV pellets and used as qPCR quantification reference) was also designed and used as control for northern blot (Figure 2.3B).

We firstly attempted to detect the 3' fragments due to their higher abundance observed from RNA sequencing (Figure 4.6A). PAGE successfully separated the size markers and small RNAs in samples with 5S and 5.8S ribosomal RNA identifiable in cellular RNA samples (Figure 4.8A). Although some RNA remained unseparated and was observed at the top of the gel due to larger size. Following Northern blot, we observed bands for full-length vtRNA (~100 nt) in all cellular RNA lanes and in FNB6 10k, 100k, SCC4 100k EV-RNA lanes. However, no bands corresponding to 3' vtRNA fragments were observed (Figure 4.8B). We then attempted to blot for miR-23a-3p, which was also not detected in EV-RNA by northern blot (data not shown). Although 5' fragments were not probed in this experiment, they would be unlikely to be detected by northern blot due to their even lower abundance in our samples than the 3' fragments (Figure 4.7). Further optimisation of the northern blotting protocol was needed; however, this was delayed due to the lab shutdown during the Covid-19 pandemic.

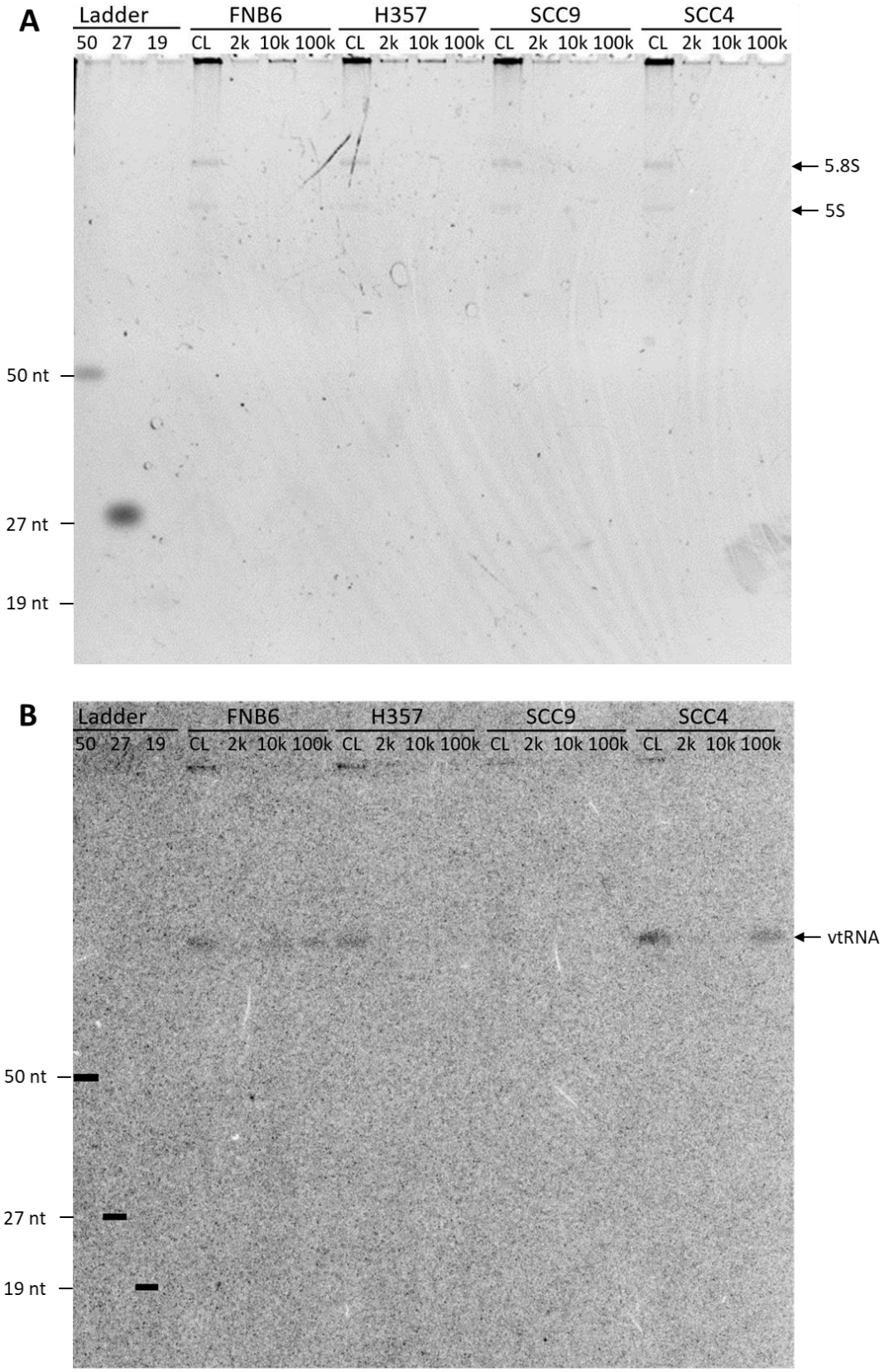

Figure 4.8 Gel image following PAGE and northern blot for vtRNA fragments detection.
A) Ethidium bromide-stained polyacrylamide gel showing RNA separation. 100 ng total cellular or EV RNA was loaded into each well, arrows indicate 5S (120 nt) and 5.8S (150 nt) ribosomal RNA. DNA oligos with known size (50 nt, 27 nt, and 19 nt) were loaded as markers. **B)** Northern blot showing full-length vtRNA detected at ~100 nt following 3 days exposure to a screen.

4.2.3 Establishing vtRNA-Broccoli expressing OSCC cell lines

Since we were not able to visualise the abundance of vtRNA fragments in EV by northern blot, we next attempted to establish OSCC cell lines expressing vtRNA fused with an RNA aptamer "Broccoli" tag. The RNA aptamer was firstly developed by Filonov *et al*. to be appended to RNA molecules and resemble the GFP fluorophore in live cells (Filonov *et al.*, 2014). The dimeric Broccoli (dBroccoli) tag used in this study is composed of two Broccoli units in one stem-loop with the total length of 92 nt and an F30 scaffold that enhances the performance of the dBroccoli. Upon the correct folding of the tag and the scaffold, the inactive substrate DFHBI-1T can bind to the secondary structure and exhibit GFP-like green fluorescence (Figure 2.5) (Filonov *et al.*, 2014, 2015). This novel technique has enabled the visualisation and imaging of single RNA molecules in live cells. Our experimental design was to tag the 3' end of the full length vtRNA 1-1 with the dBroccoli aptamer, upon successful cell transfection and fusion gene expression, it would allow us to determine the cellular localisation and dynamic trafficking of vtRNA and its 3' end fragments by live cell imaging. As vtRNA and vtRNA fragments were found abundant in EV pellets, the establishment of vtRNA 1-1-Broccoli expressing cells would also help us gain a better understanding of the RNA cargo sorting into EVs as well as the EV-mediated intercellular exchange of such molecules.

4.2.3.1 Establishment of vtRNA 1-1-Broccoli constructs

To establish the constructs used for transfection, pAV U6+27 plasmid was used as the transfection vector for the foreign inserts (Good *et al.*, 1997). This plasmid was chosen due to the presence of the RNA polymerase III driven U6 promoter (vtRNAs are transcribed by RNA polymerase III). Sequences encoding vtRNA 1-1 and vtRNA 1-1-F30-2× Broccoli (that were purchased in a pMA GeneArt holding vector, Life Technologies) were inserted between the SalI and XbaI restriction sites of pAV U6+27, resulting in the pAV U6+27-vtRNA 1-1 construct and the pAV U6+27-vtRNA 1-1-F30-2× Broccoli construct, respectively (Figure 4.9, 4.10). To provide positive control for the green fluorescence generated by the aptamer, the pAVU6+27-F30-2×dBroccoli plasmid (Filonov *et al.*, 2015), and a GFP expressing plasmid (pcDNA3.1(+)IRES GFP-FLAG-Tag CRTC1-MAML2, a kind gift from Dr Esra Amoura) were also included in the transfection experiments (Figure 4.10).

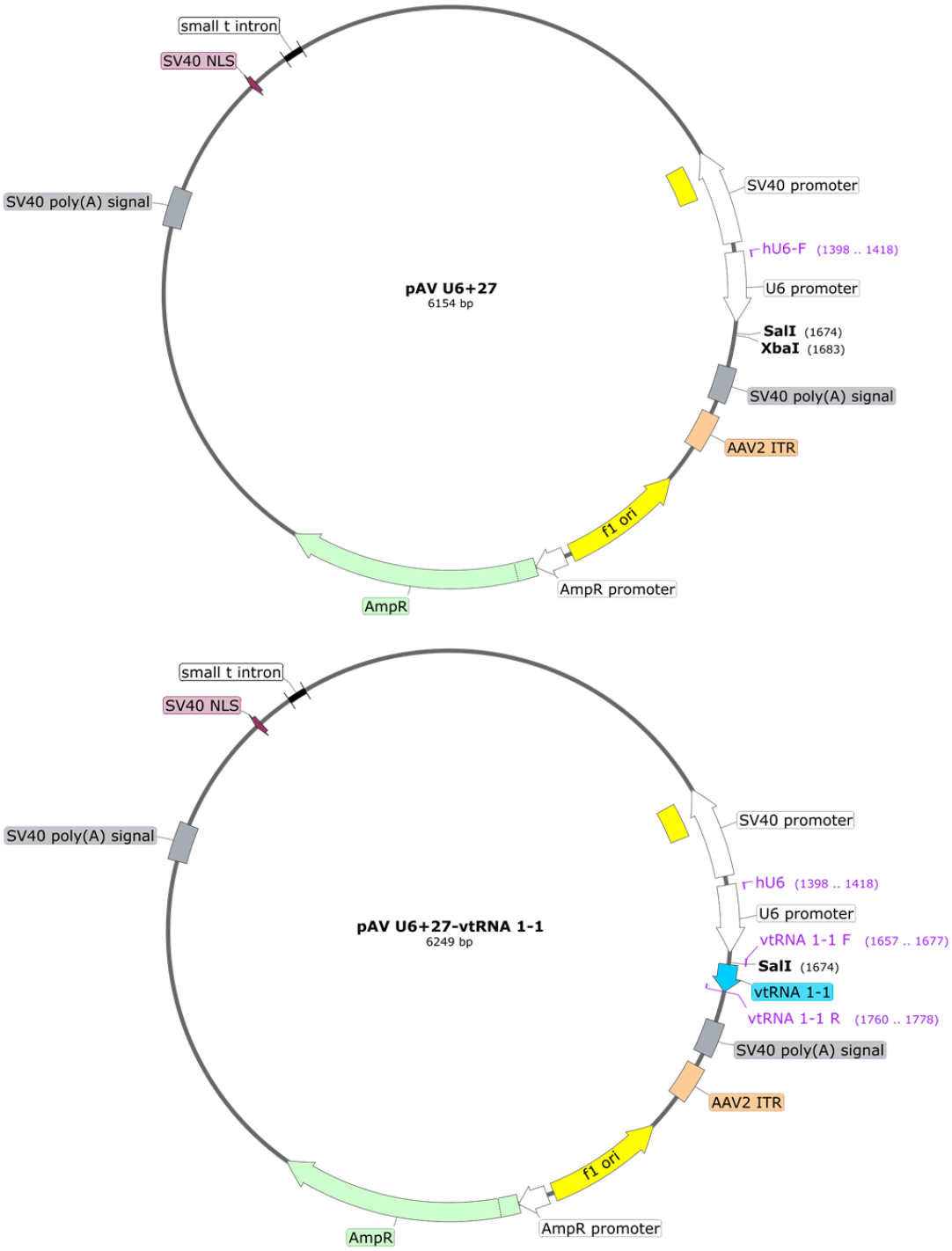

Figure 4.9 DNA maps of plasmids (1).
Diagrams showing DNA map of the plasmids used for mammalian cell transfection experiments. pAV U6+27 vector was purchased from Addgene (#25709), sequences encoding vtRNA 1-1 were inserted between the SalI and XbaI sites, resulting in the pAV U6+27-vtRNA 1-1 plasmid.

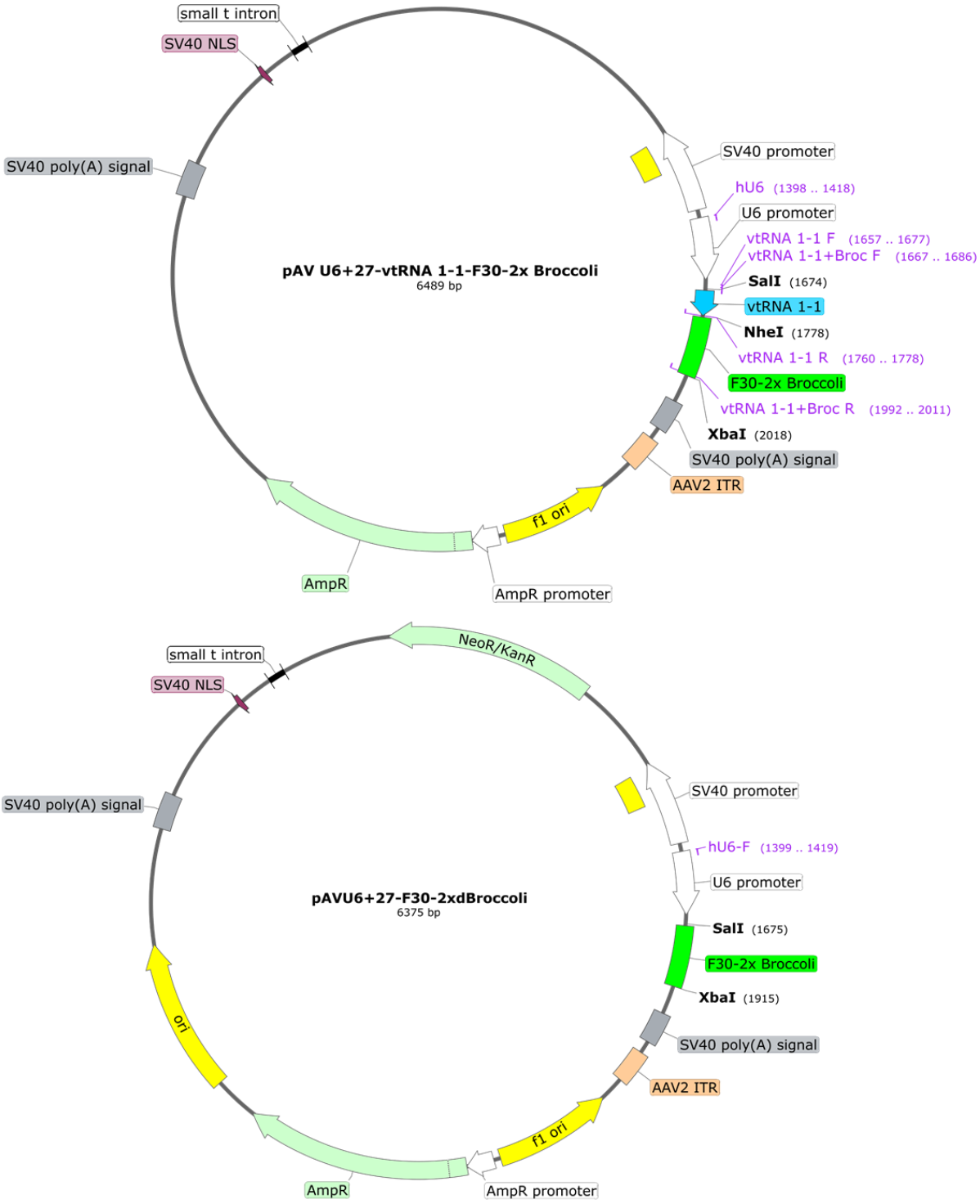

Figure 4.10 DNA maps of plasmids (2).
Diagrams showing DNA map of the plasmids used for mammalian cell transfection experiments. pAV U6+27 vector was purchased from Addgene (#25709), sequences encoding vtRNA 1-1-Broccoli were inserted between the SalI and XbaI sites, resulting in the pAV U6+27-vtRNA 1-1-F30-2x Broccoli plasmid. pAVU6+27-F30-2xdBroccoli was also purchased from Addgene (#66842) and included as a tag-only positive control.

4.2.3.2 Assessment of transient transfection efficiency

The construct expression in pooled cells was firstly confirmed 48 h post transfection by PCR using primers targeting vtRNA 1-1 and vtRNA 1-1-Broccoli sequences. The ~100 bp vtRNA 1-1 bands were observed in pAV U6+27-vtRNA 1-1 plasmid, gDNA and cDNA from H357 cells transfected with the pAV U6+27-vtRNA 1-1 plasmid, whereas no specific amplification was found in gDNA and cDNA from H357 control cells (transfected with transfection reagent only, no foreign DNA). Similarly, vtRNA 1-1-Broccoli bands (~300 bp) were only detected in pAV U6+27-vtRNA 1-1-F30-2× Broccoli plasmid lane, gDNA and cDNA from transfected H357 with the pAV U6+27-vtRNA 1-1-F30-2× Broccoli plasmid, but not from the control H357 cells (Figure 4.11A).

In the pAV U6+27 plasmid constructs, the vtRNA 1-1 and vtRNA 1-1-Broccoli sequences were inserted after the human U6 (hU6) promoter (Figure 4.9, 4.10), which is a strong type III RNA polymerase III promoter in most cells (Nie *et al.*, 2010). Therefore, the cellular expression of vtRNA 1-1 in transfected cells was determined at 24 h and 48 h post transfection by qPCR using TaqMan (Figure 4.11B) and SYBR primers (Figure 4.11C). Compared to the transfection controls, both cell lines transfected with pAV U6+27-vtRNA 1-1 and pAV U6+27-vtRNA 1-1-F30-2× Broccoli had higher vtRNA 1-1 expression at both time points (Figure 4.11B, C). In H357, cells harvested at 48 h post transfection showed better transfection efficiency as the fold changes of vtRNA 1-1 expression almost doubled from those at 24 h post transfection. Between the two plasmids, pAV U6+27-vtRNA 1-1 caused higher overexpression of vtRNA 1-1 in the transfected H357 cells at each time point. SCC4 cells also showed ~20-fold overexpression of vtRNA 1-1 when transfected with both plasmids however varied results were seen when detecting with different types of qPCR primers. TaqMan primer detected a 50-fold increase of vtRNA 1-1 expression in SCC4 transfected with pAV U6+27-vtRNA 1-1-F30-2× Broccoli plasmid at 24 h post transfection, whilst SYBR green primers suggested a 40-fold overexpression at 48 h transfected with pAV U6+27-vtRNA 1-1 plasmid (Figure 4.11B, C). Overall, transient transfection with plasmids encoding vtRNA 1-1 with or without the dBroccoli tag led to the overexpression of vtRNA 1-1 in OSCC cells at 24 h and 48 h post transfection, in addition, the time point at 48 h post transfection may provide a better transfection efficiency.

Next, we moved onto determining whether green fluorescence can be generated by dBroccoli tag binding to the DFHBI-1T in live cells. Following Filonov and Jaffrey's protocol, cells transfected with all five plasmids were harvested at 48 h post transfection and 40 µM DFHBI-1T was added to the cells followed by flow cytometry analysis (Filonov and Jaffrey, 2016). As expected, no green fluorescence was observed from cells transfected with empty vector (pAV U6+27 plasmid) and plasmid with vtRNA 1-1 insert (pAV U6+27-vtRNA 1-1 plasmid). However, we also failed to detect fluorescence in cells transfected with Broccoli-tagged vtRNA 1-1 (pAV U6+27-vtRNA 1-1-F30-2× Broccoli plasmid). In addition, only ~1% H357 and ~5% SCC4 cells transfected with Broccoli-only positive control plasmid (pAVU6+27-F30-2×dBroccoli plasmid) were detected in the FITC channel, whilst cells transfected with GFP positive control plasmid (pcDNA3.1(+)IRES GFP-FLAG-Tag CRTC1-MAML2 plasmid) have shown 10-20% positive rates out of all single cell events detected (Figure 4.12).

The transient transfection experiments suggested transfection with the vtRNA 1-1 and vtRNA 1-1-Broccoli constructs can cause overexpression of vtRNA 1-1 for up to 48 h post transfection. Although the vtRNA 1-1-Broccoli fusion transcripts were detected at gDNA and cDNA levels, we failed to detect any green fluorescence generated by the Broccoli tag from the fusion RNA products in live cells.

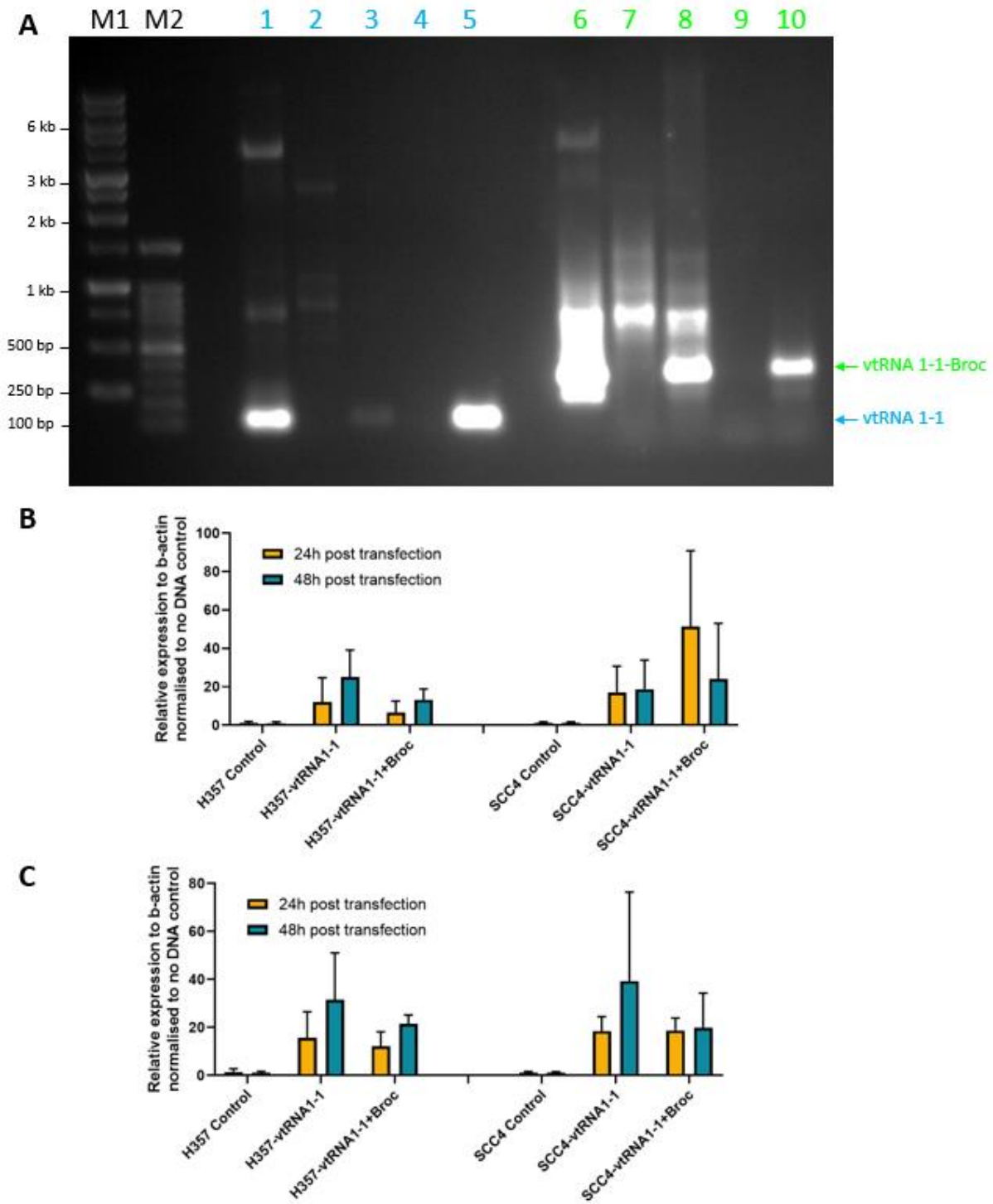

Figure 4.11 Transient transfection efficiency of the vtRNA/vtRNA-Broccoli constructs.
A) 2% (w/v) agarose gel electrophoresis was used to confirm the presence of vtRNA1-1 (in blue lanes)/vtRNA1-1-Broccoli (in green lanes) sequence in transfection plasmids, gDNA, and reverse-transcripted cDNA derived from transfected H357 cells. Lane M1 and M2: GeneRuler 1 kb and 100 bp DNA ladders (Thermo Fisher Scientific), respectively; lane 1: pAV U6+27-vtRNA 1-1 plasmid; lane 2: gDNA from H357 control cells; lane 3: gDNA from H357 cells transfected with pAV U6+27-vtRNA 1-1 plasmid; lane 4 and 5: cDNA synthesised using RNA extracted from H357 cells used for lane 2 and 3, respectively; lane 6: pAV U6+27-vtRNA 1-1-F30-2x dBroccoli plasmid; lane 7: gDNA from H357 control cells; lane 8: gDNA from H357 cells transfected with pAV U6+27-vtRNA 1-1-F30-2x dBroccoli plasmid; lane 9 and 10: cDNA synthesised using RNA extracted from H357 cells used for lane 7 and 8, respectively. Primers used were described in Table 2.6. Expression levels of vtRNA 1-1 in transfected H357 and SCC4 cells relative to control cells at 24 h and 48 h post transfection detected by qPCR using **B)** TaqMan and **C)** SYBR primers. Primer details are listed in Table 2.10 and 2.11.

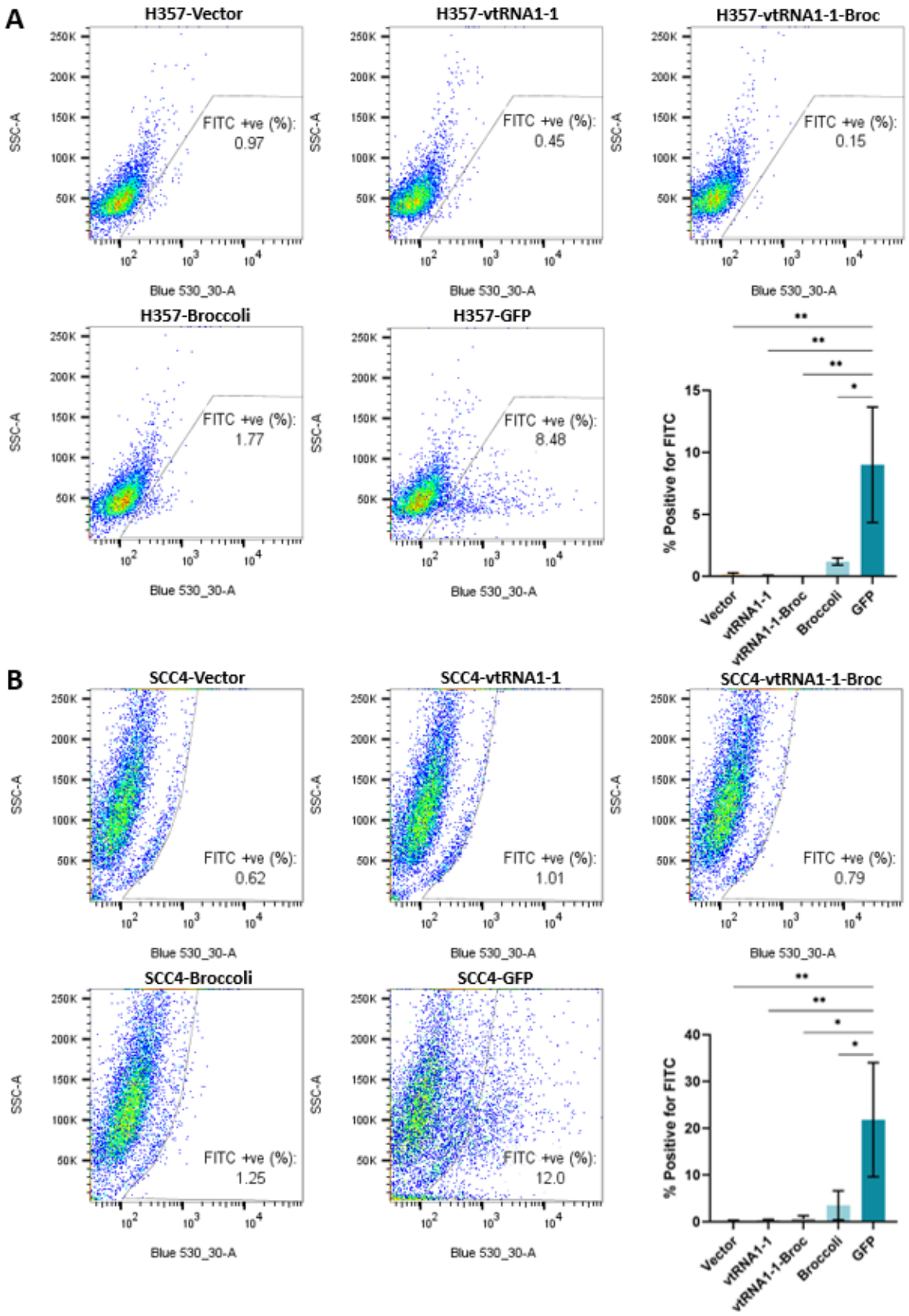

Figure 4.12 Assessment of the vtRNA-Broccoli constructs expression efficiency by flow cytometry. FACS analysis of **A)** H357 and **B)** SCC4 cells transfected with plasmids described in Figure 4.9, 4.10 as well as the pcDNA3.1(+)IRES GFP-FLAG-Tag CRTC1-MAML2 plasmid described in Table 2.5 as a positive control for green fluorescence. Quantification shows the percentage of FITC-positive cells detected by flow cytometry 48 h post transfection. Data shown are means ± SD, n=3 except for Broccoli groups n=2. *$p < 0.05$, **$p < 0.01$ by one-way ANOVA with Tukey's tests.

4.2.3.3 Selection and assessment of stably transfected clones

Although the Broccoli-tagged vtRNA 1-1 did not exhibit fluorescence when assayed by flow cytometry, we still decided to select stably transfected OSCC cell clones and expand into cell lines. As they seemed to express increased level of vtRNA 1-1 compared to the wild type cells, the vtRNA 1-1 overexpressing lines could be established as a tool for further investigation into the molecular function of the cellular and EV-vtRNA in OSCC.

To select cell clones with the foreign sequences incorporated into the genome, a kill curve of the selection antibiotic G418 was firstly established to determine the optimal working concentration to kill all the wild type cells after 10 days for each cell type. Cells were seeded in 96-well plates and maintained for 10 days whilst a range of G418 concentration was added to each well (0-500 µg/ml for H357 and 0-300 µg/ml for SCC4, Figure 2.4). After 10 days, an MTT assay was performed to determine the percentage of viable cells in each well (Figure 4.13A, B). H357 cells showed no viable cells after ten days at 450 µg/ml (Figure 4.13A). SCC4 cells were more sensitive to G418 treatment and all cells were killed at 200 µg/ml after ten days (Figure 4.13B).

48 h post transfected cells were serially diluted and seeded in 96-well plates at approximately 1 cell per well. Cells were closely monitored and maintained in antibiotic-free growth medium for up to a week. Growth medium containing G418 (concentration used for each cell type was empirically determined) was added to the wells and replaced every 3-5 days until single cells expanded into colonies. Unfortunately, transfected SCC4 cells did not survive the selection process.

Eventually, we obtained 4 stably transfected H357 cell lines following single clone selection (two for vtRNA 1-1 and two for vtRNA 1-1-Broccoli). gDNA was extracted from all 4 cell lines which were then amplified with primers targeting either vtRNA 1-1 or vtRNA 1-1-Broccoli fusion sequences. The specific vtRNA 1-1 was detected in both vtRNA 1-1-expressing stable lines whilst vtRNA 1-1-Broccoli was only seen in stable line #4, using the bands observed in lanes loaded with plasmid DNA as size references (Figure 4.13C). We then tested the amount of vtRNA 1-1 transcripts in the stably transfected cell lines by qPCR. All four cell lines showed similar level of vtRNA 1-1 transcripts when

compared to that in the transfection control cells (no foreign DNA transfected), apart from vtRNA 1-1-Broccoli-expressing stable line #4 showed ~3-fold increase when tested using SYBR Green primers (Figure 4.13D).

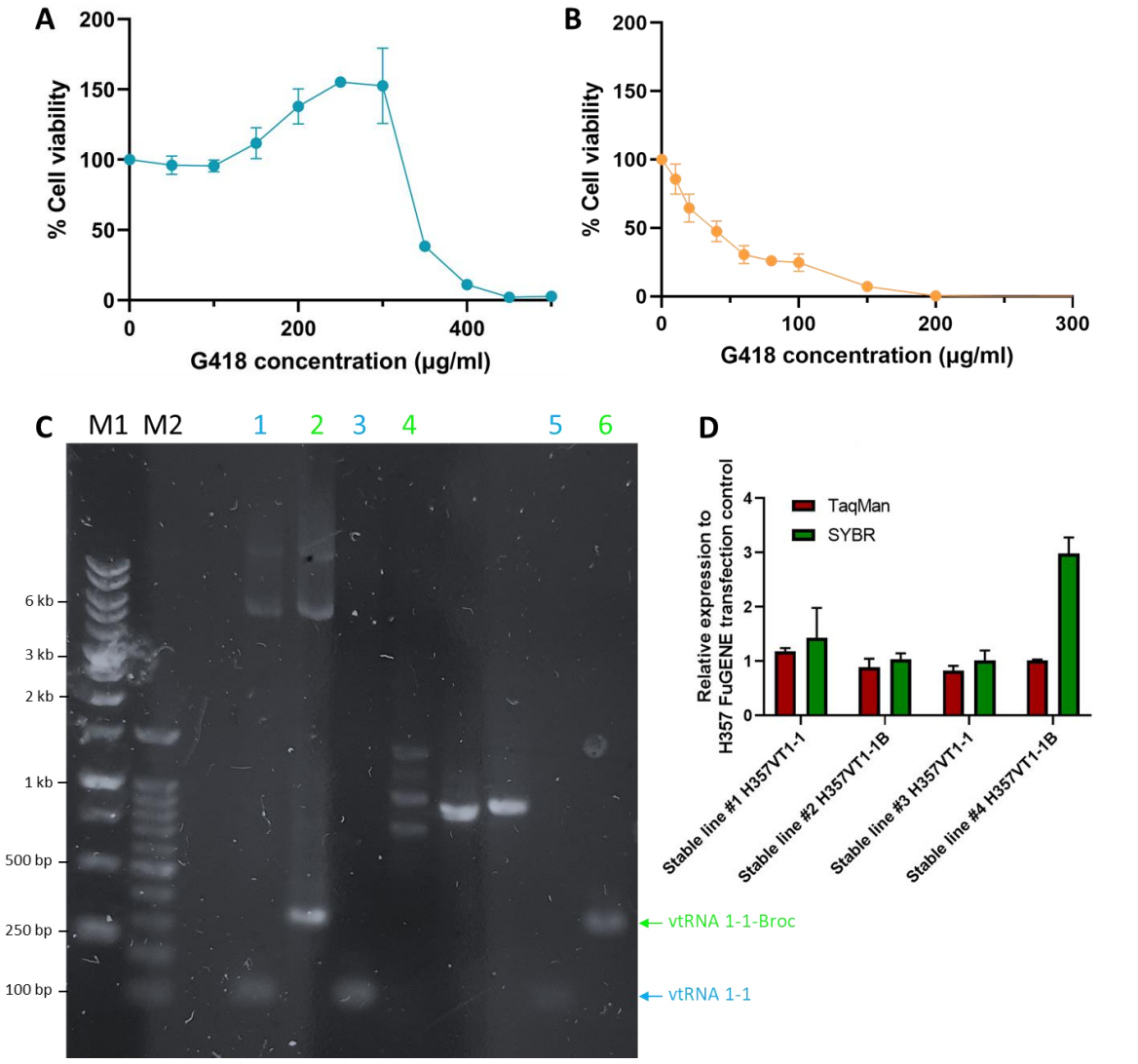

Figure 4.13 Assessment of stably transfected H357 vtRNA 1-1/vtRNA 1-1-Broccoli expressing cell lines. A, B) Establishment of G418 kill curves for H357 (shown in A) and SCC4 (shown in B) cells to determine the optimal G418 concentration for stably transfected clone selection. Cells were seeded in 96-well plates and allowed to attach overnight. Fresh media containing a series of concentrations of G418 (shown in Figure 2.4) was added and replaced every 3 days. Finally, cell viability measured by MTT assay on day 10 was plotted against the G418 concentration added to the specific wells, and concentrations that killed 100% cells were selected to be used in single clone selection process. Data shown are means ± SD, n=3. **C)** 2% (w/v) agarose gel electrophoresis was used to confirm the presence of vtRNA1-1 (in blue lanes)/vtRNA1-1-Broccoli (in green lanes) sequence in transfection plasmids and gDNA from stably transfected H357 cell clones. Lane M1 and M2: GeneRuler 1 kb and 100 bp DNA ladders (Thermo Fisher Scientific), respectively; lane 1: pAV U6+27-vtRNA 1-1 plasmid; lane 2: pAV U6+27-vtRNA 1-1-F30-2x dBroccoli plasmid; lane 3 and lane 5: gDNA from stably transfected H357 cell clones #1 and #3 using pAV U6+27-vtRNA 1-1 plasmid; lane 4 and lane 6: gDNA from stably transfected H357 cell clones #2 and #4 using pAV U6+27-vtRNA 1-1-F30-2x dBroccoli plasmid. Primers used were described in Table 2.6. **D)** Relative expression of vtRNA 1-1 in four stably transfected H357 cell lines with either pAV U6+27-vtRNA 1-1 (H357VT1-1) or pAV U6+27-vtRNA 1-1-F30-2x dBroccoli (H357VT1-1B) plasmids assessed using TaqMan and SYBR primers. Data shown are means ± SD, normalised to no DNA transfection control, n=3.

4.3 Discussion

4.3.1 Distinct Small RNA profiles from FNB6-EV and OSCC-EV isolates

Agreeing with a previous report, the Bioanalyzer traces revealed abundant small RNAs across all EV pellets in our study (Wei *et al.*, 2017). Across all cell lines, only 10k EV pellets showed peaks for 18S and 28S rRNA, whilst 100k EV pellets (supposedly enriched with exosomes) had undetectable or very small rRNA peaks. This result is consistent with the RNA traces reported by another study using the same techniques and conditions to isolate 2k, 10k, and 100k EVs from colon carcinoma cells (Ji *et al.*, 2014), suggesting that the pattern observed is not oral cancer-specific. In the literature, no rRNA was detected in exosomal RNA from human plasma samples and cell culture (Eldh *et al.*, 2012; Huang *et al.*, 2013), but a small amount was reported by others in exosomes from both normal and cancer cells (Valadi *et al.*, 2007; Jenjaroenpun *et al.*, 2013). This observation could be due to the heterogeneous composition of larger EV subpopulations, which may contain co-precipitated cellular fragments carrying rRNAs of cellular origin. Overall, our total EV pellet RNA profiles appeared to be consistent with those reported in the literature and were of sufficient quantity for small RNA sequencing.

It has been well established that cancer-derived EVs carry cargo that differ greatly to those encapsulated in EVs from non-cancerous cells (Melo *et al.*, 2014). Small RNA sequencing of EV pellets derived from both cancer and immortalised non-tumorigenic cell lines in our study revealed large number of RNA species that were uniquely present in FNB6-derived EV pellets. This observation is an addition to the general consensus that cancer EVs contain more variated cargo, as most studies have only evidenced the increased EV release from cancer cells when comparing to normal cells with differentiated expression (DE) of the RNA molecules being identified between the two (Joyce, Kerin and Dwyer, 2016; Zhu *et al.*, 2019; Huang *et al.*, 2020). Meanwhile, only 0.4-2.4% small RNA was seen in OSCC-EVs that was not found in FNB6-EVs. This means the majority of the small RNA content in cancer derived EVs and non-cancerous cell derived EVs are similar, with a very small proportion being cancer cell specific. Validation of disease-related biomarker from this subgroup could be useful for identifying new candidates for early-stage cancer screening.

Consistent with the literature, we did observe different expression profiles of small RNA in cancer and normal cell derived EVs. We were unable to perform DE analysis for this dataset due to insufficient number of biological repeat (n=1), which was limited by the initial experimental design and funding availability. Therefore, we took the top 20 most enriched small RNA detected in FNB6-EVs and OSCC-EVs as a snapshot of the most abundant RNA species present in these EV pellets. miRNA have been a research focus in the EV research field because they are reported to be enriched in exosomes and can perform regulatory functions in the recipient cells (Yu, Odenthal and Fries, 2016). They were the most common small RNA type on the top 20 list from both FNB6 and OSCC EVs, with 10% more seen in OSCC EVs. RNA sequencing of exosomal RNA extracted from liver cancer cells identified 22% of the reads being miRNA, whilst others reported only 0.26% from breast cancer cell-derived vesicle RNA (Tosar *et al.*, 2015; Zhu *et al.*, 2019). The big variation of EV miRNA proportion can be cancer type specific, as seen in the comparison between colon cancer and glioblastoma cell lines assessed by the same study (Jeppesen *et al.*, 2019). It could also be related to different EV isolation and RNA extraction techniques used, both our study and Tosar *et al*. applied different adaptions to the original differential centrifugation approach to isolate EVs (Tosar *et al.*, 2015). The small RNA sequencing library preparation is another factor that can affect the RNA species identified. Some protocols rely on gel extraction that specifically excise miRNA-sized molecules (Morin *et al.*, 2010; Kukurba and Montgomery, 2015), whilst others rely on a bead-based size selection (that has a broader selection range) (Hilaire *et al.*, 2020). Our study used the latter in combination with the Ion Torrent sequencing platform, which could partly explain the lower proportion of miRNA identified. Another varied RNA type between the two lists is tRNA, which accounted for 20% of the top 20 small RNA in FNB6 EVs but only 5% in OSCC EVs. Agreeing with our results, Zhu *et al*. reported 5% tRNA in total small RNA composition from liver cancer cell line. By comparing plasma exosomes from liver cancer patients and healthy donors, they further reported enrichment of tRNA-derived small RNA (tsRNA) in patient-derived samples (Zhu *et al.*, 2019). The same enrichment was also seen by Tosar *et al*. in breast cancer-derived EVs as well as non-malignant breast epithelial cell-derived EVs (Tosar *et al.*, 2015). These fragmented small non-coding RNAs themselves can serve as novel diagnostic biomarkers, whilst a wide range of important regulatory

functions have also been suggested (He *et al.*, 2018; Zhu *et al.*, 2019; Fang *et al.*, 2020). The presence and enrichment of small RNA fragments in EVs with regulatory functions is relevant to the current study as fragments from vtRNA were identified in sequencing data (discussed below).

4.3.2 Vault RNA and vtRNA fragments are enriched in OSCC-EV isolates

Our study revealed, for the first time, the detection of vtRNAs in OSCC-derived EV isolates by small RNA sequencing and qPCR, they were found particularly enriched in small EV (100k) pellets. Although we did not provide direct comparison between cellular and EV vtRNA abundance, many have evidenced their EV enrichment relative to their expression in parental cells. For example, vtRNAs were found enriched in glioma microvesicles whilst they were virtually undetectable in parental cells (Li *et al.*, 2013). In non-malignant cell line, a 6-fold increase was seen in exosomal vtRNA abundance compared to cells (van Balkom *et al.*, 2015). vtRNA 1-1, 1-2, and 1-3 represent the majority of the vtRNA reads in our EV pellets, whilst vtRNA 2-1 and 3-1P contributed very few reads. vtRNA 2-1 is also known as non-coding RNA nc886 (Lee, 2015). It has been reported to be neither co-localised nor co-regulated with other paralogues, and it is repressed in multiple cancer cell lines due to its role as a tumour suppressor gene (Lee *et al.*, 2011, 2014). According to the data, vtRNA 2-1 was not detected in any OSCC-EVs, thus only vault-associated vtRNAs were transported into the extracellular space. Our data are consistent with a study focusing on melanoma-derived EVs, where vtRNAs were found to be enriched in all EV subtypes relative to their cellular abundance, with the most enrichment in exosomes (Lunavat *et al.*, 2015). Together with our finding in OSCC, these results suggest a common pattern of vtRNA in multitype cancer derived EVs. In contrast to our finding that only vtRNA 1-1 and vtRNA 1-3 were found enriched in FNB6-EVs, Shurtleff *et al*. reported the enrichment of all three vault-associated vtRNA paralogs in HEK293T-exosomes though a YBX1-dependent manner (Shurtleff *et al.*, 2017). Vault RNAs have long been linked to multidrug resistance, by either directly binding to the chemotherapeutic compounds or working as a regulator of a key enzyme in drug metabolism (Gopinath *et al.*, 2005; Mashima *et al.*, 2008; Persson *et al.*, 2009). However, while enrichment of vtRNAs seemed to be commonly reported in EVs isolated from cancer and non-cancerous cells, no functional studies of EV-vtRNA have been published so far.

Previous studies have revealed the presence of at least four vtRNA 1-1 fragments in human fibroblasts and MCF7 cells (Persson *et al.*, 2009; Hussain *et al.*, 2013). Pre-mature and mature forms of svRNAs can be generated from both 3' and 5' ends of full-length vtRNA upon post-transcriptional processing via a Dicer-dependent manner. These svRNAs have been shown to have miRNA-like regulatory functions, including mediating drug resistance (Hussain *et al.*, 2013). Li *et al*. also reported svRNA sequences predominantly mapping to 3' ends of vtRNA 1-1 and 1-2 transcripts, however 5' end fragments of vtRNA 1-1 were shown to be dominant by Persson et al. (Persson *et al.*, 2009; Li *et al.*, 2013). The contradictory findings reported in the literature might be due to tissue specific processing of vtRNA to form specific svRNAs. Our data indicates the presence of both 5' and 3' vtRNA fragments in OSCC EV isolates, but with enrichment of 3' vtRNA fragments from vtRNA 1-1 and vtRNA 1-2. Noticeably, the vtRNA 1-1 fragments with the most reads identified in our small RNA sequencing matched almost exactly to the svRNA2 and svRNA4 (matched to 5' and 3' end fragments, respectively) reported by Hussain *et al*., and pre-svRNAb and svRNAa* (matched to 5' and 3' end fragments, respectively) reported by Persson *et al.* (Persson *et al.*, 2009; Hussain *et al.*, 2013). The identical 5' fragments of vtRNA 1-1 and vtRNA 1-2 observed by us were named pre-svRNAb by the previous study, whose sequence contains two smaller overlapping fragments svRNAa and svRNAb (Persson *et al.*, 2009). The expression levels of svRNAs were reported to be 10 times higher than a pro-metastatic miRNA in breast cancer cells, suggesting this process is somehow important to cellular activities. Moreover, similar to our findings, the enrichment of vtRNA fragments was seen in human endothelial cell-derived exosomes, whilst the authors also reported a similar fragment distribution when mapping to the full-length vtRNAs in parental cells (van Balkom *et al.*, 2015). Taken altogether, the evidence described suggests a prevalent cellular event causing full-length vtRNA to be processed into several small vtRNA fragments by a Dicer-dependent manner, which can then be found enriched in EVs.

4.3.3 Investigation of vtRNA fragments in OSCC-EVs

Small non-coding RNAs are prone to undergo further processing to form shorter fragments which exhibit miRNA-like regulatory functions. For example, several snoRNA derived RNAs (sdRNAs)

resemble miRNAs by associating with Argonaute proteins and mediating repressed translation (Li, Saraiya and Wang, 2011; Falaleeva and Stamm, 2013). Similar to sdRNAs, six distinct svRNAs have been identified, in which svRNAb has been shown to downregulate drug metabolism by exhibiting miRNA-like Ago2-dependent repression of semi-complementary targets, providing evidence of vtRNA-regulated multidrug resistance mechanisms (Persson *et al.*, 2009). As observed by van Balkom *et al*., these small non-coding RNA fragments, including vtRNA fragments, are more abundant in EVs compared to cells, suggesting a potential enrichment mechanism of small non-coding RNA fragments into EVs (van Balkom *et al.*, 2015). To further investigate the role of the EV-encapsulated vtRNA fragments, we firstly aimed to validate the observation from small RNA sequencing by an alternative method. Although we have validated the full-length vtRNA abundance by qPCR, this technique is unsuitable for the detection of smaller fragments as they are an insufficient size for traditional primer based qPCR. Stem-loop primers designed to bind to the 3' fragments would also bind to the full-length precursors.

Our first validation attempt was by northern blot, a conventional RNA detection technique that allows direct visualisation of the molecules of interest and their length variants (Wiegard *et al.*, 2021). Following total EV-RNA separation by PAGE, hybridisation with probes designed to target the vtRNA fragments would enable separate detection of both fragments and the full-length vtRNA containing the fragment sequences, by which the relative abundance of the specific fragments in relation to the full-length vtRNA can be estimated. However, hybridisation with a probe complimentary to the 3' end of vtRNA 1-1 detected the full-length vtRNA in the cell lysate samples and a few EV pellet samples (FNB6 10k, 100k, and SCC4 100k pellets), but no vtRNA fragments were visible. As FNB6 and SCC4 100k were the EV pellets with the most vtRNA reads detected by both small RNA sequencing and qPCR (FNB6 10k were also found to be relatively enriched with vtRNA 1-1), we suspect that the absence of vtRNA fragments may be due to insufficient input RNA (i.e. they were below the detection limit). Apart from vtRNA fragments, we also attempted the hybridisation with a probe targeting miR-23a-3p, as it was found relatively abundant across all EV samples and was used as an endogenous control for EV-RNA qPCR normalisation. No bands for

miR-23a-3p were detected, potentially because its read numbers in total EV-RNA were found to be at similar levels to the vtRNAs. We then attempted the AT-tailing approach which amplifies the signal by elongating the probe with an d(A-T) oligo tag in the presence of the labelled nucleotide (Nakajima *et al.*, 1999). This method has significantly increased the resolution for northern blot hybridisation and revealed undetectable bands using original probes when 2 µg total RNA was loaded per lane (Nakajima *et al.*, 1999). However, this approach did not work for us, which may be because the maximum loading we could achieve was 100 ng for EV-RNA. When searching previous studies performing the same technique, Li *et al*. also only detected full-length vtRNA but not their fragments in glioma microvesicles, despite a large number of 3' vtRNA 1-1 fragment reads detected by RNA sequencing (Li *et al.*, 2013). Whilst Persson *et al*. managed to detect both full-length and 3' fragment of vtRNA (pre-svRNAb) but not smaller svRNAs, suggesting the technical difficulty could increase as the size of the target molecule decreases (Persson *et al.*, 2009). The authors then applied RNase protection assay for the svRNA validation, in which the RNA targets and a labelled antisense RNA probe were hybridised to form double-strand products prior to the RNase digestion and gel separation and detection (Einspanier and Plath, 1998; Persson *et al.*, 2009). Compared to northern blot, the RNase protection assay is more sensitive and holds the advantage of being able to detect RNA of interest even from partially degraded samples (Einspanier and Plath, 1998). However, both techniques are very similar in the way that they rely on the detection of the signal from the original input of target molecules and no signal amplification is applied in either of them. Therefore, we decided to try to solve the problem by a different approach.

The dye-binding RNA aptamers were firstly invented by Grate and Wilson in 1999, which formed a foundation for the development of the Spinach aptamer and its cognate fluorophore, DFHBI, by the Jaffrey Lab 10 years ago (Grate and Wilson, 1999; Paige, Wu and Jaffrey, 2011). By fusing the Spinach aptamer to an RNA molecule, the resulting transcript (with correct folding) should bind to the fluorophore, enabling the live cell imaging of specific RNA molecules. The second generation vegetable tag Broccoli and its cognate fluorophore DFHBI-1T further improved the stability and infinity from the previous generation whilst producing a brighter signal with less background (Filonov

et al., 2014; Song *et al.*, 2014). The fluorescent signal produced upon binding can be visualised *in vitro* in gel, by flow cytometry (as DFHBI/DFHBI-1T is membrane permeable and non-toxic to cells), and by live cell imaging (Filonov and Jaffrey, 2016). So far, the wide applications of this novel technique has been seen in mammalian cells, *Escherichia coli* cells, and yeast (Spille and Kubitscheck, 2015; Filonov and Jaffrey, 2016; Zinskie *et al.*, 2018), yet it has not been utilised to study EV-RNA in published studies.

Our experimental design was to establish OSCC cell lines expressing vtRNA 1-1 tagged with a dBroccoli in a F30 scaffold on its 3' end, hoping to visualise the tagged vtRNA 1-1 and its 3' fragments in live cells by fluorescence microscopy with addition of the DFHBI-1T substrate. Although we have followed the protocols described by Filonov and Jaffrey (2016) from cell transfection to signal detection (for flow cytometry detection and live cell imaging), we were unable to detect the expected fluorescence signal from the cells transfected with vtRNA1-1-dBroccoli fusion constructs with addition of 40 μM DFHBI-1T after 48 h, despite an overall ~20-fold increase in vtRNA 1-1 transcript as seen by qPCR. We also detected the vtRNA 1-1-dBroccoli bands from both genomic DNA and complementary DNA (synthesised by reverse transcription using total RNA as template) from transiently transfected cells using primers specifically designed for the fusion sequence, indicating that transcription of the foreign sequences had occurred. The ~10-20% positive rate detected in GFP-transfected control cells by flow cytometry suggested the transfection efficiency was at a relatively low level. Cells transfected with Broccoli-only plasmid (purchased directly from Addgene) showed only ~1-2% positive rate, whilst ~30% cells were detected positive for green fluorescence in the original protocol (Filonov and Jaffrey, 2016). Apart from an unsatisfactory transfection efficiency, we also suspect the unsuccessful results in vtRNA 1-1-dBroccoli transfected cells could be due to incorrect folding of the RNA secondary structure, as the mFold RNA prediction web server has suggested 22 possible folding structures for the fusion transcript (Supplementary Figure S1), and none of the predicted structures contained correctly folded dBroccoli (Supplementary Figure S2) (Zuker, 2003). With additional time, optimisation of the transfection protocol or a different transfection method/reagent could be attempted to improve transfection efficiency. For example, a

combined use of Lipofectamine LTX and FuGENE HD transfection reagents was suggested to result in increased efficiency of gene transfer compared with the use of either reagent alone (Ishiguro *et al.*, 2017).

Although we were unable to achieve the initial objective of establishing a cell line expressing Broccoli-tagged vtRNA, we still moved forward to carry out stably transfected single clone selection, hoping to obtain vtRNA 1-1-overexpressing OSCC cell lines. G418 kill curves displayed different tolerance to the selection antibiotic within the two cell lines tested, with SCC4 being more sensitive. Both working concentrations determined for the two cell lines fell into the commonly used G418 concentration range which is 200-500 µg/ml depending on the culture conditions. Despite SCC4 cells being treated with lower concentration of G418, clones from this cell line did not survived the selection process, as they did not attach to tissue culture plastic and divide when seeded at 1 cell per well. As a result, four H357 cell clones were derived from the G418 selection and were expanded into cell lines. However, qPCR analysis using TaqMan probes detected no overexpression of vtRNA 1-1 from the stable cell lines. A 3-fold increase in vtRNA 1-1 transcripts was seen in one of the stable lines transfected with vtRNA 1-1-Broccoli construct when tested with SYBR Green primers, however we would expect a stronger overexpression of the vtRNA 1-1 under a human U6 promoter from a successful transfection as it is accepted as a strong RNA polymerase III promotor in most cell types and is specifically used for small RNA expression in mammalian cells (Nie *et al.*, 2010; Roelz *et al.*, 2010). The reason why TaqMan probe did not detect an increase in vtRNA 1-1 expressione is unclear, though the two types of primers do perform with different mechanisms. TaqMan probes hold the advantages of providing higher specificity based on dual labelled oligonucleotide and exonuclease activity of the Taq polymerase enzyme, whereas SYBR Green primers can produce non-specific binding of the fluorescent dye to any double-stranded DNA (Singh and Roy-Chowdhuri, 2016). That being said, with optimisation of qPCR conditions and extra care being paid in sample loading, SYBR Green primers were proved to be able to exhibit comparable specificity and performance as TaqMan (Tajadini, Panjehpour and Javanmard, 2014). Here, the error bars for both datasets were tight, therefore the results shown were considered genuine.

Overall, this chapter explored the small RNA transcriptome of isolated EV pellets from a panel of immortal oral keratinocyte cell lines (derived from normal and cancer cells). Specifically, we closely inspected the vtRNA subpopulation in the EV pellets and validated the enrichment of vtRNA in 100k EV pellets from OSCC. In addition, we also observed high abundance of vtRNA fragments by small RNA sequencing, which adds to the limited research focusing on svRNAs, especially in EVs (Persson *et al.*, 2009; Hussain *et al.*, 2013; Sajini *et al.*, 2019). To further investigate the potential enrichment mechanism and the role of vtRNA fragments in OSCC-EVs, we aimed to establish a methodology that would allow us to detect the fragments in addition to full length vtRNAs, which was unfortunately not achieved due to technical difficulties. Due to the time limit of the study, we were unable to further optimise the methodology. Nevertheless, the EV-encapsulated vtRNA fragments were still of great research interest and could be indirectly investigated in the future using the MVP knockout cell lines established in this study (described in chapter 6).

Chapter 5 Investigation of vault particle contamination in EV preparations and strategic solutions

5.1 Introduction

One of the biggest challenges that currently hinders the development of EV related research is the lack of a universally accepted method for EV isolation, which is partially due to EV heterogeneity, their presence in different complex biological liquids and the availability of specialist equipment. With new isolation techniques constantly emerging and evolving, commonly used EV purification techniques include differential centrifugation, SEC, density gradient centrifugation, precipitation and immunoaffinity capture. However, comprehensive comparison studies have demonstrated co-purified proteins and particles when using different separation techniques, and none of the above techniques has been proved perfect (Webber and Clayton, 2013; Pužar Dominkuš *et al.*, 2018; Dong *et al.*, 2020). Therefore, it is essential for researchers to be aware of the pros and cons of the selected purification methods, and to challenge the results before drawing strong conclusions regarding EV cargo.

In addition to our findings that vault particle proteins and vtRNAs were enriched in EV pellets derived by differential centrifugation, unpublished mass spectrometry data from the Hunt Lab also detected MVP in EV preparations isolated by SEC. Meanwhile, similar results have been reported by numerous individual studies. By searching the ExoCarta database (Keerthikumar *et al.*, 2016), we found both MVP and vtRNA had been repeatedly reported as EV cargo or to be associated with EVs (Herlevsen *et al.*, 2007; Nolte'T Hoen *et al.*, 2012; Lässer *et al.*, 2017). However, despite 14 studies identifying MVP as exosome-associated (isolated from multiple biological sources), none had determined whether vault components were *bona fide* EV cargo, nor which EV subtypes vault components were enriched in.

Part way through the current study, Jeppesen *et al*. suggested that the presence of MVP in EV isolates, together with vtRNAs, is the result of an exosome-independent release, and therefore they should not be considered as small EV cargo (Jeppesen *et al.*, 2019). In this study, exosomes were isolated by density gradient fractionation from human colon (DKO-1) and glioblastoma (Gli36) cancer cell lines, and vault components were found to be enriched in non-vesicular fractions. However, the other larger EV populations were not examined. The heterogeneous nature of EVs (produced by one cell type and between different cell types) leads us to question whether vault particles are a regular contaminant in EV preparations or if vault components can be EV cargo in some instances. If they are simply contaminants, how can we achieve EV isolation that is free of vaults and other similar-sized particles?

In 2014, ISEV published a minimal set of standards to be followed when carrying out EV research, which was then reviewed and updated with more detail and specific guidelines in 2018 (Lötvall *et al.*, 2014; Théry *et al.*, 2018). Noticeably, MISEV2018 provided advice for using a biochemical approach to further assess the topological association of putative EV cargo (Théry *et al.*, 2018).

Due to yielding the highest EV protein and RNA among the OSCC cell panel, EVs from SCC4 cells were examined in this chapter. We firstly determined whether vault proteins and RNAs present in DC-EVs are *bona fide* EV cargo by proteinase and RNase protection assays as suggested by MISEV2018. We also compared EVs isolated by other commonly used techniques (i.e. SEC and immunocapture) for the presence of vault particle components. Finally, a vault-free EV isolation strategy using Dynabeads was developed, by which marker-positive EVs were isolated from as little as 5 ml conditioned medium.

5.2 Results

5.2.1 Assessment of vault particle components in DC-EVs

At the same time that we were conducting these experiments, Jeppesen *et al*. stated that MVP and vtRNAs are not associated with exosomes isolated by density gradient fractionation (Jeppesen *et al.*, 2019). We further investigated the sub-location of vault components in all three EV pellets separated by differential centrifugation at 2,000 × *g* (2k), 10,000 × *g* (10k), and 100,000 × *g* (100k) centrifugal

force (Section 2.4.3.1) from 60 ml SCC4 conditioned medium. Protocols for the proteinase and RNase protection assays were developed and optimised in this study based on the MISEV2018 guidelines (Théry *et al.*, 2018).

5.2.1.1 Assessment of vault proteins as EV cargo by proteinase K protection assay

The location of vault proteins was determined by treatment of resuspended DC-derived pellets with combinations of proteinase K and the membrane-permeabilising reagent Triton X-100. DC-EV pellets were divided into four equal parts and each was treated with: (-PK -TX) PBS only; (+PK -TX) 20 µg/ml proteinase K to digest non-EV encapsulated proteins; (-PK +TX) 0.1% (v/v) Triton-X 100 to permeabilise the EV lipid bilayer membrane; (+PK +TX) 20 µg/ml proteinase K and 0.1% (v/v) Triton-X 100 to digest all proteins (Figure 5.1A).

Following incubation of DC-derived pellets as described above, western blots were performed to detect if proteins of interest were intact or degraded (Figure 5.1B). MVP in 10k and 100k pellets was not protected from proteinase K-mediated degradation in the absence of Triton X-100, suggesting that MVP is not protected by an EV membrane. MVP was also largely degraded in 2k pellets under the same incubation conditions (Figure 5.1B). In contrast, TSG101, a core component of the ESCRT-I complex that has also been commonly used as an intraluminal EV marker (Katzmann, Babst and Emr, 2001; Théry *et al.*, 2018), was protected by the EV membrane and was only fully degraded by proteinase K in the presence of the membrane permeabilising detergent Triton X-100. In addition, samples were blotted for CD63, another common EV marker that is part of the transmembrane tetraspanin family (Pols and Klumperman, 2009). According to the manufacturer (Abcam) the antibody was generated against a synthetic peptide that represents an extracellular domain of CD63 (within amino acids 100-200), but the exact peptide sequence is not stated due to being commercially sensitive. We had expected that the antibody binding site would be available to proteinase K in the absence of Triton X-100. However, the blots for CD63 did not show the pattern that we expected and CD63 appeared resistant to proteolytic degradation in all conditions.

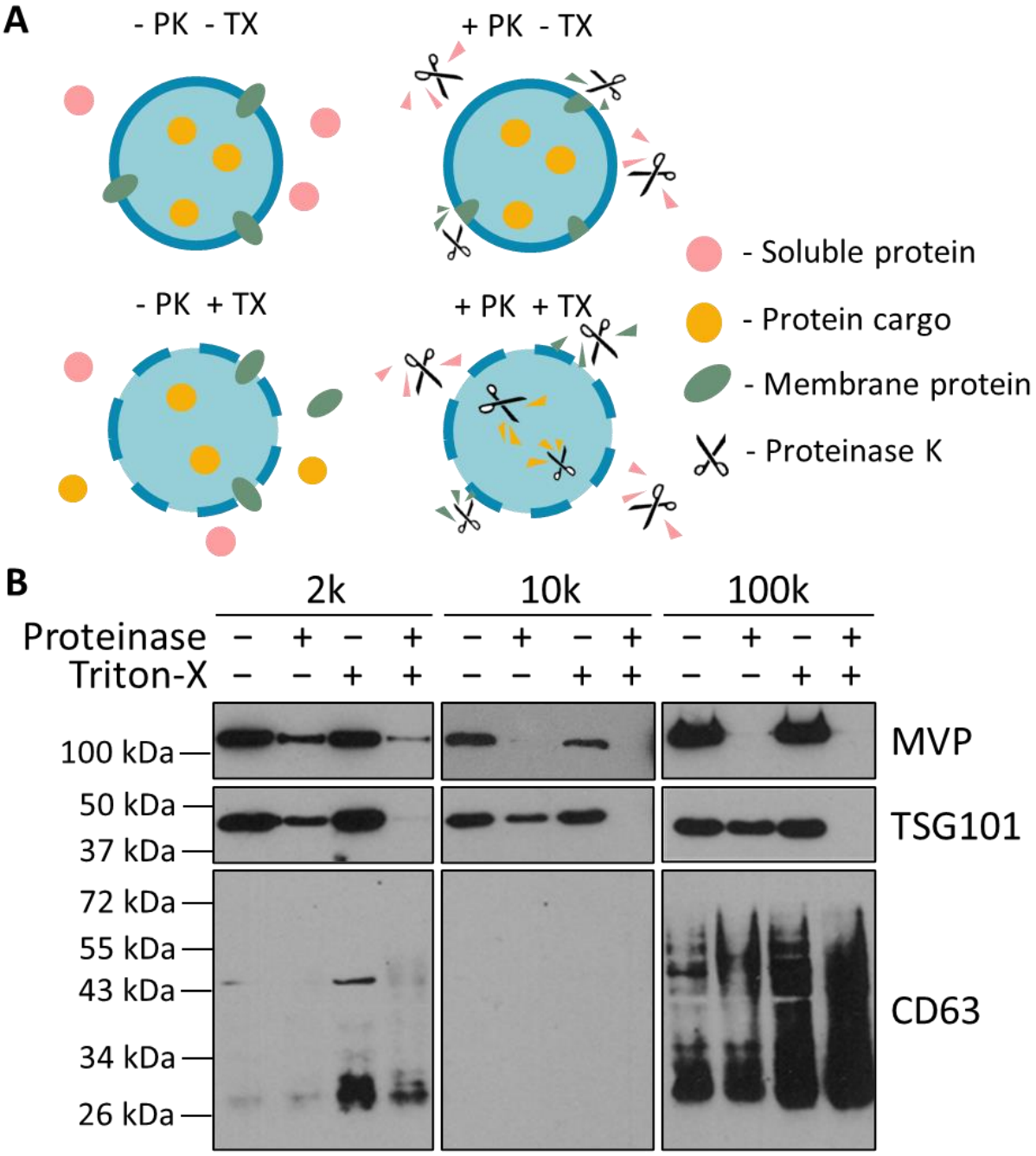

Figure 5.1 Proteinase K protection assay on DC-EV pellets followed by western blot to detect vault proteins and EV markers.
A) Illustration shows how different protein compositions in EV isolates may be degraded/protected following incubation in the presence (+) or absence (-) of proteinase K (PK) and Triton X-100 (TX). **B)** Western blots detecting vault protein and EV markers after proteinase and membrane-permeabilising treatments. Blots are representative of three biological repeats.

5.2.1.2 Assessment of vtRNAs as EV cargo by RNase A protection assay

An RNase protection assay coupled with qPCR was performed to assess whether the vtRNAs detected in DC-derived pellets are part of the EV luminal cargo. Vault particles are composed of a protein shell with vtRNA protected within. Whereas, EV luminal contents are protected by a lipid bilayer membrane. Here we incubated resuspended DC-derived pellets with combinations of RNase A, proteinase K, and Triton X-100 (Figure 5.2A). RNA was then extracted and vtRNA abundance analysed by qPCR, which was compared to the average expression of three miRNAs (miR-21a-3p, miR-30d-5p and miR-31-5p) that were selected due to their abundant and relatively even number of reads among the EV pellet samples from the previous small RNA sequencing experiment (Section 4.2.1). When compared to the control samples (nothing added, NA), it was expected that treatment with RNase alone should not cause significant changes in either vtRNA nor EV-RNA. However, the addition of proteinase K would digest the protein shell of the vault particle that is mainly composed of MVP (as seen in Figure 5.1B). Thus, providing access for RNase to the RNA contents in vault particles, but not in EVs (due to an intact lipid bilayer). Addition of the membrane-permeabilising reagent, Triton X-100, should facilitate RNase entry into EVs, but not vaults. The combined addition of all three reagents should disrupt vault and EV integrity, making all RNA available to degradation.

The data for the 100k EV pellets was the clearest to interpret, most likely due to the higher abundance of vtRNA in these samples. There was a significant decrease (except in vtRNA 1-3, despite a large reduction was seen) in relative vtRNA abundance when samples were treated with RNase and proteinase K, compared to RNase alone (Figure 5.2B). Disruption of EV membrane by Triton X-100 and incubation with RNase did not result in degradation of vtRNAs. Instead, there was significant increase in relative vtRNA abundance (Figure 5.2B), which can be explained by the degradation of the miRNA used to calculate relative abundance. This was especially evident when examining miR-30d-5p and miR-31-5p levels in samples treated with RNase and Triton X-100 (Figure 5.2C). Similar to this, the addition of all three reagents (RNase A, proteinase K and Triton X-100) also led to increased relative vtRNA abundance (Figure 5.2B). However, qPCR data was only obtained for one biological repeat due to the very low amount of total RNA recovered following the treatment for the

other two repeats. RNase treatment in the presence of Triton X-100 resulted in the reduction of miR-30d-5p and miR-31-5p, especially in 100k pellets. However, miR-23a-3p appeared more resistant to RNase degradation in the presence of Triton X-100. Further degradation of this miRNA was observed when samples were incubated with RNase A, proteinase K and Triton X-100 (Figure 5.2C), suggesting that it might be protected as part of a protein-nucleic acid complex that is within an EV membrane. This experiment suggests that vtRNAs present in DC-derived pellets are not protected within the EV lumen like the miRNAs tested, instead, they are likely to be within protein-shelled structures, such as vaults.

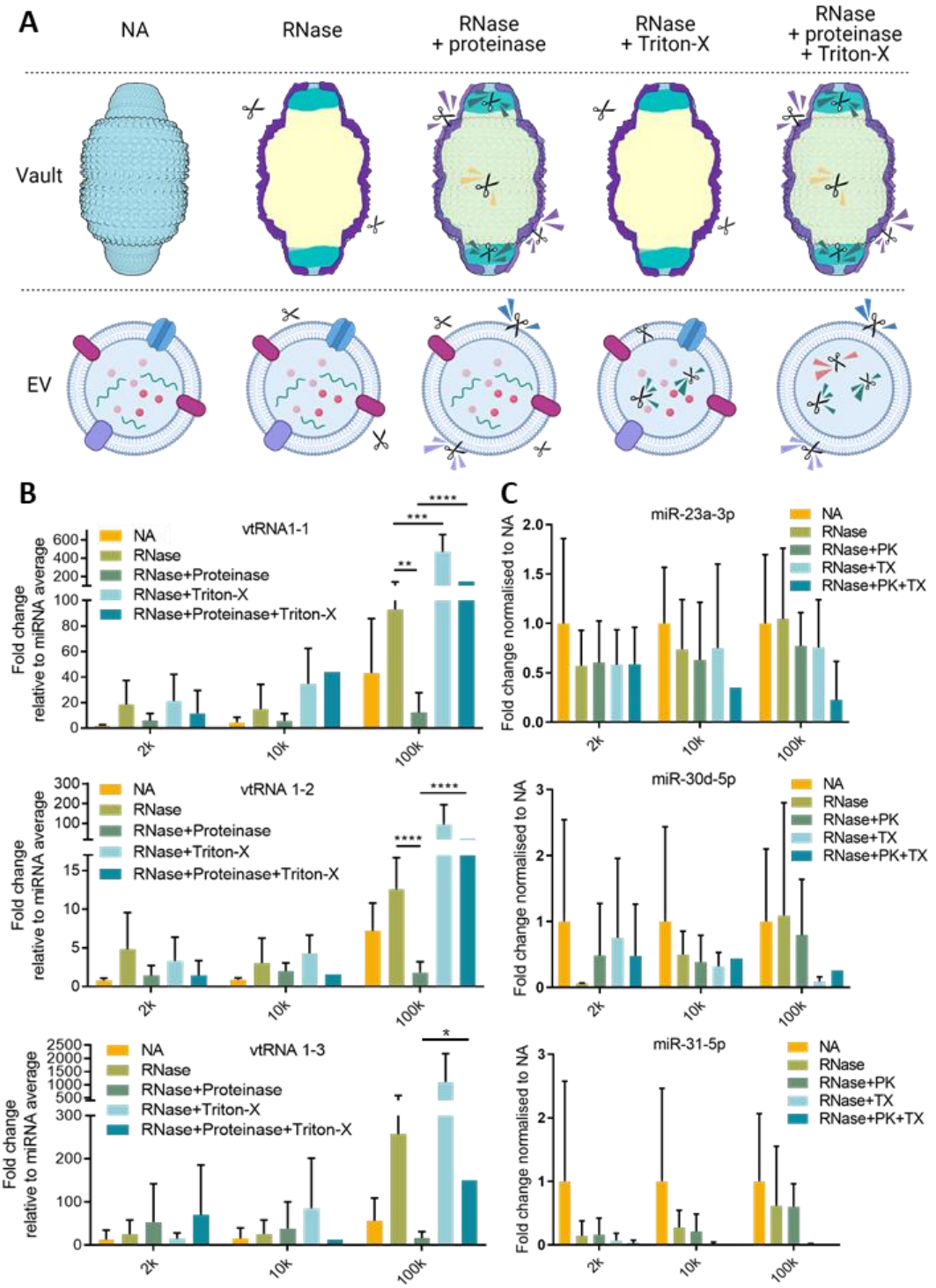

Figure 5.2 RNase A protection assay on DC-EV pellets followed by qPCR determining vtRNA and miRNA expressions.

A) Illustration shows how components of vaults and EVs were digested upon different combinations of RNase, proteinase and Triton-X. In vaults, purple area indicates the protein shell composed of MVP. Yellow area shows the lumen of vault where TEP1 and PARP4 are located, and blue area shows the vtRNAs located in the vault caps. Scissors indicate RNase and/or proteinase. **B)** RNase protection assay followed by qPCR shows abundance of vtRNA1-1, 1-2, and 1-3 upon treatments to EV pellets. Data are means ± SD, n=3 (except for RNase + proteinase + Triton-X treatment to 10k and 100k pellets n=1, due to insufficient RNA material for qPCR analysis after treatment). Statistical significance was assessed by multiple t tests corrected with the Holm-Sidak method, **p<0.01, ***p<0.001, ****p<0.0001. **C)** Abundance of miR-23a-3p, miR-30d-5p, and miR-31-5p following RNase protection assay, data were normalised to the NA group expressions. Data are means ± SD, n=3 (except for RNase + proteinase + Triton-X treatment to 10k and 100k pellets n=1, due to insufficient RNA material for qPCR analysis after treatment).

5.2.2 Vault particle-like structures were imaged in EV pellets by cryo-EM

Following the biochemical assays, which indicated that vault proteins and RNAs are not EV associated, we investigated the possibility that vault particles can contaminate OSCC EV pellets derived from differential centrifugation.

Freshly prepared EV pellets (100k) were derived from 60 ml conditioned medium by differential centrifugation (as described in Section 2.4.3.1) and imaged by cryo-EM. As well as numerous EVs of varied size and featuring a bilayer membrane (Figure 5.3C), barrel-shaped vault-like particles were repeatedly observed (Figure 5.3A, 5.3B). They were in the same size range as small EVs, measuring 85.2 ± 9 nm × 41.6 ± 3.7 nm (mean ± SD, n=13). Depending on their orientation, these 3D structures can appear to be round (plan view), elliptical (oblique view), or barrel-shaped (side view) (Figure 5.3B). Although we have observed vesicular structures in the preparation, vault-like particles were not found to be physically associated nor within any EV-like vesicles. Taking together, these findings suggested vault components are not enriched in EVs. Instead, vault particles can be a major contaminant to differential centrifugation EV preparations, possibly due to the particle aggregation caused by high centrifugal speed.

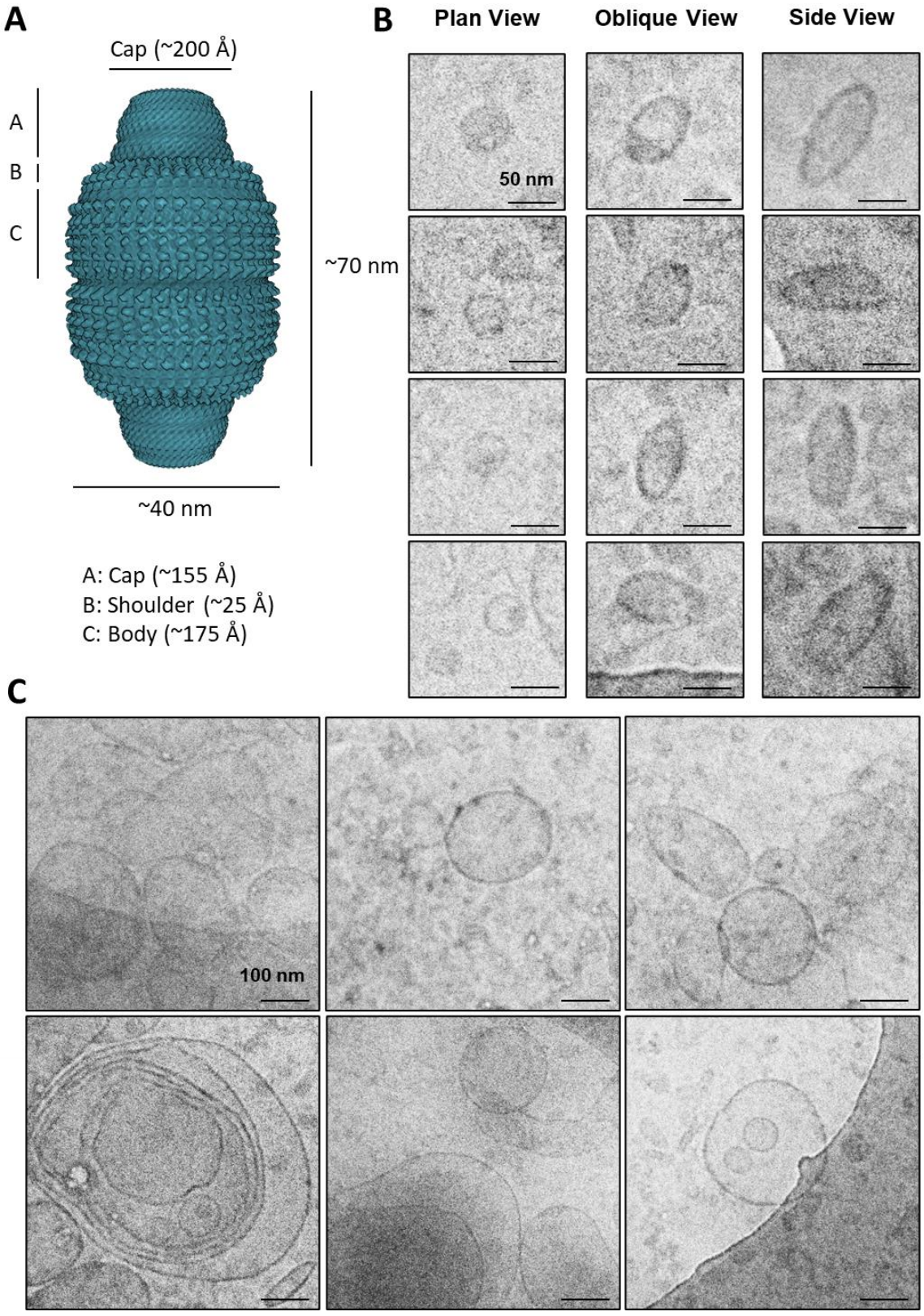

Figure 5.3 Cryo-EM imaging of vault-like particles and EVs.
A) Vault particle illustration shows the size and morphological structure (PDB id: 6BP7). **B)** Collage of vault-like particles in plan (Diameter = 41.2 ± 3.8nm, Mean ± SD, n=9), oblique and side view (length = 85.2 ± 9nm, width = 41.6 ± 3.7nm, Mean ± SD, n=13). **C)** Example images of single and multivesicular EVs ranging from 50 to 500nm in diameter but not observed to be physically in contact with any vault like structure the EV membrane of within EV structures.

5.3.3 SEC co-purifies vaults with EVs

Following confirmation of the presence of intact vaults in EV pellets derived by differential centrifugation, we next investigated whether SEC, another commonly used EV isolation approach (Tiwari *et al.*, 2021), is capable of separating vaults from EVs. Compared to DC, SEC has the advantages of being more time-efficient and does not require specialised equipment such as an ultracentrifuge. It has also been stated that SEC yields purer EVs with low soluble protein content and more intact vesicular structures (Monguió-Tortajada *et al.*, 2019).

Conditioned medium was clarified (by centrifugation at 300 × *g* for 10 min) to remove debris. However, high speed centrifugation (10,000 × *g*) was avoided to reduce the risk of particle aggregation. 30 ml clarified conditioned medium was concentrated by passing through a 100 kDa molecular weight cut off column until <1 ml final volume was recovered. The concentrated conditioned medium was then fractionated using a Sepharose CL-2B column and individual 0.5 ml fractions were used in downstream analysis. NTA demonstrated that particles started to be eluted from fraction 6 with the majority detected between fractions 7-9 (Figure 5.4A). Western blotting revealed all three vault proteins were present in these fractions as well as the common EV markers CD63, CD9 and TSG101 (Figure 5.4B). Thus, suggesting that EVs and vault particles co-elute in the same SEC fractions.

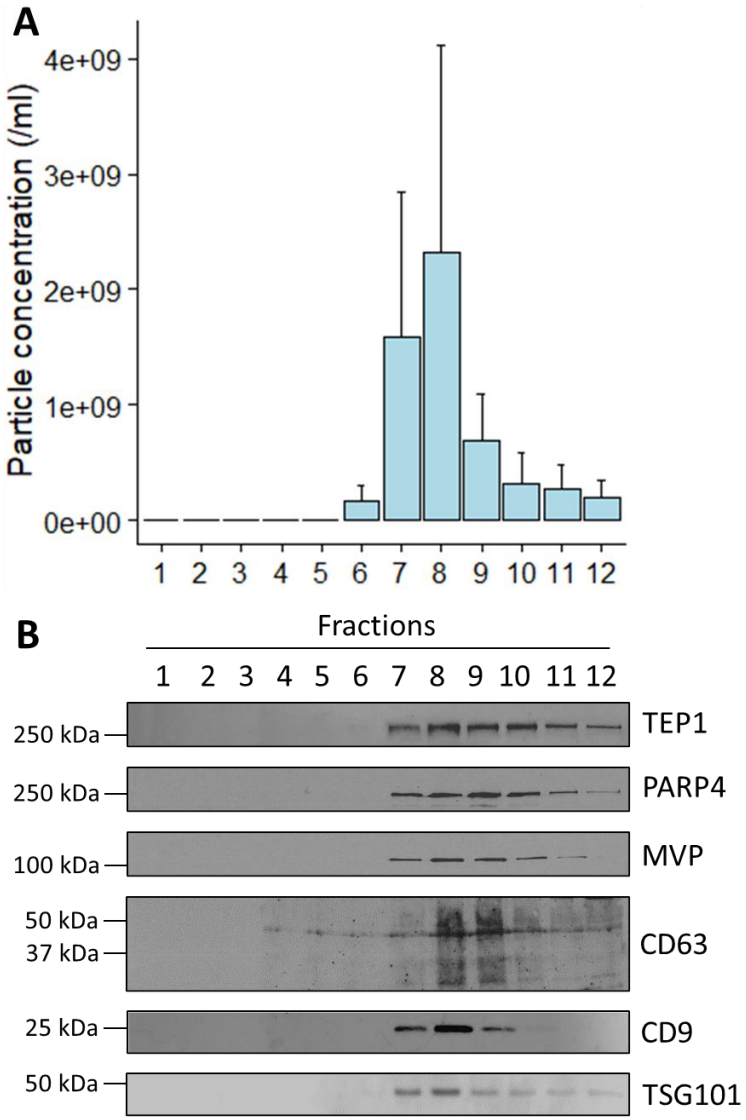

Figure 5.4 SEC co-elutes vaults with EVs.
A) NTA shows the particle concentration of the first 12 eluted SEC fractions. Data are means ± SD, n=3. **B)** Western blotting to detect vault proteins (TEP1, PARP4 and MVP) and EV markers (CD63, CD9 and TSG101) in SEC fractions. Blots are representative of three independent repeats.

5.3.4 DC-derived EVs cannot be purified by immunocapture due to particle aggregation

Having realised the limitations of size-based isolation techniques, we moved onto experimenting with commercially available Dynabeads that capture EVs by immunoaffinity to certain surface markers, which should eliminate contamination of EVs with similarly-sized particles (such as vaults).

Previous EV characterisation by ExoView analysis determined that EVs released by H357 and SCC4 cells were positive for the tetraspanin markers CD9, CD63, and CD81 (Section 3.2.2). In this study, we combined Dynabeads pre-conjugated with anti-CD9, anti-CD63, and anti-CD81 antibodies into a tetraspanin Dynabead cocktail, which contained 100 µl CD63+ beads (1×10^7 beads/ml), 40 µl CD9+ beads (1.3×10^8 beads/ml) and 40 µl CD81+ beads (1.3×10^8 beads/ml) for each capture. The volume of each type of beads used was based on the recommended protocol provided by the manufacturer.

To determine whether immunocapture was sufficient to pull-out the marker positive EVs from the crude pellets yielded from DC, the pellets were resuspended in PBS and incubated with the tetraspanin Dynabead cocktail to allow the bead-bound antibodies to bind to the antigens present on the EV surface. EV-Dynabead complexes were then pulled out of solution using a magnetic rack, whilst unbound particles were collected and pelleted by ultracentrifugation (Figure 5.5A). After solubilisation, both the EV elutes and unbound fractions were analysed by western blotting for MVP and the EV marker CD63.

Western blotting detected MVP and CD63 in the eluted and unbound fractions from the tetraspanin beads. In addition, MVP was eluted from the mIgG control beads, but the EV marker CD63 was undetectable (Figure 5.5B). Dynabead-EV complexes were resin-embedded, sectioned and imaged by TEM. Tetraspanin Dynabeads were surrounded by highly aggregated EVs/particles (Figure 5.5C).

This experiment suggested that immunoaffinity-based purification may not be suitable for subsequent purification of DC-derived EVs, due to aggregation of EVs and other particles.

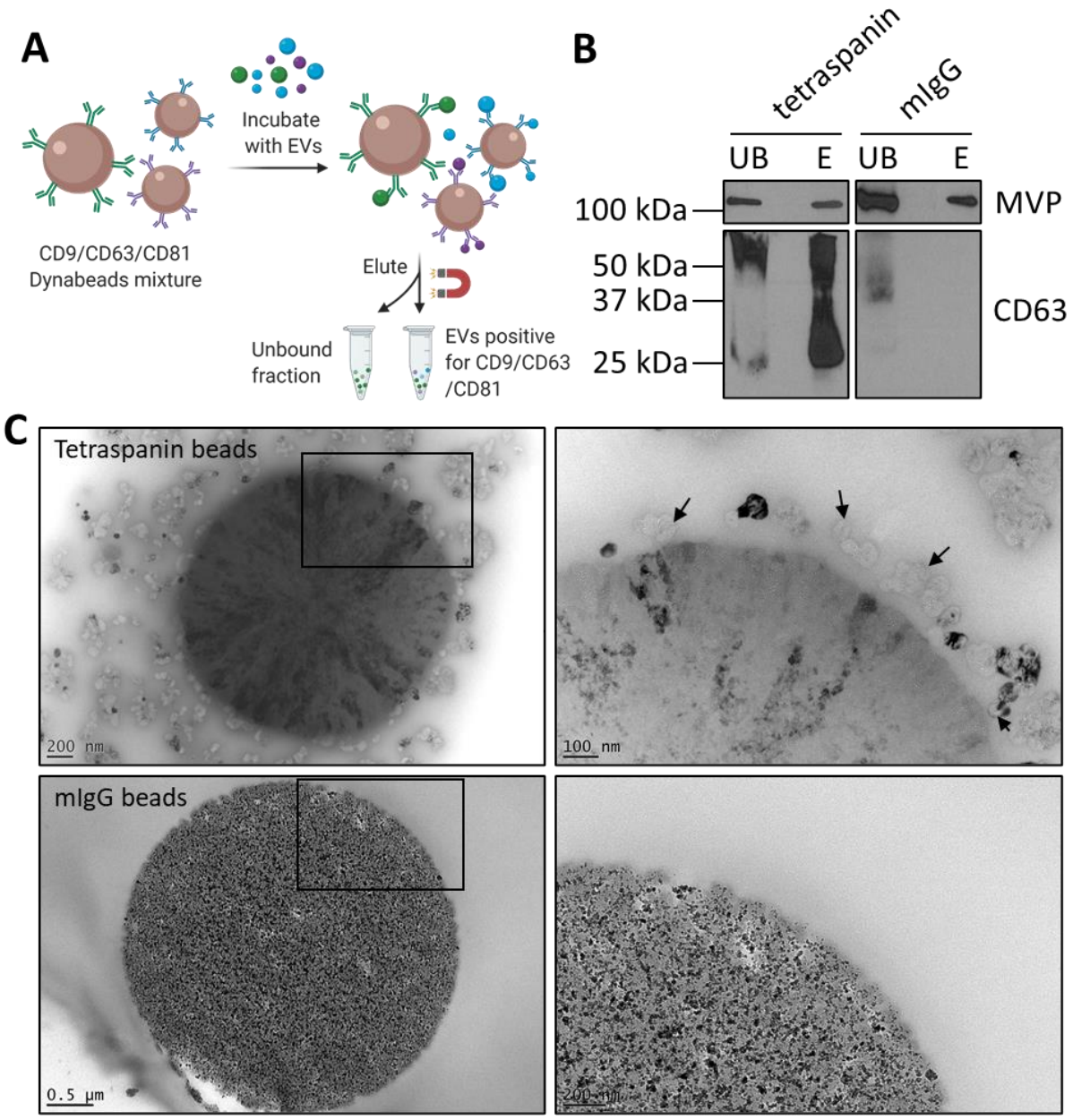

Figure 5.5 Purification of DC-EVs using Dynabeads.
A) Diagram illustrating the experimental design of incubating DC-EV pellets with Dynabeads cocktail (CD9+/CD63+/CD81+ Dynabeads), followed by separation of marker-positive EVs from unbound fraction using a magnet. **B)** Western blot detecting MVP and CD63 in unbound (UB) and eluted (E) fractions from tetraspanin Dynabeads and mIgG control after mixing with 100k EV pellets overnight. Blots are representative of three biological repeats. **C)** Upper: CD9+/CD63+/CD81+ Dynabeads captured DC-derived (100k) EVs with high levels of aggregation showed in enlarged view; Lower: mIgG Dynabeads with enlarged view. Images were obtained by negatively stained resin embedded TEM. Black arrows indicate EVs.

5.3.5 Vault-free EV isolation from conditioned medium using Dynabeads

Based on the above observation, we next sought to develop an isolation strategy that can yield EVs free of vault contaminants. Since Dynabeads were able to pull out and concentrate EVs (Figure 5.5B, 5.5C), we employed immunocapture directly on cell-free conditioned medium, without first pelleting EVs by high speed ultracentrifugation. 5 ml conditioned medium was concentrated to 1 ml using a 100 kDa molecular weight cut off column and mixed with either tetraspanin Dynabead cocktail or mIgG control beads overnight. Both captured EVs (E) and re-concentrated unbound fractions (UB) were analysed by immunoblot.

TEM imaging of the resin embedded Dynabead-EV complexes suggested minimal aggregation of the bound particles, compared to the captured DC-EVs shown above (Figure 5.6A). Although, fewer EVs were captured by individual Dynabeads, which is most likely due to the reduced input quantity. More importantly, western blotting showed no vault proteins were associated with the tetraspanin Dynabeads and only EV markers were enriched and eluted from the tetraspanin beads (Figure 5.6B). This suggested that EVs in pre-concentrated conditioned medium can be separated from vaults by immunoaffinity pull-down.

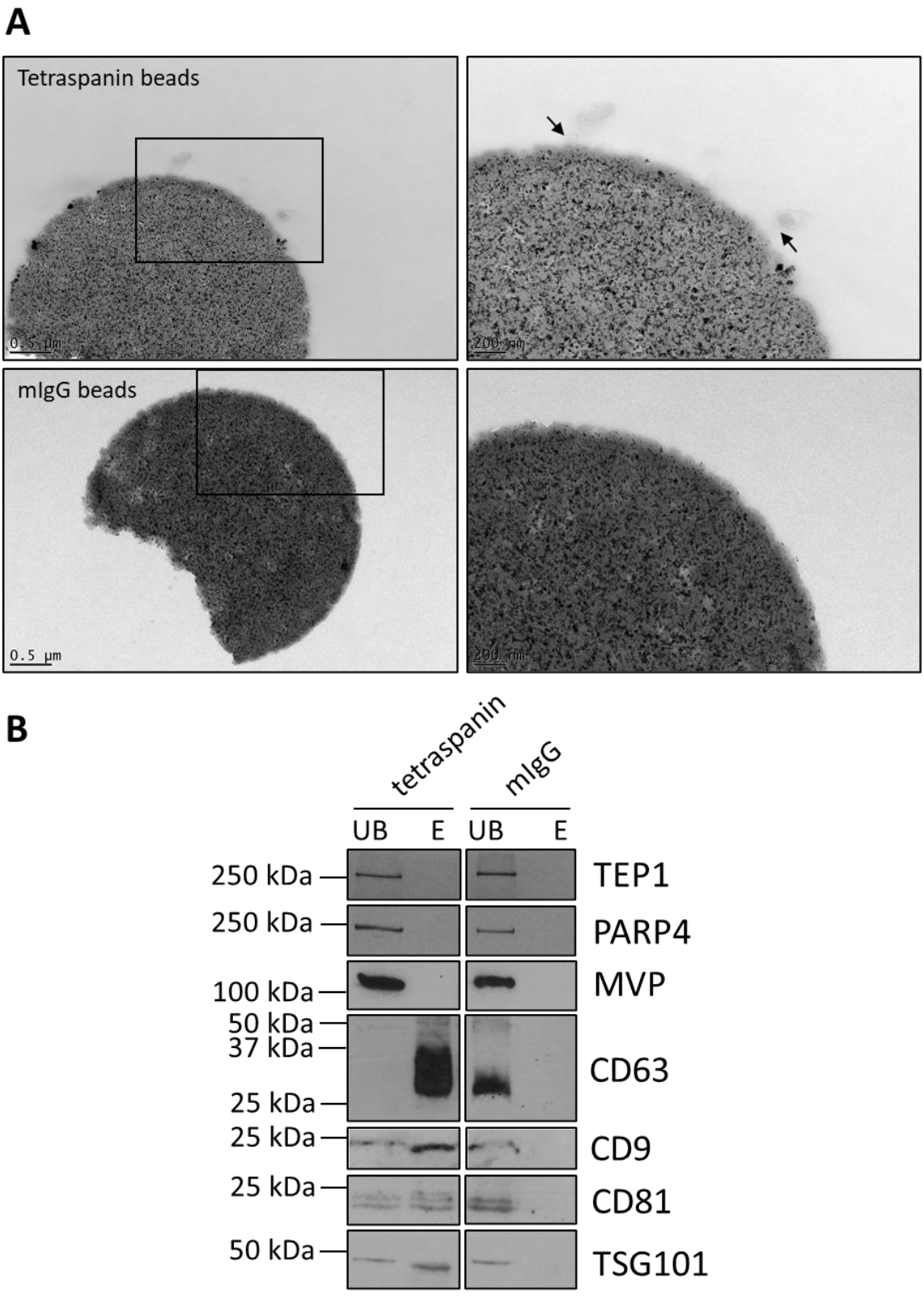

Figure 5.6 Dynabeads capture of vault-free EVs from conditioned medium.
A) Upper: CD9+/CD63+/CD81+ Dynabeads capturing EVs from conditioned medium with no aggregation (with enlarged view); Lower: mIgG bead control with enlarged view. Images were obtained by negatively stained resin embedded TEM. Black arrows indicate EVs. **B)** Western blot detecting vault proteins and EV markers in unbound (UB) and eluted (E) fractions from tetraspanin Dynabead mix and mIgG control after mixing with 1 ml concentrated conditioned medium (original volume 5 ml) overnight. Blots are representative of three biological repeats.

5.4 Discussion

5.4.1 Vault components are not *bona fide* EV cargo

Vault proteins and vtRNAs have been repeatedly reported as EV-associated molecules (Admyre *et al.*, 2007; Buschow *et al.*, 2010; van Balkom *et al.*, 2015). In studies isolating EVs by DC and precipitation techniques, individual vault components have been repeatedly reported as part of the EV cargo (Admyre *et al.*, 2007; Gonzales *et al.*, 2009; Buschow *et al.*, 2010). It was reported that the minor vault protein TEP1 is responsible for vtRNA-binding in vaults (Poderycki *et al.*, 2005). However, it has also been claimed that MVP is involved in facilitating the transport of RNA into exosomes (Teng *et al.*, 2017; Statello *et al.*, 2018). Meanwhile others have suggested the transport of MVP and vtRNAs to the extracellular space is the result of an exosome-independent release (Jeppesen *et al.*, 2019), but the other EV subtypes were not considered. In this chapter, the sublocation of vault proteins and vtRNAs present in DC-EV preparations was firstly assessed by biochemical assays as recommended by the MISEV2018 guidelines (Théry *et al.*, 2018). This is, to the best of our knowledge, the first study to investigate the topology of vault components in EV isolates in depth.

By employing proteinase K protection assay, vault proteins and EV markers were tested to determine if they were protected by the EV membrane from proteinase-mediated digestion, and whether any protection can be abolished by addition of a membrane-permeabilising reagent (Triton X-100). Our data indicates that MVP is not protected by an EV membrane. The incomplete proteinase digestion of MVP in 2k pellets when Triton X-100 was absent and present could be due to higher total protein content and complexity of the pellets compared to 10k and 100k. A 10 min centrifuge step at 2,000 × *g* could still sediment cell debris and fragments that were not pelleted at 300 × *g*, as well as apoptotic bodies. This is also the reason why some established methodologies have employed 2,000 × *g* centrifugation to eliminate debris prior to vesicle separation (Livshts *et al.*, 2015; Shahin *et al.*, 2021). Increased incubation time or proteinase K concentration could have resulted in complete MVP digestion in these samples. As a comparison to vault proteins, we also tested the integrity of EV markers in response to proteinase and Triton X-100 treatment. Whilst the intraluminal EV marker

TSG101 appeared to be protected by a lipid EV membrane, as reported previously (Cvjetkovic *et al.*, 2016), the results for CD63 – a tetraspanin family member with four transmembrane domains that serves as a surface marker in EV characterisation (Théry *et al.*, 2018), were more difficult to interpret. The CD63 antibody used in this study was stated to target an extracellular domain of CD63 (within amino acids 100-200), which should have been available to proteinase K cleavage. However, CD63 is known to be highly and variably N-glycosylated (Latysheva *et al.*, 2006). Although its unglycosylated molecular weight is 25 kDa, the glycosylated forms of CD63 are present as multiple bands on a western blot ranging from 25 kDa to ~70 kDa. Interestingly, same resistance of CD63 to proteinase K digestion was also reported in plasma and serum-derived exosomes (Diaz *et al.*, 2018). Looking into protein N-glycosylation, it was reported to cause higher resistance to pepsin digestion (Niu *et al.*, 2016). Hence we suspect the many glycosylated forms of CD63 may have interfered with the proteinase K digestion and potentially antibody binding, and therefore the actual presence of CD63 following the protection assay could be masked by the spread of the glycosylated bands (Tominaga *et al.*, 2014). Instead, future protection assays to determine protein sublocation in EV preparations could include other tetraspanins such as CD81, as it was reported to be undetectable in proteinase K treated EVs (Cvjetkovic *et al.*, 2016).

A similar strategy was employed to assess the sub-location of vtRNA in DC-EV preparation. RNase protection assay data revealed a significant reduction in vtRNA abundance when treating 100k pellets with RNase and proteinase K, in the absence of Triton X-100. Thus, suggesting that the vtRNA present in 100k preparations are protected within a protein-shelled structure (such as the vault particle) that is external to the EV lumen. A previous study identified vtRNA1-2 and vtRNA 1-3 as EV cargo due to their sensitivity to combined RNase and detergent treatment, whilst vtRNA1-1 was reported to be protected by protein (Shurtleff *et al.*, 2017). However, in the current study, the same pattern was observed for all vtRNA paralogues, with all three apparently protected by a protein structure outside of the EV lumen. Because EVs are heterogeneous and contain diverse nucleic acid species, there is currently no agreed internal control for small RNAs in the EV field (Théry *et al.*, 2018). However, by interrogating our small RNA sequencing data, we identified three miRNAs (miR-

23a-3p, miR-30d-5p, and miR-31-5p) that showed abundant and relatively even reads across all EV pellets from an OSCC cell panel, and employed the average abundance of these three miRNAs as internal controls for the RNase protection assay. All three miRNAs have been identified among the most abundant exosomal miRNAs from various sources (Barceló *et al.*, 2018; H. Hu *et al.*, 2020; Liu *et al.*, 2020). Additionally, circulating miR-30d-5p and miR-31-5p have been reported to be disease-specific biomarkers in cholangiocarcinoma and oral cancer, respectively (Lu *et al.*, 2019; Han *et al.*, 2020). As well as those being transferred as EV cargo, circulating miRNAs have also been found in microparticle-free form. Some can attach to high-density lipoproteins or bind to RNA binding proteins such as argonaute 2 (Ago2) (Creemers, Tijsen and Pinto, 2012), which could explain the large reduction in abundance of miR-30d-5p and miR-31-5p following the RNase only treatment. The decreases of the average abundance of miRNA controls could result in a false increase in the vtRNA relative fold changes. The seemingly high abundance of vtRNAs in the RNase + Triton X-100 and RNase + proteinase + Triton X-100 groups is likely due to the very low abundance of miRNAs detected.

When combining the above findings, a conclusion could be drawn that the majority of the vault components present in EV isolates from this study are not EV-associated. However, low levels of vtRNA were still detected following the RNase and proteinase treatment. This could be explained by incomplete digestion due to insufficient enzyme concentration or incubation time, which could be tested experimentally. It is tempting to speculate that a small proportion of vtRNA may in fact be contained within an EV lumen. We would expect these molecules to be resistant to RNase and proteinase treatment even at elevated enzyme concentration and prolonged incubation time.

Furthermore, although the vast majority of the vtRNA in EV preparations was not EV-associated, this could not be elucidated for the vtRNA fragments we observed in small RNA sequencing data. vtRNAs are naturally relatively small (~100 nt), and their fragments, which are similar in size to miRNAs, would be unsuitable for qPCR detection (Sajini *et al.*, 2019). Alternative detection methods attempted in Chapter 4 have also failed to detect these small fragments. Therefore, further investigation into vtRNA fragments still relies on highly sensitive techniques that require less input

material like RNA sequencing. Data obtained in this chapter has provided us with a better understanding of how vault particles contaminate EV preparations and can confound EV cargo 'omics' studies. One way to enable a confident validation of EV-related vtRNA is to develop a reliable EV isolation strategy that separates EVs from vaults, which has been illustrated in this chapter. Alternatively, preventing the intracellular assembly of vault particles could also result in vault-deficient donor cells and vault-free EV preparations that can be used for EV cargo characterisation studies.

5.4.2 Vault particles can contaminate EV preparations

Despite vault components having been repeatedly reported as EV cargo, vault particles were firstly identified and imaged as non-vesicular contents in crude EV isolates from colon cancer and glioblastoma cell lines in 2019 (Jeppesen *et al.*, 2019). By imaging 100k EV pellets with cryo-EM, we have observed similar non-EV associated vault-like structures in our DC preparations, suggesting their presence is likely to be universal rather than cell line-specific. In addition to being present in cell culture-derived EV preparations, vault components have also been found in EV isolates derived from multiple body fluids and tissues (Admyre *et al.*, 2007; Gonzalez-Begne *et al.*, 2009; Skogberg *et al.*, 2013; Pienimaeki-Roemer *et al.*, 2015), suggesting that their presence in the current study is not an artefact of *in vitro* cell culture. The mechanisms of how and why these particles are released by cells to the extracellular space remains unclear as there are no reports of active export or release of vault particles.

Vault particles are of a similar size to small EVs with overall dimensions of 70 nm × 40 nm × 40 nm. They were firstly discovered as a major contaminant in intraluminal vesicle preparation when centrifuging whole cell lysates at 100,000 × *g* (Kedersha and Rome, 1986). In this chapter, we determined the association of vault components with EVs isolated by three commonly used techniques. We firstly demonstrated vault particles can be co-isolated with EVs by DC, which could explain the reduced exosomal RNA level upon MVP knockout in some studies (Teng *et al.*, 2017). It seems that vaults are capable of contaminating EV pellets from 2k and 10k centrifugation steps even though we expect them to only be pelleted at high speed ultracentrifugation. This may be due to

particle aggregation at these speeds. Based on a study comparing EV yield using different centrifugal speed, higher speed (2500 × *g*) resulted in lower levels of EVs (compared to 1500 × *g*), suggesting the possible occurrence of particle aggregation even at low (~2000 × *g*) centrifugal speed (Vila-Liante *et al.*, 2016).

In addition to DC, SEC is one of the most utilised EV isolation methods. Vaults have been previously identified in non-vesicular fractions generated by density gradient ultracentrifugation (Jeppesen *et al.*, 2019). Although SEC was shown to yield comparably pure EVs to density gradient ultracentrifugation (Lobb *et al.*, 2015), we have shown that vault proteins were found in all the EV-rich SEC fractions. Despite SEC being the gold standard method of EV isolation, SEC-derived EVs from human plasma have also been shown to be contaminated with albumin and lipoproteins (Baranyai *et al.*, 2015; Stranska *et al.*, 2018). SEC has the advantage of timesaving and yielding more intact EVs (Monguió-Tortajada *et al.*, 2019). Similar to differential centrifugation, it is also a size based EV isolation technique. Although it does not involve the concentrating process under high centrifugal speed, our data suggests that vault particles can be co-eluted with EVs by SEC which is likely due to their similarity in size. Hence, researchers should be aware of the possibility of contaminants such as vaults when using SEC to enrich EVs.

Furthermore, ultracentrifugation has been proposed as a pre-enrichment step prior to further purification using magnetic beads (Pedersen, Kierulf and Neurauter, 2017). We demonstrated that a downstream purification step by Dynabead immunocapture failed to separate marker-positive EVs from vaults, implying the effect of high-speed centrifuge on particle aggregation in EV isolates can be persistent and irreversible.

Taking together, these findings provide evidence indicating that EV preparations may be frequently contaminated with vault particles (and their components) and that without further investigation they could be categorised as EV-associated molecules. Noticeably, this has been identified by the MISEV2018 guidelines as one of the main challenges that EV researches encounter. Hence, using biochemical approaches to further demonstrate the topological association with EVs was highly recommended (Théry *et al.*, 2018).

5.4.3 Isolating vault-free EVs by Dynabead immunocapture

Finally, we demonstrated an immunoaffinity-based isolation strategy using Dynabeads that separates vaults from EVs. From our experiments we were able to pull out the marker-positive EVs using magnetic bead/antibody complexes against specific well-defined EV markers and leave detectable vault proteins behind. Although Dynabead capture seems to be less cost-effective when compared to traditional methods like DC and SEC, it in fact generated isolated EVs that were detectable by western blotting from as little as 5 ml conditioned medium. In addition, immunocapture-derived EVs appeared morphologically intact by TEM, making them suitable for downstream analyses. This isolation strategy may aid research focusing on EV cargo in marker-positive EV subpopulations, and could also be used as a negative selection strategy to assist broader studies on other non-vesicular extracellular particles like vaults. All these features make this technique a competitive candidate when high-purity EVs are required from a small amount of starting material. It can be particularly useful in EV isolation from biological fluids as most body fluid-EVs are currently isolated by precipitation methods, which are prone to be crude and often contain aggregated contaminants (Musante *et al.*, 2012; Gámez-Valero *et al.*, 2016; Paolini *et al.*, 2016). While Dynabead isolation provides a solution to the above problems, it also inevitably has the drawback of being marker-specific and only isolating a certain subpopulation of EVs. However, with an increasing number of EV markers being rapidly revealed, a Dynabead cocktail containing antibodies against multiple markers may be a prospective solution.

Chapter 6 Investigating the effect of MVP on the extracellular transport of vtRNA in OSCC

6.1 Introduction

With the expansion of our knowledge concerning the different classes of RNAs being encapsulated in EVs, the underlying mechanisms explaining the intracellular packaging of RNA into EVs are also gradually being discovered. RNA-binding proteins (RBPs) have been shown to be largely involved in the sorting and packaging of coding and non-coding RNAs. There are currently a number of proteins that have been reported as RBPs in EVs isolated from multiple sources including hnRNP family members, YBX1, AGO2, ALIX, FUS, MVP, LIN28, QKI, TERT, and more (Fabbiano *et al.*, 2020). These RBPs were found in EVs either along with their substrate RNAs (e.g. hnRNPA2B1, YBX1, AGO2) or were detected alone (e.g. FUS, MVP) but the substrate RNA targets were predicted based on the enriched RNA recognition motifs (Kamelgarn *et al.*, 2016; Balaguer *et al.*, 2018; Sproviero *et al.*, 2018; Lee *et al.*, 2019). In other scenarios, RNA transcripts were found in the EVs containing the sequence motifs mirroring RBP activities, such as QKI and LIN28 (Wang *et al.*, 2017; Alicka *et al.*, 2019).

MVP was firstly suggested as an RBP by Teng *et al*. in 2017 (Teng *et al.*, 2017). By analysing the miRNA distribution patterns in exosomes isolated from primary mouse colon cancer, colon cancer liver metastases, and naive colon tissues, the authors reported the highest level of tumour-suppressive miR-193a in metastasis-derived exosomes, which interacted with MVP. In addition, MVP knockout resulted in the accumulation of miR-193a in cells rather than in exosomes, leading to repressed tumour growth (Teng *et al.*, 2017). These results suggested the selective extracellular sorting of miRNA was possibly mediated by MVP, contributing to a tumourgenic phenotype. The effect of MVP on EV-RNA was further evidenced upon MVP silencing, which caused a ~50% decrease in total exosomal RNA level (Statello *et al.*, 2018). In this study, the RNA-binding property of MVP was validated via an RNA-pull-down assay performed on exosomes derived from biotinylated MVP-

expressing donor cells. Moreover, the transfection of MVP in cells also caused higher recovery of exosomal RNA compared to non-transfected cells, which indicated the potential involvement of MVP in the sorting of miRNA and mRNA species into EVs (Statello *et al.*, 2018).

On the other hand, extracellular MVP, together with full-length vtRNA, have been shown to be non-EV associated in the form of intact vault particles, evidenced by Jeppesen *et al*. (2019) and this current study. These results contradicted the observation that MVP was found in EVs as an RBP (Statello *et al.*, 2018), however they could not rule out the possibility that MVP can work as a cellular modulator for small RNA sorting into EVs thus contributing to the changes in total extracellular RNA profile mentioned above. Furthermore, although the majority of the full-length vtRNA was proven to be non-exosomal, the repeated discovery of small vtRNA or vtRNA fragments in EVs suggested a potential trafficking and sorting mechanism prior to their detection in the extracellular space. However, this is currently unknown and requires further research (Nolte'T Hoen *et al.*, 2012; van Balkom *et al.*, 2015; Jeppesen *et al.*, 2019).

MVP knockout has been shown to prevent the assembly of vault particles, due to it being the major and structural component of the complex (Kickhoefer *et al.*, 1998; Berger *et al.*, 2009). Meanwhile, MVP deficient mice showed no observable abnormalities, suggesting it is unlikely to be involved in fundamental life activities (Mossink *et al.*, 2002). Here we attempted to generate vault-deficient OSCC cells by knockdown/knockout of MVP. EVs isolated from such cells should not be contaminated with vault particles even if they were isolated by less stringent techniques such as differential centrifugation. Furthermore, removing the confounding factor of full-length vtRNA carried by intact vaults (that we have shown contaminate EV preparations) would allow an assessment of vtRNA and their fragments in EVs.

6.2 Results

6.2.1 MVP silencing by siRNA transfection

6.2.1.1 The effect of MVP silencing on vault components in cells

To determine whether the small RNAs in EV preparations would be affected by the disruption of MVP (and therefore vault particles), MVP expression in OSCC cells was firstly silenced by transient siRNA transfection. The transfection experiments were performed in SCC4 cells because of their high EV yield and high cellular MVP expression among the OSCC cell panel, as determined in previous experiments.

The transfection of SCC4 cells with MVP siRNA resulted in an 11-fold decrease in cellular MVP transcript expression ($p < 0.01$) compared to the negative control siRNA (Figure 6.1A), whereas no significant change was observed in TEP1 and PARP4 expression tested by TaqMan qPCR (Figure 6.1B, C). Furthermore, with vtRNA 1-1 and vtRNA 1-3 being the most abundant paralogs in SCC4 cells, their transcript levels also showed a significant increase ($p < 0.05$) in MVP siRNA-transfected cells (Figure 6.1D, F), but no statistical significance was observed in vtRNA 1-2 and vtRNA 2-1 (Figure 6.1E, G). The effect of MVP knockdown on other small RNA (with no reported relationship in the literature) was also assessed by using miR-23a-3p as an example. There was no statistically significant difference in expression between MVP silenced and control cells (Figure 6.1H).

Next, gene expression data was validated at the protein level by western blotting. Transfection of SCC4 cells with MVP siRNA resulted in an over 50% decrease of MVP protein abundance compared to the negative control ($p < 0.01$) (Figure 6.2A). Similar to the gene expression data, no significant change was observed in TEP1 and PARP4 proteins abundance (Figure 6.2B,C).

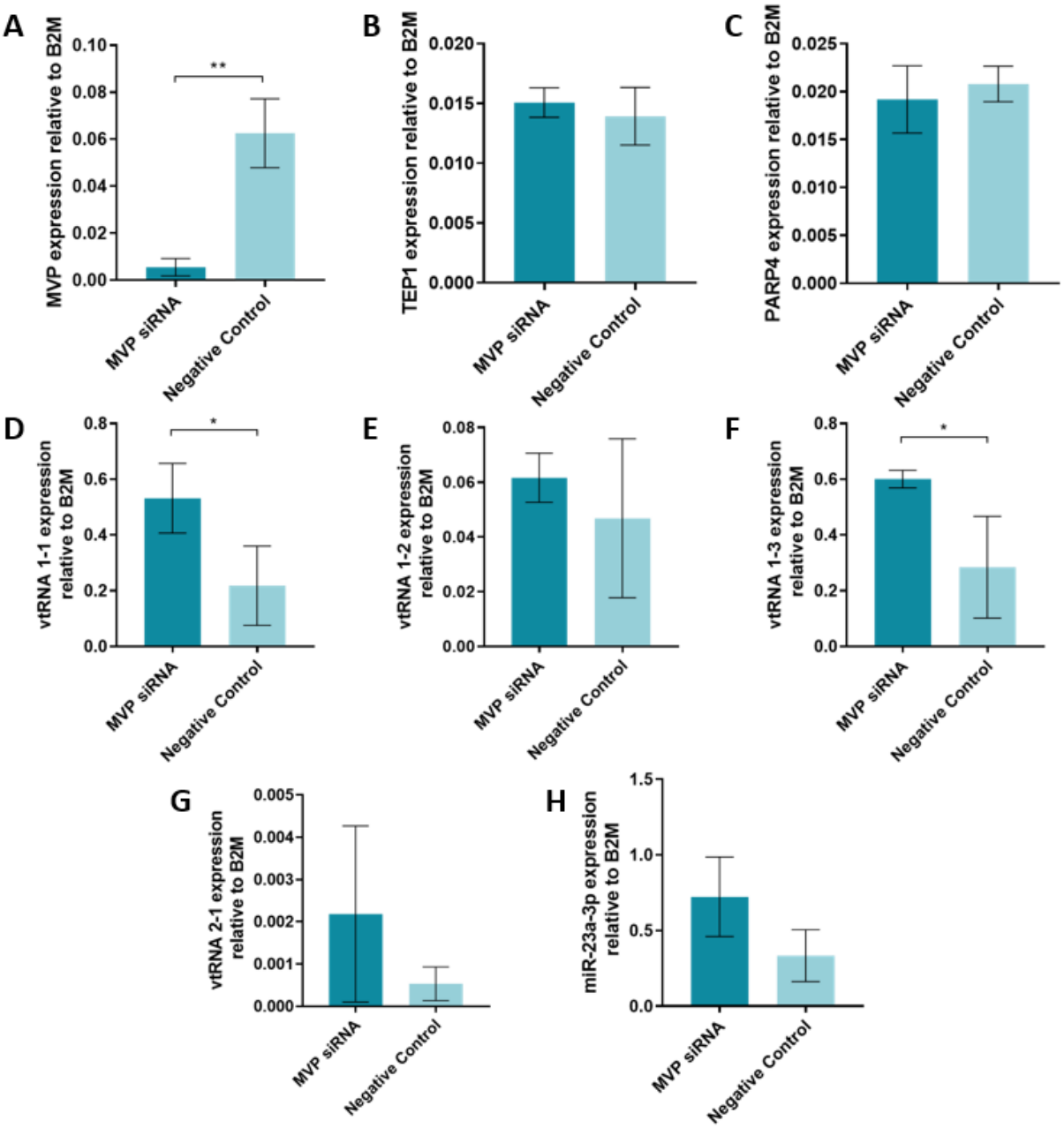

Figure 6.1 Altered cellular gene expression of vault components after knockdown of MVP.
Following transfection with either MVP-silencing siRNA or negative control siRNA, the cellular expression of **A)** MVP, **B)** TEP1, **C)** PARP4, **D)** vtRNA1-1, **E)** vtRNA1-2, **F)** vtRNA1-3, **G)** vtRNA2-1, and **H)** miR-23a-3p in SCC4 cells were determined by qPCR using TaqMan primers with B2M as an endogenous control. Data shown are means ± SD, n=3. *$p < 0.05$, **$p < 0.01$ by Student's t-test.

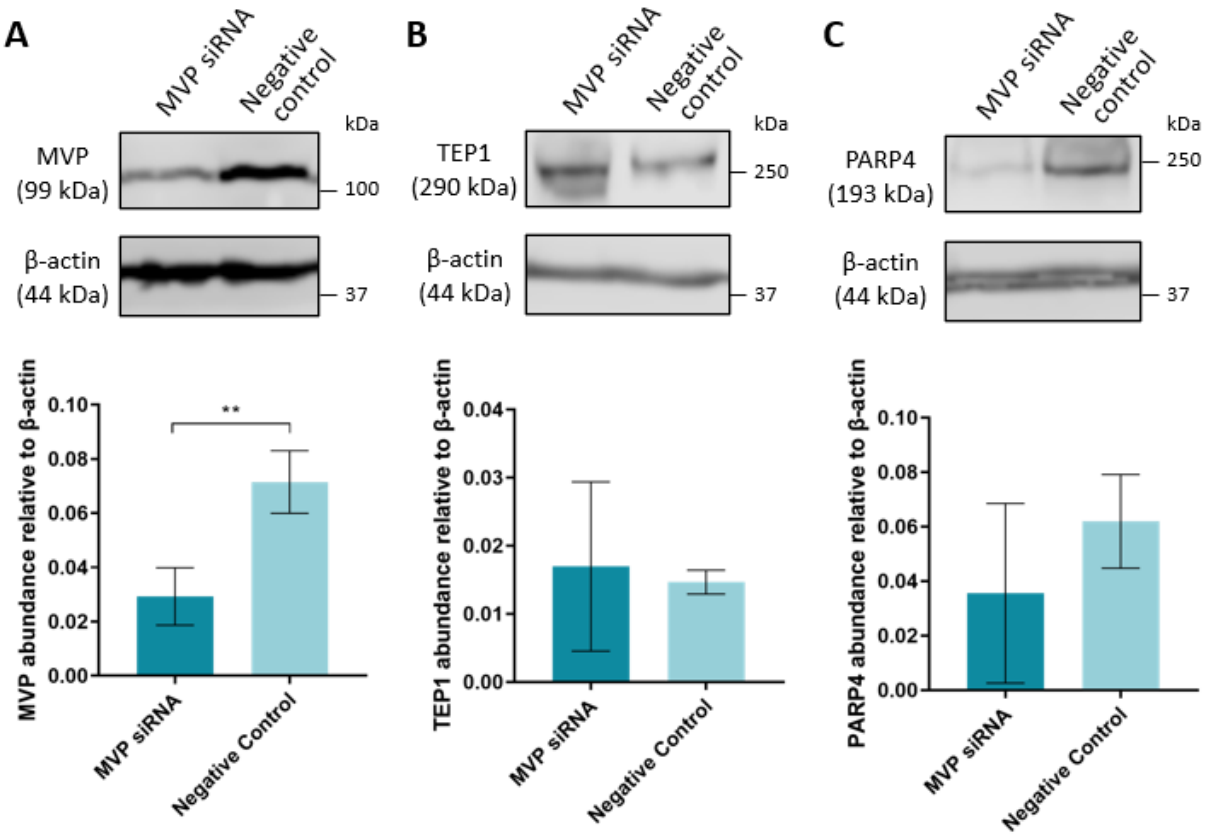

Figure 6.2 Altered abundance of vault proteins following MVP knockdown.
Representative images and densitometry of western blot for **A)** MVP, **B)** TEP1, and **C)** PARP4 following transfection with MVP siRNA or negative control siRNA. Data shown are means ± SD, n=3. $^{**}p < 0.01$ by Student's t-test.

6.2.1.2 The effect of MVP silencing on vtRNA in EV pellets

To understand the effect of MVP knockdown on extracellular vtRNA abundance, the conditioned medium from transfected SCC4 cells of both experimental groups was collected and processed by differential centrifugation to obtain 2k, 10k, and 100k pellets enriched with extracellular particles (EPs) including EVs. Although we were aware that the vtRNA abundance in these pellets may be still affected by vault contaminants (as MVP was not fully eliminated from the parental cells) it was anticipated that the extracellular vtRNA abundance would still be reduced in response to MVP knockdown.

As observed previously, vtRNAs appeared enriched in EP pellets compared to their cellular abundance, although the vtRNA abundance in cells and EPs were normalised using different endogenous controls (Figure 6.3). For vtRNA 1-1 and vtRNA 1-3, the majority of these vtRNA were

found in 100k pellets, with a significant decrease seen between EPs from MVP knockdown cells compared to the negative control. In 2k and 10k pellets, the abundance of these two vtRNAs were very low with no significant difference between the transfection groups observed (Figure 6.3A, C). The next most abundant paralog was vtRNA 1-2, which was found mostly in 2k and 100k EP pellets. Similar to other vault particle-associated vtRNAs, decreased vtRNA 1-2 abundance was only detected in 100k pellets in comparison to the negative control (Figure 6.3B). vtRNA 2-1 was in general detected at very low levels in cells and in all EP pellets, with the least being detected in 100k pellets. qPCR data shown for this vtRNA was not complete as the abundance was below the detection limit in some samples, therefore no statistical test was performed for this vtRNA (Figure 6.3D). Furthermore, the abundance of the three miRNAs in the pellets in response to MVP knockdown in the donor cells was also determined. Compared to the negative control group, miR-23a-3p showed decreased abundance ($p < 0.05$) in MVP-silenced 2k pellets (Figure 6.3E), whilst miR-30d-5p was seen decreased in 2k and 100k pellets ($p < 0.01$ and $p < 0.05$, respectively) (Figure 6.3F). No changes were observed in miR-31-5p abundance in the MVP-KD EP pellets (Figure 6.3G).

Overall, MVP knockdown using siRNA transfection resulted in a significant reduction in cellular MVP level, whilst other vault proteins were not affected. This also had impact on cellular vtRNA abundance as an increase was seen in vtRNA 1-1 and vtRNA 1-3 levels in cells with silenced MVP expression. MVP knockdown in parental cells led to a significant reduction in vtRNAs 1-1, 1-2 and 1-3 in 100k EP pellets.

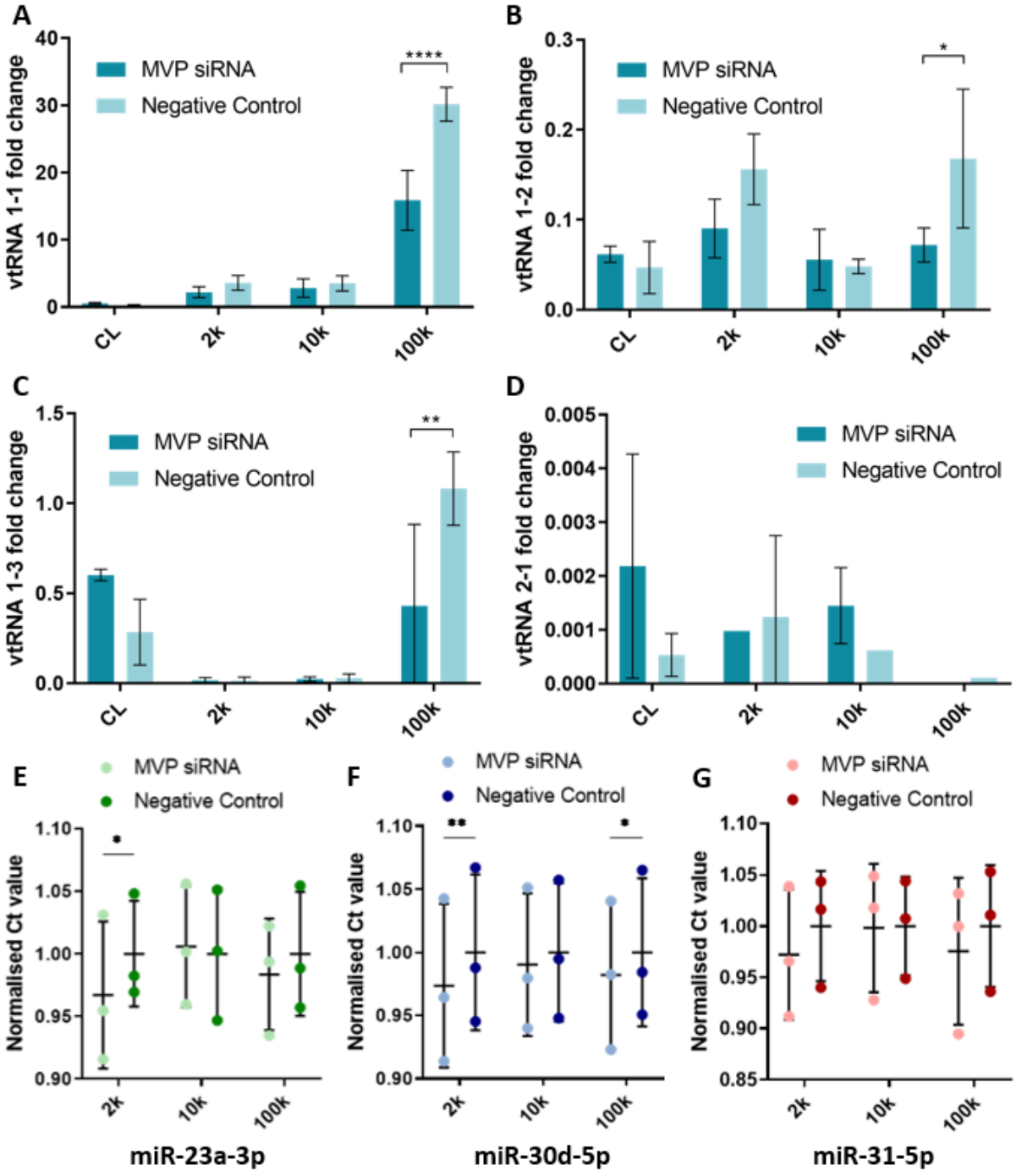

Figure 6.3 vtRNA abundance in cells and EP pellets following MVP knockdown.
Abundance of **A)** vtRNA1-1, **B)** vtRNA1-2, **C)** vtRNA1-3, and **D)** vtRNA2-1 in SCC4 cell line transfected with MVP siRNA or negative control siRNA was determined by TaqMan qPCR, normalised to cellular B2M expression. The conditioned medium was collected from both transfection groups and was processed by differential centrifugation to pellet EPs. vtRNA in 2k, 10k, and 100k EP pellets were determined by qPCR, average abundance of three miRNAs (miR-23a-3p, miR-30d-5p and miR-31-5p) was used as endogenous control for data normalisation. miRNA transcript levels of **E)** miR-23a-3p, **F)** miR-30d-5p, and **G)** miR-31-5p in 2k, 10k, and 100k pellets from MVP or negative control siRNA-transfected donor cells. Data shown are means ± SD, n=3(except for vtRNA 2-1, data fell below the detectable range). *$p < 0.05$, **$p < 0.01$, ****$p < 0.0001$ by two-way ANOVA with Šídák's multiple comparisons test.

6.2.2 MVP knockout in OSCC

6.2.2.1 CRISPR-Cas9 gene editing

Using siRNA transfection, we obtained evidence suggesting that reduced MVP expression in cells could contribute to altered distribution of vtRNA in cells and pellets containing extracellular particles. However, siRNA transfection can only provide insights for the short-term effects. To better understand the impact of MVP on the normal expression of other vault components, and the possible role MVP/vault particles play in extracellular export of small RNA, in particular vtRNA, we performed CRISPR-Cas9 gene editing in OSCC cells to permanently knockout MVP. The knockout experiments were carried out in two OSCC cell lines, H357 and SCC4, to rule out cell-line specific effects. They were chosen for their high and reproducible EV yield, high cellular expressions of most vault components, and transfection protocols established previously in our research group.

The CRISPR gene editing workflow was summarised in Figure 2.6. Pre-designed primers amplifying a 903 bp sequence within the MVP gene containing the protospacer adjacent motif (PAM) site for Cas9 cleavage were tested for efficiency, where a band at ~900 bp was observed, indicating the designed MVP primers amplified the CRISPR target region from the normal H357 genome (Figure 6.4A).

The mutation caused by gene editing events was detected via successful T7EI recognition and cleavage of mismatched DNA heteroduplexes, where the full-length amplicon and two different sized cleavage products were observed. As shown in Figure 6.4B lane 10, heteroduplex and homoduplex DNA formed by control A and control B PCR products (which contain a 6 bp mismatch) was cleaved by T7EI, resulting in two bands showing cleaved products of 268 bp and 442 bp, as well as the uncleaved homoduplex band at 670 bp. Whereas in lane 9, loading with control A showed only full-length products, suggesting no digestion activity of the T7EI enzyme occurred.

In our CRISPR experiments carried out in H357 (Figure 6.4B, blue lanes) and SCC4 (Figure 6.4B, yellow lanes) cells, T7EI cleavage was observed in the HPRT+ controls in both cell lines (lane 3 and lane 7), reflected by cleaved fragment bands at 256 bp and 827 bp. Meanwhile, only bands indicating

full-length amplicon at 1083 bp was seen in the HPRT− controls in both cell lines (lane 4 and lane 8). This suggested both HPRT controls for CRISPR editing worked as expected, and the amplicon cleavage results from T7EI assay can be trusted as indication for successful gene editing events. Similar cleavage results were observed in the MVP-RNP transfected group in both cell lines (lane 1 and lane 5) where full-length MVP amplicon bands (~900 bp) and cleaved fragment bands (~650 bp and ~250 bp) were observed (Figure 6.4B). In SCC4 negative control cells transfected with Cas9 enzyme, only full-length amplicon band was observed (Figure 6.4B, lane 6), suggesting no occurrence of genome mutation. However, in H357 negative control (Figure 6.4B, lane 2), bands suggesting cleaved products were observed despite no guide RNA being transfected into the cells. The sizes of the fragments were slightly different to those in lane 1 and lane 5, where MVP-RNP was transfected, the reason for this is unclear (Figure 6.4B).

Whilst half of the transfected cells were used for confirmation of gene editing events by T7EI assay, the other half were serial diluted in suspension and eventually seeded in 96-well plates at 1 cell per well. Cells were maintained in penicillin-streptomycin-free normal growth medium until colonies started to appear in the wells. The colonies were closely monitored to make sure they originated from single cells whilst being further expanded. Finally, 7 H357 clones and 1 SCC4 clone from the MVP knockout groups were obtained. To screen the clones for complete functional MVP knockout, total cellular protein from the putative MVP-KO clones and WT cells was analysed by western blotting for MVP and β-actin (Figure 6.4C). From all 7 clones obtained from H357 cells, 6 displayed complete MVP protein depletion (lane 2-7), only one (lane 8) was found to have a similar level of MVP expressed as in H357 WT cells. The SCC4 MVP-KO clone also showed no MVP protein expression, however it did not survive further expansion into a cell line (Figure 6.4C). Therefore, our CRISPR-Cas9 gene editing to knockout MVP in OSCC cells resulted in six H357-MVP-KO cell lines that produced no detectable MVP protein.

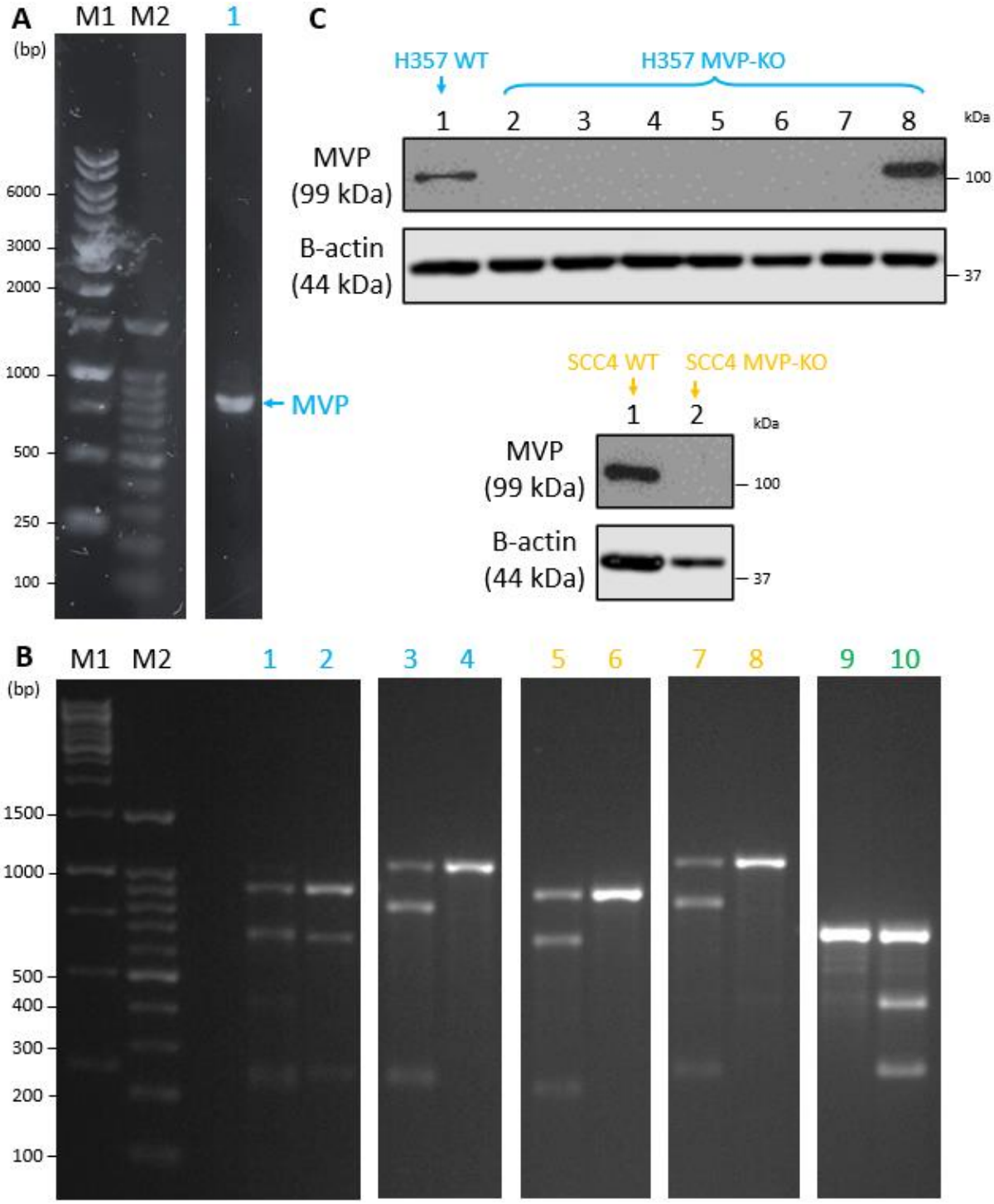

Figure 6.4 Validation of CRISPR knockout of MVP in OSCC cells.
A) PCR was conducted using genomic DNA extracted from wildtype (WT) H357 and primers designed to amplify a 903 bp-sized product from MVP gene. Lane M1 and M2: GeneRuler 1 kb and 100 bp DNA ladders (Thermo Fisher Scientific), respectively; lane 1: PCR products separated on a 2% (w/v) agarose gel showing bands indicating the correct size product. **B)** CRISPR-Cas9 gene editing in OSCC cells was confirmed by T7EI digestion following PCR amplification with MVP primers using gDNA from transfected cells and heteroduplex/homoduplex formation, digested products were separated on a gel. Lane M1 and M2: GeneRuler 1 kb and 100 bp DNA ladders (Thermo Fisher Scientific), respectively. Blue lanes are gDNA from H357 cells transfected with ribonucleoprotein complexes composing Cas9 enzyme and MVP guide RNA (lane 1), HPRT positive guide RNA (lane 3), and HPRT negative guide RNA (lane 4) or Cas9 only (lane 2). Yellow lanes (lane 5-8) are gDNA from SCC4 cells with same order in H357. Green lanes are homoduplex control (lane 9) and heteroduplex control (lane 10) for T7EI digestion. **C)** Western blot validation of MVP knockout (MVP-KO) in H357 and SCC4 cells. 10 µg total protein was loaded per lane, n=1.

6.2.2.2 The effect of MVP knockout in OSCC cells

All six MVP knockout cell lines were further passaged and tested again to confirm loss of MVP protein expression before they were stored in liquid nitrogen for later studies. Out of the six mutants, two (H357-MVP-A8 and H357-MVP-D6) were selected for carrying out further experiments in this study because of their similar morphology and growth speed to the H357 WT cells in their early passages. The MVP-KO cell lines displayed polygonal morphology, measuring ~40-60 μm in diameter, visually similar to the parental H357 WT cells (Figure 6.5A).

MVP is the major component of the vault particle. Therefore, after confirmation of functional MVP knockout, we also assessed how this would affect other vault proteins in the MVP-KO cells (Figure 6.5B). TEP1 and PARP4 proteins showed lower abundance in MVP-KO cells than WT cells, with PARP4 reduction being statistically significant ($p < 0.01$) in both cell lines. Specifically, H357-MVP-A8 cells did not show significant changes in TEP1 expression as H357 WT cells whilst no PARP4 can be visually observed by western blot for this cell line (Figure 6.5C, D).

In addition to protein abundance, we also determined the expression of all vault components in the WT and MVP-KO cells at the transcript level by TaqMan qPCR (Figure 6.6). Although MVP protein was absent in the knockout cell lines, we only observed a significant decrease ($p < 0.0001$ for H357-MVP-A8 and $p < 0.05$ for H357-MVP-D6) in MVP mRNA levels in both MVP-KO cell lines (as opposed to a complete loss of expression) (Figure 6.6A). TEP1 transcript levels were slightly increased in the H357-MVP-A8 cells ($p < 0.01$) compared to the WT cells (Figure 6.6B). Both MVP-KO cell lines also showed significantly lowered ($p < 0.05$) PARP4 transcript expression, consistent with the observed decreased PARP4 protein abundance (Figure 6.6C).

No significant changes in vtRNA abundance were observed between H357 WT and MVP-KO cells (Figure 6.6D-G).

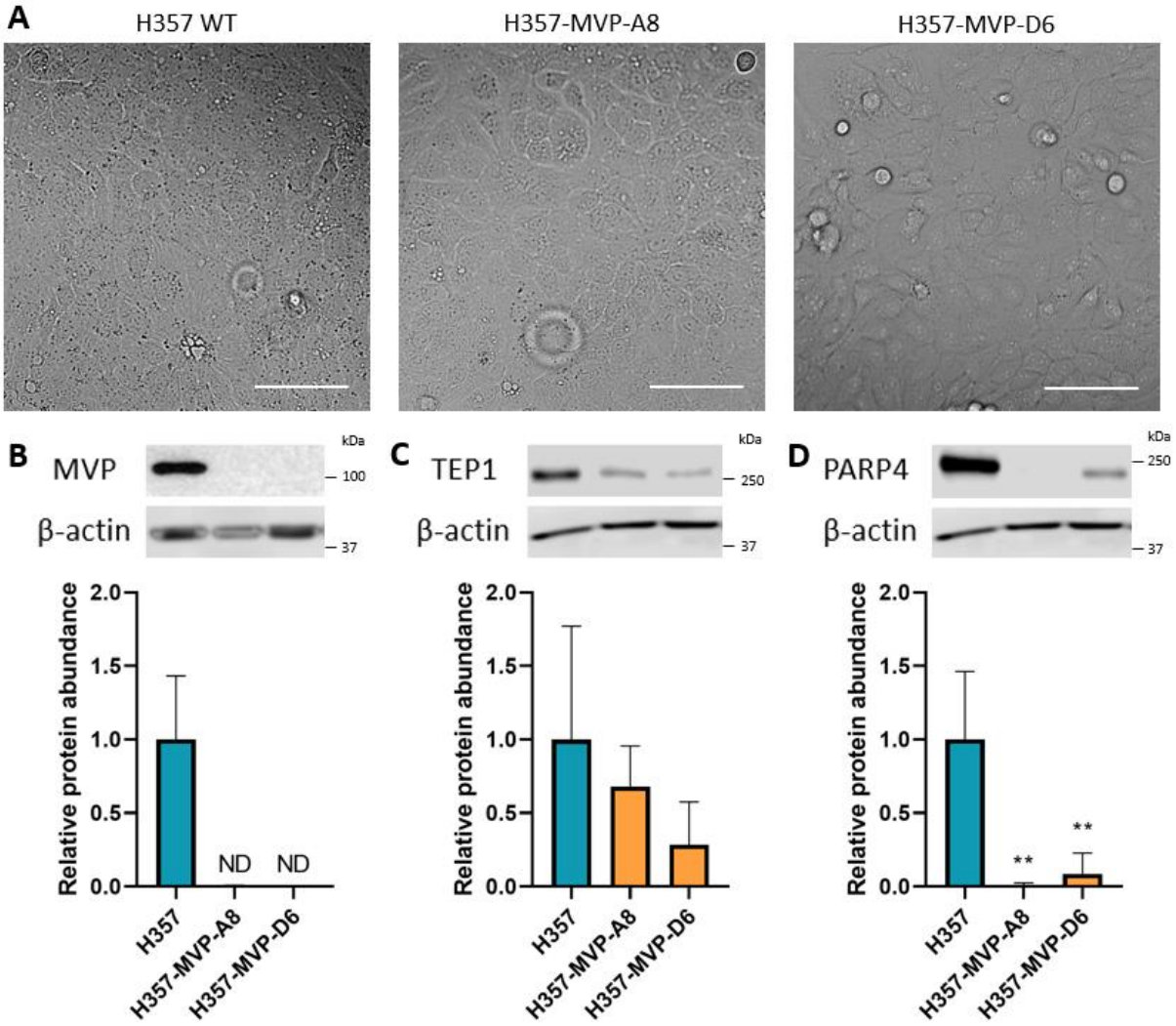

Figure 6.5 The effect of MVP knockout in H357 cells.
A) Cell images of H357 WT and MVP-KO cell lines (H357-MVP-A8, H357-MVP-D6) at 100% confluency. Scale bars indicate 100 µM. Representative western blot images and densitometry showing the relative abundance of **B)** MVP, **C)** TEP1, and **D)** PARP4 in H357 MVP-KO cells compared to H357 WT. Vault protein abundance was normalised to β-actin before relative abundance was calculated. Data shown are means ± SD, n=3. ND = not detected. $^{**}p < 0.01$ by Dunnett's multiple comparisons test.

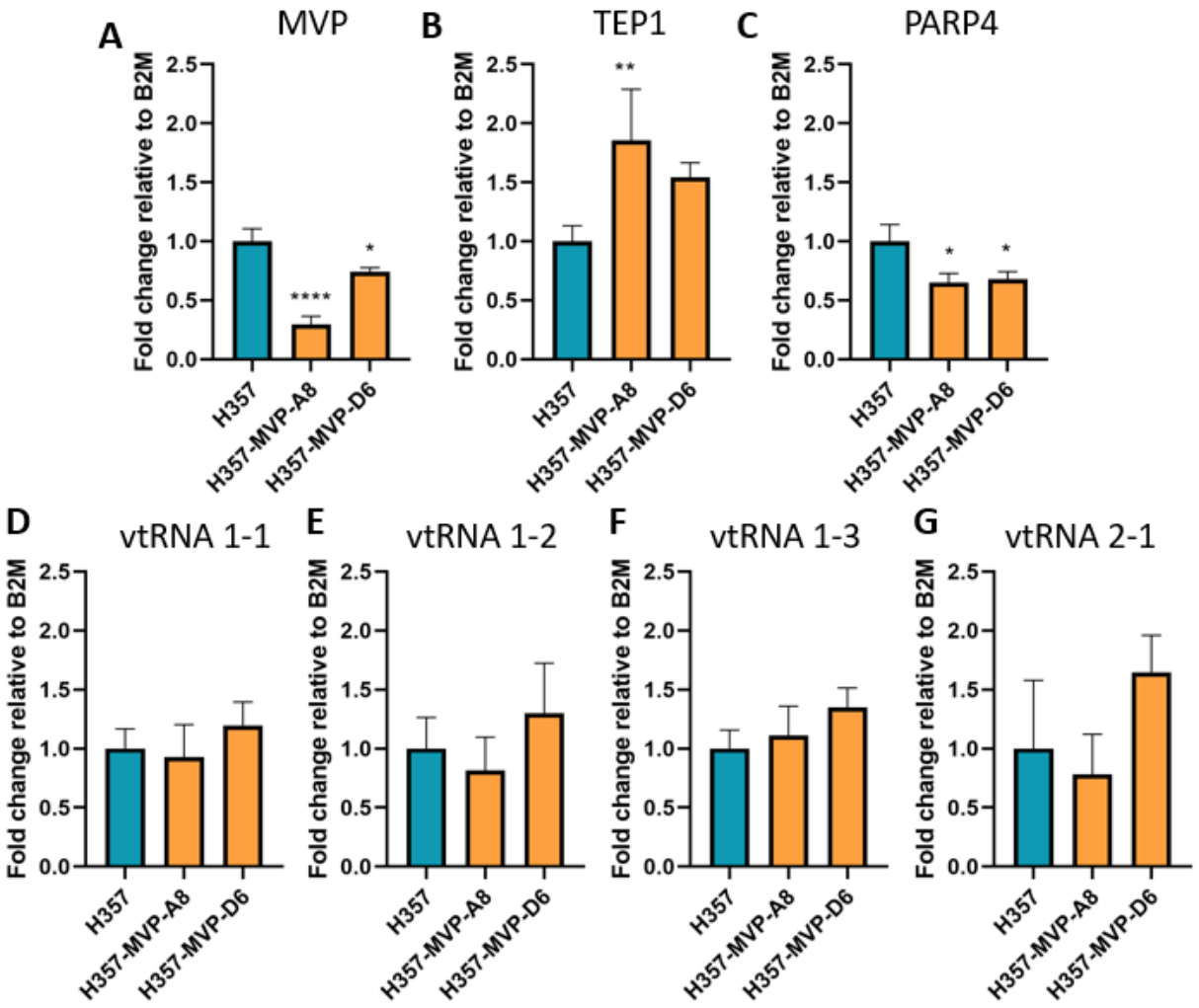

Figure 6.6 qPCR detecting vault components transcripts in H357 and H357 MVP-KO cells.
The transcript abundance of **A)** MVP, **B)** TEP1, **C)** PARP4, **D)** vtRNA1-1, **E)** vtRNA1-2, **F)** vtRNA1-3, and **G)** vtRNA2-1 in H357 WT and H357 MVP-KO cells (H357-MVP-A8 and H357-MVP-D6) was measured by TaqMan qPCR assay. Data shown are means ± SD, n=3. *$p < 0.05$, **$p < 0.01$, ****$p < 0.0001$ by Dunnett's multiple comparisons test.

6.2.2.3 Assessment of EVs derived from MVP knockout cell lines

To investigate whether MVP knockout in OSCC cells had an impact on EVs we characterised the particle concentration and protein markers of EV isolates from H357 WT and MVP-KO cells. Conditioned media from H357 WT and H357 MVP-KO cell lines were subject to differential centrifugation, resulting in 2k, 10k, and 100k pellets enriching different EV subpopulations.

Firstly, 100k pellets derived from H357 WT cells and H357-MVP-A8 cells were loaded on a Flow NanoAnalyzer (NanoFCM), where the particle counts were analysed by Dr Ben Peacock. 100k pellets were chosen for analysis due to the enrichment of vault components seen in previous experiments.

Loss of MVP (and therefore vault particles) should be most evident in these pellets. 100k pellets from H357-MVP-A8 resuspended in PBS had significantly lower ($p < 0.01$) particle concentration than those from WT cells (Figure 6.7A). Due to the time limit of the experiment, only H357-MVP-A8 cells were assessed for extracellular particle concentration as a representative of H357 MVP-KO cells.

Next, to understand whether MVP deficiency in parental cells would result in changes in detectable vault components within extracellular particles, all vault proteins were probed alongside common EV markers in pellets derived from H357 WT and MVP-KO cell lines (Figure 6.7B). All vault proteins were detected in 100k pellets from H357 WT cells, where they were found most enriched previously, but not in 10k pellets. Low abundance of MVP was also seen in 2k pellets from the WT cells. Whereas in all pellets derived from both MVP-KO cell lines, none of the vault proteins were detected. In addition, western blot of three common EV markers detected similar patterns of protein abundance across all three cell lines tested: CD63 positive bands ranged from 25-75 kDa (due to its heavily glycosylated forms) and was of similar abundance in 2k and 100k pellets from in cell lines. However, only a single high molecular weight band, which could represent its fully glycosylated form, was evident 10k pellets. Probing for CD9 resulted in two bands around 25 kDa in all pellets, with enrichment in 2k and 100k pellets. TSG101 was mostly detected in 100k pellets from H357 WT and H357-MVP-A8 cells, however faint bands were also observed in H357 WT 2k, H357-MVP-A8 2k, H357-MVP-D6 2k and 100k pellets (Figure 6.7B).

In summary, these results suggested 100k extracellular particle pellets derived from MVP-KO cell line contained less particles than those from WT cells. Additionally, they also contained no vault proteins but comparable levels of EV markers when compared to WT pellets.

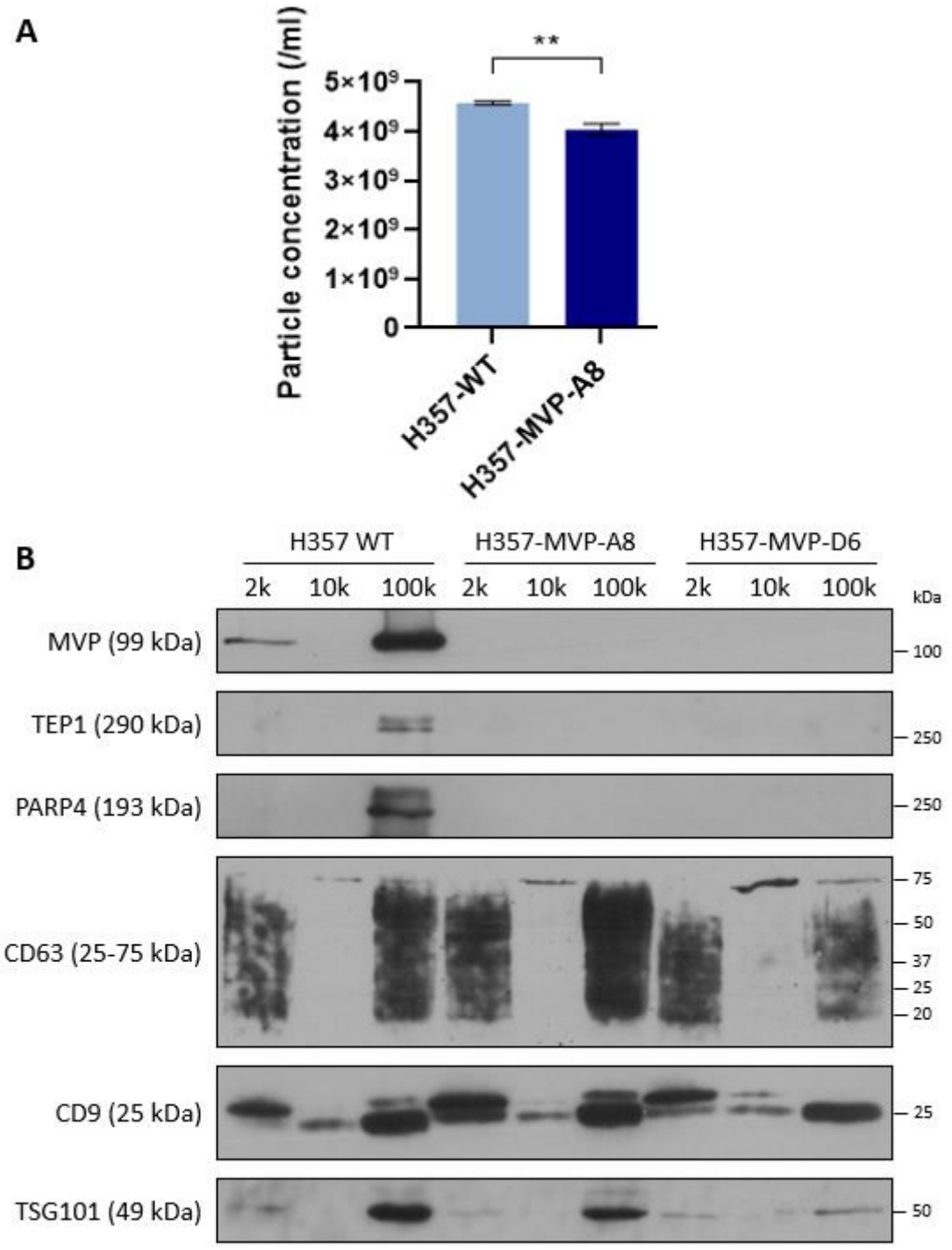

Figure 6.7 Assessment of EVs derived from H357 WT cells and MVP-KO cells.
A) Particle counts per ml of resuspended 100k pellets derived from H357 WT cells and H357-MVP-A8 cells by differential centrifugation. Data shown are means ± SD, n=3. $^{**}p < 0.01$ by Student's t-test. **B)** Western blots detecting vault proteins (MVP, TEP1, and PARP4) and EV markers (CD63, CD9, and TSG101) from 2k, 10k, and 100k pellets derived from H357 WT cells and H357 MVP-KO cells by differential centrifugation. Images shown are representative images of three biological repeats for MVP and CD63, and the result of one biological repeat for the other proteins.

6.2.2.4 Assessment of the impact of MVP-KO in donor cells on small RNA in EVs

Next, the established MVP-KO cells were utilised as a tool to examine the presence of any vtRNA and vtRNA fragments in OSCC-EVs. The experimental workflow was summarised in Figure 6.8. In brief, 15 ml conditioned medium from H357 WT cells and MVP-KO cells (H357-MVP-A8) was collected and subject to differential centrifugation. The conditioned medium was centrifuged at 2,000 × *g* and 10,000 × *g* before the supernatant was further centrifuged at 100,000 × *g* and 100k pellets were obtained. Meanwhile, another 15 ml conditioned medium from WT cells were subject to direct immunocapture by incubating with CD9/CD63/CD81 Dynabead cocktail. Following overnight incubation and several wash steps, the bead-bound EVs were collected. 100k pellets from both cell lines following differential centrifugation and Dynabead-captured EVs from WT conditioned medium were lysed with RNA lysis buffer. Only 100k pellets were included in the RNA sequencing experiment due to limited sample space and high EV and vault abundance compared to other pellets. RNA was then isolated with a Norgen Total RNA miniprep kit with an on-column DNase treatment. The integrity of isolated RNA was firstly checked on an Agilent 2100 Bioanalyzer prior to RNA sequencing.

Unfortunately, at the time of thesis submission the RNA sequencing and data analysis had not been completed due to delays in delivery of essential library preparation reagents.

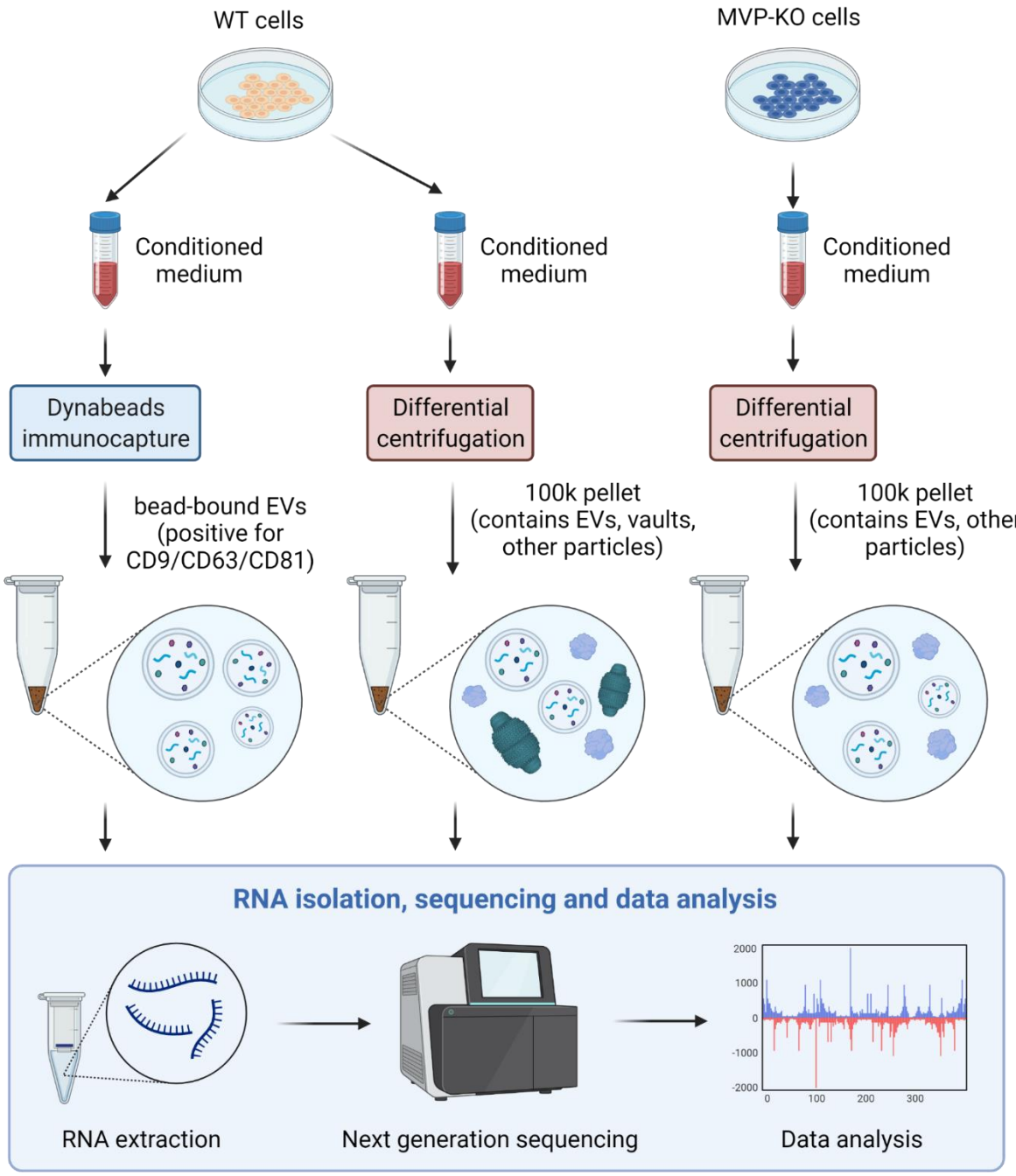

Figure 6.8 Schematic illustration of RNA sequencing experimental design.
Workflow of RNA sequencing experiment of WT and MVP-KO cell derived EVs. Conditioned medium from H357 WT cells and MVP-KO cells (H357-MVP-A8) will be subject to differential centrifugation to obtain 100k pellets. Meanwhile, WT-conditioned medium will also be processed for immunocapture and incubated with CD9/CD63/CD81 Dynabeads cocktail, bead-bound EVs following incubation will be collected. All EV preparations will then be subject to total RNA isolation, which will then be used for RNA sequencing.

6.3 Discussion

6.3.1 The effect of MVP knockdown in OSCC

In this chapter, we firstly determined the effect of MVP silencing on other vault components using siRNA transfection in OSCC. Within the transfected cells, knockdown of MVP by siRNA transfection showed a significant decrease in MVP expression at both RNA and protein levels, whilst TEP1 and PARP4 expression were unaffected. In the literature, siRNA knockdown experiments of vault proteins in several drug-resistant ovarian and colon cancer cell lines reported cell line-dependent effects on the expression of other vault proteins and cell viability (Wojtowicz *et al.*, 2017). For example, in two topotecan-resistant ovarian cancer cell lines, lower MVP and PARP4 protein abundance were seen when treated with either MVP siRNA or PARP4 siRNA, whereas in doxorubicin-resistant colon cancer cells, PARP4 was absent in response to MVP knockdown, but a similar effect was not observed the other way around (Wojtowicz *et al.*, 2017). These results suggested although the effect of vault protein knockdown seemed to differ between different cell lines and cancer types, a common observation from this drug-resistant cell panel was that MVP knockdown by siRNA always caused reduced PARP4 abundance (as measured by western blotting without quantification). In our study, a similar trend was observed by western blot showing that PARP4 seemed more responsive to MVP knockdown in comparison to another vault protein TEP1. However the change in PARP4 protein was not statistically significant due to variation between biological repeats, which could be caused by different transfection efficiencies amongst the repeats.

In addition to the impact on other vault proteins, MVP knockdown has been shown to also affect cell proliferation and apoptosis in cancers (Pasillas *et al.*, 2015; Lee *et al.*, 2017; Bai *et al.*, 2019). For instance, RNAi-introduced MVP knockdown resulted in accelerated proliferation and suppressed apoptosis in lung cancer cells, whilst induced apoptosis was reported in hepatocellular carcinoma and breast cancer cells (Pasillas *et al.*, 2015; Lee *et al.*, 2017; Bai *et al.*, 2019). The contradiction can be explained by the multiple mechanisms MVP is involved in. In this study, we did not investigate these phenotypes in OSCC cells due to our focus was the effect of MVP silencing on extracellular vtRNA.

However, due to the major implications active cell growth and apoptosis can have on EV release and cargo sorting, it would be valuable to take these factors into account in any future experiments.

Furthermore, cellular vtRNA 1-1 and 1-3 expressions determined by TaqMan primers showed a significant increase in response to the silencing of MVP, which may suggest a role for MVP in extracellular export of vtRNAs. Extracellularly, a decrease in the vtRNA levels in 100k pellets derived from differential centrifugation was observed in all vault-associated vtRNA paralogs, whist no significant changes were found in 2k and 10k pellets. These results suggested the vtRNAs enriched in the 100k pellets of EPs were the most responsive to decreased MVP level in the parental cells. Combining with our findings from Chapter 5, this observation can be explained by the reduction of extracellular vault particles upon MVP knockdown in the donor cells, which were found mostly enriched in the 100k pellets. It also provided partial evidence suggesting that cells with complete MVP knockout should no longer secret vault particles into the extracellular space, therefore, they could be the ideal model for investigating the possible EV-enclosed vtRNA and/or vtRNA fragments.

Apart from vtRNA, MVP knockdown in SCC4 cells also resulted in lower abundance of some miRNA in the EP pellets. Two out of three miRNAs used as endogenous control for extracellular small RNA quantification were found decreased in 2k pellets from MVP-KD cells, in which miR-50d-5p was also found reduced in 100k pellets. Another study also reported a lower level of miR-193a was found in exosomes derived from MVP knockdown cells, along with inversely correlated abundance in the parental cells (Teng *et al.*, 2017). In our experiments, although the increased expression of miR-23a-3p in MVP-KD cells was not statistically significant, we have also observed similar accumulation in MVP-deficient cells in vtRNA. Collectively, these observations suggest that MVP knockdown may cause the intracellular accumulation of some small RNAs and a corresponding decrease in EVs, suggesting a potential MVP-dependent mechanism of small RNA export. Additionally, the same study also reported a global decrease of exosomal RNA levels following MVP knockdown in parental cells. The authors have linked this to a major role that MVP plays as an RBP facilitating many small RNAs sorting into EVs (Teng *et al.*, 2017). However, Jeppesen *et al*. have reported that extracellular

MVP is vault-associated, and therefore is unlikely to serve as an RBP to be detected in EVs (Jeppesen *et al.*, 2019).

6.3.2 Establishment of MVP-KO cell lines using CRISPR-Cas9 technology

In the previous chapters, we demonstrated co-isolated vault particles can be a major contamination source to EV preparations, hence they can heavily confound the genuine EV-related small RNA population. We also reported the presence of enriched vtRNA fragments in OSCC-derived EV preparations, as observed previously in other biological samples (Persson *et al.*, 2009; Hussain *et al.*, 2013; Li *et al.*, 2013; van Balkom *et al.*, 2015). Following the unsuccessful attempts to validate vtRNA fragments in EVs described in Chapter 4, we then decided to apply an indirect approach to achieve the same objective in this chapter. As the main structural component of vaults, the disruption of MVP has previously been used to prevent the assembly of the vault particle (Berger *et al.*, 2009). Vault formation is largely dependent on the expression of MVP rather than the minor vault proteins (TEP1, PARP4), suggesting that the presence of MVP is the prior condition for vault particle being assembled (Kickhoefer *et al.*, 1998). By knocking out MVP in OSCC cells, the objective was to obtain vault particle deficient cells, which could yield EV pellets free of vault contamination.

CRISPR-Cas9 system is one of only three techniques available for targeted genome editing, together with zinc finger nucleases (ZFNs) and transcription activator like effector nucleases (TALENs) (Cong *et al.*, 2013; Gupta *et al.*, 2019). Compared to the previously used technologies, CRISPR-Cas9 system provides a fast, highly efficient, easy and cheap method for altering genes in the cell. The mechanisms briefly include the locating and guiding activities of a guide RNA and the cleaving activity of Cas9 enzyme on double stranded DNA. Following a precise cut in the target region, an altered genome can be achieved by natural DNA repair mechanisms, resulting in regional insertions and deletions in the original genome. So far, this technique has been applied effectively for numerous purposes, including but not limited to gene knockout/silencing, gene activation, nuclear organisation and epigenetic modifications, and high-throughput gene screening (Qi *et al.*, 2013; Konermann *et al.*, 2015; Polstein and Gersbach, 2015; Poirier, 2017; Hong *et al.*, 2018). The most common limitation of this technique has been the off-target effect of the Cas enzymes, which could be dramatically reduced by using

optimised Cas9 or paired nickase instead (Mali *et al.*, 2013a; Mali *et al.*, 2013b). Alternatively, different strategies were also developed to detect the off-target effects in the CRISPR edited cells, such as the DISCOVER-Seq method by tracking down the recruitment of a DNA repair factor MRE11 (Wienert *et al.*, 2019).

For the MVP knockout experiments in this study, we selected the Alt-R CRISPR-Cas9 system from Integrated DNA Technologies, the system consisted of customised crRNA targeting MVP, tracrRNA, HiFi Cas9 nuclease V3, Lipofectamine CRISPRMAX transfection reagent, genome editing control kit and detection kit. This RNP transfection-based system provided more efficient editing and less off-target effects due to the controlled and limited Cas9 enzyme transfected, compared to the conventional Cas9 expression in cells (Kim *et al.*, 2014; Zuris *et al.*, 2015). In addition, the *in vitro* assembly of RNA duplexes and RNP delivery also provided higher flexibility, stability, transfection and editing efficiency, and required less time than *in vivo* expression. These advantages were reflected by the high success rate in our colony screening, where seven out of eight colonies screened showed complete MVP depletion. Furthermore, the T7EI mismatch cleavage assay also effectively detected the occurrence and the estimated efficiency of the genome editing, following visualisation on an agarose gel. Successful editing was detected by T7EI in cells transfected with RNP targeting MVP and the HPRT positive controls in both cell lines. Whilst no cleavage was expected from the HPRT negative controls and no RNA negative controls, fragments of cleaved DNA were however observed following T7EI digestion in H357 cells transfected with Cas9 only. This observation was validated as a consistent result by two separate experiments and was only observed in H357 cells but not in SCC4. We were unable to explain the unexpected mutation of the loci in MVP gene despite no guide RNA was introduced to the cell. As the sizes of the cleaved fragments seemed to differ from the designed sizes resulted from MVP knockout, we suspected this was a result of off-target effects of the Cas9 enzyme.

Eventually, we obtained six MVP-KO H357 sublines from the knockout experiments. Unfortunately, clones from SCC4 did not survive the selection process as the cells appeared to be more sensitive to the selection procedure. In other transfection experiments carried out in SCC4 cells, the authors have

reported data by analysing the bulk population of transfected cells, or by selecting positive clones using drug resistance combined with flow cytometry cell sorting (Papillon-Cavanagh *et al.*, 2017; Mendes *et al.*, 2020). However, both strategies would result in a mixed population of mutated cells, whose phenotypes could dramatically change as some cells gradually take over the culture. To tackle the problem, we could attempt to scale up the selection process for this cell line in future experiments, hoping to obtain more individual clones.

The safety of MVP knockout in mammalian cells has been illustrated by an MVP knockout mouse model, in which the mice were healthy and showed no observable abnormalities (Mossink *et al.*, 2002). Among all the established MVP-KO H357 clones, we have observed minor changes of cell phenotypes in some, such as altered growing speed and different cell morphology. As all clones were closely monitored and MVP expression was repeatedly measured to ensure complete knockout, we suspect these differences could be the result of off-target effects in individual clones rather than the effect of MVP knockout. Compared to another CRISPR-mediated MVP knockout experiment using lentivirus and single guide RNA, our study achieved 100% protein depletion in six H357 clones, which surpassed the incomplete knockout reported previously (Teng *et al.*, 2017). These mutants can then be further characterised to ensure high similarity to the parental cells other than targeted knockout, after which they can be a useful model assisting with understanding the role of MVP in multiple cellular activities in OSCC.

6.3.3 Using MVP-KO cells to investigate vtRNA and vtRNA fragments in EVs

Despite our findings indicating that most extracellular vtRNA is vault particle-associated, it is not possible to rule out the possibility that some full length vtRNA are EV cargo. This study has also highlighted the potential enrichment of vtRNA fragments in OSCC-EVs. However, due to their smaller size and low abundance, it was technically challenging to verify the observation from small RNA sequencing using other techniques. In this chapter, we characterised the cellular and extracellular abundance of all vault components in MVP-KO H357 cells, with the objective to utilise them as a tool to explore the presence of EV-associated vtRNA and vtRNA fragments.

As expected from the knockout experiment, both MVP-KO cell lines had no observable MVP protein expression. Compared to the WT cells, both KO cell lines also showed lowered MVP mRNA transcript levels, with more significant reduction seen in H357-MVP-A8. This suggested in these cell lines, the CRISPR-Cas9 gene editing has resulted in mutations that hindered normal protein translation and to some extent reduced gene transcription or transcript stability. The MVP deficiency would result in prevention of vault particle assembly in cells (Berger *et al.*, 2009). In an average vault particle in mammalian cells, there are approximately two copies of TEP1 and eight copies of PARP4. Both minor vault proteins are also present in the cytoplasm and nucleus in a non-vault associated manner, involved in multiple cellular activities (van Zon, M. H. Mossink, *et al.*, 2003). Our observation was, compared to TEP1, the more abundant PARP4 showed higher sensitivity to altered MVP level. This could be due to more non-vault related telomerase activities that TEP1 displays in another cellular ribonucleoprotein complex (Saito *et al.*, 1997; Kickhoefer, Stephen, *et al.*, 1999). Moreover, MVP knockout did not cause major changes in vtRNA levels in cells, this was inconsistent to what was observed previously in MVP-KD experiments. Apart from the vault particle-bound vtRNAs, 95% of the vtRNA are non-vault associated and free within cells, regulating multiple cellular activities such as autophagy, apoptosis, and proliferation (Hahne, Lampis and Valeri, 2021). Therefore, it is reasonable to hypothesise that the vast majority of vtRNA are not affected by the MVP abundance. Hence, the effects of MVP knockout on cells are mainly limited to the vault particle, including abolished vault formation and decreased minor vault protein abundance.

Due to the vault deficiency in such mutants, they became an ideal tool for us to investigate the vtRNA fragments in EVs, since there would be no vault particle released from the cells to contaminate EV preparations. A reduction of extracellular particle counts, on the NanoAnalyzer, from MVP-KO cells compared to WT cells could be due to the missing subpopulation of vault particles released from the MVP-KO cells. In addition, no vault protein could be detected in the EV pellets from the knockout cells, whilst similar levels of EV markers were observed from WT EVs and MVP-KO EVs, indicating that EV pellets from MVP-KO cells are free of vault particles and enriched with a similar amount of EVs as pellets from WT cells.

Based on these results, we also designed experiments to assess the impact of MVP/vault deficiency in parental cells on extracellular RNA. EVs from H357 WT cells were isolated by DC and Dynabead immunocapture, whilst EVs from MVP-KO cells were also isolated by DC. Total RNA was extracted from all three groups and was subject to RNA sequencing. However, the experiment was unfortunately uncompleted at the time of submission due to time limit and a delay in delivery of sequencing reagents.

From results reported in previous chapters, we knew that DC-EV pellets from OSCC cells contain EVs, vault particles and other similar sized particles and aggregates, whereas EVs captured by Dynabeads from same conditioned medium sample would only enrich a subpopulation of EVs that are positive for the tetraspanin markers and are free from vault contamination. In addition, DC-EVs from MVP-KO cells would enrich a mixed population of EVs and other similar sized particles but would also be vault-free. By performing RNA sequencing of total RNA extracted from all three groups, we could gain an insight of the RNA varieties and abundance contained by different extracellular particle subpopulations. For example, by comparing the sequencing results of EV pellets from WT and MVP-KO conditioned medium, the proportion of vault-associated vtRNA in all extracellular vtRNA can be assessed, and any vtRNA detected in EV pellets from MVP-KO cells would be more likely to be EV-associated. The high sensitivity and customed size selection of small RNA sequencing would also reveal the abundance of vtRNA fragments in EVs without the confounding effects from vault-associated vtRNAs. More importantly, by comparing the RNA abundance in EVs captured from WT conditioned medium and EV pellets from MVP-KO conditioned medium, we would be able to determine the impact of MVP/vault deficiency in donor cells on the extracellular export of RNA molecules, including vtRNA and vtRNA fragments. The role of MVP in facilitating the cargo soring and extracellular transport would therefore be further elucidated.

Chapter 7 Final discussion

7.1 Seeing is believing? - Limitations of current methods of EV isolation and EV content identification

There has been a rapid increase in research interest into EVs due to their wide involvement in multiple intercellular activities and their potential application in disease settings including screening, diagnosis and therapy development (Xu *et al.*, 2016). For these purposes, well-defined, intact and high purity EV isolation is necessary. However, due to the heterogeneous nature of EVs, current EV isolation and techniques are unable to separate different EV subpopulations (Mathieu *et al.*, 2019), hindering the development of EV subclass research. Traditional EV purification techniques utilise the biophysical properties of EVs (e.g. size, density), which can also result in co-purification of other extracellular particles with similar characteristics (Cocozza *et al.*, 2020). These particles include lipid based but non-vesicular structures such as lipoproteins (high-, intermediate-, low-, or very-low-density lipoprotein) and exomeres (Karimi *et al.*, 2018; Mathieu *et al.*, 2019), the latter was recently identified and have a similar size range to small EVs (Zhang *et al.*, 2018). Other protein complexes that have been identified in EV preparations include vault particles, argonautes, and nucleosomes, which were proven to be non-EV-associated (Jeppesen *et al.*, 2019).

In the current study, we assessed three commonly used EV isolation techniques and their ability to separate EVs and other similar sized particles, focusing on vaults, which were found to be a contaminant in our EV preparations. As summarised in Figure 7.1, vault particles can contaminate EV preparations isolated by standard DC and SEC. In our hands, DC followed by magnetic bead purification was not sufficient to break vault-EV aggregation. Finally, we demonstrated a vault-free EV isolation strategy using direct immunocapture which allowed more precise determination of EV contents from little starting material. Although the immunocapture method has been to shown to yield purer EVs than conventional methods (Chen *et al.*, 2020), it also has the drawback of only selecting specific EV populations that are positive for the selection markers. EVs with other surface markers or

no surface markers will therefore not be purified. Furthermore, EVs also express different markers when isolated from different biological sources or using different enrichment techniques (Alvarez *et al.*, 2012; Ji *et al.*, 2013), or sometimes from the same cellular origin but when cells were of a different status (e.g. stressed vs actively growing) (Rutter and Innes, 2017), which could result in inconsistent EV yield and EV content between experiments.

To tackle the above issues and facilitate better isolation of EV subtypes, more modern isolation techniques have been developed. These new techniques take advantage of size, charge, and affinity for the separation of different EV subpopulations with better resolution and yield, resulting in EVs with suitable purity and integrity for the desired applications (Liangsupree, Multia and Riekkola, 2021). For example, the AF4 method is the most popular among the modern size-based isolation techniques, which separates macromolecules based on their diffusion coefficients (Sitar *et al.*, 2015). In combination with light scattering detectors, AF4 could also provide precise measurement of EV size distribution, morphology, and aggregation status (Liangsupree, Multia and Riekkola, 2021). However, even such a technique cannot fully separate individual EV subtypes and requires further concentrating steps and small loading amount to avoid self-association (Liangsupree, Multia and Riekkola, 2021). Whilst absolute purification of EVs from other entities is an unrealistic goal, a solution to achieve EV isolation with higher purity and specificity than any currently available techniques could be obtained through a combination of isolation techniques based on different biophysical properties. For example, Multia *et al*., (2020) have demonstrated reproducible and fast isolation of EV subpopulations via immunoaffinity chromatography coupled with the AF4 method. EVs derived from this method were of high purity, integrity and concentration (Multia *et al.*, 2020). However, it also has the limitations of requiring highly specific equipment and trained operators, whilst the EV yield is largely dependent on the selective markers and size ranges.

The difficulties in EV isolation and separation from contaminants have made identification of *bona fide* EV cargo very challenging. Similar to EVs, many of the other extracellular particles contain protein, lipids, and nucleic acid components. Reporting every single molecule identified from an EV preparation as EV cargo has become undesirable in the EV research community. The MISEV2018

guidelines have provided guidance to determine the topology of EV-associated components by performing biochemical assays, which helps identify the contents of membrane-enclosed structures (e.g. EVs) and protein/protein-shielded complexes (e.g. lipoproteins, vaults, nucleosomes) by treating the EV preparations with proteinase and nuclease with/without membrane-permeabilising detergent (Théry *et al.*, 2018). In the current study, we presented convincing evidence suggesting MVP and vtRNAs were not protected by an EV membrane from degradation by proteinase and RNase. Many studies have reported the presence of vault components in the extracellular space (Herlevsen *et al.*, 2007; Nolte'T Hoen *et al.*, 2012; Lässer *et al.*, 2017), however, it now seems that the majority of these are not EV cargo and vaults can be a major contaminant to EV preparations from many sources. Alternatively, the topology of the molecule of interest can be determined by exposed antigen binding with/without permeabilisation assessed by flow cytometry or immunolabeling, which also has the merit of providing additional information characterising the topology among particles of different sizes. To summarise, consideration should be paid when choosing EV isolation techniques and even more when drawing strong conclusions regarding EV composition. Seeing a particular RNA or protein listed in an EV 'omics' screen does not necessarily mean that it is a *bona fide* EV cargo.

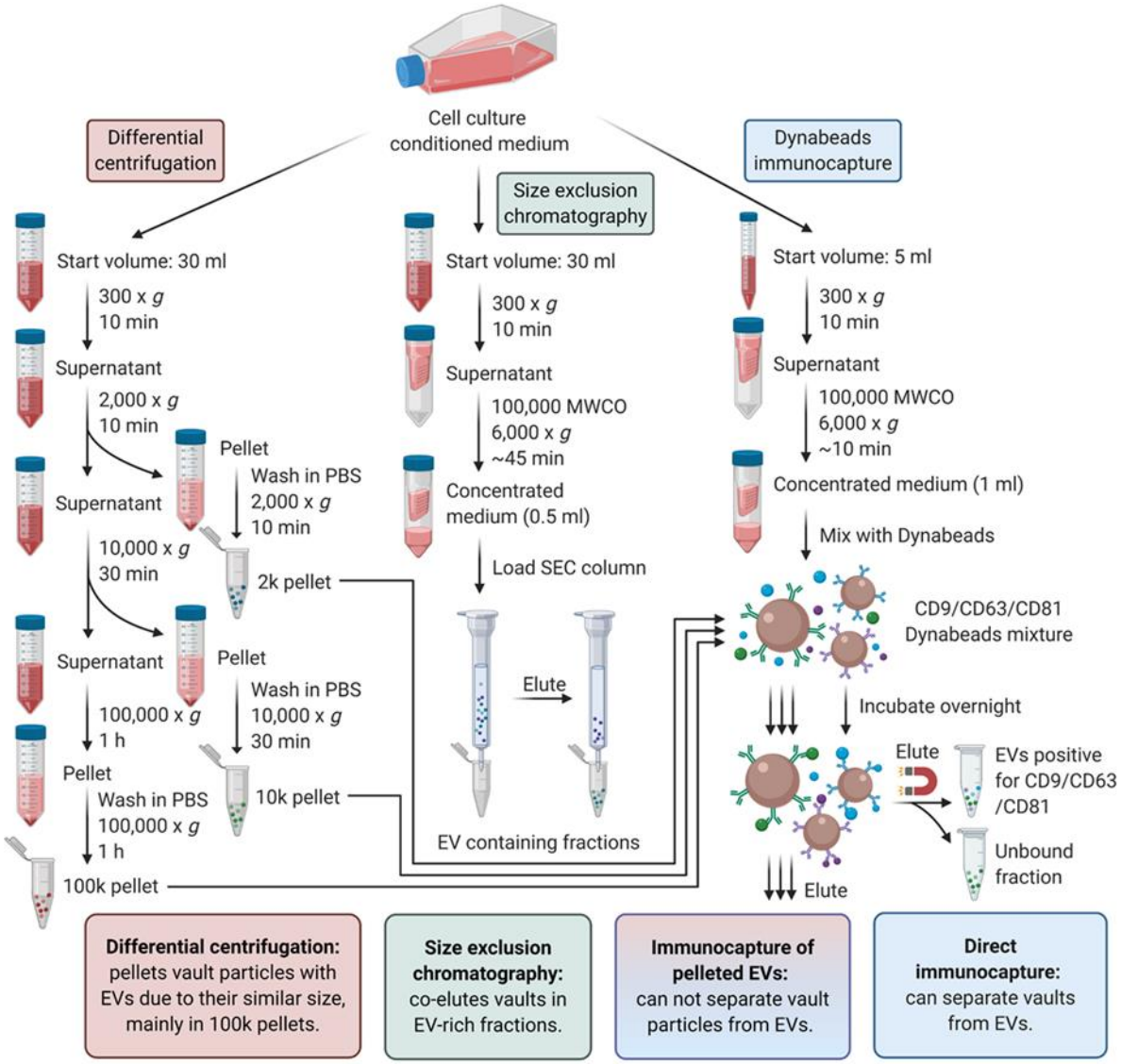

Figure 7.1 Schematic of EV isolation techniques assessed in this study and outcomes.
In this study, EVs from cell culture conditioned medium were isolated by three techniques: DC, SEC, and Dynabead immunocapture. In which, DC and SEC co-purified vault particles with EVs. Further purification of DC-derived pellets by immunocapture also resulted in EVs with particle aggregation. However, direct capturing from conditioned medium using Dynabeads led to eluted EVs that were positive for the selected markers (CD9/CD63/CD81) and free of vault protein contamination.

7.2 The distribution of vtRNA among different extracellular particles

Data from Jeppesen *et al.*, 2019 and the biochemical assays in this study, suggested MVP and the majority of the full-length vtRNA are not EV cargo. This observation is unlikely to be cell line specific nor disease specific because it has been observed in three cell lines of three different cancer types (Jeppesen *et al.*, 2019). With visual evidence provided by cryo-EM, we concur with the conclusion drawn by Jeppesen *et al*. that vault particles can be present in the extracellular space and can contaminate EV preparations. Therefore, vault components can be mistaken as EV contents. However, low abundance vtRNAs were detected by long RNA-sequencing from large and small EV fractions by Jeppesen et al. and by qPCR analysis following RNase + proteinase treatment of particle pellets in the current study. These findings hint that a small subgroup of full-length extracellular vtRNA could be protected by an EV membrane.

Several previous studies have described the presence of svRNA, which are processed from full-length vtRNA through a Dicer-dependent manner and have shown potential miRNA-like gene regulatory functions (Persson *et al.*, 2009; Hussain *et al.*, 2013; Li *et al.*, 2013). However, only one study reported their enrichment in DC-EV pellets and another postulated their extracellular presence through short RNA-sequencing reads mapped to vtRNA (van Balkom *et al.*, 2015; Jeppesen *et al.*, 2019). Our study provided additional evidence suggesting vtRNA fragments are abundant in EV pellets from immortal oral keratinocytes and OSCC cells.

Whilst the majority of full-length vtRNA appear to be carried by vaults, we cannot rule out the possibility that a small proportion could be encapsulated within EVs, perhaps alongside svRNA (Figure 7.2). vtRNA has been closely linked with multidrug resistance and repressed cell death in cancers (Mashima *et al.*, 2008), moreover, vtRNA fragment has been suggested to show miRNA-like regulatory function on the expression of a key enzyme involved in drug metabolism (Persson *et al.*, 2009). Upon uptake by recipient cells, EV-transmitted vtRNAs could play a role in spreading a drug resistant phenotype locally or distantly.

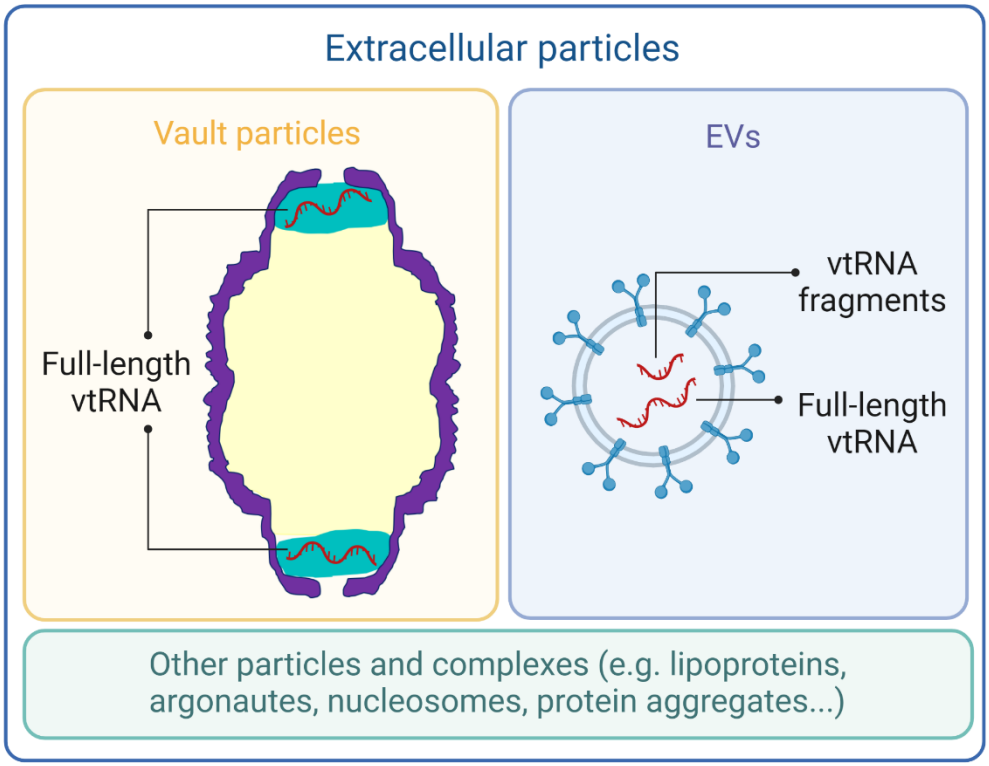

Figure 7.2 Proposed forms of vtRNA associated with extracellular particles.
Extracellular particles present in the cell culture conditioned medium include EVs, vault particles, lipoproteins, argonautes, nucleosomes, protein aggregates, and other particles. The majority of the extracellular vtRNA are vault-bound, whilst vtRNA fragments are likely to be EV associated. Nevertheless, a small proportion of full-length vtRNA could also exist as EV cargo.

7.3 Is there a novel mechanism of extracellular export and intercellular transmission of vault particles?

The detection of non-EV associated vault components and intact vault particles has raised an interesting question: How and why are they in the extracellular space?

It is becoming apparent that the EP population is extremely heterogeneous just like EVs (Théry *et al.*, 2018; Choi, Montermini, *et al.*, 2019). EVs account for a large proportion of all EPs, but other macromolecules/complexes have been identified including but not limited to exomeres, lipoproteins, argonautes, nucleosomes, chromatinmeres and vaults (Karimi *et al.*, 2018; Zhang *et al.*, 2018; Choi, Montermini, *et al.*, 2019; Jeppesen *et al.*, 2019). Compared to EVs, the biogenesis and extracellular secretion mechanisms of these particles are less understood, whilst no study has been published regarding the export of vaults into the extracellular space. Here, we combine our findings from the current study with mechanisms of EP complex release suggested by the literature, to propose hypothetical mechanisms of extracellular vault particle release (Figure 7.3).

The vault particle has been long to be associated with multidrug resistance (Mossink *et al.*, 2003). One of the mechanisms proposed was drug efflux caused by vault-mediated intracellular transport (Mossink *et al.*, 2003). Vault particles have been shown to mainly locate in the cytoplasm whilst they were also found within the nucleus and to be associated with the nuclear membrane/nuclear pore (Kedersha and Rome, 1990; Chugani, Rome and Kedersha, 1993; Hamill and Suprenant, 1997; Abbondanza *et al.*, 1998). A role in nucleocytoplasmic transport of chemotherapeutic drugs was suggested based on their subcellular localisation and typical hollow structure (Figure 7.3A). Vaults were found with close proximity to the nuclear pore complexes, where they could ‘pick up or drop off’ macromolecules such as chemotherapeutic drugs (Chugani, Rome and Kedersha, 1993). Drug efflux from nuclei can be inhibited by anti-MVP antibodies in cells, suggesting vaults could mediate drug resistance by transporting drugs away from their subcellular targets (e.g. nuclei) (Kitazono *et al.*, 1999). Vaults were also observed to be associated with cytoskeleton elements and were actively transported within axons between the soma and the nerve terminal (Kedersha and Rome, 1990; Hamill

and Suprenant, 1997; Li *et al.*, 1999). The cytoskeletal-mediated transport would enable vaults to shuttle cargo towards certain locations in the cell. One hypothesis was that drug molecules were transported to exocytotic machinery, based on that vaults were observed near secretory organelles (Herrmann *et al.*, 1999), where they could be sequestered into exocytotic vesicles and exocytosed to the extracellular space (Mossink *et al.*, 2003). Alternatively, drugs could be shuttled to the efflux pumps where they could then be effluxed through ATP-binding cassette transporter present in the plasma membrane (Mossink *et al.*, 2003; Vasiliou, Vasiliou and Nebert, 2009). Based on the current observation of extracellular vaults, we also propose another possibility that vaults could be secreted by cells through an unknown mechanism, which could facilitate the export of potential vault cargo such as chemotherapeutic drugs. The cargo carrying capability of vaults has been suggested by cryo-EM imaging in which electron dense materials were found in isolated vault particles (Kong *et al.*, 1999), however, more evidence is needed to corroborate the hypothesis. Moreover, studies focusing on the localisation and dynamics of vaults are also needed to verify the cytoskeleton-associated transport.

By reassessment of exosome composition, Jeppesen *et al*. have reported the amphisome-mediated EV-independent nucleosome extracellular release (Jeppesen *et al.*, 2019). The cytoplasmic chromatin fragments including double-stranded DNA (dsDNA) can be sequestered as a phagophore, which can expand into a double-membraned autophagosome specified by microtubule-associated protein 1A/1B-light chain 3 (LC3) surface marker (Jeppesen *et al.*, 2019). Following normal autophagy process, the autophagosome can fuse with lysosomes after which the autophagic cargo can be degraded (Tanida, Ueno and Kominami, 2008). Alternatively, the autophagosome could merge with tetraspanin (CD63) positive multivesicular bodies, resulting in the formation of an amphisome. Following fusion with the plasma membrane, amphisome cargo, originally endosome cargo (exosomes) and autophagosome cargo (dsDNA/histone complexes), can be released into the extracellular space (Jeppesen *et al.*, 2019). In the current study, although we concluded that the majority of vault components are not EV cargo, we did observe colocalisation of MVP/vaults and endosomal markers in a subpopulation of cells. Considering the important role that vtRNA 1-1 plays in regulating selective autophagy by directly

binding to p62 (Horos, Büscher, Sachse, *et al.*, 2019), which is required for cargo sorting into phagophore and is also degraded together with the cargo (Ciuffa *et al.*, 2015), it is reasonable to postulate that vault particles can be secreted through autophagosome-amphisome pathway just like nucleosomes, which would also explain why vault components co-localise with endosomal compartments (Figure 7.3B). This theory could be further tested by detection of extracellular vault particles upon inhibited selective autophagy.

Lastly, the detection of vaults in EP preparations could simply be the result of natural cell death or a cell culture artefact, as both our study and Jeppesen *et al.*, 2019 utilised *in vitro* models (Figure 7.3C). However, this is unlikely as vault components have been repeatedly reported as "EV cargo" in particles isolated from *ex vivo* biological fluids, including breast milk and saliva (Admyre *et al.*, 2007; Gonzalez-Begne *et al.*, 2009).

Vaults are currently being engineered to encapsulate drugs/molecules to be used in disease treatment (Rome and Kickhoefer, 2012). Engineered vault nanoparticles have achieved delivery of biomacromolecules into the cytoplasm through endocytosis (Han *et al.*, 2011; Galbiati *et al.*, 2018). The clathrin-mediated endocytic uptake of isolated vault particles has been observed in normal fibroblasts and glioblastoma, but not in carcinoma cell lines, therefore the researchers suspected a specific receptor is needed for successful vault uptake (Galbiati *et al.*, 2018). Since vault particles are present in the extracellular space and can be endocytosed by neighbouring cells, it is tempting to speculate that vaults could be another type of extracellular particle that facilitates intercellular molecular exchange just like EVs (Figure 7.3D). As vtRNA has been associated with multidrug resistance, autophagy regulation, cell death and suppression of apoptosis, the potential intercellular shuttling of vaults could thus contribute to the spread of a drug-resistant and apoptosis-resistant phenotype within the tumour microenvironment.

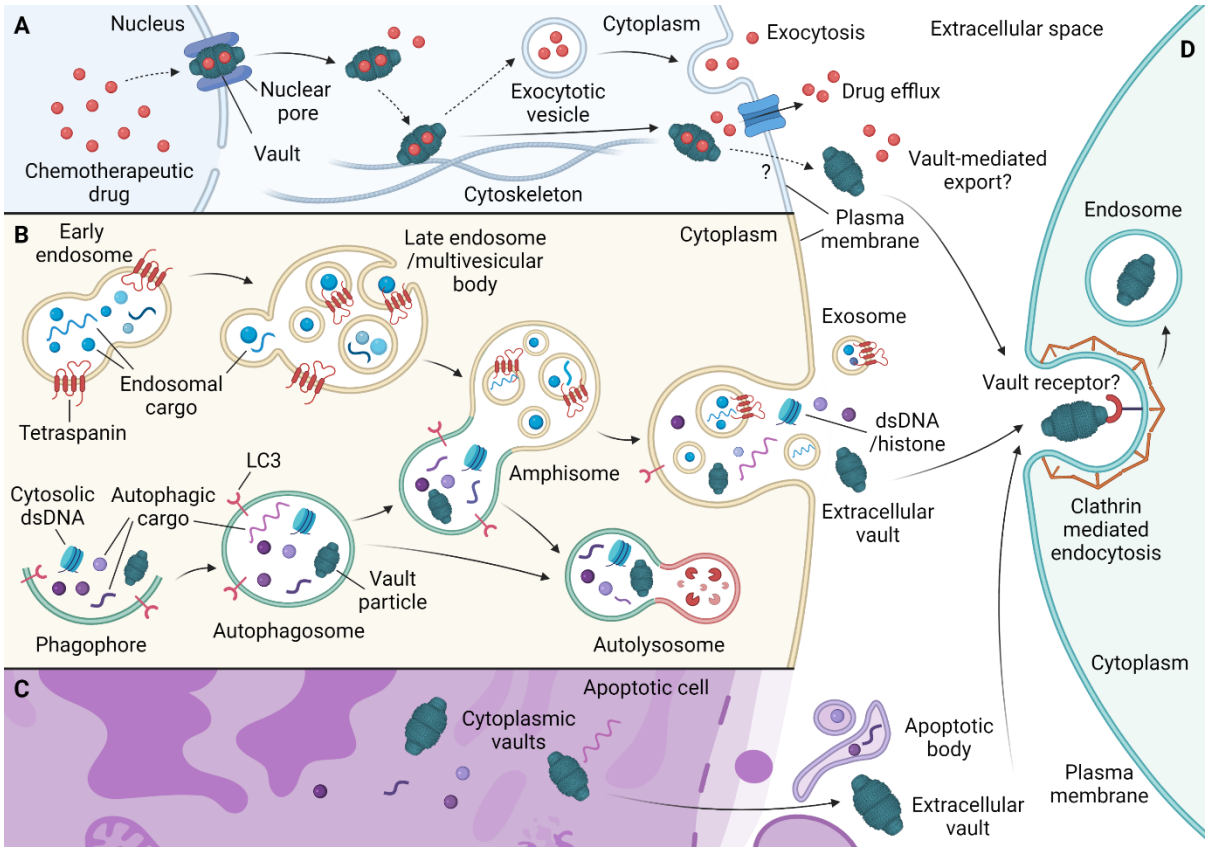

Figure 7.3 Hypothetical pathways of the extracellular transport of vault particle.
A) Vault may be involved in the nucleocytoplasmic transport of chemotherapeutic drugs. Upon drug loading at the nuclear pore and shuttling away from the nucleus, vault may transport through cytoskeleton compartments, after which drugs could be loaded into exocytotic vesicles and exported through exocytosis. Alternatively, vaults may transport drug molecules to the efflux pumps, after which drugs would be extruded outside the cell, or by an unknown vault-mediated export mechanism that could release vaults into the extracellular space with the drugs. **B)** Vault may be included in the phagophore which then forms into autophagosome. The autophagosome could be degraded upon fusion with lysosomes. They could also merge with late endosome/multivesicular bodies, which forms an amphisome. Amphisomes can fuse with the plasma membrane to release cargo (endosomal cargo and autophagic cargo) into the extracellular space. **C)** Vault may be released from the cell due to normal cell death/apoptosis. **D)** Vault particles can be taken up by recipient cells through clathrin mediated endocytosis, by which they may facilitate the intercellular exchange of vtRNA and other cargo. Solid arrows indicate reported mechanisms with evidence, dotted arrows indicate postulated mechanisms, question marks indicate unknown mechanisms.

7.4 Limitations, future work and final thoughts

Reflecting on this study, there are several limitations that we could improve. First of all, four months (March – July 2020) of this study fell into the duration of national lockdown due to the Covid-19 pandemic, during which no laboratory access could be obtained, followed by limited laboratory access until the time of submission due to social distancing policy. This has directly resulted in delay and interruption of certain experiments. For example, a few unsuccessful attempts described in the previous chapters could have been further optimised during this period of time, including the detection of vtRNA fragments by northern blot, and the establishment of vtRNA-dBroccoli overexpressing cell lines (as described in Chapter 4). Additionally, until the time of submission we were waiting for the results of RNA sequencing experiments from the sequencing facility at The Children's Hospital due to a delay in reagent delivery. This experiment was designed to detect full-length vtRNA and vtRNA fragments in extracellular particle pellets isolated from WT cells and MVP-KO cells, as well as in marker-positive EVs separated by immunoaffinity capture (described in Chapter 6). Results from this experiment could have helped us understand the distribution of extracellular vtRNAs between EVs and vault particles, and to test the hypothesis that a small proportion of vtRNA are enclosed within an EV membrane. By comparing the abundance of vtRNA in H357 WT and MVP-KO cell-derived EVs, we could also gain an insight into whether intracellular MVP/vault particle plays a role in the export of vtRNA fragments.

Many of the early experiments were performed without the realisation that extracellular vaults can be a major contamination source to DC-EV preparations. Following the discovery that vault particles are contaminants, a large proportion of this study has focused on comparing and validating the ability of different EV isolation techniques to separate vaults from EVs. Although we have covered the two most common EV isolation techniques – DC and SEC, we cannot make conclusions for other purification methods that are also popular within the EV research community. There might be other techniques that are superior in separating EVs from other EPs than the immunocapture workflow suggested by the current study. For example, density gradient centrifugation has been utilised by many studies to generate EP fractions of high resolution, in which EVs and vault particles were

enriched in different fractions (Jeppesen *et al.*, 2019), although it was suggested to have lower specificity than the immunocapture method (Cocozza *et al.*, 2020). In future studies of EV isolation method comparison, the aim should be to provide more convincing evidence from multiple perspectives (e.g. imaging, biochemical assays, single particle analysis) whilst including more techniques that are currently available.

Moving forward, future work will firstly focus on the validation of the findings from the current study. We will complete the outstanding RNA sequencing analysis and interpret the data, so that we can answer the question whether a proportion of vtRNA and vtRNA fragments are EV-associated, and the impact of MVP/vault deficiency on extracellular vtRNA (Figure 7.4). If any vtRNA/svRNA seems to be EV-associated, future studies could explore their functional role as EV cargo in OSCC. Furthermore, it would be beneficial to validate the EV-independent vault particle export in biological fluid, such as saliva, to rule out the possibility that it is a cell culture artefact. If vault release was proven to be a universal phenomenon, future work could pursue the underlying mechanism(s) with focus on the hypothetical pathways mentioned above. As such, an elucidated export mechanism could help us understand whether vaults are a novel type of ribonucleoprotein complex that can be secreted and taken up by cells, and the potential role it plays in cancer biology or even in general cell biology.

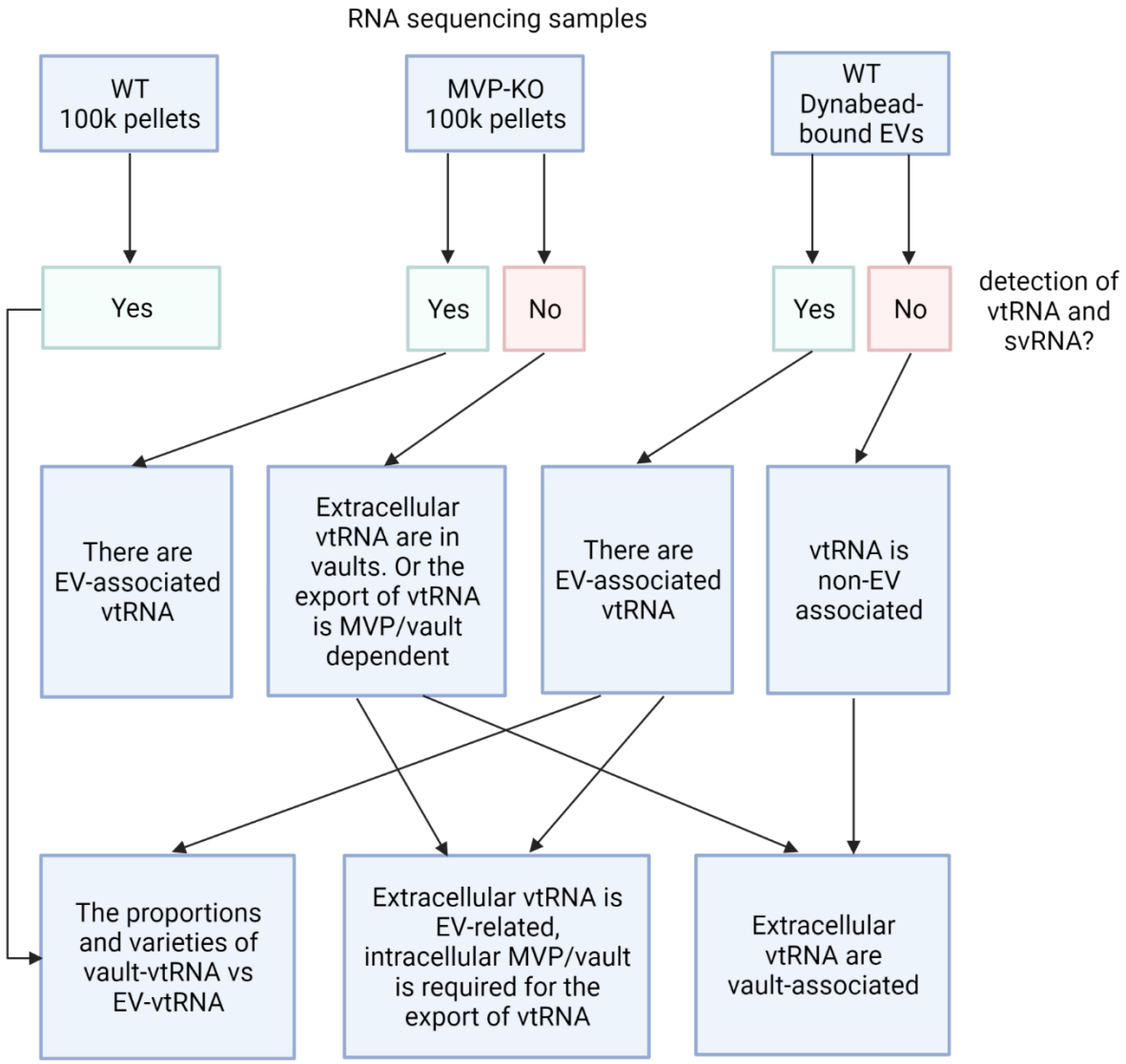

Figure 7.4 Flow chart of RNA sequencing result interpretation.
Flow chart showing interpretation of the association of vtRNA/svRNA in EVs and vaults according to the detection by RNA sequencing described in Chapter 6.

Supplementary materials

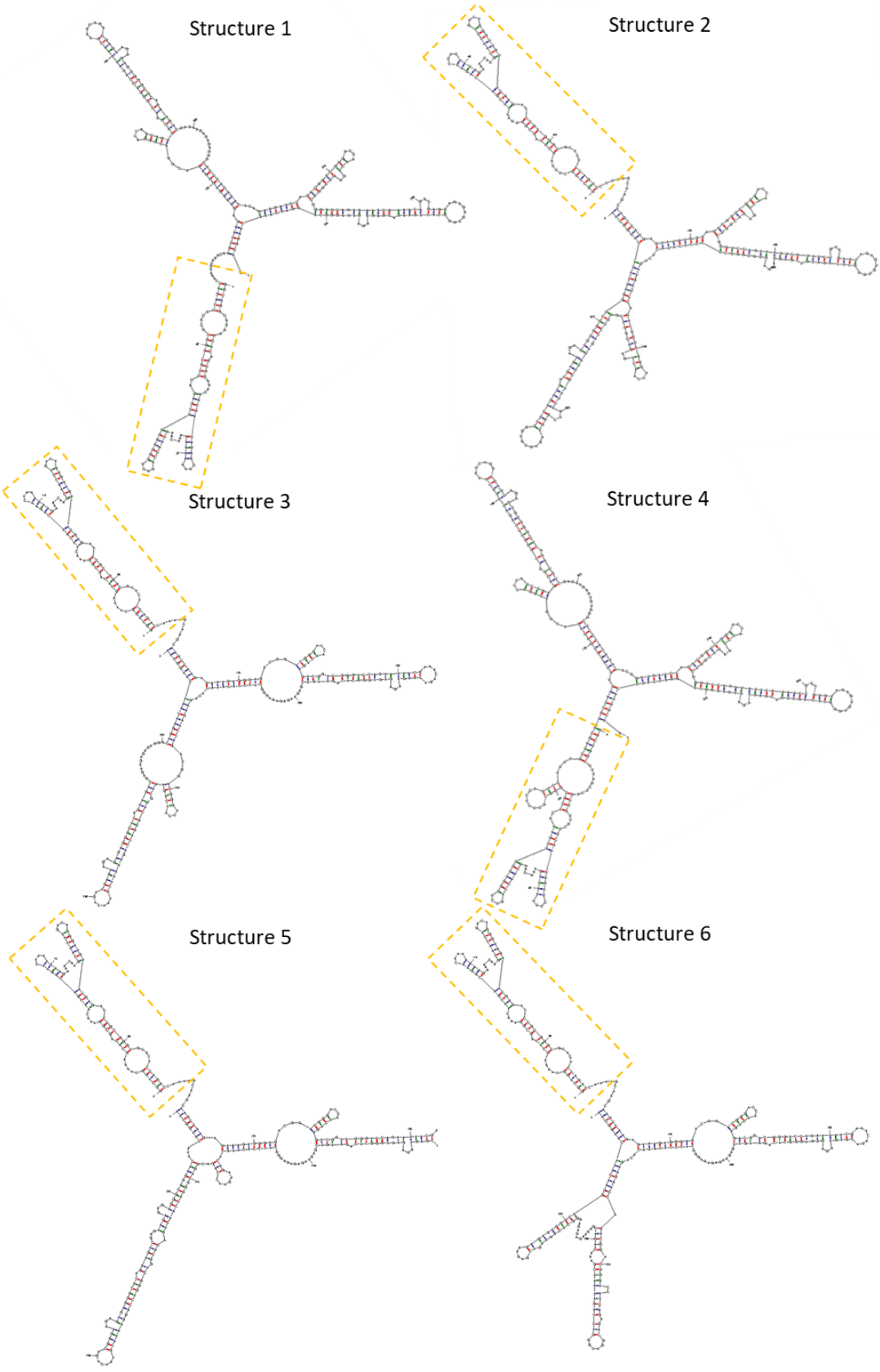

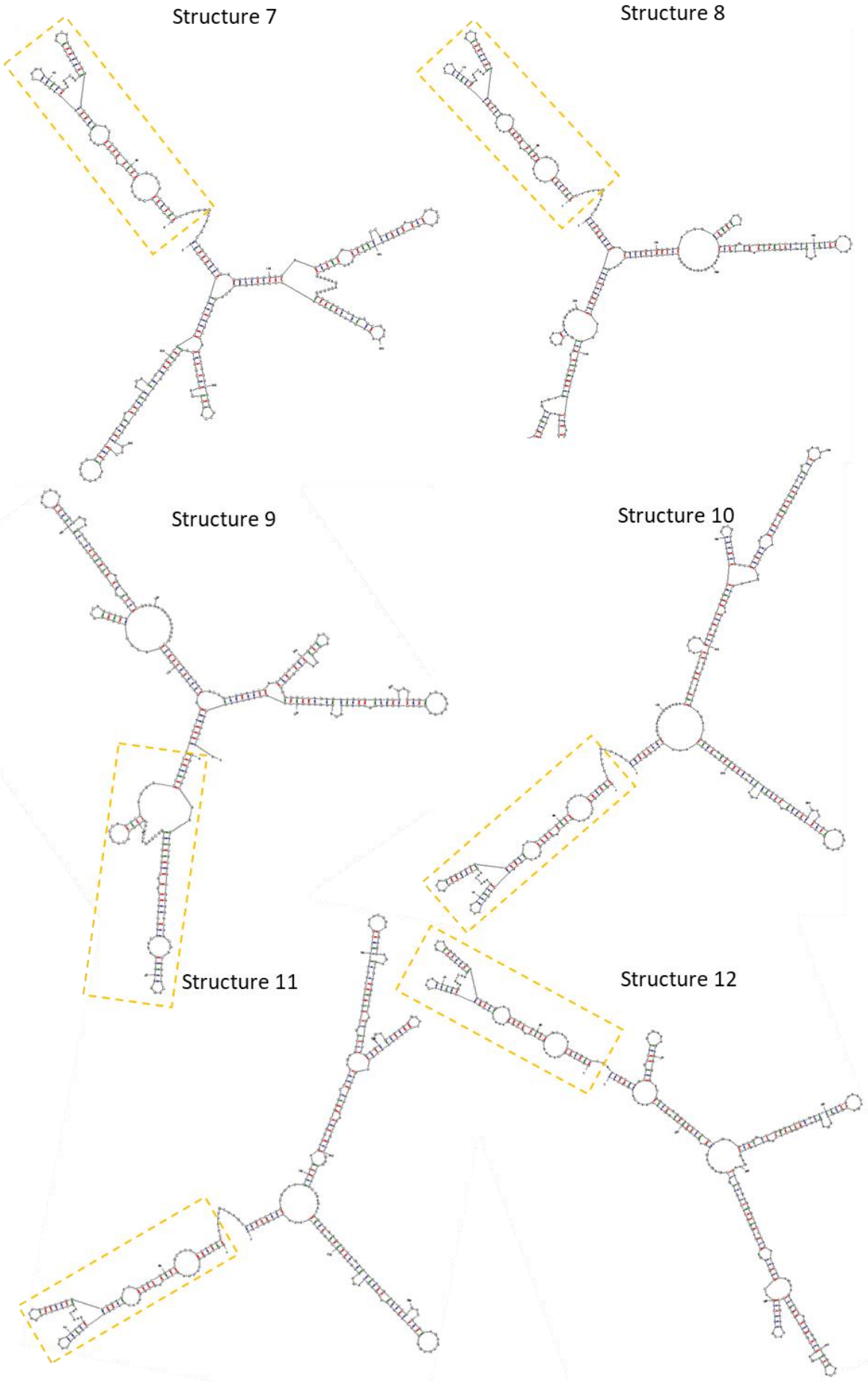
Structure 7
Structure 8
Structure 9
Structure 10
Structure 11
Structure 12

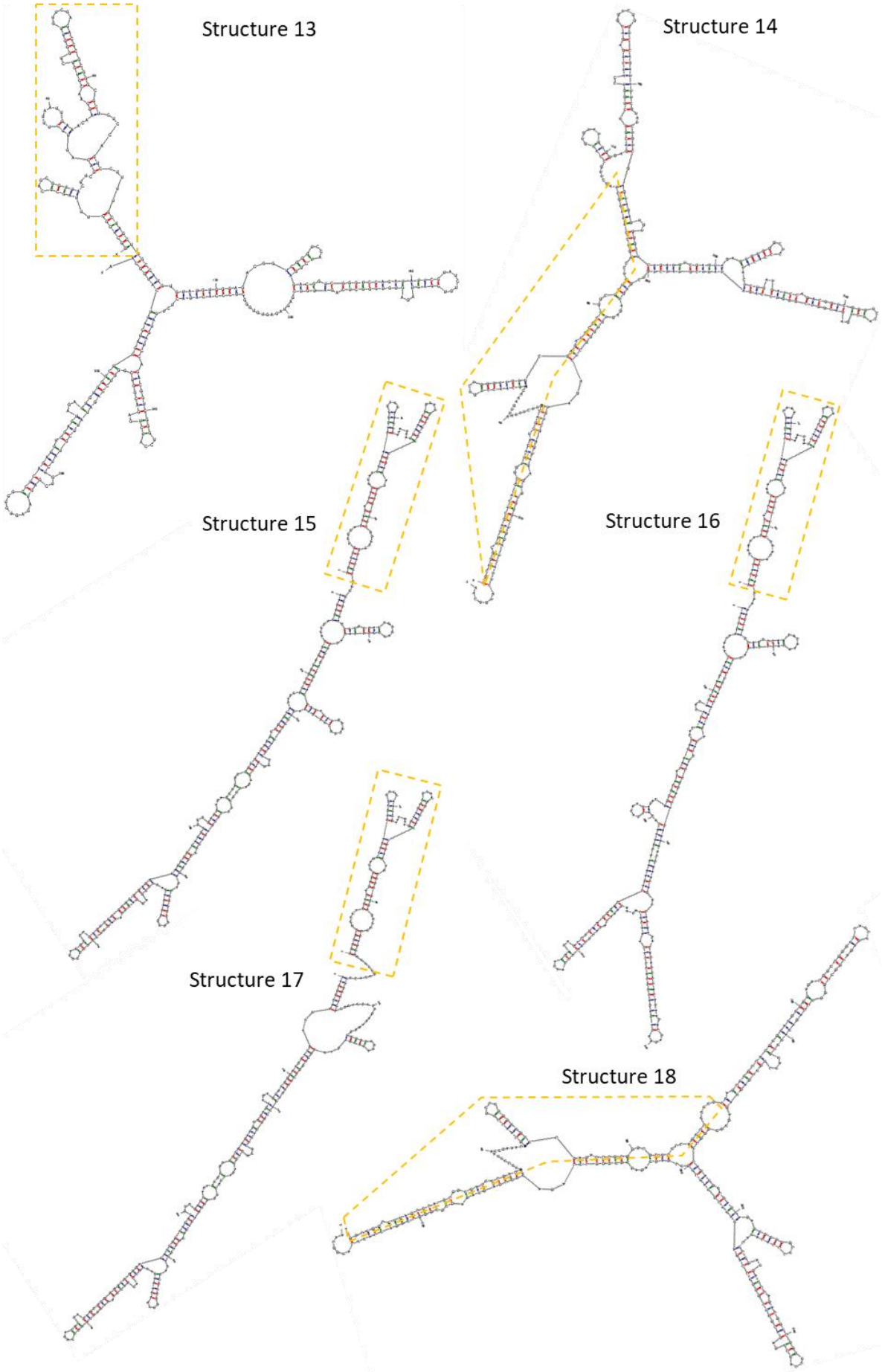
Structure 13
Structure 14
Structure 15
Structure 16
Structure 17
Structure 18

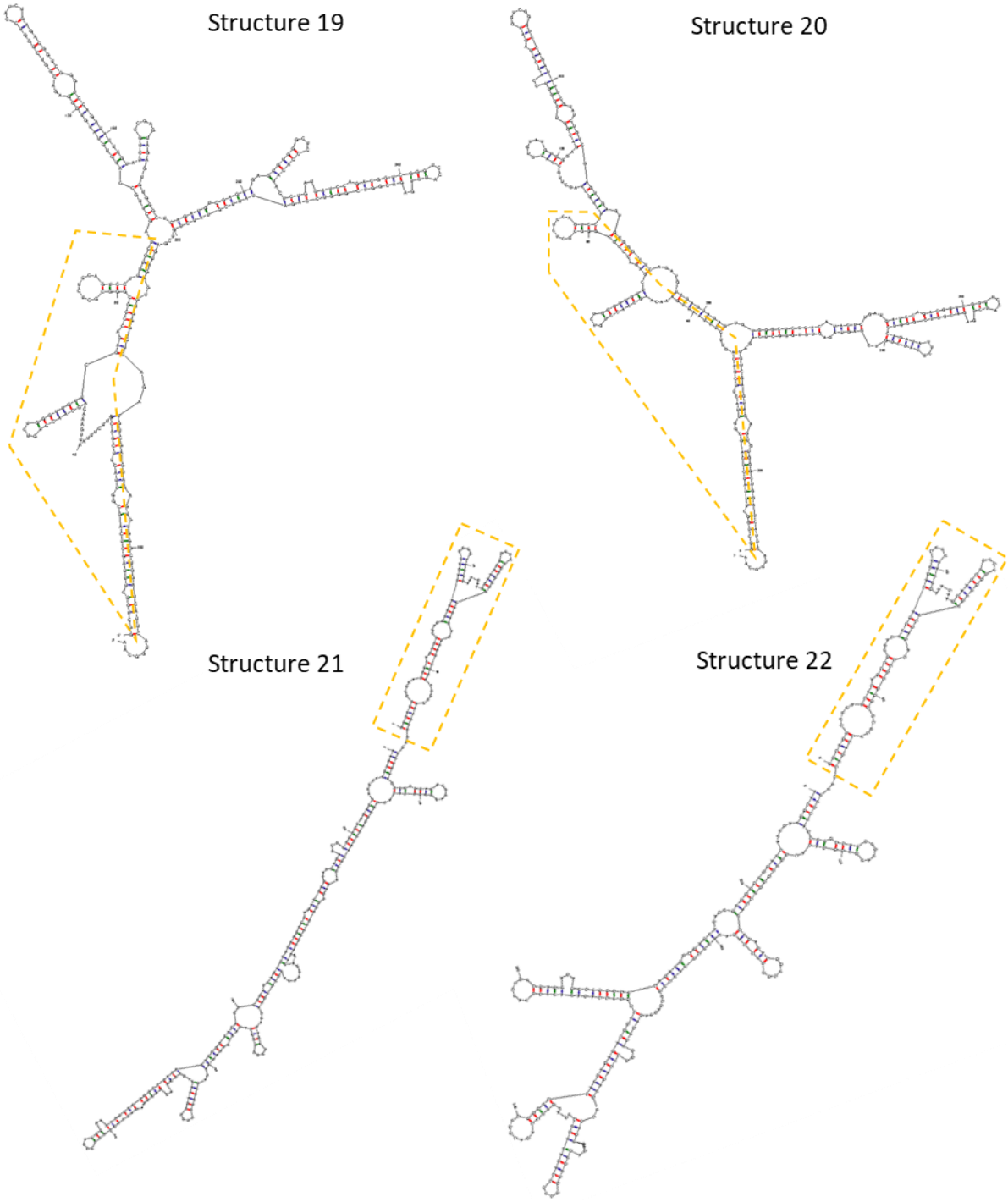

Figure S1 Predicted folding of vtRNA 1-1-Broccoli transcripts.
RNA secondary structures of vtRNA 1-1-Broccoli transcripts (sequence: 5'- GGCTGGCTTT AGCTCAGCGG TTACTTCGAC AGTTCTTTAA TTGAAACAAG CAACCTGTCT GGGTTGTTCG AGACCCGCGG GCGCTCTCCA GTCCTTTTGC TAGCUUGCCA UGUGUAUGUG GGAGACGGUC GGGUCCAUCU GAGACGGUCG GGUCCAGAUA UUCGUAUCUG UCGAGUAGAG UGUGGGCUCA GAUGUCGAGU AGAGUGUGGG CUCCCACAUA CUCUGAUGAU CCAGACGGUC GGGUCCAUCU GAGACGGUCG GGUCCAGAUA UUCGUAUCUG UCGAGUAGAG UGUGGGCUCA GAUGUCGAGU AGAGUGUGGG CUGGAUCAUU CAUGGCAA -3', yellow: vtRNA 1-1, grey: NheI restriction size, blue: F30 scaffold, green: dBroccoli) were predicted by the mFold RNA prediction web server when folded at 37°C (Zuker, 2003). Structures were listed in the order of least to most energy required. Yellow boxes indicate vtRNA 1-1.

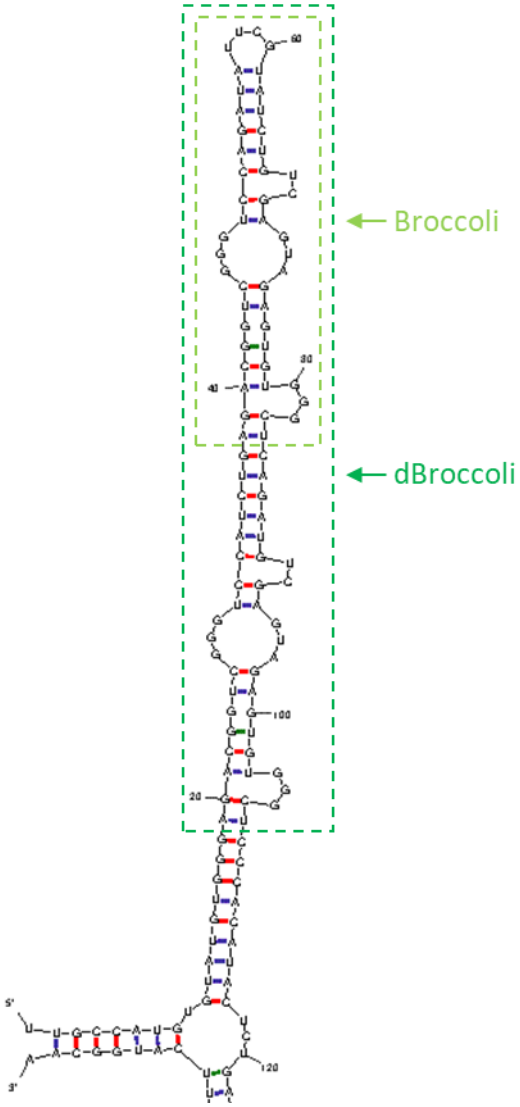

Figure S2 Correct folding of dBroccoli.
RNA secondary structures of dBroccoli transcripts on scaffold predicted by the mFold RNA prediction web server when folded at 37°C (Zuker, 2003). Sequence: 5'- UUGCCA UGUGUAUGUG GGAGACGGUC GGGUCCAUCU GAGACGGUCG GGUCCAGAUA UUCGUAUCUG UCGAGUAGAG UGUGGGCUCA GAUGUCGAGU AGAGUGUGGG CUCCCACAUA CUCUGA -3', blue: F30 scaffold, green: dBroccoli. Light green box indicates Broccoli structure and dark green box indicates dBroccoli structure.

References

Abbondanza, C. *et al.* (1998) 'Interaction of Vault Particles with Estrogen Receptor in the MCF-7 Breast Cancer Cell', *The Journal of Cell Biology*, 141(6), pp. 1301-1310. doi:10.1083/JCB.141.6.1301.

Abels, E.R. and Breakefield, X.O. (2016) 'Introduction to Extracellular Vesicles: Biogenesis, RNA Cargo Selection, Content, Release, and Uptake', *Cellular and Molecular Neurobiology*, pp. 301–312. doi:10.1007/s10571-016-0366-z.

Abrami, L. *et al.* (2013) 'Hijacking Multivesicular Bodies Enables Long-Term and Exosome-Mediated Long-Distance Action of Anthrax Toxin', *Cell Reports*, 5(4), pp. 986–996. doi:10.1016/J.CELREP.2013.10.019.

Admyre, C. *et al.* (2007) 'Exosomes with Immune Modulatory Features Are Present in Human Breast Milk', *The Journal of Immunology*, 179(3), pp. 1969–1978. doi:10.4049/JIMMUNOL.179.3.1969.

Aheget, H. *et al.* (2020) 'Exosome: A New Player in Translational Nanomedicine', *Journal of Clinical Medicine 2020, Vol. 9, Page 2380*, 9(8), p. 2380. doi:10.3390/JCM9082380.

Ahn, J.-H. *et al.* (2018) 'nc886 is induced by TGF-β and suppresses the microRNA pathway in ovarian cancer', *Nature Communications*, 9(1), p. 1166. doi:10.1038/s41467-018-03556-7.

Al-Nedawi, K. *et al.* (2008) 'Intercellular transfer of the oncogenic receptor EGFRvIII by microvesicles derived from tumour cells', *Nature Cell Biology*, 10(5), pp. 619–624. doi:10.1038/ncb1725.

Alexander, M. *et al.* (2015) 'Exosome-delivered microRNAs modulate the inflammatory response to endotoxin', *Nature Communications*, 6(1), p. 7321. doi:10.1038/ncomms8321.

Alicka, M. *et al.* (2019) 'Adipose-Derived Mesenchymal Stem Cells Isolated from Patients with Type 2 Diabetes Show Reduced "Stemness" through an Altered Secretome Profile, Impaired Anti-Oxidative Protection, and Mitochondrial Dynamics Deterioration', *Journal of Clinical Medicine*, 8(6), p. 765. doi:10.3390/JCM8060765.

Alvarez, M.L. *et al.* (2012) 'Comparison of protein, microRNA, and mRNA yields using different methods of urinary exosome isolation for the discovery of kidney disease biomarkers', *Kidney International*, 82(9), pp. 1024–1032. doi:10.1038/KI.2012.256.

Amort, M. *et al.* (2015) 'Expression of the vault RNA protects cells from undergoing apoptosis', *Nature Communications*, 6(1), p. 7030. doi:10.1038/ncomms8030.

An, H.-J. *et al.* (2009) 'Age associated high level of major vault protein is p53 dependent', *Cell Biochemistry and Function*, 27(5), pp. 289–295. doi:10.1002/cbf.1571.

de Andrade, A.L.D.L. *et al.* (2018) 'Extracellular vesicles from oral squamous carcinoma cells display pro- and anti-angiogenic properties', *Oral Diseases*, 24(5), pp. 725–731. doi:10.1111/odi.12765.

Atkin-Smith, G.K. *et al.* (2015) 'A novel mechanism of generating extracellular vesicles during apoptosis via a beads-on-a-string membrane structure', *Nature Communications*, 6(1), p. 7439. doi:10.1038/ncomms8439.

Augsten, M. *et al.* (2009) 'CXCL14 is an autocrine growth factor for fibroblasts and acts as a multi-modal stimulator of prostate tumor growth', *Proceedings of the National Academy of Sciences of the United States of America*, 106(9), pp. 3414–3419. doi:10.1073/PNAS.0813144106/SUPPL_FILE/0813144106SI.PDF.

Bachurski, D. *et al.* (2019) 'Extracellular vesicle measurements with nanoparticle tracking analysis –

An accuracy and repeatability comparison between NanoSight NS300 and ZetaView', *Journal of Extracellular Vesicles*, 8(1). doi:10.1080/20013078.2019.1596016.

Bai, H. *et al.* (2019) 'Major vault protein suppresses lung cancer cell proliferation by inhibiting STAT3 signaling pathway', *BMC Cancer*, 19(1). doi:10.1186/S12885-019-5665-6.

Baietti, M.F. *et al.* (2012) 'Syndecan–syntenin–ALIX regulates the biogenesis of exosomes', *Nature Cell Biology*, 14(7), pp. 677–685. doi:10.1038/ncb2502.

Baig, M.S. *et al.* (2020) 'Tumor-derived exosomes in the regulation of macrophage polarization', *Inflammation Research*, pp. 435–451. doi:10.1007/s00011-020-01318-0.

Baj-Krzyworzeka, M. *et al.* (2006) 'Tumour-derived microvesicles carry several surface determinants and mRNA of tumour cells and transfer some of these determinants to monocytes', *Cancer Immunology, Immunotherapy*, 55(7), pp. 808–818. doi:10.1007/s00262-005-0075-9.

Balaguer, N. *et al.* (2018) 'Heterogeneous nuclear ribonucleoprotein C1 may control miR-30d levels in endometrial exosomes affecting early embryo implantation', *Molecular Human Reproduction*, 24(8), pp. 411–425. doi:10.1093/molehr/gay026.

Balaj, L. *et al.* (2011) 'Tumour microvesicles contain retrotransposon elements and amplified oncogene sequences', *Nature Communications*, 2(1), p. 180. doi:10.1038/ncomms1180.

van Balkom, B.W.M. *et al.* (2015) 'Quantitative and qualitative analysis of small RNAs in human endothelial cells and exosomes provides insights into localized RNA processing, degradation and sorting', *Journal of Extracellular Vesicles*, 4(1), p. 26760. doi:10.3402/jev.v4.26760.

Baranyai, T. *et al.* (2015) 'Isolation of exosomes from blood plasma: Qualitative and quantitative comparison of ultracentrifugation and size exclusion chromatography methods', *PLoS ONE*, 10(12). doi:10.1371/journal.pone.0145686.

Barceló, M. *et al.* (2018) 'Exosomal microRNAs in seminal plasma are markers of the origin of azoospermia and can predict the presence of sperm in testicular tissue', *Human Reproduction*, 33(6), pp. 1087–1098. doi:10.1093/humrep/dey072.

Becker, A. *et al.* (2016) 'Extracellular vesicles in cancer: cell-to-cell mediators of metastasis', *Cancer cell*, 30(6), p. 836. doi:10.1016/J.CCELL.2016.10.009.

Bellingham, S.A., Coleman, B.M. and Hill, A.F. (2012) 'Small RNA deep sequencing reveals a distinct miRNA signature released in exosomes from prion-infected neuronal cells.', *Nucleic acids research*, 40(21), pp. 10937–49. doi:10.1093/nar/gks832.

Ben, J. *et al.* (2013) 'Major Vault Protein Regulates Class A Scavenger Receptor-mediated Tumor Necrosis Factor-α Synthesis and Apoptosis in Macrophages', *Journal of Biological Chemistry*, 288(27), pp. 20076–20084. doi:10.1074/jbc.M112.449538.

Ben, J. *et al.* (2019) 'Major vault protein suppresses obesity and atherosclerosis through inhibiting IKK–NF-κB signaling mediated inflammation', *Nature Communications*, 10(1). doi:10.1038/S41467-019-09588-X.

Berger, W. *et al.* (2009) 'Vaults and the major vault protein: Novel roles in signal pathway regulation and immunity', *Cellular and Molecular Life Sciences*, 66(1), pp. 43–61. doi:10.1007/s00018-008-8364-z.

Berger, W., Elbling, L. and Micksche, M. (2000) 'Expression of the major vault protein LRP in human non-small-cell lung cancer cells: activation by short-term exposure to antineoplastic drugs.', *International journal of cancer*, 88(2), pp. 293–300. Available at: http://www.ncbi.nlm.nih.gov/pubmed/11004683 (Accessed: 11 February 2019).

Blatt, S. *et al.* (2017) 'Biomarkers in diagnosis and therapy of oral squamous cell carcinoma: A review of the literature', *Journal of Cranio-Maxillofacial Surgery*, 45(5), pp. 722–730.

doi:10.1016/J.JCMS.2017.01.033.

Blot, W.J. *et al.* (1988) 'Smoking and drinking in relation to oral and pharyngeal cancer.', *Cancer research*, 48(11), pp. 3282–7. Available at: http://www.ncbi.nlm.nih.gov/pubmed/3365707 (Accessed: 24 October 2018).

Böing, A.N. *et al.* (2014) 'Single-step isolation of extracellular vesicles by size-exclusion chromatography', *Journal of Extracellular Vesicles*, 3(1), p. 23430. doi:10.3402/jev.v3.23430.

Booth, A.M. *et al.* (2006) 'Exosomes and HIV Gag bud from endosome-like domains of the T cell plasma membrane', *The Journal of Cell Biology*, 172(6), pp. 923–935. doi:10.1083/jcb.200508014.

Boulbitch, A.A. (1998) 'Deflection of a cell membrane under application of a local force', *Physical Review E*, 57(2), pp. 2123–2128. doi:10.1103/PhysRevE.57.2123.

Bray, F. *et al.* (2018) 'Global cancer statistics 2018: GLOBOCAN estimates of incidence and mortality worldwide for 36 cancers in 185 countries', *CA: A Cancer Journal for Clinicians*, 68(6), pp. 394–424. doi:10.3322/CAAC.21492.

Buschow, S.I. *et al.* (2010) 'MHC class II-associated proteins in B-cell exosomes and potential functional implications for exosome biogenesis', *Immunology and Cell Biology*, 88(8), pp. 851–856. doi:10.1038/icb.2010.64.

Cai, J. *et al.* (2019) 'Oral squamous cell carcinoma-derived exosomes promote M2 subtype macrophage polarization mediated by exosome-enclosed miR-29a-3p', *American Journal of Physiology - Cell Physiology*, 316(5), pp. C731–C740. doi:10.1152/ajpcell.00366.2018.

Cai, Y. *et al.* (2020) 'NSAID therapy for PIK3CA-Altered colorectal, breast, and head and neck cancer', *Advances in Biological Regulation*, 75, p. 100653. doi:10.1016/J.JBIOR.2019.100653.

Caldieri, G. *et al.* (2018) 'EGFR Trafficking in Physiology and Cancer', *Progress in molecular and subcellular biology*, pp. 235–272. doi:10.1007/978-3-319-96704-2_9.

Cancer Research UK (2018) *Head and neck cancers incidence statistics | Cancer Research UK*. Available at: https://www.cancerresearchuk.org/health-professional/cancer-statistics/statistics-by-cancer-type/head-and-neck-cancers/incidence (Accessed: 31 August 2021).

Cancer Research UK (2020) *Head and neck cancers incidence statistics | Cancer Research UK*. Available at: https://www.cancerresearchuk.org/health-professional/cancer-statistics/statistics-by-cancer-type/head-and-neck-cancers/incidence#ref-2 (Accessed: 31 August 2021).

Canella, D. *et al.* (2010) 'Defining the RNA polymerase III transcriptome: Genome-wide localization of the RNA polymerase III transcription machinery in human cells', *Genome Research*, 20(6), pp. 710–721. doi:10.1101/gr.101337.109.

Capomaccio, S. *et al.* (2019) 'Equine adipose-derived mesenchymal stromal cells release extracellular vesicles enclosing different subsets of small RNAs', *Stem Cells International*, 2019. doi:10.1155/2019/4957806.

Cengiz, B. *et al.* (2007) 'Fine deletion mapping of chromosome 2q21-37 shows three preferentially deleted regions in oral cancer', *Oral oncology*, 43(3), pp. 241–247. doi:10.1016/J.ORALONCOLOGY.2006.03.004.

Chakrabortty, S.K. *et al.* (2015) 'Extracellular vesicle-mediated transfer of processed and functional RNY5 RNA', *RNA*, 21(11), pp. 1966–1979. doi:10.1261/rna.053629.115.

Chalmin, F. *et al.* (2010) 'Membrane-associated Hsp72 from tumor-derived exosomes mediates STAT3-dependent immunosuppressive function of mouse and human myeloid-derived suppressor cells', *Journal of Clinical Investigation*, 120(2), pp. 457–71. doi:10.1172/JCI40483.

Channavajjhala, S.K. *et al.* (2019) 'Urinary Extracellular Vesicle Protein Profiling and Endogenous

Lithium Clearance Support Excessive Renal Sodium Wasting and Water Reabsorption in Thiazide-Induced Hyponatremia', *Kidney International Reports*, 4(1), pp. 139–147. doi:10.1016/j.ekir.2018.09.011.

Chen, G. *et al.* (2018) 'Exosomal PD-L1 contributes to immunosuppression and is associated with anti-PD-1 response', *Nature*, 560(7718), pp. 382–386. doi:10.1038/s41586-018-0392-8.

Chen, J. *et al.* (2018) 'Vault RNAs partially induces drug resistance of human tumor cells MCF-7 by binding to the RNA/DNA-binding protein PSF and inducing oncogene GAGE6', *PLoS ONE*, 13(1). doi:10.1371/journal.pone.0191325.

Chen, S. *et al.* (2020) 'Two-step magnetic bead-based (2MBB) techniques for immunocapture of extracellular vesicles and quantification of microRNAs for cardiovascular diseases: A pilot study', *PLoS ONE*, 15(2). doi:10.1371/JOURNAL.PONE.0229610.

Cheng, S.H. *et al.* (2000) 'Low-Level Doxorubicin Resistance in Benzo[a]pyrene-Treated KB-3-1 Cells Is Associated with Increased LRP Expression and Altered Subcellular Drug Distribution', *Toxicology and Applied Pharmacology*, 164(2), pp. 134–142. doi:10.1006/taap.2000.8903.

Chiu, Y.-W. *et al.* (2016) 'Tyrosine 397 phosphorylation is critical for FAK-promoted Rac1 activation and invasive properties in oral squamous cell carcinoma cells', *Laboratory Investigation*, 96(3), pp. 296–306. doi:10.1038/labinvest.2015.151.

Choi, D., Montermini, L., *et al.* (2019) 'Mapping Subpopulations of Cancer Cell-Derived Extracellular Vesicles and Particles by Nano-Flow Cytometry', *ACS Nano*, 13(9), pp. 10499–10511. doi:10.1021/ACSNANO.9B04480.

Choi, D., Spinelli, C., *et al.* (2019) 'Oncogenic Regulation of Extracellular Vesicle Proteome and Heterogeneity', *PROTEOMICS*, 19(1–2), p. 1800169. doi:10.1002/pmic.201800169.

Choi, S. and Myers, J.N. (2008) 'Molecular Pathogenesis of Oral Squamous Cell Carcinoma: Implications for Therapy', *Journal of Dental Research*, 87(1), pp. 14–32. doi:10.1177/154405910808700104.

Chow, L.Q.M. (2020) 'Head and Neck Cancer', *New England Journal of Medicine*, 382(1), pp. 60–72. doi:10.1056/NEJMRA1715715.

Christianson, H.C. *et al.* (2013) 'Cancer cell exosomes depend on cell-surface heparan sulfate proteoglycans for their internalization and functional activity', *Proceedings of the National Academy of Sciences of the United States of America*, 110(43), pp. 17380–17385. doi:10.1073/PNAS.1304266110/-/DCSUPPLEMENTAL/PNAS.201304266SI.PDF.

Christov, C.P. *et al.* (2006) 'Functional requirement of noncoding Y RNAs for human chromosomal DNA replication.', *Molecular and cellular biology*, 26(18), pp. 6993–7004. doi:10.1128/MCB.01060-06.

Chugani, D.C., Rome, L.H. and Kedersha, N.L. (1993) 'Evidence that vault ribonucleoprotein particles localize to the nuclear pore complex', *Journal of Cell Science*, 106(1), pp. 23–29. doi:10.1242/JCS.106.1.23.

Cirri, P. and Chiarugi, P. (2012) 'Cancer-associated-fibroblasts and tumour cells: a diabolic liaison driving cancer progression', *Cancer and Metastasis Reviews*, 31(1–2), pp. 195–208. doi:10.1007/s10555-011-9340-x.

Cittelly, D.M. *et al.* (2010) 'Downregulation of miR-342 is associated with tamoxifen resistant breast tumors', *Molecular Cancer*, 9(1), p. 317. doi:10.1186/1476-4598-9-317.

Ciuffa, R. *et al.* (2015) 'The Selective Autophagy Receptor p62 Forms a Flexible Filamentous Helical Scaffold', *Cell Reports*, 11(5), pp. 748–758. doi:10.1016/J.CELREP.2015.03.062.

Cocozza, F. *et al.* (2020) 'SnapShot: Extracellular Vesicles', *Cell*, 182(1), pp. 262-262.e1.

doi:10.1016/J.CELL.2020.04.054.

Colley, H.E. *et al.* (2011) 'Development of tissue-engineered models of oral dysplasia and early invasive oral squamous cell carcinoma.', *British journal of cancer*, 105(10), pp. 1582–92. doi:10.1038/bjc.2011.403.

Conde-Vancells, J. *et al.* (2008) 'Characterization and comprehensive proteome profiling of exosomes secreted by hepatocytes.', *Journal of proteome research*, 7(12), pp. 5157–66. Available at: http://www.ncbi.nlm.nih.gov/pubmed/19367702 (Accessed: 9 February 2019).

Cong, L. *et al.* (2013) 'Multiplex Genome Engineering Using CRISPR/Cas Systems', *Science*, 339(6121), pp. 819–823. doi:10.1126/SCIENCE.1231143.

Creemers, E.E., Tijsen, A.J. and Pinto, Y.M. (2012) 'Circulating MicroRNAs: Novel biomarkers and extracellular communicators in cardiovascular disease?', *Circulation Research*, pp. 483–495. doi:10.1161/CIRCRESAHA.111.247452.

Cristaldi, M. *et al.* (2019) 'Salivary Biomarkers for Oral Squamous Cell Carcinoma Diagnosis and Follow-Up: Current Status and Perspectives', *Frontiers in Physiology*, 10, p. 1476. doi:10.3389/FPHYS.2019.01476.

Cvjetkovic, A. *et al.* (2016) 'Detailed Analysis of Protein Topology of Extracellular Vesicles–Evidence of Unconventional Membrane Protein Orientation', *Scientific Reports 2016 6:1*, 6(1), pp. 1–12. doi:10.1038/srep36338.

D'Souza-Schorey, C. and Clancy, J.W. (2012) 'Tumor-derived microvesicles: shedding light on novel microenvironment modulators and prospective cancer biomarkers', *Genes & Development*, 26(12), pp. 1287–1299. doi:10.1101/gad.192351.112.

Das, D. *et al.* (2016) 'Major vault protein regulates cell growth/survival signalling through oxidative modifications', *Cellular signalling*, 28(1), p. 12. doi:10.1016/J.CELLSIG.2015.10.007.

Demory Beckler, M. *et al.* (2013) 'Proteomic Analysis of Exosomes from Mutant KRAS Colon Cancer Cells Identifies Intercellular Transfer of Mutant KRAS', *Molecular & Cellular Proteomics*, 12(2), pp. 343–355. doi:10.1074/mcp.M112.022806.

Depraetere, V. (2000) '"Eat me"signals of apoptotic bodies', *Nature Cell Biology*, 2(6), pp. E104–E104. doi:10.1038/35014098.

Deregibus, M.C. *et al.* (2007) 'Endothelial progenitor cell derived microvesicles activate an angiogenic program in endothelial cells by a horizontal transfer of mRNA', *Blood*, 110(7), pp. 2440–2448. doi:10.1182/blood-2007-03-078709.

Desrochers, L.M., Antonyak, M.A. and Cerione, R.A. (2016) 'Extracellular Vesicles: Satellites of Information Transfer in Cancer and Stem Cell Biology', *Developmental Cell*, 37(4), pp. 301–309. doi:10.1016/j.devcel.2016.04.019.

Diaz, G. *et al.* (2018) 'Protein Digestion, Ultrafiltration, and Size Exclusion Chromatography to Optimize the Isolation of Exosomes from Human Blood Plasma and Serum', *Journal of Visualized Experiments : JoVE*, 2018(134), p. 57467. doi:10.3791/57467.

Dieci, G. *et al.* (2007) 'The expanding RNA polymerase III transcriptome', *Trends in Genetics*, 23(12), pp. 614–622. doi:10.1016/j.tig.2007.09.001.

Dong, L. *et al.* (2020) 'Comprehensive evaluation of methods for small extracellular vesicles separation from human plasma, urine and cell culture medium', *Journal of Extracellular Vesicles*, 10(2). doi:10.1002/jev2.12044.

Driedonks, T.A.P. and Nolte-'t Hoen, E.N.M. (2019) 'Circulating Y-RNAs in Extracellular Vesicles and Ribonucleoprotein Complexes; Implications for the Immune System', *Frontiers in Immunology*, 9, p. 3164. doi:10.3389/fimmu.2018.03164.

Duray, A. *et al.* (2012) 'Human papillomavirus DNA strongly correlates with a poorer prognosis in oral cavity carcinoma', *The Laryngoscope*, 122(7), pp. 1558–1565. doi:10.1002/LARY.23298.

Duz, M.B. *et al.* (2016) 'Identification of miR-139-5p as a saliva biomarker for tongue squamous cell carcinoma: a pilot study', *Cellular Oncology*, 39(2), pp. 187–193. doi:10.1007/s13402-015-0259-z.

Economopoulou, P. and Psyrri, A. (2017) *Epidemiology, Risk factors and Pathogenesis of Squamous Cell Tumours, Head & Neck Cancers: Essentials for Clinicians*. Available at: http://oncologypro.esmo.org/content/download/113133/1971849/file/2017-ESMO-Essentials-for-Clinicians-Head-Neck-Cancers-Chapter-1.pdf (Accessed: 24 October 2018).

Einspanier, R. and Plath, A. (1998) 'Detecting mRNA by Use of the Ribonuclease Protection Assay (RPA)', *Molecular Biomethods Handbook*, pp. 51–57. doi:10.1007/978-1-59259-642-3_5.

Eldh, M. *et al.* (2012) 'Importance of RNA isolation methods for analysis of exosomal RNA: Evaluation of different methods', *Molecular Immunology*, 50(4), pp. 278–286. doi:10.1016/J.MOLIMM.2012.02.001.

Elliott, M.R. *et al.* (2009) 'Nucleotides released by apoptotic cells act as a find-me signal to promote phagocytic clearance.', *Nature*, 461(7261), pp. 282–6. doi:10.1038/nature08296.

Fabbiano, F. *et al.* (2020) 'RNA packaging into extracellular vesicles: An orchestra of RNA-binding proteins?', *Journal of Extracellular Vesicles*, 10(2). doi:10.1002/JEV2.12043.

Fahey, M.S. *et al.* (1996) 'Dysregulation of autocrine TGF-β isoform production and ligand responses in human tumour-derived and Ha-ras-transfected keratinocytes and fibroblasts', *British Journal of Cancer*, 74(7), pp. 1074–1080. doi:10.1038/bjc.1996.492.

Falaleeva, M. and Stamm, S. (2013) 'Processing of snoRNAs as a new source of regulatory non-coding RNAs snoRNA fragments form a new class of functional RNAs', *BioEssays : news and reviews in molecular, cellular and developmental biology*, 35(1), p. 46. doi:10.1002/BIES.201200117.

Fang, S. *et al.* (2020) 'Osteogenic Effect of tsRNA-10277-Loaded Exosome Derived from Bone Mesenchymal Stem Cells on Steroid-Induced Osteonecrosis of the Femoral Head', *Drug Design, Development and Therapy*, 14, p. 4579. doi:10.2147/DDDT.S258024.

Feng, D. *et al.* (2010) 'Cellular internalization of exosomes occurs through phagocytosis', *Traffic (Copenhagen, Denmark)*, 11(5), pp. 675–687. doi:10.1111/J.1600-0854.2010.01041.X.

Filipe, V., Hawe, A. and Jiskoot, W. (2010) 'Critical Evaluation of Nanoparticle Tracking Analysis (NTA) by NanoSight for the Measurement of Nanoparticles and Protein Aggregates', *Pharmaceutical Research*, 27(5), p. 796. doi:10.1007/S11095-010-0073-2.

Filonov, G.S. *et al.* (2014) 'Broccoli:Rapid Selection of an RNA Mimic of GreenFluorescent Protein by Fluorescence-Based Selection and Directed Evolution', *Journal of the American Chemical Society*, 136(46), p. 16299. doi:10.1021/JA508478X.

Filonov, G.S. *et al.* (2015) 'In-gel imaging of RNA processing using Broccoli reveals optimal aptamer expression strategies', *Chemistry & biology*, 22(5), p. 649. doi:10.1016/J.CHEMBIOL.2015.04.018.

Filonov, G.S. and Jaffrey, S.R. (2016) 'RNA Imaging with Dimeric Broccoli in Live Bacterial and Mammalian Cells', *Current protocols in chemical biology*, 8(1), pp. 1–28. doi:10.1002/9780470559277.ch150174.

Friedl, P., Vischer, P. and Freyberg, M.A. (2002) 'The role of thrombospondin-1 in apoptosis.', *Cellular and molecular life sciences : CMLS*, 59(8), pp. 1347–57. Available at: http://www.ncbi.nlm.nih.gov/pubmed/12363037 (Accessed: 6 February 2019).

Frühbeis, C. *et al.* (2013) 'Neurotransmitter-triggered transfer of exosomes mediates oligodendrocyte-neuron communication', *PLoS biology*, 11(7). doi:10.1371/JOURNAL.PBIO.1001604.

Gai, C. *et al.* (2018) 'Salivary extracellular vesicle-associated miRNAs as potential biomarkers in oral squamous cell carcinoma.', *BMC cancer*, 18(1), p. 439. doi:10.1186/s12885-018-4364-z.

Galbiati, E. *et al.* (2018) 'A fast and straightforward procedure for vault nanoparticle purification and the characterization of its endocytic uptake', *Biochimica et Biophysica Acta (BBA) - General Subjects*, 1862(10), pp. 2254–2260. doi:10.1016/j.bbagen.2018.07.018.

Gámez-Valero, A. *et al.* (2016) 'Size-Exclusion Chromatography-based isolation minimally alters Extracellular Vesicles' characteristics compared to precipitating agents', *Scientific Reports 2016 6:1*, 6(1), pp. 1–9. doi:10.1038/srep33641.

Ghossoub, R. *et al.* (2014) 'Syntenin-ALIX exosome biogenesis and budding into multivesicular bodies are controlled by ARF6 and PLD2', *Nature Communications*, 5(1), p. 3477. doi:10.1038/ncomms4477.

Giard, D.J. *et al.* (1973) 'In vitro cultivation of human tumors: establishment of cell lines derived from a series of solid tumors.', *Journal of the National Cancer Institute*, 51(5), pp. 1417–23. Available at: http://www.ncbi.nlm.nih.gov/pubmed/4357758 (Accessed: 23 September 2018).

Gillison, M.L. *et al.* (2008) 'Distinct Risk Factor Profiles for Human Papillomavirus Type 16–Positive and Human Papillomavirus Type 16–Negative Head and Neck Cancers', *JNCI: Journal of the National Cancer Institute*, 100(6), pp. 407–420. doi:10.1093/jnci/djn025.

Goldenberg, D. *et al.* (2004) 'Habitual Risk Factors for Head and Neck Cancer', *Otolaryngology-Head and Neck Surgery*, 131(6), pp. 986–993. doi:10.1016/j.otohns.2004.02.035.

Golec, E. *et al.* (2019) 'The Noncoding RNA nc886 Regulates PKR Signaling and Cytokine Production in Human Cells.', *Journal of immunology*, 202(1), pp. 131–141. doi:10.4049/jimmunol.1701234.

Gonzales, P.A. *et al.* (2009) 'Large-Scale Proteomics and Phosphoproteomics of Urinary Exosomes', *Journal of the American Society of Nephrology : JASN*, 20(2), p. 363. doi:10.1681/ASN.2008040406.

Gonzalez-Begne, M. *et al.* (2009) 'Proteomic analysis of human parotid gland exosomes by multidimensional protein identification technology (MudPIT)', *Journal of Proteome Research*, 8(3), pp. 1304–1314. doi:10.1021/pr800658c.

Good, P. *et al.* (1997) 'Expression of small, therapeutic RNAs in human cell nuclei', *Gene Therapy 1997 4:1*, 4(1), pp. 45–54. doi:10.1038/sj.gt.3300354.

Gopinath, S.C.B. *et al.* (2005) 'Human vault-associated non-coding RNAs bind to mitoxantrone, a chemotherapeutic compound.', *Nucleic acids research*, 33(15), pp. 4874–81. doi:10.1093/nar/gki809.

Gopinath, S.C.B., Wadhwa, R. and Kumar, P.K.R. (2010) 'Expression of Noncoding Vault RNA in Human Malignant Cells and Its Importance in Mitoxantrone Resistance', *Molecular Cancer Research*, 8(11), pp. 1536–1546. doi:10.1158/1541-7786.MCR-10-0242.

Graner, M.W. *et al.* (2009) 'Proteomic and immunologic analyses of brain tumor exosomes', *The FASEB Journal*, 23(5), pp. 1541–1557. doi:10.1096/fj.08-122184.

Grapp, M. *et al.* (2013) 'Choroid plexus transcytosis and exosome shuttling deliver folate into brain parenchyma', *Nature Communications*, 4(1), p. 2123. doi:10.1038/ncomms3123.

Grate, D. and Wilson, C. (1999) 'Laser-mediated, site-specific inactivation of RNA transcripts', *Proceedings of the National Academy of Sciences of the United States of America*, 96(11), p. 6131. doi:10.1073/PNAS.96.11.6131.

Greither, T. *et al.* (2017) 'Salivary miR-93 and miR-200a as post-radiotherapy biomarkers in head and neck squamous cell carcinoma', *Oncology Reports*, 38(2), pp. 1268–1275. doi:10.3892/OR.2017.5764.

Gruber, A.R. *et al.* (2008) 'The Vienna RNA Websuite', *Nucleic Acids Research*, 36(suppl_2), pp. W70–W74. doi:10.1093/NAR/GKN188.

Gupta, D. *et al.* (2019) 'CRISPR-Cas9 system: A new-fangled dawn in gene editing', *Life Sciences*, 232, p. 116636. doi:10.1016/J.LFS.2019.116636.

Guzzi, N. *et al.* (2018) 'Pseudouridylation of tRNA-Derived Fragments Steers Translational Control in Stem Cells', *Cell*, 173(5), pp. 1204-1216.e26. doi:10.1016/J.CELL.2018.03.008.

Haderk, F. *et al.* (2017) 'Tumor-derived exosomes modulate PD-L1 expression in monocytes.', *Science immunology*, 2(13), p. eaah5509. doi:10.1126/sciimmunol.aah5509.

Hahne, J.C., Lampis, A. and Valeri, N. (2021) 'Vault RNAs: hidden gems in RNA and protein regulation', *Cellular and Molecular Life Sciences*, 78(4), p. 1487. doi:10.1007/S00018-020-03675-9.

Hamill, D.R. and Suprenant, K.A. (1997) 'Characterization of the Sea Urchin Major Vault Protein: A Possible Role for Vault Ribonucleoprotein Particles in Nucleocytoplasmic Transport', *Developmental Biology*, 190(1), pp. 117–128. doi:10.1006/dbio.1997.8676.

Han, H.S. *et al.* (2020) 'Bile-derived circulating extracellular miR-30d-5p and miR-92a-3p as potential biomarkers for cholangiocarcinoma', *Hepatobiliary and Pancreatic Diseases International*, 19(1), pp. 41–50. doi:10.1016/j.hbpd.2019.10.009.

Han, M. *et al.* (2011) 'Targeted Vault Nanoparticles Engineered with an Endosomolytic Peptide Deliver Biomolecules to the Cytoplasm', *ACS Nano*, 5(8), pp. 6128–6137. doi:10.1021/NN2014613.

zur Hausen, H. and de Villiers, E.-M. (1994) 'HUMAN PAPILLOMA VIRUSES', *Annu. Rev. Microbial. 1994*, 48, pp. 427–474. Available at: www.annualreviews.org (Accessed: 31 August 2021).

Hauser, P., Wang, S. and Didenko, V. V. (2017) 'Apoptotic Bodies: Selective Detection in Extracellular Vesicles', in *Methods in molecular biology*, pp. 193–200. doi:10.1007/978-1-4939-6759-9_12.

He, L. *et al.* (2020) 'Salivary exosomal miR-24-3p serves as a potential detective biomarker for oral squamous cell carcinoma screening', *Biomedicine & Pharmacotherapy*, 121, p. 109553. doi:10.1016/J.BIOPHA.2019.109553.

He, M. *et al.* (2015) 'Hepatocellular carcinoma-derived exosomes promote motility of immortalized hepatocyte through transfer of oncogenic proteins and RNAs', *Carcinogenesis*, 36(9), pp. 1008–1018. doi:10.1093/carcin/bgv081.

He, X. *et al.* (2018) 'Human tRNA-Derived Small RNAs Modulate Host–Oral Microbial Interactions':, *https://doi.org/10.1177/0022034518770605*, 97(11), pp. 1236–1243. doi:10.1177/0022034518770605.

Heijnen, H.F. *et al.* (1999) 'Activated platelets release two types of membrane vesicles: microvesicles by surface shedding and exosomes derived from exocytosis of multivesicular bodies and alpha-granules.', *Blood*, 94(11), pp. 3791–9. Available at: http://www.ncbi.nlm.nih.gov/pubmed/10572093 (Accessed: 27 January 2019).

Hembruff, S.L. *et al.* (2010) 'Loss of Transforming Growth Factor-β Signaling in Mammary Fibroblasts Enhances CCL2 Secretion to Promote Mammary Tumor Progression through Macrophage-Dependent and -Independent Mechanisms', *Neoplasia*, 12(5), pp. 425–433. doi:10.1593/NEO.10200.

Hemler, M.E. (2005) 'Tetraspanin functions and associated microdomains', *Nature Reviews Molecular Cell Biology*, 6(10), pp. 801–811. doi:10.1038/nrm1736.

Henne, W.M., Stenmark, H. and Emr, S.D. (2013) 'Molecular mechanisms of the membrane sculpting ESCRT pathway.', *Cold Spring Harbor perspectives in biology*, 5(9), p. a016766. doi:10.1101/cshperspect.a016766.

Henríquez-Hernández, L.A. *et al.* (2012) 'MVP expression in the prediction of clinical outcome of locally advanced oral squamous cell carcinoma patients treated with radiotherapy.', *Radiation oncology*, 7, p. 147. doi:10.1186/1748-717X-7-147.

Herlevsen, M. *et al.* (2007) 'Depletion of major vault protein increases doxorubicin sensitivity and nuclear accumulation and disrupts its sequestration in lysosomes', *Molecular Cancer Therapeutics*, 6(6), pp. 1804–1813. doi:10.1158/1535-7163.MCT-06-0372.

Herrmann, C. *et al.* (1999) 'Recombinant major vault protein is targeted to neuritic tips of PC12 cells.', *The Journal of cell biology*, 144(6), pp. 1163–72. Available at: http://www.ncbi.nlm.nih.gov/pubmed/10087261 (Accessed: 10 February 2019).

Hilaire, B.G.S. *et al.* (2020) 'A rapid, low cost, and highly sensitive SARS-CoV-2 diagnostic based on whole genome sequencing', *bioRxiv*, p. 2020.04.25.061499. doi:10.1101/2020.04.25.061499.

Hirata, S. *et al.* (2000) 'Expression of drug resistance-related genes in head and neck squamous cell carcinomas and normal mucosa.', *Japanese journal of cancer research : Gann*, 91(1), pp. 84–90. Available at: http://www.ncbi.nlm.nih.gov/pubmed/10744048 (Accessed: 1 March 2019).

Holme, P.A. *et al.* (1994) 'Demonstration of platelet-derived microvesicles in blood from patients with activated coagulation and fibrinolysis using a filtration technique and western blotting.', *Thrombosis and haemostasis*, 72(5), pp. 666–71. Available at: http://www.ncbi.nlm.nih.gov/pubmed/7900071 (Accessed: 27 January 2019).

Hong, Y. *et al.* (2018) 'Comparison and optimization of CRISPR/dCas9/gRNA genome-labeling systems for live cell imaging', *Genome Biology 2018 19:1*, 19(1), pp. 1–10. doi:10.1186/S13059-018-1413-5.

Horos, R., Büscher, M., Kleinendorst, R., *et al.* (2019) 'The Small Non-coding Vault RNA1-1 Acts as a Riboregulator of Autophagy', *Cell*, 176(5), pp. 1054-1067.e12. doi:10.1016/J.CELL.2019.01.030.

Horos, R., Büscher, M., Sachse, C., *et al.* (2019) 'Vault RNA emerges as a regulator of selective autophagy', *Autophagy*, 15(8), p. 1463. doi:10.1080/15548627.2019.1609861.

Hu, H. *et al.* (2020) 'miR-23a-3p-abundant small extracellular vesicles released from Gelma/nanoclay hydrogel for cartilage regeneration', *Journal of Extracellular Vesicles*, 9(1). doi:10.1080/20013078.2020.1778883.

Hu, W. *et al.* (2020) 'Comprehensive landscape of extracellular vesicle-derived RNAs in cancer initiation, progression, metastasis and cancer immunology', *Molecular Cancer*. doi:10.1186/s12943-020-01199-1.

Huang, X. *et al.* (2013) 'Characterization of human plasma-derived exosomal RNAs by deep sequencing', *BMC Genomics*, 14(1), p. 319. doi:10.1186/1471-2164-14-319.

Huang, X. *et al.* (2020) 'RNA sequencing of plasma exosomes revealed novel functional long noncoding RNAs in hepatocellular carcinoma', *Cancer Science*, 111(9), p. 3338. doi:10.1111/CAS.14516.

Hübbers, C.U. and Akgül, B. (2015) 'HPV and cancer of the oral cavity', *https://doi.org/10.1080/21505594.2014.999570*, 6(3), pp. 244–248. doi:10.1080/21505594.2014.999570.

Hussain, S. *et al.* (2013) 'NSun2-mediated cytosine-5 methylation of vault noncoding RNA determines its processing into regulatory small RNAs', *Cell Reports*, 4(2), pp. 255–261. doi:10.1016/j.celrep.2013.06.029.

Ikeda, R. *et al.* (2008) 'Hyperosmotic stress up-regulates the expression of major vault protein in SW620 human colon cancer cells', *Experimental Cell Research*, 314(16), pp. 3017–3026. doi:10.1016/j.yexcr.2008.07.001.

Ishiguro, K. *et al.* (2017) 'Combinational use of lipid-based reagents for efficient transfection of primary fibroblasts and hepatoblasts', *BioTechniques*, 63(1), pp. 37–39. doi:10.2144/000114569.

Ishii, G., Ochiai, A. and Neri, S. (2016) 'Phenotypic and functional heterogeneity of cancer-associated fibroblast within the tumor microenvironment', *Advanced Drug Delivery Reviews*, 99(Pt B), pp. 186–196. doi:10.1016/j.addr.2015.07.007.

Jang, D.H. *et al.* (2015) 'A Transcriptional Roadmap to the Senescence and Differentiation of Human Oral Keratinocytes', *The Journals of Gerontology: Series A*, 70(1), pp. 20–32. doi:10.1093/gerona/glt212.

Jenjaroenpun, P. *et al.* (2013) 'Characterization of RNA in exosomes secreted by human breast cancer cell lines using next-generation sequencing', *PeerJ*, 1(1). doi:10.7717/PEERJ.201.

Jennings, L.R. *et al.* (2016) 'Development and characterization of in vitro human oral mucosal equivalents derived from immortalized oral keratinocytes', *Tissue Engineering - Part C: Methods*, 22(12), pp. 1108–1117. doi:10.1089/ten.tec.2016.0310.

Jeppesen, D.K. *et al.* (2019) 'Reassessment of Exosome Composition', *Cell*, 177(2), pp. 428-445.e18. doi:10.1016/j.cell.2019.02.029.

Ji, H. *et al.* (2013) 'Proteome profiling of exosomes derived from human primary and metastatic colorectal cancer cells reveal differential expression of key metastatic factors and signal transduction components', *PROTEOMICS*, 13(10–11), pp. 1672–1686. doi:10.1002/PMIC.201200562.

Ji, H. *et al.* (2014) 'Deep sequencing of RNA from three different extracellular vesicle (EV) subtypes released from the human LIM1863 colon cancer cell line uncovers distinct mirna-enrichment signatures', *PLoS ONE*, 9(10). doi:10.1371/journal.pone.0110314.

Jiang, S. and Dong, Y. (2017) 'Human papillomavirus and oral squamous cell carcinoma: A review of HPV-positive oral squamous cell carcinoma and possible strategies for future', *Current Problems in Cancer*, 41(5), pp. 323–327. doi:10.1016/J.CURRPROBLCANCER.2017.02.006.

Johnson, D.E. *et al.* (2020) 'Head and neck squamous cell carcinoma', *Nature reviews. Disease primers*, 6(1), p. 92. doi:10.1038/S41572-020-00224-3.

Johnstone, R.M. *et al.* (1987) 'Vesicle formation during reticulocyte maturation. Association of plasma membrane activities with released vesicles (exosomes).', *The Journal of biological chemistry*, 262(19), pp. 9412–20. Available at: http://www.ncbi.nlm.nih.gov/pubmed/3597417 (Accessed: 16 January 2019).

Joyce, D.P., Kerin, M.J. and Dwyer, R.M. (2016) 'Exosome-encapsulated microRNAs as circulating biomarkers for breast cancer', *International Journal of Cancer*, 139(7), pp. 1443–1448. doi:10.1002/IJC.30179.

Kalluri, R. and LeBleu, V.S. (2020) 'The biology, function, and biomedical applications of exosomes', *Science (New York, N.Y.)*, 367(6478). doi:10.1126/SCIENCE.AAU6977.

Kamelgarn, M. *et al.* (2016) 'Proteomic analysis of FUS interacting proteins provides insights into FUS function and its role in ALS', *Biochimica et biophysica acta*, 1862(10), p. 2004. doi:10.1016/J.BBADIS.2016.07.015.

Kaminagakura, E. *et al.* (2012) 'High-risk human papillomavirus in oral squamous cell carcinoma of young patients', *International Journal of Cancer*, 130(8), pp. 1726–1732. doi:10.1002/IJC.26185.

Karimi, N. *et al.* (2018) 'Detailed analysis of the plasma extracellular vesicle proteome after separation from lipoproteins', *Cellular and Molecular Life Sciences*, 75(15), p. 2873. doi:10.1007/S00018-018-2773-4.

Kashyap, T. *et al.* (2018) 'Crosstalk between Raf-MEK-ERK and PI3K-Akt-GSK3β signaling networks promotes chemoresistance, invasion/migration and stemness via expression of CD44

variants (v4 and v6) in oral cancer', *Oral Oncology*, 86, pp. 234–243. doi:10.1016/J.ORALONCOLOGY.2018.09.028.

Katzmann, D.J., Babst, M. and Emr, S.D. (2001) 'Ubiquitin-dependent sorting into the multivesicular body pathway requires the function of a conserved endosomal protein sorting complex, ESCRT-I', *Cell*, 106(2), pp. 145–155. doi:10.1016/S0092-8674(01)00434-2.

Kawakubo-Yasukochi, T. *et al.* (2018) 'miR-200c-3p spreads invasive capacity in human oral squamous cell carcinoma microenvironment', *Molecular Carcinogenesis*, 57(2), pp. 295–302. doi:10.1002/mc.22744.

Kedersha, N.L. *et al.* (1990) 'Vaults. II. Ribonucleoprotein structures are highly conserved among higher and lower eukaryotes.', *The Journal of cell biology*, 110(4), pp. 895–901. Available at: http://www.ncbi.nlm.nih.gov/pubmed/1691193 (Accessed: 10 February 2019).

Kedersha, N.L. *et al.* (1991) 'Vaults. III. Vault ribonucleoprotein particles open into flower-like structures with octagonal symmetry.', *The Journal of cell biology*, 112(2), pp. 225–35. Available at: http://www.ncbi.nlm.nih.gov/pubmed/1988458 (Accessed: 11 February 2019).

Kedersha, N.L. and Rome, L.H. (1986) 'Isolation and characterization of a novel ribonucleoprotein particle: large structures contain a single species of small RNA.', *The Journal of cell biology*, 103(3), pp. 699–709. doi:10.1083/jcb.103.3.699.

Kedersha, N.L. and Rome, L.H. (1990) 'Vaults: large cytoplasmic RNP's that associate with cytoskeletal elements.', *Molecular biology reports*, 14(2–3), pp. 121–2. Available at: http://www.ncbi.nlm.nih.gov/pubmed/1694556 (Accessed: 10 February 2019).

Keerthikumar, S. *et al.* (2016) 'ExoCarta: A Web-Based Compendium of Exosomal Cargo', *Journal of Molecular Biology*, 428(4), pp. 688–692. doi:10.1016/J.JMB.2015.09.019.

Khayrullin, A. *et al.* (2019) 'Very Long-Chain C24:1 Ceramide Is Increased in Serum Extracellular Vesicles with Aging and Can Induce Senescence in Bone-Derived Mesenchymal Stem Cells', *Cells*, 8(1), p. 37. doi:10.3390/cells8010037.

Khoo, X.H. *et al.* (2019) 'Cisplatin-resistance in oral squamous cell carcinoma: Regulation by tumor cell-derived extracellular vesicles', *Cancers*, 11(8). doi:10.3390/cancers11081166.

Kickhoefer, V.A. *et al.* (1998) 'Vaults are up-regulated in multidrug-resistant cancer cell lines.', *The Journal of biological chemistry*, 273(15), pp. 8971–4. Available at: http://www.ncbi.nlm.nih.gov/pubmed/9535882 (Accessed: 10 February 2019).

Kickhoefer, V.A., Siva, A.C., *et al.* (1999) 'The 193-kD vault protein, VPARP, is a novel poly(ADP-ribose) polymerase.', *The Journal of cell biology*, 146(5), pp. 917–28. Available at: http://www.ncbi.nlm.nih.gov/pubmed/10477748 (Accessed: 11 February 2019).

Kickhoefer, V.A., Stephen, A.G., *et al.* (1999) 'Vaults and telomerase share a common subunit, TEP1.', *The Journal of biological chemistry*, 274(46), pp. 32712–7. doi:10.1074/JBC.274.46.32712.

Kickhoefer, V.A. *et al.* (2001) 'The Telomerase/vault-associated protein TEP1 is required for vault RNA stability and its association with the vault particle.', *The Journal of cell biology*, 152(1), pp. 157–64. Available at: http://www.ncbi.nlm.nih.gov/pubmed/11149928 (Accessed: 10 February 2019).

Kickhoefer, V.A. *et al.* (2002) 'The La RNA-binding Protein Interacts with the Vault RNA and Is a Vault-associated Protein', *Journal of Biological Chemistry*, 277(43), pp. 41282–41286. doi:10.1074/JBC.M206980200.

Kim, E. *et al.* (2006) 'Crosstalk between Src and major vault protein in epidermal growth factor-dependent cell signalling', *FEBS Journal*, 273(4), pp. 793–804. doi:10.1111/j.1742-4658.2006.05112.x.

Kim, S. *et al.* (2014) 'Highly efficient RNA-guided genome editing in human cells via delivery of

purified Cas9 ribonucleoproteins', *Genome Research*, 24(6), p. 1012. doi:10.1101/GR.171322.113.

Kim, S., Lee, J.W. and Park, Y.S. (2020) 'The Application of Next-Generation Sequencing to Define Factors Related to Oral Cancer and Discover Novel Biomarkers', *Life 2020, Vol. 10, Page 228*, 10(10), p. 228. doi:10.3390/LIFE10100228.

King, H.W., Michael, M.Z. and Gleadle, J.M. (2012) 'Hypoxic enhancement of exosome release by breast cancer cells', *BMC Cancer*, 12(1), p. 421. doi:10.1186/1471-2407-12-421.

Kitazono, M. *et al.* (1999) 'Multidrug resistance and the lung resistance-related protein in human colon carcinoma SW-620 cells.', *Journal of the National Cancer Institute*, 91(19), pp. 1647–53. Available at: http://www.ncbi.nlm.nih.gov/pubmed/10511592 (Accessed: 10 February 2019).

Kitazono, M. *et al.* (2001) 'Reversal of LRP-associated drug resistance in colon carcinoma SW-620 cells.', *International journal of cancer*, 91(1), pp. 126–31. Available at: http://www.ncbi.nlm.nih.gov/pubmed/11149411 (Accessed: 11 February 2019).

Koh, Y.Q. *et al.* (2018) 'Exosome enrichment by ultracentrifugation and size exclusion chromatography.', *Frontiers in bioscience (Landmark edition)*, 23, pp. 865–874. Available at: http://www.ncbi.nlm.nih.gov/pubmed/28930577 (Accessed: 27 January 2019).

Konermann, S. *et al.* (2015) 'Genome-scale transcriptional activation by an engineered CRISPR-Cas9 complex', *Nature*, 517(7536), p. 583. doi:10.1038/NATURE14136.

Kong, L.B. *et al.* (1999) 'Structure of the vault, a ubiquitous celular component.', *Structure (London, England : 1993)*, 7(4), pp. 371–9. Available at: http://www.ncbi.nlm.nih.gov/pubmed/10196123 (Accessed: 10 February 2019).

Konoshenko, M.Y. *et al.* (2018) 'Isolation of Extracellular Vesicles: General Methodologies and Latest Trends', *BioMed Research International*, 2018. doi:10.1155/2018/8545347.

Kornilov, R. *et al.* (2018) 'Efficient ultrafiltration-based protocol to deplete extracellular vesicles from fetal bovine serum.', *Journal of extracellular vesicles*, 7(1), p. 1422674. doi:10.1080/20013078.2017.1422674.

Kouketsu, A. *et al.* (2016) 'Detection of human papillomavirus infection in oral squamous cell carcinoma: a cohort study of Japanese patients', *Journal of Oral Pathology & Medicine*, 45(8), pp. 565–572. doi:10.1111/JOP.12416.

Kukurba, K.R. and Montgomery, S.B. (2015) 'RNA Sequencing and Analysis', *Cold Spring Harbor protocols*, 2015(11), p. 951. doi:10.1101/PDB.TOP084970.

Kwok, H.-H. *et al.* (2019) 'Transfer of Extracellular Vesicle-Associated-RNAs Induces Drug Resistance in ALK-Translocated Lung Adenocarcinoma', *Cancers*, 11(1), p. 104. doi:10.3390/cancers11010104.

de la Torre Gomez, C. *et al.* (2018) '"Exosomics"—A Review of Biophysics, Biology and Biochemistry of Exosomes With a Focus on Human Breast Milk', *Frontiers in Genetics*, 9, p. 92. doi:10.3389/fgene.2018.00092.

Langevin, S. *et al.* (2017) 'Comprehensive microRNA-sequencing of exosomes derived from head and neck carcinoma cells <i>in vitro</i> reveals common secretion profiles and potential utility as salivary biomarkers', *Oncotarget*, 8(47), pp. 82459–82474. doi:10.18632/oncotarget.19614.

Lässer, C. *et al.* (2017) 'Two distinct extracellular RNA signatures released by a single cell type identified by microarray and next-generation sequencing', *RNA Biology*, 14(1), pp. 58–72. doi:10.1080/15476286.2016.1249092.

Latysheva, N. *et al.* (2006) 'Syntenin-1 Is a New Component of Tetraspanin-Enriched Microdomains: Mechanisms and Consequences of the Interaction of Syntenin-1 with CD63', *Molecular and Cellular Biology*, 26(20), pp. 7707–7718. doi:10.1128/mcb.00849-06.

Law, Z.-J. *et al.* (2021) 'Extracellular Vesicle-Mediated Chemoresistance in Oral Squamous Cell Carcinoma', *Frontiers in Molecular Biosciences*, 8. doi:10.3389/FMOLB.2021.629888.

Lee, H. *et al.* (2019) 'Caveolin-1 selectively regulates microRNA sorting into microvesicles after noxious stimuli', *The Journal of Experimental Medicine*, 216(9), p. 2202. doi:10.1084/JEM.20182313.

Lee, H.M. *et al.* (2017) 'Cell-surface major vault protein promotes cancer progression through harboring mesenchymal and intermediate circulating tumor cells in hepatocellular carcinomas', *Scientific Reports*, 7(1), p. 13201. doi:10.1038/s41598-017-13501-1.

Lee, K. *et al.* (2011) 'Precursor miR-886, a novel noncoding RNA repressed in cancer, associates with PKR and modulates its activity', *RNA*, 17(6), pp. 1076–1089. doi:10.1261/rna.2701111.

Lee, K.K.-S. *et al.* (2014) 'nc886, a non-coding RNA of anti-proliferative role, is suppressed by CpG DNA methylation in human gastric cancer', *Oncotarget*, 5(11), pp. 3944–55. doi:10.18632/oncotarget.2047.

Lee, Y.S. (2015) 'A Novel Type of Non-coding RNA, nc886, Implicated in Tumor Sensing and Suppression', *Genomics & Informatics*, 13(2), p. 26. doi:10.5808/GI.2015.13.2.26.

Lehuédé, C. *et al.* (2019) 'Adipocytes promote breast cancer resistance to chemotherapy, a process amplified by obesity: role of the major vault protein (MVP)', *Breast Cancer Research*, 21(1), p. 7. doi:10.1186/s13058-018-1088-6.

Li, C.C.Y. *et al.* (2013) 'Glioma microvesicles carry selectively packaged coding and non-coding RNAs which alter gene expression in recipient cells.', *RNA biology*, 10(8), pp. 1333–44. doi:10.4161/rna.25281.

Li, F. *et al.* (2015) 'Robust expression of vault RNAs induced by influenza A virus plays a critical role in suppression of PKR-mediated innate immunity.', *Nucleic acids research*, 43(21), pp. 10321–37. doi:10.1093/nar/gkv1078.

Li, J. *et al.* (2019) 'Blockage of transferred exosome-shuttled miR-494 inhibits melanoma growth and metastasis', *Journal of Cellular Physiology*, p. jcp.28234. doi:10.1002/jcp.28234.

Li, J.Y. *et al.* (1999) 'Axonal transport of ribonucleoprotein particles (vaults).', *Neuroscience*, 91(3), pp. 1055–65. Available at: http://www.ncbi.nlm.nih.gov/pubmed/10391483 (Accessed: 10 February 2019).

Li, L. *et al.* (2016) 'Exosomes derived from hypoxic oral squamous cell carcinoma cells deliver miR-21 to normoxic cells to elicit a prometastatic phenotype', *Cancer Research*, 76(7), pp. 1770–1780. doi:10.1158/0008-5472.CAN-15-1625.

Li, L. *et al.* (2019) 'γδTDEs: An Efficient Delivery System for miR-138 with Anti-tumoral and Immunostimulatory Roles on Oral Squamous Cell Carcinoma', *Molecular Therapy - Nucleic Acids*, 14, pp. 101–113. doi:10.1016/j.omtn.2018.11.009.

Li, P. *et al.* (2017) 'Progress in Exosome Isolation Techniques.', *Theranostics*, 7(3), pp. 789–804. doi:10.7150/thno.18133.

Li, S. *et al.* (2011) 'MicroRNA Expression Profiling Identifies Activated B Cell Status in Chronic Lymphocytic Leukemia Cells', *PLoS ONE*, 6(3), p. e16956. doi:10.1371/journal.pone.0016956.

Li, W., Saraiya, A.A. and Wang, C.C. (2011) 'Gene Regulation in Giardia lambia Involves a Putative MicroRNA Derived from a Small Nucleolar RNA', *PLoS Neglected Tropical Diseases*, 5(10), p. 1338. doi:10.1371/JOURNAL.PNTD.0001338.

Li, Y. yin *et al.* (2018) 'Cancer-associated fibroblasts contribute to oral cancer cells proliferation and metastasis via exosome-mediated paracrine miR-34a-5p', *EBioMedicine*, 36, pp. 209–220. doi:10.1016/j.ebiom.2018.09.006.

Liangsupree, T., Multia, E. and Riekkola, M.L. (2021) 'Modern isolation and separation techniques for extracellular vesicles', *Journal of Chromatography A*, 1636, p. 461773. doi:10.1016/J.CHROMA.2020.461773.

Liu, C. *et al.* (2020) 'Plasma exosome-derived microRNAs expression profiling and bioinformatics analysis under cross-talk between increased low-density lipoprotein cholesterol level and ATP-sensitive potassium channels variant rs1799858', *Journal of Translational Medicine*, 18(1). doi:10.1186/s12967-020-02639-8.

Liu, C.J. *et al.* (2012) 'Exploiting salivary miR-31 as a clinical biomarker of oral squamous cell carcinoma', *Head and Neck*, 34(2), pp. 219–224. doi:10.1002/hed.21713.

Liu, S. *et al.* (2015) 'Human hepatitis B virus surface and e antigens inhibit major vault protein signaling in interferon induction pathways', *Journal of Hepatology*, 62(5), pp. 1015–1023. doi:10.1016/j.jhep.2014.11.035.

Liu, Y. *et al.* (2000) 'Telomerase-associated protein TEP1 is not essential for telomerase activity or telomere length maintenance in vivo.', *Molecular and cellular biology*, 20(21), pp. 8178–84. Available at: http://www.ncbi.nlm.nih.gov/pubmed/11027287 (Accessed: 11 February 2019).

Livshts, M.A. *et al.* (2015) 'Isolation of exosomes by differential centrifugation: Theoretical analysis of a commonly used protocol', *Scientific Reports*, 5. doi:10.1038/srep17319.

Lloret, M. *et al.* (2009) 'Major Vault Protein May Affect Nonhomologous End-Joining Repair and Apoptosis Through Ku70/80 and BAX Downregulation in Cervical Carcinoma Tumors', *International Journal of Radiation Oncology*Biology*Physics*, 73(4), pp. 976–979. doi:10.1016/j.ijrobp.2008.11.013.

Lobb, R.J. *et al.* (2015) 'Optimized exosome isolation protocol for cell culture supernatant and human plasma', *Journal of Extracellular Vesicles*, 4(1), p. 27031. doi:10.3402/jev.v4.27031.

Lötvall, J. *et al.* (2014) 'Minimal experimental requirements for definition of extracellular vesicles and their functions: a position statement from the International Society for Extracellular Vesicles.', *Journal of extracellular vesicles*, 3, p. 26913. doi:10.3402/jev.v3.26913.

Lu, Z. *et al.* (2019) 'miR-31-5p Is a Potential Circulating Biomarker and Therapeutic Target for Oral Cancer', *Molecular Therapy - Nucleic Acids*, 16, pp. 471–480. doi:10.1016/j.omtn.2019.03.012.

Ludwig, S. *et al.* (2017) 'Suppression of Lymphocyte Functions by Plasma Exosomes Correlates with Disease Activity in Patients with Head and Neck Cancer', *Clinical Cancer Research*, 23(16), pp. 4843–4854. doi:10.1158/1078-0432.CCR-16-2819.

Lunavat, T.R. *et al.* (2015) 'Small RNA deep sequencing discriminates subsets of extracellular vesicles released by melanoma cells – Evidence of unique microRNA cargos', *RNA Biology*, 12(8), pp. 810–823. doi:10.1080/15476286.2015.1056975.

Maas, S.L.N., Breakefield, X.O. and Weaver, A.M. (2017) 'Extracellular vesicles: unique intercellular delivery vehicles', *Trends in cell biology*, 27(3), p. 172. doi:10.1016/J.TCB.2016.11.003.

Mali, M. *et al.* (1990) 'Sequence of human syndecan indicates a novel gene family of integral membrane proteoglycans.', *The Journal of biological chemistry*, 265(12), pp. 6884–9. Available at: http://www.ncbi.nlm.nih.gov/pubmed/2324102 (Accessed: 20 January 2019).

Mali, P., Aach, J., *et al.* (2013) 'CAS9 transcriptional activators for target specificity screening and paired nickases for cooperative genome engineering', *Nature Biotechnology 2013 31:9*, 31(9), pp. 833–838. doi:10.1038/nbt.2675.

Mali, P., Yang, L., *et al.* (2013) 'RNA-Guided Human Genome Engineering via Cas9', *Science*, 339(6121), pp. 823–826. doi:10.1126/SCIENCE.1232033.

Margiotta, A.L., Bain, L.J. and Rice, C.D. (2017) 'Expression of the Major Vault Protein (MVP) and

Cellular Vault Particles in Fish', *The Anatomical Record*, 300(11), pp. 1981–1992. doi:10.1002/ar.23645.

Martínez, M.C. and Freyssinet, J.M. (2001) 'Deciphering the plasma membrane hallmarks of apoptotic cells: phosphatidylserine transverse redistribution and calcium entry.', *BMC cell biology*, 2, p. 20. Available at: http://www.ncbi.nlm.nih.gov/pubmed/11701087 (Accessed: 6 February 2019).

Mashima, T. *et al.* (2008) 'Interactions between antitumor drugs and vault RNA', *Nucleic Acids Symposium Series*, 52(1), pp. 217–218. doi:10.1093/NASS/NRN110.

Mathieu, M. *et al.* (2019) 'Specificities of secretion and uptake of exosomes and other extracellular vesicles for cell-to-cell communication', *Nature Cell Biology*, 21(1), pp. 9–17. doi:10.1038/s41556-018-0250-9.

Mcgregor, F. *et al.* (2002) 'Molecular Changes Associated with Oral Dysplasia Progression and Acquisition of Immortality: Potential for Its Reversal by 5-Azacytidine 1', *CANCER RESEARCH*, 62, pp. 4757–4766. Available at: https://mail-attachment.googleusercontent.com/attachment/u/0/?ui=2&ik=a35186a681&attid=0.2&permmsgid=msg-f:1597270849909734978&th=162aa56012f4be42&view=att&disp=inline&realattid=f_jfs7aw1w1&saddbat=ANGjdJ9H-Ta4tYwehP-mku-nSC9iQkWYvBBRvzXsl-tBbcWNhhQQH2x_d (Accessed: 23 September 2018).

Mehanna, H. *et al.* (2013) 'Prevalence of human papillomavirus in oropharyngeal and nonoropharyngeal head and neck cancer-systematic review and meta-analysis of trends by time and region', *Head & Neck*, 35(5), pp. 747–755. doi:10.1002/hed.22015.

Melo, S.A. *et al.* (2014) 'Cancer Exosomes Perform Cell-Independent MicroRNA Biogenesis and Promote Tumorigenesis', *Cancer Cell*, 26(5), pp. 707–721. doi:10.1016/j.ccell.2014.09.005.

Melo, S.A. *et al.* (2015) 'Glypican-1 identifies cancer exosomes and detects early pancreatic cancer.', *Nature*, 523(7559), pp. 177–82. doi:10.1038/nature14581.

Menck, K. *et al.* (2017) 'Isolation and characterization of microvesicles from peripheral blood', *Journal of Visualized Experiments*, 2017(119), p. 55057. doi:10.3791/55057.

Mendes, J.M.F. *et al.* (2020) 'Effects of IGF-1 on Proliferation, Angiogenesis, Tumor Stem Cell Populations and Activation of AKT and Hedgehog Pathways in Oral Squamous Cell Carcinoma', *International Journal of Molecular Sciences*, 21(18), pp. 1–20. doi:10.3390/IJMS21186487.

Meschini, S. *et al.* (2002) 'Role of the lung resistance-related protein (LRP) in the drug sensitivity of cultured tumor cells.', *Toxicology in vitro : an international journal published in association with BIBRA*, 16(4), pp. 389–98. Available at: http://www.ncbi.nlm.nih.gov/pubmed/12110277 (Accessed: 11 February 2019).

Min, B.-M. *et al.* (1999) 'Terminal Differentiation of Normal Human Oral Keratinocytes Is Associated with Enhanced Cellular TGF-β and Phospholipase C-γ1 Levels and Apoptotic Cell Death', *Experimental Cell Research*, 249(2), pp. 377–385. Available at: http://www.ncbi.nlm.nih.gov/pubmed/10366437 (Accessed: 26 February 2019).

Momen-Heravi, F. (2017) 'Isolation of Extracellular Vesicles by Ultracentrifugation', *Methods in molecular biology (Clifton, N.J.)*, 1660, pp. 25–32. doi:10.1007/978-1-4939-7253-1_3.

Momen-Heravi, F. and Bala, S. (2018a) 'Emerging role of non-coding RNA in oral cancer', *Cellular Signalling*, pp. 134–143. doi:10.1016/j.cellsig.2017.10.009.

Momen-Heravi, F. and Bala, S. (2018b) 'Extracellular vesicles in oral squamous carcinoma carry oncogenic miRNA profile and reprogram monocytes via NF-kB pathway', *Oncotarget*, 9(78), pp. 34838–34854. doi:10.18632/oncotarget.26208.

Monguió-Tortajada, M. *et al.* (2019) 'Extracellular vesicle isolation methods: rising impact of size-exclusion chromatography', *Cellular and Molecular Life Sciences*, pp. 2369–2382. doi:10.1007/s00018-019-03071-y.

Montecalvo, A. *et al.* (2012) 'Mechanism of transfer of functional microRNAs between mouse dendritic cells via exosomes', *Blood*, 119(3), pp. 756–766. doi:10.1182/blood-2011-02-338004.

Morelli, A.E. *et al.* (2004) 'Endocytosis, intracellular sorting, and processing of exosomes by dendritic cells', *Blood*, 104(10), pp. 3257–3266. doi:10.1182/BLOOD-2004-03-0824.

Morin, R.D. *et al.* (2010) 'Preparation and Analysis of MicroRNA Libraries Using the Illumina Massively Parallel Sequencing Technology', *Methods in Molecular Biology*, 650, pp. 173–199. doi:10.1007/978-1-60761-769-3_14.

Mossink, M.H. *et al.* (2002) 'Disruption of the murine major vault protein (MVP/LRP) gene does not induce hypersensitivity to cytostatics.', *Cancer research*, 62(24), pp. 7298–304. Available at: http://www.ncbi.nlm.nih.gov/pubmed/12499273 (Accessed: 10 February 2019).

Mossink, M.H. *et al.* (2003) 'Vaults: a ribonucleoprotein particle involved in drug resistance?', *Oncogene*, 22(47), pp. 7458–7467. doi:10.1038/sj.onc.1206947.

Mrizak, D. *et al.* (2015) 'Effect of Nasopharyngeal Carcinoma-Derived Exosomes on Human Regulatory T Cells', *JNCI: Journal of the National Cancer Institute*, 107(1), p. 363. doi:10.1093/jnci/dju363.

Mughees, M. *et al.* (2021) 'Mechanism of tumour microenvironment in the progression and development of oral cancer', *Molecular Biology Reports 2021 48:2*, 48(2), pp. 1773–1786. doi:10.1007/S11033-020-06054-6.

Mulcahy, L.A., Pink, R.C. and Carter, D.R.F. (2014) 'Routes and mechanisms of extracellular vesicle uptake', *Journal of Extracellular Vesicles*, 3(1), p. 24641. doi:10.3402/jev.v3.24641.

Muller, L. *et al.* (2016) 'Tumor-derived exosomes regulate expression of immune function-related genes in human T cell subsets', *Scientific Reports*, 6(1), p. 20254. doi:10.1038/srep20254.

Multia, E. *et al.* (2020) 'Automated On-Line Isolation and Fractionation System for Nanosized Biomacromolecules from Human Plasma', *Analytical Chemistry*, 92(19), pp. 13058–13065. doi:10.1021/ACS.ANALCHEM.0C01986.

Muralidharan-Chari, V. *et al.* (2009) 'ARF6-Regulated Shedding of Tumor Cell-Derived Plasma Membrane Microvesicles', *Current Biology*, 19(22), pp. 1875–1885. doi:10.1016/j.cub.2009.09.059.

Musante, L. *et al.* (2012) 'Biochemical and Physical Characterisation of Urinary Nanovesicles following CHAPS Treatment', *PLoS ONE*, 7(7), p. 37279. doi:10.1371/JOURNAL.PONE.0037279.

Mutschelknaus, L. *et al.* (2016) 'Exosomes Derived from Squamous Head and Neck Cancer Promote Cell Survival after Ionizing Radiation', *PLOS ONE*, 11(3), p. e0152213. doi:10.1371/journal.pone.0152213.

Nabhan, J.F. *et al.* (2012) 'Formation and release of arrestin domain-containing protein 1-mediated microvesicles (ARMMs) at plasma membrane by recruitment of TSG101 protein', *Proceedings of the National Academy of Sciences*, 109(11), pp. 4146–4151. doi:10.1073/pnas.1200448109.

Nakajima, N. *et al.* (1999) 'Application of the hybridization AT-tailing method for detection of human immunodeficiency virus RNA in cells and simian immunodeficiency virus RNA in formalin-fixed and paraffin-embedded tissues', *Journal of Virological Methods*, 81(1–2), pp. 169–177. doi:10.1016/S0166-0934(99)00072-5.

Nakurte, I. *et al.* (2018) 'Colorectal Cancer Cell Line SW480 and SW620 Released Extravascular Vesicles: Focus on Hypoxia-induced Surface Proteome Changes', *Anticancer Research*, 38(11), pp. 6133–6138. doi:10.21873/anticanres.12965.

Nandy, C. *et al.* (2009) 'Epstein–Barr Virus-Induced Expression of a Novel Human Vault RNA', *Journal of Molecular Biology*, 388(4), pp. 776–784. doi:10.1016/J.JMB.2009.03.031.

Nazarenko, I. *et al.* (2010) 'Cell surface tetraspanin Tspan8 contributes to molecular pathways of exosome-induced endothelial cell activation.', *Cancer research*, 70(4), pp. 1668–78. doi:10.1158/0008-5472.CAN-09-2470.

Nie, L. *et al.* (2010) 'Regulation of U6 Promoter Activity by Transcriptional Interference in Viral Vector-Based RNAi', *Genomics, Proteomics & Bioinformatics*, 8(3), p. 170. doi:10.1016/S1672-0229(10)60019-8.

van Niel, G., D'Angelo, G. and Raposo, G. (2018) 'Shedding light on the cell biology of extracellular vesicles', *Nature Reviews Molecular Cell Biology*, 19(4), pp. 213–228. doi:10.1038/nrm.2017.125.

Niu, C. *et al.* (2016) 'N-Glycosylation Improves the Pepsin Resistance of Histidine Acid Phosphatase Phytases by Enhancing Their Stability at Acidic pHs and Reducing Pepsin's Accessibility to Its Cleavage Sites', *Applied and Environmental Microbiology*, 82(4), p. 1004. doi:10.1128/AEM.02881-15.

Nolte'T Hoen, E.N.M. *et al.* (2012) 'Deep sequencing of RNA from immune cell-derived vesicles uncovers the selective incorporation of small non-coding RNA biotypes with potential regulatory functions', *Nucleic Acids Research*, 40(18), pp. 9272–9285. doi:10.1093/nar/gks658.

O'Brien, K. *et al.* (2020) 'RNA delivery by extracellular vesicles in mammalian cells and its applications', *Nature Reviews Molecular Cell Biology*, pp. 585–606. doi:10.1038/s41580-020-0251-y.

Oliveros, J.C. (2007-2015) Venny. An Interactive Tool for Comparing Lists with Venn's Diagrams. Available at: https://www.scirp.org/%28S%28351jmbntvnsjt1aadkposzje%29%29/reference/referencespapers.aspx?referenceid=2904043 (Accessed: 22 June 2021).

Olivier, M., Hollstein, M. and Hainaut, P. (2010) 'TP53 Mutations in Human Cancers: Origins, Consequences, and Clinical Use', *Cold Spring Harbor Perspectives in Biology*, 2(1), p. a001008. doi:10.1101/CSHPERSPECT.A001008.

Ostrowski, M. *et al.* (2010) 'Rab27a and Rab27b control different steps of the exosome secretion pathway', *Nature Cell Biology*, 12(1), pp. 19–30. doi:10.1038/ncb2000.

Özcan, S. *et al.* (2016) 'Unbiased analysis of senescence associated secretory phenotype (SASP) to identify common components following different genotoxic stresses', *Aging*, 8(7), pp. 1316–1329. doi:10.18632/aging.100971.

Paige, J.S., Wu, K.Y. and Jaffrey, S.R. (2011) 'RNA mimics of green fluorescent protein', *Science*, 333(6042), pp. 642–646. doi:10.1126/science.1207339.

Paolini, L. *et al.* (2016) 'Residual matrix from different separation techniques impacts exosome biological activity', *Scientific Reports 2016 6:1*, 6(1), pp. 1–11. doi:10.1038/srep23550.

Papillon-Cavanagh, S. *et al.* (2017) 'Impaired H3K36 methylation defines a subset of head and neck squamous cell carcinomas', *Nature genetics*, 49(2), p. 180. doi:10.1038/NG.3757.

Park, J.E. *et al.* (2010) 'Hypoxic Tumor Cell Modulates Its Microenvironment to Enhance Angiogenic and Metastatic Potential by Secretion of Proteins and Exosomes', *Molecular & Cellular Proteomics*, 9(6), pp. 1085–1099. doi:10.1074/mcp.M900381-MCP200.

Parolini, I. *et al.* (2009) 'Microenvironmental pH is a key factor for exosome traffic in tumor cells', *The Journal of biological chemistry*, 284(49), pp. 34211–34222. doi:10.1074/JBC.M109.041152.

Pasillas, M.P. *et al.* (2015) 'Proteomic Analysis Reveals a Role for Bcl2-associated Athanogene 3 and Major Vault Protein in Resistance to Apoptosis in Senescent Cells by Regulating ERK1/2 Activation', *Molecular & Cellular Proteomics*, 14(1), pp. 1–14. doi:10.1074/mcp.M114.037697.

Pedersen, K.W., Kierulf, B. and Neurauter, A. (2017) 'Specific and Generic Isolation of Extracellular Vesicles with Magnetic Beads', *Methods in molecular biology*, 1660, pp. 65–87. doi:10.1007/978-1-4939-7253-1_7.

Peinado, H. *et al.* (2012) 'Melanoma exosomes educate bone marrow progenitor cells toward a pro-metastatic phenotype through MET', *Nature Medicine*, 18(6), pp. 883–891. doi:10.1038/nm.2753.

Peinado, H., Lavotshkin, S. and Lyden, D. (2011) 'The secreted factors responsible for pre-metastatic niche formation: Old sayings and new thoughts', *Seminars in Cancer Biology*, 21(2), pp. 139–146. doi:10.1016/J.SEMCANCER.2011.01.002.

Perdomo, S. *et al.* (2016) 'Head and neck cancer burden and preventive measures in Central and South America', *Cancer Epidemiology*, 44, pp. S43–S52. doi:10.1016/J.CANEP.2016.03.012.

Persson, H. *et al.* (2009) 'The non-coding RNA of the multidrug resistance-linked vault particle encodes multiple regulatory small RNAs', *Nature Cell Biology*, 11(10), pp. 1268–1271. doi:10.1038/ncb1972.

Petti, S. (2009) 'Lifestyle risk factors for oral cancer', *Oral Oncology*, 45(4–5), pp. 340–350. doi:10.1016/J.ORALONCOLOGY.2008.05.018.

Picon, H. and Guddati, A.K. (2020) 'Mechanisms of resistance in head and neck cancer.', *American journal of cancer research*, 10(9), pp. 2742–2751. Available at: http://www.ncbi.nlm.nih.gov/pubmed/33042614 (Accessed: 26 May 2021).

Pienimaeki-Roemer, A. *et al.* (2015) 'Lipidomic and proteomic characterization of platelet extracellular vesicle subfractions from senescent platelets', *Transfusion*, 55(3), pp. 507–521. doi:10.1111/trf.12874.

Pink, R.C. *et al.* (2018) 'Royal Society Scientific Meeting: Extracellular vesicles in the tumour microenvironment', *Philosophical Transactions of the Royal Society B: Biological Sciences*, 373(1737), p. 20170066. doi:10.1098/rstb.2017.0066.

Poderycki, M.J. *et al.* (2005) 'The p80 homology region of TEP1 is sufficient for its association with the telomerase and vault RNAs, and the vault particle', *Nucleic Acids Research*, 33(3), pp. 893–902. doi:10.1093/nar/gki234.

Poeta, M.L. *et al.* (2007) 'TP53 Mutations and Survival in Squamous-Cell Carcinoma of the Head and Neck', *The New England journal of medicine*, 357(25), p. 2552. doi:10.1056/NEJMOA073770.

Poirier, J.T. (2017) 'CRISPR Libraries and Screening', *Progress in Molecular Biology and Translational Science*, 152, pp. 69–82. doi:10.1016/BS.PMBTS.2017.10.002.

Pols, M.S. and Klumperman, J. (2009) 'Trafficking and function of the tetraspanin CD63', *Experimental Cell Research*, pp. 1584–1592. doi:10.1016/j.yexcr.2008.09.020.

Polstein, L.R. and Gersbach, C.A. (2015) 'A light-inducible CRISPR/Cas9 system for control of endogenous gene activation', *Nature chemical biology*, 11(3), p. 198. doi:10.1038/NCHEMBIO.1753.

Prajapati, P. and Lambert, D.W. (2016) 'Cancer-associated fibroblasts – Not-so-innocent bystanders in metastasis to bone?', *Journal of Bone Oncology*, 5(3), pp. 128–131. doi:10.1016/j.jbo.2016.03.008.

Prgomet, Z. *et al.* (2015) 'Migration and invasion of oral squamous carcinoma cells is promoted by WNT5A, a regulator of cancer progression', *Journal of Oral Pathology & Medicine*, 44(10), pp. 776–784. doi:10.1111/jop.12292.

Prime, S.S. *et al.* (1990) 'The behaviour of human oral squamous cell carcinoma in cell culture', *The Journal of Pathology*, 160(3), pp. 259–269. doi:10.1002/path.1711600313.

Principe, S. *et al.* (2013) 'Tumor-derived exosomes and microvesicles in head and neck cancer: Implications for tumor biology and biomarker discovery', *PROTEOMICS*, 13(10–11), pp. 1608–1623.

doi:10.1002/pmic.201200533.

Pužar Dominkuš, P. *et al.* (2018) 'PKH26 labeling of extracellular vesicles: Characterization and cellular internalization of contaminating PKH26 nanoparticles', *Biochimica et Biophysica Acta - Biomembranes*, 1860(6), pp. 1350–1361. doi:10.1016/j.bbamem.2018.03.013.

Qi, L.S. *et al.* (2013) 'Repurposing CRISPR as an RNA-Guided Platform for Sequence-Specific Control of Gene Expression', *Cell*, 152(5), p. 1173. doi:10.1016/J.CELL.2013.02.022.

Qin, X. *et al.* (2019) 'Exosomal miR-196a derived from cancer-associated fibroblasts confers cisplatin resistance in head and neck cancer through targeting CDKN1B and ING5', *Genome Biology*, 20(1). doi:10.1186/S13059-018-1604-0.

Ratajczak, J. *et al.* (2006) 'Membrane-derived microvesicles: important and underappreciated mediators of cell-to-cell communication', *Leukemia 2006 20:9*, 20(9), pp. 1487–1495. doi:10.1038/sj.leu.2404296.

Ravichandran, K.S. (2010) 'Find-me and eat-me signals in apoptotic cell clearance: progress and conundrums', *The Journal of Experimental Medicine*, 207(9), pp. 1807–1817. doi:10.1084/jem.20101157.

Rezende, T.M.B., Freire, M. de S. and Franco, O.L. (2010) 'Head and neck cancer', *Cancer*, 116(21), pp. 4914–4925. doi:10.1002/cncr.25245.

Rheinwald, J.G. and Beckett, M.A. (1981) 'Tumorigenic keratinocyte lines requiring anchorage and fibroblast support cultured from human squamous cell carcinomas.', *Cancer research*, 41(5), pp. 1657–63. Available at: http://www.ncbi.nlm.nih.gov/pubmed/7214336 (Accessed: 23 September 2018).

Roelz, R. *et al.* (2010) 'Of mice and men: Human RNA polymerase III promoter U6 is more efficient than its murine homologue for shRNA expression from a lentiviral vector in both human and murine progenitor cells', *Experimental Hematology*, 38(9), pp. 792–797. doi:10.1016/J.EXPHEM.2010.05.005.

Rome, L.H. and Kickhoefer, V.A. (2012) 'Development of the Vault Particle as a Platform Technology', *ACS Nano*, 7(2), pp. 889–902. doi:10.1021/NN3052082.

Rood, I.M. *et al.* (2010) 'Comparison of three methods for isolation of urinary microvesicles to identify biomarkers of nephrotic syndrome', *Kidney International*, 78(8), pp. 810–816. doi:10.1038/ki.2010.262.

Rutter, B.D. and Innes, R.W. (2017) 'Extracellular Vesicles Isolated from the Leaf Apoplast Carry Stress-Response Proteins', *Plant Physiology*, 173(1), p. 728. doi:10.1104/PP.16.01253.

Ryu, S.J. *et al.* (2008) 'On the role of major vault protein in the resistance of senescent human diploid fibroblasts to apoptosis', *Cell Death & Differentiation*, 15(11), pp. 1673–1680. doi:10.1038/cdd.2008.96.

Ryu, S.J. and Park, S.C. (2009) 'Targeting major vault protein in senescence-associated apoptosis resistance', *Expert Opinion on Therapeutic Targets*, 13(4), pp. 479–484. doi:10.1517/14728220902832705.

Saito, T. *et al.* (1997) 'Comparative gene mapping of the human and mouse TEP1 genes, which encode one protein component of telomerases.', *Genomics*, 46(1), pp. 46–50. Available at: http://www.ncbi.nlm.nih.gov/pubmed/9403057 (Accessed: 11 February 2019).

Sajini, A.A. *et al.* (2019) 'Loss of 5-methylcytosine alters the biogenesis of vault-derived small RNAs to coordinate epidermal differentiation', *Nature Communications*, 10(1). doi:10.1038/S41467-019-10020-7.

Sakha, S. *et al.* (2016) 'Exosomal microRNA miR-1246 induces cell motility and invasion through

the regulation of DENND2D in oral squamous cell carcinoma', *Scientific Reports*, 6(1), p. 38750. doi:10.1038/srep38750.

Salahshourifar, I. *et al.* (2014) 'Genomic DNA copy number alterations from precursor oral lesions to oral squamous cell carcinoma', *Oral Oncology*, 50(5), pp. 404–412. doi:10.1016/J.ORALONCOLOGY.2014.02.005.

Sansone, P. *et al.* (2017) 'Packaging and transfer of mitochondrial DNA via exosomes regulate escape from dormancy in hormonal therapy-resistant breast cancer', *Proceedings of the National Academy of Sciences of the United States of America*, 114(43), p. E9066. doi:10.1073/PNAS.1704862114.

Sapkota, D. *et al.* (2011) 'S100A14 regulates the invasive potential of oral squamous cell carcinoma derived cell-lines in vitro by modulating expression of matrix metalloproteinases, MMP1 and MMP9', *European Journal of Cancer*, 47(4), pp. 600–610. doi:10.1016/j.ejca.2010.10.012.

Savill, J. (1997) 'Recognition and phagocytosis of cells undergoing apoptosis.', *British medical bulletin*, 53(3), pp. 491–508. Available at: http://www.ncbi.nlm.nih.gov/pubmed/9374033 (Accessed: 6 February 2019).

Scheffer, G.L. *et al.* (1995) 'The drug resistance-related protein LRP is the human major vault protein.', *Nature medicine*, 1(6), pp. 578–82. Available at: http://www.ncbi.nlm.nih.gov/pubmed/7585126 (Accessed: 11 February 2019).

Scheffer, G.L. *et al.* (2000) 'Lung resistance-related protein/major vault protein and vaults in multidrug-resistant cancer', *Current Opinion in Oncology*, pp. 550–556. doi:10.1097/00001622-200011000-00007.

Scheper, R.J. *et al.* (1993) 'Overexpression of a M(r) 110,000 vesicular protein in non-P-glycoprotein-mediated multidrug resistance.', *Cancer research*, 53(7), pp. 1475–9. Available at: http://www.ncbi.nlm.nih.gov/pubmed/7680954 (Accessed: 10 February 2019).

Schmidt, O. and Teis, D. (2012) 'The ESCRT machinery', *Current Biology*, 22(4), pp. R116–R120. doi:10.1016/j.cub.2012.01.028.

Schmittgen, T.D. and Livak, K.J. (2008) 'Analyzing real-time PCR data by the comparative CT method', *Nature Protocols 2008 3:6*, 3(6), pp. 1101–1108. doi:10.1038/nprot.2008.73.

Schroeijers, A.B. *et al.* (2000) 'The Mr 193,000 vault protein is up-regulated in multidrug-resistant cancer cell lines.', *Cancer research*, 60(4), pp. 1104–10. Available at: http://www.ncbi.nlm.nih.gov/pubmed/10706131 (Accessed: 10 February 2019).

Schroeijers, A.B. *et al.* (2002) 'Up-regulation of drug resistance-related vaults during dendritic cell development.', *Journal of immunology*, 168(4), pp. 1572–8. doi:10.4049/JIMMUNOL.168.4.1572.

Shahin, H.I. *et al.* (2021) 'Microvesicles and Exosomes Released by Amnion Epithelial Cells Under Oxidative Stress Cause Inflammatory Changes in Uterine Cells', *Biology of Reproduction* [Preprint]. doi:10.1093/biolre/ioab088.

Sharma, S., Gillespie, Boyd M, *et al.* (2011) 'Quantitative Nano-structural and Single Molecule Force Spectroscopy bio-molecular analysis of human saliva derived exosomes', *Langmuir : the ACS journal of surfaces and colloids*, 27(23), p. 14394. doi:10.1021/LA2038763.

Sharma, S., Gillespie, Boyd M., *et al.* (2011) 'Quantitative Nanostructural and Single-Molecule Force Spectroscopy Biomolecular Analysis of Human-Saliva-Derived Exosomes', *Langmuir*, 27(23), pp. 14394–14400. doi:10.1021/la2038763.

Sharma, V. *et al.* (2017) 'Signature of genetic associations in oral cancer', *Tumor Biology*, 39(10), pp. 1–9. doi:10.1177/1010428317725923.

Shurtleff, M.J. *et al.* (2017) 'Broad role for YBX1 in defining the small noncoding RNA composition of exosomes', *Proceedings of the National Academy of Sciences*, 114(43), pp. E8987–E8995.

doi:10.1073/pnas.1712108114.

Sidhom, K., Obi, P.O. and Saleem, A. (2020) 'A Review of Exosomal Isolation Methods: Is Size Exclusion Chromatography the Best Option?', *International Journal of Molecular Sciences*, 21(18), pp. 1–19. doi:10.3390/IJMS21186466.

Siegel, R.L., Miller, K.D. and Jemal, A. (2016) 'Cancer statistics, 2016', *CA: A Cancer Journal for Clinicians*, 66(1), pp. 7–30. doi:10.3322/CAAC.21332.

Singh, C. and Roy-Chowdhuri, S. (2016) 'Quantitative Real-Time PCR: Recent Advances', *Methods in Molecular Biology*, 1392, pp. 161–176. doi:10.1007/978-1-4939-3360-0_15.

Sitar, S. *et al.* (2015) 'Size Characterization and Quantification of Exosomes by Asymmetrical-Flow Field-Flow Fractionation', *Analytical Chemistry*, 87(18), pp. 9225–9233. doi:10.1021/ACS.ANALCHEM.5B01636.

Skog, J. *et al.* (2008) 'Glioblastoma microvesicles transport RNA and proteins that promote tumour growth and provide diagnostic biomarkers', *Nature Cell Biology*, 10(12), pp. 1470–1476. doi:10.1038/ncb1800.

Skogberg, G. *et al.* (2013) 'Characterization of Human Thymic Exosomes', *PLoS ONE*, 8(7). doi:10.1371/journal.pone.0067554.

Slesina, M. *et al.* (2006) 'Movement of vault particles visualized by GFP-tagged major vault protein', *Cell and Tissue Research*, 324(3), pp. 403–410. doi:10.1007/s00441-006-0158-8.

Song, W. *et al.* (2014) 'Plug-and-PlayFluorophores Extend the Spectral Propertiesof Spinach', *Journal of the American Chemical Society*, 136(4), p. 1198. doi:10.1021/JA410819X.

Spille, J.-H. and Kubitscheck, U. (2015) 'Labelling and imaging of single endogenous messenger RNA particles in vivo', *Journal of Cell Science*, 128(20), pp. 3695–3706. doi:10.1242/JCS.166728.

Sproviero, D. *et al.* (2018) 'Pathological Proteins Are Transported by Extracellular Vesicles of Sporadic Amyotrophic Lateral Sclerosis Patients', *Frontiers in Neuroscience*, 12(JUL). doi:10.3389/FNINS.2018.00487.

Stachowiak, J.C. *et al.* (2012) 'Membrane bending by protein–protein crowding', *Nature Cell Biology*, 14(9), pp. 944–949. doi:10.1038/ncb2561.

Stadler, P.F. *et al.* (2009) 'Evolution of Vault RNAs', *Molecular Biology and Evolution*, 26(9), pp. 1975–1991. doi:10.1093/molbev/msp112.

Statello, L. *et al.* (2018) 'Identification of RNA-binding proteins in exosomes capable of interacting with different types of RNA: RBP-facilitated transport of RNAs into exosomes.', *PloS one*, 13(4), p. e0195969. doi:10.1371/journal.pone.0195969.

Stranska, R. *et al.* (2018) 'Comparison of membrane affinity-based method with size-exclusion chromatography for isolation of exosome-like vesicles from human plasma', *Journal of Translational Medicine*, 16(1). doi:10.1186/s12967-017-1374-6.

Stuffers, S. *et al.* (2009) 'Multivesicular Endosome Biogenesis in the Absence of ESCRTs', *Traffic*, 10(7), pp. 925–937. doi:10.1111/j.1600-0854.2009.00920.x.

Sun, X. *et al.* (2015) 'miR-181a Targets RGS16 to Promote Chondrosarcoma Growth, Angiogenesis, and Metastasis', *Molecular Cancer Research*, 13(9), pp. 1347–1357. doi:10.1158/1541-7786.MCR-14-0697.

Svensson, K.J. *et al.* (2013) 'Exosome uptake depends on ERK1/2-heat shock protein 27 signaling and lipid Raft-mediated endocytosis negatively regulated by caveolin-1', *The Journal of biological chemistry*, 288(24), pp. 17713–17724. doi:10.1074/JBC.M112.445403.

Szaflarski, W. *et al.* (2013) 'Expression profiles of vault components MVP, TEP1 and vPARP and their correlation to other multidrug resistance proteins in ovarian cancer', *International Journal of Oncology*, 43(2), pp. 513–520. doi:10.3892/IJO.2013.1975.

Tajadini, M., Panjehpour, M. and Javanmard, S.H. (2014) 'Comparison of SYBR Green and TaqMan methods in quantitative real-time polymerase chain reaction analysis of four adenosine receptor subtypes', *Advanced Biomedical Research*, 3(1), p. 85. doi:10.4103/2277-9175.127998.

Takahashi, R. *et al.* (2017) 'The role of extracellular vesicle microRNAs in cancer biology', *Clinical Chemistry and Laboratory Medicine*, 55(5), pp. 648–656. doi:10.1515/cclm-2016-0708.

Takizawa, F., Tsuji, S. and Nagasawa, S. (1996) 'Enhancement of macrophage phagocytosis upon iC3b deposition on apoptotic cells.', *FEBS letters*, 397(2–3), pp. 269–72. Available at: http://www.ncbi.nlm.nih.gov/pubmed/8955361 (Accessed: 6 February 2019).

Tanida, I., Ueno, T. and Kominami, E. (2008) 'LC3 and Autophagy', *Methods in Molecular Biology*, 445, pp. 77–88. doi:10.1007/978-1-59745-157-4_4.

Tao, S.-C. and Guo, S.-C. (2020) 'Role of extracellular vesicles in tumour microenvironment', *Cell Communication and Signaling*, 18(1). doi:10.1186/S12964-020-00643-5.

Teng, Y. *et al.* (2017) 'MVP-mediated exosomal sorting of miR-193a promotes colon cancer progression.', *Nature communications*, 8, p. 14448. doi:10.1038/ncomms14448.

Theodoraki, M.-N. *et al.* (2018) 'Clinical Significance of PD-L1 $^{+}$ Exosomes in Plasma of Head and Neck Cancer Patients', *Clinical Cancer Research*, 24(4), pp. 896–905. doi:10.1158/1078-0432.CCR-17-2664.

Théry, C. *et al.* (2001) 'Proteomic analysis of dendritic cell-derived exosomes: a secreted subcellular compartment distinct from apoptotic vesicles.', *Journal of immunology*, 166(12), pp. 7309–18. Available at: http://www.ncbi.nlm.nih.gov/pubmed/11390481 (Accessed: 9 February 2019).

Théry, C. *et al.* (2006) 'Isolation and Characterization of Exosomes from Cell Culture Supernatants and Biological Fluids', *Current Protocols in Cell Biology*, 30(1), pp. 3.22.1-3.22.29. doi:10.1002/0471143030.cb0322s30.

Théry, C. *et al.* (2018) 'Minimal information for studies of extracellular vesicles 2018 (MISEV2018): a position statement of the International Society for Extracellular Vesicles and update of the MISEV2014 guidelines', *Journal of Extracellular Vesicles*, 7(1). doi:10.1080/20013078.2018.1535750.

Thorvaldsdóttir, H., Robinson, J.T. and Mesirov, J.P. (2013) 'Integrative Genomics Viewer (IGV): high-performance genomics data visualization and exploration', *Briefings in Bioinformatics*, 14(2), p. 178. doi:10.1093/BIB/BBS017.

Tiwari, S. *et al.* (2021) 'Preparation and characterization of extracellular vesicles', *American Journal of Reproductive Immunology*, 85(2). doi:10.1111/aji.13367.

Tkach, M. *et al.* (2017) 'Qualitative differences in T-cell activation by dendritic cell-derived extracellular vesicle subtypes', *The EMBO journal*, 36(20), pp. 3012–3028. doi:10.15252/EMBJ.201696003.

Tominaga, N. *et al.* (2014) 'RPN2-mediated glycosylation of tetraspanin CD63 regulates breast cancer cell malignancy', *Molecular Cancer*, 13(1), p. 134. doi:10.1186/1476-4598-13-134.

Tominaga, N. *et al.* (2015) 'Brain metastatic cancer cells release microRNA-181c-containing extracellular vesicles capable of destructing blood–brain barrier', *Nature Communications*, 6(1), p. 6716. doi:10.1038/ncomms7716.

Tosar, J.P. *et al.* (2015) 'Assessment of small RNA sorting into different extracellular fractions revealed by high-throughput sequencing of breast cell lines', *Nucleic Acids Research*, 43(11), pp.

5601–5616. doi:10.1093/nar/gkv432.

Trajkovic, K. *et al.* (2008) 'Ceramide Triggers Budding of Exosome Vesicles into Multivesicular Endosomes', *Science*, 319(5867), pp. 1244–1247. doi:10.1126/science.1153124.

Truman, L.A. *et al.* (2008) 'CX3CL1/fractalkine is released from apoptotic lymphocytes to stimulate macrophage chemotaxis', *Blood*, 112(13), pp. 5026–5036. doi:10.1182/blood-2008-06-162404.

Valadi, H. *et al.* (2007) 'Exosome-mediated transfer of mRNAs and microRNAs is a novel mechanism of genetic exchange between cells', *Nature Cell Biology*, 9(6), pp. 654–659. doi:10.1038/ncb1596.

Vasiliou, V., Vasiliou, K. and Nebert, D.W. (2009) 'Human ATP-binding cassette (ABC) transporter family', *Human Genomics*, 3(3), p. 281. doi:10.1186/1479-7364-3-3-281.

Vila-Liante, V. *et al.* (2016) 'Impact of sample processing on the measurement of circulating microparticles: storage and centrifugation parameters', *Clinical Chemistry and Laboratory Medicine*, 54(11), pp. 1759–1767. doi:10.1515/CCLM-2016-0036.

Di Vizio, D. *et al.* (2009) 'Oncosome Formation in Prostate Cancer: Association with a Region of Frequent Chromosomal Deletion in Metastatic Disease', *Cancer Research*, 69(13), pp. 5601–5609. doi:10.1158/0008-5472.CAN-08-3860.

Wang, F. *et al.* (2017) 'Extracellular vesicles-mediated transfer of miR-208a/b exaggerate hypoxia/reoxygenation injury in cardiomyocytes by reducing QKI expression', *Molecular and Cellular Biochemistry*, 431(1), pp. 187–195. doi:10.1007/S11010-017-2990-4.

Wang, S. *et al.* (2016) 'MicroRNA-1246 promotes growth and metastasis of colorectal cancer cells involving CCNG2 reduction', *Molecular Medicine Reports*, 13(1), pp. 273–280. doi:10.3892/MMR.2015.4557.

Wang, T. *et al.* (2014) 'Hypoxia-inducible factors and RAB22A mediate formation of microvesicles that stimulate breast cancer invasion and metastasis.', *Proceedings of the National Academy of Sciences of the United States of America*, 111(31), pp. E3234-42. doi:10.1073/pnas.1410041111.

Wang, W. *et al.* (2020) 'Major vault protein plays important roles in viral infection', *Iubmb Life*, 72(4), p. 624. doi:10.1002/IUB.2200.

Wang, Z. *et al.* (2015) 'MiR-30a-5p is induced by Wnt/β-catenin pathway and promotes glioma cell invasion by repressing NCAM', *Biochemical and Biophysical Research Communications*, 465(3), pp. 374–380. doi:10.1016/j.bbrc.2015.08.007.

Warda, A.S. *et al.* (2017) 'Human METTL16 is a N6-methyladenosine (m6A) methyltransferase that targets pre-mRNAs and various non-coding RNAs', *EMBO Reports*, 18(11), p. 2004. doi:10.15252/EMBR.201744940.

Webber, J. and Clayton, A. (2013) 'How pure are your vesicles?', *Journal of Extracellular Vesicles*, 2(1). doi:10.3402/jev.v2i0.19861.

Wei, Z. *et al.* (2017) 'Coding and noncoding landscape of extracellular RNA released by human glioma stem cells', *Nature Communications 2017 8:1*, 8(1), pp. 1–15. doi:10.1038/s41467-017-01196-x.

Welton, J.L. *et al.* (2010) 'Proteomics analysis of bladder cancer exosomes', *Molecular and Cellular Proteomics*, 9(6), pp. 1324–1338. doi:10.1074/mcp.M000063-MCP201.

Wiegard, J.C. *et al.* (2021) 'Northern Blot Detection of Tiny RNAs', *Methods in Molecular Biology*, 2300, pp. 41–58. doi:10.1007/978-1-0716-1386-3_5.

Wienert, B. *et al.* (2019) 'Unbiased detection of CRISPR off-targets in vivo using DISCOVER-Seq', *Science*, 364(6437), p. 286. doi:10.1126/SCIENCE.AAV9023.

Winck, F. V. *et al.* (2015) 'Insights into immune responses in oral cancer through proteomic analysis of saliva and salivary extracellular vesicles', *Scientific Reports*, 5. doi:10.1038/SREP16305.

Wojtowicz, K. *et al.* (2017) 'vPARP Adjusts MVP Expression in Drug-resistant Cell Lines in Conjunction with MDR Proteins', *Anticancer Research*, 37(6), pp. 3015–3023. doi:10.21873/anticanres.11656.

Wyckoff, J. *et al.* (2004) 'A Paracrine Loop between Tumor Cells and Macrophages Is Required for Tumor Cell Migration in Mammary Tumors', *Cancer Research*, 64(19), pp. 7022–7029. doi:10.1158/0008-5472.CAN-04-1449.

Xiao, Y.-S. *et al.* (2019) 'Major vault protein is a direct target of Notch1 signaling and contributes to chemoresistance in triple-negative breast cancer cells', *Cancer Letters*, 440–441, pp. 156–167. doi:10.1016/j.canlet.2018.09.031.

Xu, R. *et al.* (2015) 'Highly-purified exosomes and shed microvesicles isolated from the human colon cancer cell line LIM1863 by sequential centrifugal ultrafiltration are biochemically and functionally distinct', *Methods*, 87, pp. 11–25. doi:10.1016/j.ymeth.2015.04.008.

Xu, R. *et al.* (2016) 'Extracellular vesicle isolation and characterization: toward clinical application', *The Journal of Clinical Investigation*, 126(4), p. 1152. doi:10.1172/JCI81129.

Yamada, T. *et al.* (2013) 'Cell Infectivity in Relation to Bovine Leukemia Virus gp51 and p24 in Bovine Milk Exosomes', *PLoS ONE*, 8(10). doi:10.1371/journal.pone.0077359.

Yang, J.-S. *et al.* (2008) 'A role for phosphatidic acid in COPI vesicle fission yields insights into Golgi maintenance', *Nature Cell Biology*, 10(10), pp. 1146–1153. doi:10.1038/ncb1774.

Yokoi, A. *et al.* (2017) 'Malignant extracellular vesicles carrying MMP1 mRNA facilitate peritoneal dissemination in ovarian cancer', *Nature Communications*, 8, p. 14470. doi:10.1038/ncomms14470.

Yoshioka, Y. *et al.* (2013) 'Comparative marker analysis of extracellular vesicles in different human cancer types.', *Journal of extracellular vesicles*, 2. doi:10.3402/jev.v2i0.20424.

Yu, X., Odenthal, M. and Fries, J.W.U. (2016) 'Exosomes as miRNA Carriers: Formation–Function–Future', *International Journal of Molecular Sciences*, 17(12). doi:10.3390/IJMS17122028.

Yuan, D. *et al.* (2016) 'Extracellular miR-1246 promotes lung cancer cell proliferation and enhances radioresistance by directly targeting DR5', *Oncotarget*, 7(22), pp. 32707–22. doi:10.18632/oncotarget.9017.

Yuan, L. *et al.* (2021) 'Major vault protein (MVP) negatively regulates osteoclastogenesis via calcineurin-NFATc1 pathway inhibition', *Theranostics*, 11(15), p. 7247. doi:10.7150/THNO.58468.

Zarovni, N. *et al.* (2015) 'Integrated isolation and quantitative analysis of exosome shuttled proteins and nucleic acids using immunocapture approaches', *Methods*, 87, pp. 46–58. doi:10.1016/j.ymeth.2015.05.028.

Zhang, B. *et al.* (2012) 'The expression and significance of MRP1, LRP, TOPOIIβ, and BCL2 in tongue squamous cell carcinoma', *Journal of Oral Pathology & Medicine*, 41(2), pp. 141–148. doi:10.1111/j.1600-0714.2011.01066.x.

Zhang, H. *et al.* (2018) 'Identification of distinct nanoparticles and subsets of extracellular vesicles by asymmetric flow field-flow fractionation.', *Nature cell biology*, 20(3), pp. 332–343. doi:10.1038/s41556-018-0040-4.

Zheng, C.-L. *et al.* (2004) 'Characterization of MVP and VPARP assembly into vault ribonucleoprotein complexes', *Biochemical and Biophysical Research Communications*, 326(1), pp. 100–107. doi:10.1016/J.BBRC.2004.11.006.

Zhou, P. *et al.* (2016) 'miR-17-92 plays an oncogenic role and conveys chemo-resistance to cisplatin

in human prostate cancer cells', *International Journal of Oncology*, 48(4), pp. 1737–1748. doi:10.3892/IJO.2016.3392.

Zhou, Y. *et al.* (2018) 'Exosomes in Nasopharyngeal Carcinoma', *Journal of Cancer*, 9(5), p. 767. doi:10.7150/JCA.22505.

Zhu, L. *et al.* (2019) 'Exosomal tRNA-derived small RNA as a promising biomarker for cancer diagnosis', *Molecular Cancer*, 18(1). doi:10.1186/S12943-019-1000-8.

Zinskie, J.A. *et al.* (2018) 'Live-cell imaging of small nucleolar RNA tagged with the broccoli aptamer in yeast', *FEMS Yeast Research*, 18(8), p. 93. doi:10.1093/FEMSYR/FOY093.

Zlotogorski-Hurvitz, A. *et al.* (2016) 'Morphological and molecular features of oral fluid-derived exosomes: oral cancer patients versus healthy individuals.', *Journal of cancer research and clinical oncology*, 142(1), pp. 101–10. doi:10.1007/s00432-015-2005-3.

van Zon, A. *et al.* (2001) 'Multiple Human Vault RNAs', *Journal of Biological Chemistry*, 276(40), pp. 37715–37721. doi:10.1074/jbc.M106055200.

van Zon, A., Mossink, Marieke H, *et al.* (2003) 'The formation of vault-tubes: a dynamic interaction between vaults and vault PARP', *Journal of Cell Science*, 116(21), pp. 4391–4400. doi:10.1242/jcs.00749.

van Zon, A., Mossink, M. H., *et al.* (2003) 'The vault complex', *Cellular and Molecular Life Sciences*, 60(9), pp. 1828–1837. doi:10.1007/s00018-003-3030-y.

Zuker, M. (2003) 'Mfold web server for nucleic acid folding and hybridization prediction', *Nucleic Acids Research*, 31(13), pp. 3406–3415. doi:10.1093/NAR/GKG595.

Zuris, J.A. *et al.* (2015) 'Efficient Delivery of Genome-Editing Proteins In Vitro and In Vivo', *Nature biotechnology*, 33(1), p. 73. doi:10.1038/NBT.3081.